

RICE UNIVERSITY

Bose-Einstein Condensation of ^{84}Sr

by

Yenny Natali Martinez de Escobar

A THESIS SUBMITTED
IN PARTIAL FULFILLMENT OF THE
REQUIREMENTS FOR THE DEGREE

Doctor of Philosophy

APPROVED, THESIS COMMITTEE:

Thomas C. Killian, Chairman
Associate Professor of Physics and
Astronomy

Han Pu
Assistant Professor of Physics and
Astronomy

Qianfan Xu
Assistant Professor of Electrical and
Computer Engineering

HOUSTON, TEXAS

DECEMBER 2012

ABSTRACT

Bose-Einstein Condensation of ^{84}Sr

by

Yenny Natali Martinez de Escobar

The achievement in 1995 of Bose-Einstein condensates (BEC) in dilute gases of alkali-metal atoms was one of the most important experimental results in recent times. Fifteen years later, the study of quantum fluids is a vibrant field exploring topics such as the effects of dimensionality and disorder on quantum fluids and the modeling of condensed-matter systems with BECs in optical lattices. This thesis describes the achievement of BEC in the alkaline-earth metal atom strontium (Sr). This new addition to the family of elements that have been Bose-condense opens new possibilities, such as the use of an optical Feshbach resonance to tune atom-atom interactions with relatively low atomic losses. Equally exciting theoretical proposals have been made for using quantum fluids made of alkaline-earth metal atoms, like creating exotic quantum magnetism states and demonstrating quantum computation in optical lattices. Previous efforts at achieving BEC with Sr focused on using the

most abundant isotopes, ^{88}Sr and ^{86}Sr , without success. This thesis also describes our use of two-photon photoassociation spectroscopy (PAS) for accurate determination of the s-wave scattering length a (a measure of the interaction strength) for all the Sr isotopes and isotope mixtures. This result was essential for determining that bosonic ^{84}Sr possesses the ideal collisional properties for efficient evaporative cooling to quantum degeneracy. ^{84}Sr would not otherwise be the isotope of choice because its natural abundance is very low (0.6%). The PAS results also showed that ^{88}Sr and ^{86}Sr have unfavorable collision properties, which explains the difficulties encountered when attempting to form quantum degenerate ^{88}Sr and ^{86}Sr .

Acknowledgments

I feel greatly indebted to my advisor, Dr. Thomas Killian, for the role he played in my development as a scientist. I was very fortunate to have such an advisor: extraordinary patient, intelligent and driven. Whatever abilities I developed in these eight years as a graduate student were mostly thanks to him. I really appreciate the time Dr. Han Pu, Dr. Qianfan Xu and Dr. Randall Hulet set aside to serve on my defense committee. I especially thank Dr. Pu and Dr. Hulet for being like second advisors to me during my graduate career. Many people at Rice served to mold me into what I have become after these years, and I really appreciate their encouragement, hope and concern for me.

The Killian lab will hold a special place in my heart. We lived many different things, from personal craziness to experimental triumph. I thank the past members of the lab for the good times when I was learning about myself and our research (especially Clayton and Sarah). But particularly, I feel extremely grateful for Pascal's companionship. Thank you for sticking around a little longer. Brian and Mi, thank you for your hard work and company. And I thank the plasma group (Jose and Patrick) for bringing saneness and humor to the group.

Quiero agradecerle a mi familia por el apoyo y amor que me han brindado durante

estos 12 (por ahí va...) años de estudio. A mis amados amigos y amigas que me quieren a pesar de que los he abandonado por bastante tiempo. Y al amor de mi vida, Melvin Ismael Escobar: nadie ha tenido mejor esposo que yo. Le agradezco a mi Padre por tenerte en mi vida.

Contents

Abstract	ii
Acknowledgments	iv
List of Illustrations	ix
List of Tables	xiii
1 Introduction	1
1.1 BEC of alkaline-earth metal atoms to now	3
1.2 Essential properties of BECs	5
1.3 Producing a BEC	8
1.3.1 Using magnetic traps for evaporative cooling	9
1.3.2 Using optical dipole traps for evaporative cooling	13
1.4 Photoassociative spectroscopy (PAS) and the scattering length	14
1.5 Thesis outline	16
2 Laser cooling and trapping Sr	19
2.1 Basic concepts of laser cooling and trapping	19
2.1.1 Atomic structure of Sr	22
2.1.2 Limits on laser cooling	25
2.2 Cooling with the 1S_0 - 1P_1 transition	26
2.2.1 Blue frequency control (magnetic cell)	30
2.3 Narrow line MOT	34
2.3.1 689 nm light	38
2.3.2 Doppler-free saturated absorption	38
2.4 Multimode optical dipole trap (ODT)	41
2.4.1 Profiling the ODT beams	44
2.4.2 Measuring trap frequencies	45
2.4.3 Modeling the ODT trap	48
2.5 Imaging techniques	50
3 PAS of Sr using an intercombination transition	54
3.1 Ultracold collision theory	56
3.1.1 Scattering length theory	60
3.2 Molecular potentials and levels	62
3.3 PA loss theory	64
3.3.1 One-photon PAS limit	69

3.4	The PAS lasers	69
3.5	The one-photon PAS experiment	72
3.5.1	Determining K_{eff} from one-photon measurements	74
3.5.2	Determining the stimulated width γ_s	76
3.5.3	Determining the relative ac Stark shift χ	79
4	Measuring the binding energy of the least-bound state	
	b_2	81
4.1	Quantum optical effect due to two laser beams	81
4.2	Experimental details	84
4.2.1	Determining K_{eff}	89
4.2.2	Frequency uncertainties	92
4.3	The scattering length a	93
4.3.1	Collisional cross section vs. energy (^{88}Sr)	95
5	Evaporative Cooling Of ^{84}Sr	98
5.1	The BEC phase transition for a nonuniform ideal gas	98
5.2	Theory of forced evaporative cooling in an ODT	104
5.2.1	Forced evaporation trajectory	108
5.3	Evaporation characteristics of ^{84}Sr	110
5.3.1	Free evaporation (thermalization)	111
5.3.2	Forced evaporation	113
6	Determining T_c	120
6.1	Analyzing the thermal component	121
6.2	Experiment with Gaussian fitting (classical)	124
6.3	Experiment with Bose-enhanced fitting	130
7	BEC in ^{84}Sr	134
7.1	Mean-field Gross-Pitaevskii equation	135
7.2	Effect of interactions: Thomas-Fermi limit	138
7.3	Making and analyzing the BEC	140
7.3.1	Castin-Dum model	144
8	Conclusion	151
A	Experimental details from Natali's notebooks	153
A.1	Data taken with ^{86}Sr	153
A.2	Calibrating pixel size with atom samples	154
A.3	Details about ^{87}Sr slave lasers setup	157
A.4	ECDL (master ^{88}Sr laser) and ^{88}Sr slave laser details	163

	viii
A.5 689 nm saturated absorption system details	164
A.6 High Finesse Fabry-Perot Cavity	179
A.7 Characteristics of our 689 nm HF FP cavity	200
A.8 922 nm laser sources and 461 nm cavities	203
A.9 Details about the 1064 nm multimode laser ODT	206
A.10 Specific details - Neutral Atoms experimental chamber	211
A.11 AutoCAD drawings	225
B Lynx 922 nm laser Status Report	233
C “Cross-over” transitions in the 689 nm sat. abs. error signal	239
Bibliography	244

Illustrations

1.1	Thermal atoms versus BEC in a harmonic trap	6
1.2	Boltzmann energy distributions before and after removing high-energy atoms	10
1.3	Zeeman energy versus magnetic field for $I = \frac{1}{2}$	11
1.4	Schematic of one- and two-photon PAS	16
2.1	Schematic of the scattering force on an atom	21
2.2	Simplified energy level diagram for ^{88}Sr	23
2.3	Naturally abundant bosonic isotopes for Sr	24
2.4	Schematic drawing of the experimental setup	27
2.5	Timing diagrams for PAS and BEC experiments	29
2.6	AutoCAD drawing of 461 nm saturation-absorption cell	30
2.7	Schematic of 461 nm saturation absorption setup	32
2.8	461 nm saturated absorption error signals	35
2.9	Timing diagram for experimental components in 689 nm MOT operation	37
2.10	689 nm laser system	39
2.11	Schematic of 689 nm saturation absorption setup	40
2.12	Schematic drawing of 1064 nm ODT setup	43
2.13	Typical ODT beam profile before traversing the vacuum chamber	45
2.14	Trap frequency measurements for 9.8 W and 5.3 W traps	46
2.15	Calculated trap depth and mean oscillation frequency versus ODT beam power	50
2.16	A sample absorption image	51
2.17	461 nm image beam spectrum of ^{84}Sr atoms	52
3.1	Two-photon PAS diagram	55
3.2	Schematic of a scattering event	57
3.3	Scattering length a as a function of square potential well energy parameter	61
3.4	Schematic of photoassociation lasers	70
3.5	One-photon PA spectra	74
3.6	Timing diagram for one-photon PAS	75
3.7	One-photon PA spectral area	77

4.1	Dressed atom picture of coupled atom states by bound-bound laser	82
4.2	Initial two-photon PAS scans	85
4.3	PAS suppression spectra for the $J = 0, v = 62$ ro-vibrational bound level	86
4.4	PAS suppression spectra for the $J = 2, v = 62$ ro-vibrational bound level	86
4.5	Autler-Townes doublet spectra	88
4.6	Timing diagram for two-photon PAS scans	89
4.7	VCO frequency calibration uncertainty	92
4.8	Energy dependence of elastic collisional cross section for Sr	97
5.1	Behavior of chemical potential	102
5.2	Maximum number in thermal cloud at T_c	103
5.3	Comparing thermalization behavior of ^{84}Sr and ^{88}Sr	111
5.4	Modeling thermalization curves for ^{84}Sr and ^{88}Sr	113
5.5	Trap model calculations for ODT characteristics during forced evaporation trajectory	114
5.6	$N, T,$ and PSD along a typical evaporation trajectory for the ^{84}Sr BEC experiment	115
5.7	Comparing scaling law for N versus ODT trap depth to measurements	117
5.8	Comparing scaling law for PSD versus N to measurements	118
5.9	Comparing scaling law for γ as a function of ODT trap depth to measurements	119
6.1	Column density profiles of 2D absorption images fitted with gaussian function	126
6.2	2D false color images of BEC formation	127
6.3	Remaining atom distribution after subtracting gaussian fit from data	128
6.4	Comparing gaussian fit function to fugacity fit function	131
6.5	Fugacity values from data fits	132
7.1	Representative 1D slice of condensate column density with Thomas-Fermi fit	140
7.2	1D slices of condensate column density with TF fit profile	142
7.3	Chemical potential for typical experimental parameters	143
7.4	The parameter $(N_0 a)/a_{ho}$ for typical experimental mean trap oscillator frequencies	143
7.5	Condensate radius after release from the trap	146
7.6	BEC one- and three-body loss rate fits	149
A.1	^{86}Sr one-photon PAS candidates	155
A.2	^{87}Sr laser setup	158
A.3	^{87}Sr laser setup power measurements	159
A.4	^{87}Sr slave lasers connections	161

A.5	RF power delivered to 1.3 GHz AOM	162
A.6	Drawing of assembled 689 nm sat. abs. cell	165
A.7	Drawing of 689 nm sat. abs. cell body	166
A.8	Drawings of 689 nm sat. abs. cell flanges	167
A.9	Drawing of 689 nm sat. abs. cell attachment piece	168
A.10	Drawing of 689 nm sat. abs. cell mount for Swagelok connection	168
A.11	Drawing of 689 nm sat. abs. cell mounts for horizontal arms	169
A.12	689 nm sat. abs. cell thermocouple and heater placements	171
A.13	Image 1 from Natali’s notebooks on the 689 nm sat. abs. cell assembly	173
A.14	Image 2 from Natali’s notebooks on the 689 nm sat. abs. cell assembly	174
A.15	Image 3 from Natali’s notebooks on the 689 nm sat. abs. cell assembly	174
A.16	High finesse FP cavity calculated modes for original design	181
A.17	Drawing of assembled internal HF cavity	184
A.18	High finesse cavity Invar spacer	185
A.19	High finesse cavity internal mirror mounts	186
A.20	High finesse cavity “groove” piece	187
A.21	Vacuum can external mount	188
A.22	External vacuum can window flange	189
A.23	External vacuum can window holder	190
A.24	Teflon washers for external vacuum can windows	191
A.25	Principle of mode matching	194
A.26	High bandwidth photodiode to measure HF cavity transmission signals	195
A.27	Schematic of HF cavity optical and electronic components layout	196
A.28	Stand-alone active fast path circuit schematic	197
A.29	Stand-alone passive fast path circuit schematic	197
A.30	HF cavity ringdown measurement at 16 Hz frequency sweep	201
A.31	HF cavity Free Spectral Range (FSR) measurement	202
A.32	TA protective circuit	205
A.33	Pillar for first ODT beam focusing lens	207
A.34	Pillar for collecting first pass of ODT beam	208
A.35	Pillar for crossed ODT	209
A.36	Assembled Sr atom beam source	212
A.37	Nozzle cap for the Sr atom beam source	213
A.38	Heat shield for Sr atom beam source	213
A.39	Sr atom beam source heater holder	214
A.40	Sr atom beam source holder	214
A.41	Sr atom beam source nozzle nut	215
A.42	First version of HV chamber	216
A.43	First version of HV chamber (view #2)	217
A.44	Information about chamber ports for first version of HV chamber	218
A.45	Two plans to introduce Ti-sub pump in first version of HV chamber	219
A.46	Second version of HV chamber	220

A.47 Second version of HV chamber (view #2)	221
A.48 Information about chamber ports for second version of HV chamber .	222
A.49 Depiction of MOT chamber window placement	223
A.50 Base for 689 nm slave lasers (original design)	225
A.51 Base for ^{87}Sr slave laser #2 (second slave laser design)	226
A.52 Melles Griot lens holder for 689 nm slave lasers	227
A.53 First version of flexible collimating lens mount	228
A.54 Second version of flexible collimating lens mount	229
A.55 Miniature laser diode mount cap	230
A.56 Miniature laser diode mount	231
A.57 Assembled miniature laser diode collimating system	232

Tables

1.1	Current list of BEC observations using atoms with two valence electrons	5
4.1	Experimental and theoretical level energies for ground molecular potential	94
4.2	Published values of scattering lengths a	96
A.1	^{86}Sr spectroscopic measurements	154
A.2	Measured sat. abs. cell temperatures	172
A.3	689 nm saturated absorption and red MOT AOM frequencies	175
A.4	Characteristics of saturated absorption AOM setup	177
A.5	PerkinElmer 7265 Lock-in amplifier settings	178
A.6	HF Fabry-Perot cavity theoretical and measured characteristics	179
A.7	VLOC optics order for high-finesse FP cavity	183
A.8	1064 nm optics used with ODT	209
A.9	MOT experimental chamber windows	224

Chapter 1

Introduction

The observation of Bose-Einstein condensation (BEC) in dilute atomic gases nearly 15 years ago [1, 2, 3, 4] proved to be one of the most important advances of atomic physics. Its realization occurs at sufficiently low temperatures and high densities that individual atomic wavepackets (whose size grows as the atom's temperature decreases) begin to overlap. At these temperatures, quantum mechanical effects become important because individual atoms are no longer distinguishable, and atoms that obey Bose statistics collapse into the lowest energy state of their trapping potential. Signatures of this effect from the first successful experiments with alkali metal atoms came from time-of-flight images as a narrow peak in the velocity distribution of an expanding cloud [1, 2, 3, 4]. Observations of BEC have extended to include divalent atom gases such as ytterbium (Yb) and alkaline-earth metal atoms. The strong drive in producing BECs of these kinds of atoms is a result of the many new properties and possibilities these systems offer.

Experimental and theoretical research on BEC began much earlier in systems other than dilute atomic gases. Albert Einstein [5] predicted that a phase transition, analogous to that theorized by S. Bose for light quanta [6], would occur for noninteracting atoms with interger spin due to their quantum statistical behavior. Later, two

independent groups (P. Kapitza [7] in Moscow and J. F. Allen and A. D. Misener [8] at Cambridge University) demonstrated superfluidity of liquid helium-4 (^4He). Very soon after, F. London [9] considered superfluidity in ^4He as a manifestation of BEC.

The usefulness of this phase transition in describing systems other than bosons is evident in the phenomena of superconductivity and superfluidity with fermions. Superconductivity in mercury (Hg) was discovered in 1911 by H. Kamerlingh-Onnes [10], but its explanation did not come until 1957 in the context of BCS theory [11, 12]. In the BCS theory, two fermions pair to create a composite boson known as a Cooper pair. These Cooper pairs, which in this case are electron pairs in Hg, can then form a BEC and exhibit superconducting properties. Superfluidity in liquid ^3He , discovered by D. Osheroff, R. C. Richardson and D. M. Lee in 1972 [13], was also successfully explained by BCS theory [14]. Similarly to the case of superconductivity, fermionic ^3He atoms also form pairs and undergo condensation.

Many aspects of superfluidity in liquid ^4He are difficult to calculate and explain because of strong atom-atom interactions. Evidence of a significant atom number in the superfluid's zero-momentum state proved difficult to obtain directly because the strong atomic interactions reduced the occupancy of the ground state, but was eventually achieved with neutron-scattering measurements of the momentum distribution of ^4He atoms [15]. This circumstance creates a strong motivation to achieve BEC in dilute gases for which interactions can be treated as a small perturbation. Spin-polarized hydrogen (H) was proposed as a good candidate for such a weakly

interacting BEC because it was predicted to stay a gas down to zero temperature due to extremely small interactions [16, 17]. Considerable effort was put forth to reach quantum degeneracy with H and crucial techniques in trapping atoms with magnetic fields were developed [18, 19, 20, 21, 22]. In the meantime, dramatic advances in laser cooling and trapping techniques of the alkali atoms also made these attractive candidates for BEC experiments of weakly-interacting atomic gases, and they were eventually the first types of atoms to successfully demonstrate a gaseous BEC [1, 2, 3, 4]. However, the alkali atom experiments benefited greatly from techniques developed in the H experiments, namely, magnetic trapping of atoms and removing the most energetic ones in a process known as evaporative cooling, discussed in Section 1.3 and Chapter 5 [23].

1.1 BEC of alkaline-earth metal atoms to now

Increasing interest in systems with narrow intercombination lines such as the alkaline-earth metal atoms has produced intense work toward cooling them to quantum degeneracy (see Table 1.1 for a current summary of BECs produced with this class of atoms). Most of the attractive features of these atoms are due to their two valence electrons, which result in spin singlet and spin triplet states that have important consequences for laser cooling and optical frequency standards. The closed-shell 1S_0 ground state has no electronic magnetic moment and simplifies the atomic level structure. Furthermore, various stable isotopes exist that can vary in collisional properties

and quantum mechanical behavior (fermions or bosons). Strontium (Sr) is one of the most rigorously studied (experimentally and theoretically) alkaline-earth atom because it possesses these qualities. Since the first laser cooling experiments with Sr in 1990 [24], this atom has proven to be an exceedingly favorable tool for optical clocks and metrology, studies of ultracold plasmas, and now, quantum degenerate gases.

Unfortunately, the traditional approach of producing quantum degenerate gases with alkali atoms, i.e., that of evaporative cooling in a magnetic trap, is not possible for alkaline-earth atoms due to the missing magnetic moment in the ground state. The only option available is evaporatively cooling atoms held in conservative traps formed by focused, intense laser beams. Indeed, this was the approach taken by several groups working with two-valence-electron atoms. Chapter 2 describes the characteristics of Sr in greater detail.

Quantum degenerate gases of divalent atoms in optical lattices are proposed as simulators for exotic forms of magnetism and condensed matter systems [32, 33, 34]. Combining the technology developed in optical clocks and frequency standards [35] with atoms in a Mott insulator state [36, 37] has led to exciting predictions for quantum computing applications [38, 39, 40, 41]. Ultracold homonuclear molecules produced from a BEC with laser light (in a process called photoassociation [42]) also offer the potential to measure the stability of fundamental constants of nature [43]. Furthermore, using optical Feshbach resonances [44, 45] to manipulate atom-atom interactions could create novel quantum fluids and nonlinear matter-wave effects

Year	Group	Atomic isotope	N_{BEC}	a
2003	Takahashi (Japan) [25]	^{174}Yb	5×10^3	$105 a_0$
2007	Takahashi (Japan) [26]	^{170}Yb	10^4	$64 a_0$
2009	Takahashi (Japan) [27]	^{176}Yb	> 0	$-24 a_0$
2009	Riehle (Germany) [28]	^{40}Ca	2×10^4	$340 a_0 - 700 a_0$
2009	Grimm (Austria) [29]	^{84}Sr	1.5×10^5	$123 a_0$
2009	Killian (USA) [30]	^{84}Sr	3×10^5	$123 a_0$
2010	Killian (USA) [31]	^{88}Sr	10^4	$-2 a_0$

Table 1.1 : Current list of BEC observations using atoms with two valence electrons. Scattering lengths a are given in units of $a_0 = 0.053$ nm.

[46, 47, 48]. All these distinct possibilities encourage the production of quantum gases of these class of atoms.

1.2 Essential properties of BECs

The peculiar behavior of bosons at low temperatures results from the fact that the mean occupation number \bar{n}_i of a state i with energy ϵ_i can be unbounded, with the restriction that $\sum_i \bar{n}_i = N$, N being the total number of particles. This is in sharp contrast to the behavior of fermions, who obey the Pauli exclusion principle that restricts the number of particles occupying a quantum mechanical state to one. Determining the distribution of bosonic particles in the grand canonical ensemble subjected to the above-mentioned condition on the number of particles N produces

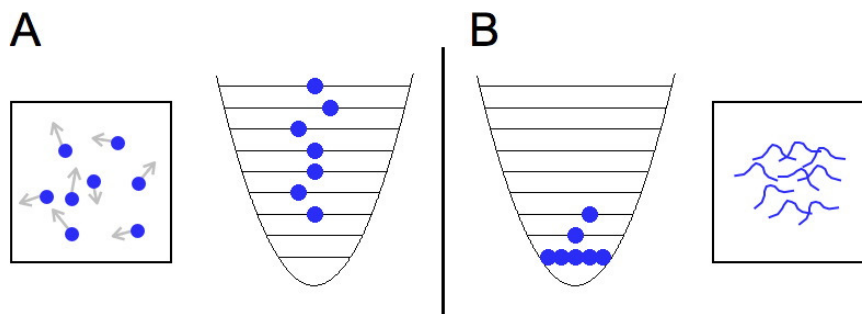


Figure 1.1 : Thermal atoms versus BEC in a harmonic trap. (A) Atoms behave like classical particles at high temperatures. They distribute among the many energy eigenstates of the harmonic trap and there is no multiple occupation of a single energy level. (B) At temperatures near the critical temperature for BEC, individual particle's wavepacket overlap and their quantum statistical behavior dominates. This leads more than one particle to occupy the same ground state.

the well-known Bose distribution function \bar{n}_i ,

$$\bar{n}_i = \frac{1}{e^{(\epsilon_i - \mu)/k_B T} - 1}.$$

Here, μ is the chemical potential, T is the temperature of the gas, and k_B is Boltzmann's constant. The effects of bosonic statistics is displayed in Fig. 1.1: When the Bose gas has enough thermal energy, the particles can occupy many excited trap states, and the particles can be thought of as classical particles. As the temperature drops, the particles' wavefunctions begin to overlap and the indistinguishability of bosons becomes important. This quantum statistical behavior leads to a macroscopic occupation of the trap's ground state.

The fact that BECs are produced in trapped samples with dilute atomic gases leads to two facts about these systems: densities are inhomogeneous and the samples have finite size. In addition, two-body interactions are responsible for collective excitations

in the condensate and produce important modifications to measurable quantities such as the condensate density. The collective effects of inhomogeneity, finite sample size and atom-atom interactions on the condensate have important consequences that are briefly discussed here [49].

Because trapped gases are highly inhomogeneous, signatures of BEC show up both in momentum and coordinate space, in sharp contrast to homogeneous systems like superfluid ^4He that exhibit it only in momentum space. Therefore there is dual detection possibilities, with a sharp peak noticeable in either the spatial or velocity distribution. The density distribution of the condensate in the trap is measured directly with dispersive light scattering (e.g., [50]). However, time-of-flight analysis of the condensate is the more commonly utilized detection scheme. In this approach, one turns off the trap and measures the density of the expanding condensate with light absorption, which gives information about the samples' velocity distribution and kinetic energy at the beginning of the drop time. The sharp density peak observed over a broader density distribution is one of the main signatures of BEC [1].

Interactions in inhomogeneous systems greatly decrease the central density of real atomic gases compared to noninteracting ones at very low temperatures. For an ideal (noninteracting) gas the density predicted in a harmonic trap can be one or two orders of magnitude larger than that observed for an interacting, albeit dilute, Bose gas.

Much smaller effects occur due to the finite size of the sample. A finite number of particles causes a reduced condensate fraction and lower transition temperature

when compared to the $N \rightarrow \infty$ case. Furthermore, the transition to macroscopic occupation of the lowest energy state is not immediate as expected, but actually “rounded off” when compared to the $N \rightarrow \infty$ limit due to the lack of discontinuities in the thermodynamic functions.

Despite these effects, which complicate the many-body problem, great advances have been made by considering the dilute Bose gases in two ways: as an ideal gas and as a weakly-interacting gas. Mean-field approaches to solving a weakly-interacting gas turn out to be very effective in describing their static, dynamic and thermodynamic properties, as we shall see in Chapter 7.

1.3 Producing a BEC

To produce a BEC in a dilute Bose gas, the sample temperature must be reduced to temperatures on the order of $1 \mu\text{K}$ or less so that the atoms’ quantum mechanical behavior causes them to avalanche to the zero-momentum state. Although laser cooling techniques have produced remarkably cold samples (e.g., [51]), they cannot produce the necessary densities (n) for quantum effects to set in. This situation highlights an important criterion in producing BECs: it is not just temperature that is important, but phase-space density (PSD) ρ , defined as $\rho = n \left(\frac{2\pi\hbar^2}{mk_B T} \right)^{3/2}$. Here, m is the particle mass and \hbar is Planck’s constant divided by 2π .

As mentioned above, the eventual production of BECs of dilute Bose gases came about by combining laser cooling procedures with evaporative cooling in a magnetic

trap. This essential technique, reviewed extensively in many papers (e.g., [52, 53]), removes the most energetic atoms from an atomic sample, so that the remaining, less energetic atoms thermalize through elastic interactions to a colder and more dense sample. Figure 1.2 illustrates this process: a sample with a Boltzmann distribution of energies characterized by temperature T_i (Fig. 1.2a) becomes colder (Fig. 1.2c) after atoms with the highest energies leave the trap (Fig. 1.2b) and the remaining atoms re-establish thermal equilibrium at a lower temperature T_f . Even though the evaporation process removes atoms from the sample, the density can increase, or at least not decrease very much, such that the PSD actually increases. This section gives a brief overview of how evaporative cooling works in magnetic traps. Optical dipole traps (ODTs) are currently important tools in evaporation experiments and are also discussed. More details about the evaporation process is found in Chapter 5.

1.3.1 Using magnetic traps for evaporative cooling

Alkali-metal atoms in their ground electronic state are characterized* by their single valence electron with spin $S = \frac{1}{2}$ and nuclear spin I , where $F = I + S$ is the total angular momentum of the atom. The coupling between I and S create hyperfine structure in the ground state, with the states separated by the hyperfine interaction energy $\Delta E_{hf} \propto (I + \frac{1}{2})$. An external magnetic field B also interacts with the magnetic moments of the electron and nucleus, giving rise to splitting of atomic energy levels

*The total angular momentum $F = I + S$ when the electronic orbital angular momentum $L = 0$.

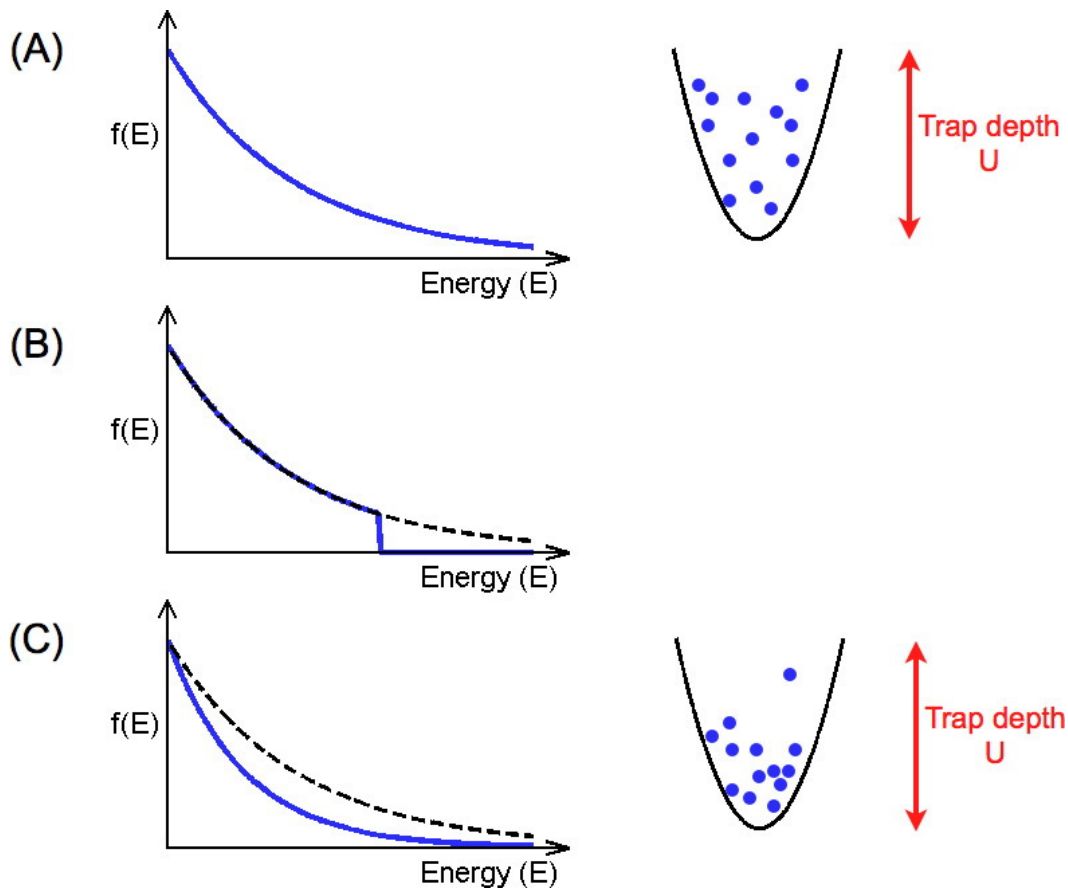


Figure 1.2 : Boltzmann energy distributions before and after removing high-energy atoms. (A) A potential of height U traps a thermal atom sample of temperature T_i (right) with an initial Boltzmann distribution $f(E) \propto \exp(-E/k_B T_i)$ (left). (B) One can remove the high-energy atoms via evaporation. This is analogous to truncating the original Boltzmann energy distribution at some energy E . The solid line shows the energy distribution immediately after the evaporation process, while the dashed line demonstrates the original distribution. (C) Collisions among the atoms redistribute the remaining energy and the sample thermalizes to a lower temperature T_f . The atoms now reside near the bottom of the trap. The original Boltzmann distribution is shown by the dashed line, while the solid line represents the new energy distribution $f(E) \propto \exp(-E/k_B T_f)$. Adapted from [54].

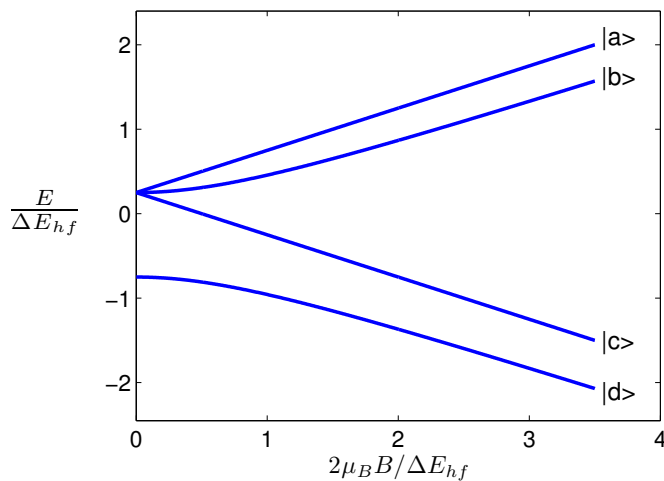


Figure 1.3 : Zeeman energy versus magnetic field for $I = \frac{1}{2}$. The interaction between nuclear and electronic spins create hyperfine states separated by energy ΔE_{hf} . An external magnetic field B also interacts with the spins. At low B , the coupled spins interact with the field. This interaction lifts the degeneracy of the hyperfine states, and the non-degenerate states depend linearly with B . At large B , individual spins interact with the field, and the non-degenerate states separate into “low-field-seeking” ($|a\rangle$ and $|b\rangle$) and “high-field-seeking” ($|c\rangle$ and $|d\rangle$) states. Magnetic traps are able to trap low-field-seeking states only, because of the magnetic field minimum. Adapted from [55].

depending on the strength of B (Zeeman effect). For weak fields, the splitting of the magnetic sublevels is linear with B . At strong fields states separate into groups of “low-field-seeking” and “high-field-seeking” states. These different regimes are displayed in Fig. 1.3 for $I = \frac{1}{2}$. Atoms whose magnetic energy decreases with decreasing magnetic field (states $|a\rangle$ and $|b\rangle$ in Fig. 1.3) are the low-field-seeking states, and states $|c\rangle$ and $|d\rangle$ are the high-field-seeking states.

If B is inhomogeneous with a local minimum, atoms in low-field-seeking states will feel a magnetic force toward the field minimum. This is the idea behind magnetic trapping: confining atoms near the minimum of the magnetic field. With trapped

atoms, one can proceed with the evaporation process by setting a potential height that allows energetic atoms with larger energies to escape. Since the first successful demonstrations of BEC, magnetic traps are continually employed in producing quantum degenerate gases of alkali-metal atoms.

The original method of evaporative cooling performed in the lab of D. Kleppner and T. J. Greytak relied on energetic atoms escaping the magnetic trap depth over a saddle point in the magnetic field [56]. This approach worked up to when the rate at which atoms escaped became comparable to competing loss mechanisms that reduced the PSD. Experiments with alkali-metal atoms improved this evaporation method by actually expelling energetic atoms via radio-frequency (rf) transitions to states that are not trappable [57, 58]. Since the potential is position-dependent, so is the frequency of the rf signal necessary to be on-resonance with the non-trapped state to eject atoms. Therefore, one can set the “height” of the potential over which energetic atoms will escape by changing the frequency of the rf signal. An important consequence of how magnetic trapping works is that only atoms in certain states are trappable (low-field-seeking states). This disadvantage can be overcome by implementing ODTs either to conclude the evaporation process or to perform the whole process altogether. In this way, the atoms can then be prepared in the desired state in the ODT.

1.3.2 Using optical dipole traps for evaporative cooling

Another technique commonly used to produce BECs is evaporatively cooling trapped atoms from a trap produced with far detuned, highly focused laser light [59]. The interaction between the atomic electric dipole and the laser's electric field gives rise to shifts of the atomic energy levels known as ac Stark shifts. By focusing the laser light, a position-varying electric field emerges which induces spatially-varying energy shifts. Similarly to magnetic trapping, atoms then feel a dipole force that attracts them to the most intense part of a red-detuned laser.

Because the wavelength of the trapping laser is far-detuned from any atomic transition, the optical excitation can be kept extremely low. Consequently, photon scattering is kept low, resulting in negligible radiation force and low heating rates. ODTs offer great versatility for trapping experiments, since traps of varying symmetries can be realized relatively easily. The ubiquity of ODTs in atom trapping experiments can be attributed to its ability of trapping atoms regardless of their particular internal state, thereby making experiments relying on state preparation possible. In recent years, there has been an increase of ODTs in evaporation experiments, either as the primary trap or integrated into the final stages of forced evaporative cooling in a magnetic trap. Barrett et al. [60] produced the first BEC by all-optical means: a laser cooling stage followed by forced evaporation in an ODT.

Forced evaporation in an ODT is currently the only tool available to reach quan-

tum degeneracy in Sr because it lacks a magnetic moment in the ground state[†]. The procedure for evaporative cooling in an ODT is very similar to the concept initially developed in the magnetic trapping experiments of H: energetic atoms escape the optical trap's height set by the trap bottom and a saddle point in the potential "walls", which have a height proportional to the laser's intensity, $U_{dip}(r) \propto I(r)$. The remaining atoms thermalize via elastic collisions to a lower temperature. Eventually, the hottest atoms of the new, cooler ensemble of atoms lack the sufficient energy to leave the trap. Therefore, it is important to continuously decrease the trap height to keep the evaporation going by lowering the trap laser's power.

1.4 Photoassociative spectroscopy (PAS) and the scattering length

It is obvious that atom-atom collisions enable the Bose gas to redistribute the remaining energy during evaporative cooling. Because of the dilute nature of the samples used, the interactions are predominantly two-body collisions. Furthermore, the ultracold temperatures dealt with in these experiments ensure that atomic energies are very low and that collisions only take place through *s*-wave collisions, which are parametrized by the scattering length a . The cross section for an atom, proportional to a^2 , determines whether collisions are strong and whether the collision rate for ther-

[†]Although the fermionic isotope ^{87}Sr has a weak magnetic moment in the ground state due to its nuclear spin of $I = \frac{9}{2}$, it is still not magnetically trappable.

malization is high. Therefore, to understand the behavior of ultracold collisions, it is essential to determine a .

Photoassociation spectroscopy (PAS) has been extremely effective for deducing the scattering length of atoms because it allows a reconstruction of the long-range molecular wave function, which depends heavily on a . The technique is illustrated in Fig. 1.4: two colliding ultracold atoms can resonantly absorb a laser photon to produce a bound, excited molecule that then dissociates into free, energetic atoms. The emerging atoms are primarily lost from the trap, resulting in increased atom losses from the sample. Loss peaks occur for each resonant transition between the dissociation limit of the ground state and a bound excited level. The resulting absorption spectrum then maps out the position of the excited molecular potential. But most importantly, the intensity of the transition can be related to the structure of the ground state wavefunction and hence the scattering length a . As will be seen in Chapter 3, a is proportional to the phase shift experienced by the wave function during a collision.

Furthermore, utilizing two lasers to promote the colliding atom pair to a bound state in the ground molecular potential allows one to accurately measure the positions of the bound vibrational states of the ground molecular potential. The two-photon version of PAS has proven to be the most powerful approach of determining a because a is extremely sensitive on the position of the least-bound state in the ground molecular potential. Depending on how close the least-bound state is to the dissociation

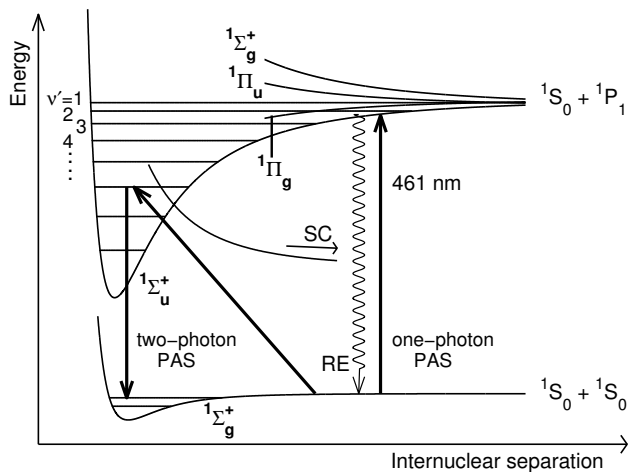


Figure 1.4 : Schematic of one- and two-photon PAS. The 1S_0 - 1S_0 and 1S_0 - 1P_1 molecular potentials for Sr are shown. Resonant excitation (with 461 nm light) to a bound state in the excited molecular potential can lead to atom loss via state-changing collisions (SC) or radiative escape (RE) [61]. By changing the frequency of the PA laser, one maps out the position of the bound states in the excited molecular potential. A two-laser combination can be used to measure the binding energies of the least bound states in the ground molecular potential.

limit, a can range from a very large positive or negative value to zero.

The collisional properties of Sr were unknown until we performed a series of PAS experiments to determine them [62, 63]. Our two-photon PAS studies will be discussed in detail in Chapters 3 and 4 of this thesis. The results from two-photon PAS established that ^{84}Sr possessed favorable collisional qualities for evaporative cooling.

1.5 Thesis outline

The work of this thesis comprises the achievement of BEC of ^{84}Sr (published in [30]) as well as our use of two-photon PAS to accurately determine the s -wave scattering

length a for all the Sr isotopes and isotope mixtures (published in [63]) . Previous efforts at achieving BEC with Sr focused on using the most abundant isotopes ^{86}Sr and ^{88}Sr , without success [64, 65]. Our determination of the scattering lengths for the Sr isotopes established that ^{84}Sr possessed ideal collisional properties for efficient evaporative cooling. These topics are presented in the chapters following this introduction.

Chapter 2 describes the procedure for laser cooling and trapping ^{88}Sr and ^{84}Sr in our experiment. It begins with a brief theoretical overview of laser cooling sufficient to understand the content of the chapter. Afterwards, the details of our experiment are described. This includes the magneto-optical traps for both the dipole-allowed and narrow transitions, the ODT setup, and our imaging techniques. Chapter 3 explains the theory behind ultracold collisions and PAS. It then focuses on determining the different contributions to the 1S_0 - 3P_1 resonance lineshift, in preparatory to correctly measure the binding energy of the least bound state in the 1S_0 - 1S_0 molecular potential. The explanations in Chapter 3 serve as the background for Chapter 4, where our two-photon PAS experiment is described in detail. The two-photon PAS measurements, along with short-range potential measurements and theoretical models used by our theoretical collaborators, enabled accurate determination of the scattering lengths for the isotopes of Sr.

Chapter 5 presents an overview of evaporative cooling in an ODT and the BEC phase transition. Particular attention is given to forced evaporation of ^{84}Sr up to

the onset of BEC. Then in Chapter 6 we discuss the way we determined the BEC phase transition temperature T_c . The chapter also describes the properties of a non-interacting Bose gas near T_c . Finally, Chapter 7 discusses the characteristics of a pure condensate and our observations of BEC in ^{84}Sr .

Chapter 2

Laser cooling and trapping Sr

This chapter presents details on how we prepare atom samples for the PAS and BEC experiments described in this thesis. Different isotopes were used in the different experiments due to their unique characteristics. The most abundant isotope (^{88}Sr) for the PAS experiment would ensure high densities for strong PA signals. However, the least abundant isotope (^{84}Sr) possesses scattering properties ideal for efficient thermalization and is the best choice for BEC. Figure 2.3 schematically represents the natural abundances for the Sr bosonic isotopes.

Preparing ultracold samples of ^{88}Sr atoms differs somewhat from producing ^{84}Sr samples. We will introduce our cooling and trapping strategies in the context of ^{88}Sr atoms and insert particular details for ^{84}Sr atoms whenever necessary.

2.1 Basic concepts of laser cooling and trapping

Laser cooling and trapping techniques are well-established now since their conception nearly 35 years ago [66, 67]. These techniques are extensively described in many textbooks [68, 55] and are only briefly highlighted here to point out the special characteristics of Sr.

The process of light absorption and spontaneous emission is frequency dependent

for all atoms. Laser light with intensity I and frequency f incident on an atom will excite an atomic transition with resonance frequency f_0 at a rate equal to the scattering rate R ,

$$R = \frac{\Gamma}{2} \frac{I/I_s}{1 + I/I_s + \frac{4(2\pi\Delta - \vec{k} \cdot \vec{v})^2}{\Gamma^2}}, \quad (2.1)$$

where the rate $\Gamma = 1/\tau$ with τ being the lifetime of the excited atomic state, $I_s \equiv \pi\hbar c\Gamma/3\lambda^3$ is the saturation intensity of the transition, $\lambda = \frac{c}{f}$ is the laser wavelength ($k = 2\pi/\lambda$), and $\Delta \equiv f - f_0$ is the detuning of the laser frequency from resonance. If the atoms are in motion with velocity \vec{v} , the laser frequency f will appear shifted to the atoms in their inertial frame by an amount $-\vec{k} \cdot \vec{v}$.

In the process of absorbing laser photons, conservation of momentum requires that the photon's momentum be imparted to the atoms. Therefore, the atom's momentum will have a net momentum change in the direction of the photon's motion. This idea is the basis for using laser light to cool atoms: if the photons are directed opposite to the atom's motion, the net momentum change will reduce the atom's momentum. Spontaneous emission of the absorbed energy occurs in random directions so that, for the emission process, the net momentum imparted to the atoms averages to zero. This process is schematically shown in Fig. 2.1.

The scattering rate is significant when the detuning of the laser is near the resonance frequency of the transition. Therefore, it is important to account for the Doppler shift experienced by the atoms. To slow down atoms with a laser beam opposing atoms moving with velocity \vec{v} , the laser's frequency needs to be red-shifted

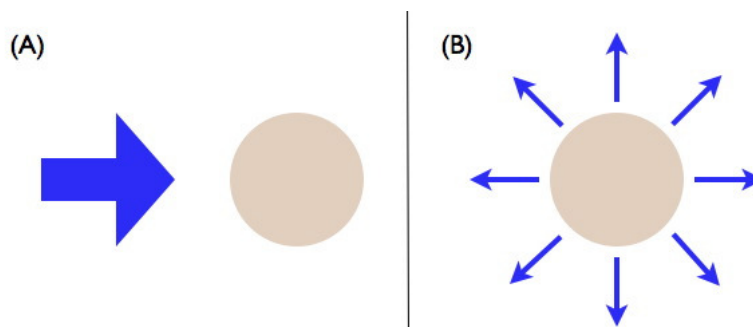


Figure 2.1 : Schematic of the scattering force on an atom. (A) Laser photons have momentum in the direction of the traveling radiation. When an atom absorb a photon, the atom's momentum changes in the direction of the photon's momentum by $\hbar k$. Therefore, an atom feels a radiation force in the direction of its momentum change. (B) After absorbing a photon, the atoms reemits a photon with energy equal to the absorbed energy $\hbar\omega = \hbar 2\pi f$. The emitted photon has a random direction and produces a recoil of the atom in the direction opposite to the emitted photon's direction of motion. The net momentum change due to the spontaneous emission of absorbed photons equals zero. The resulting effect on the atom from this entire process is a scattering force in the direction of the absorbed photons in (A).

so that, in the atom's reference frame, the photons counter-propagating against the atom are blue-shifted closer to resonance due to the $-\vec{k} \cdot \vec{v}$ term. Extending this configuration to six laser beams opposing the atoms' motion in all of the cartesian directions gives us the configuration used in a magneto-optical trap (MOT). However, the laser beams only serve to slow (cool) the atoms, which can diffuse out of the beam's intersecting area as it scatters photons from all six beams.

To make the light absorption position-dependent, an inhomogeneous magnetic field produced by two parallel current loops flowing in opposite directions is added in the center where the six beams intercept. The field $B_{MOT} = 0$ in the center and has a uniformly-increasing gradient near the center that produces position-dependent

Zeeman-shifts of the atomic energy levels. Due to the spatially-varying levels, moving atoms preferentially absorb photons from the beams opposing its motion. The Zeeman energy shift causes photons traveling in the same direction as the atom to appear off-resonance and will be minimally absorbed. MOTs have proven to be powerful setups to cool and trap atoms [69] and are ubiquitous in atomic physics laboratories.

2.1.1 Atomic structure of Sr

As mentioned in Chapter 1, the spins of the two valence electrons in Sr either align in parallel or antiparallel, resulting in spin singlet ($S = 0$) and triplet ($S = 1$) states. This electronic configuration gives Sr its important characteristics. Figure 2.2 shows a partial energy diagram that includes all the relevant states for the experiments described in this document.

Electric dipole selection rules allow a strong cycling transition from the singlet 1S_0 state to the 1P_1 state. However, the electric dipole operator does not connect states of different spin and therefore does not drive ($\Delta S = \pm 1$) transitions when spin-orbit interactions are small (when LS -coupling is valid) [54]. In this limit, the singlet and triplet states are unconnected and can be regarded as separate systems. With increasing atomic number, though, spin-orbit effects progressively increase until they begin to mix states of the same electronic terms. For a heavy atom like Sr, the spin-orbit interaction mixes some of the 1P_1 wavefunction into the 3P_1 wavefunction*. There-

*The singlet and triplet labels used for different energy levels are only approximate, but they will be used by convention.

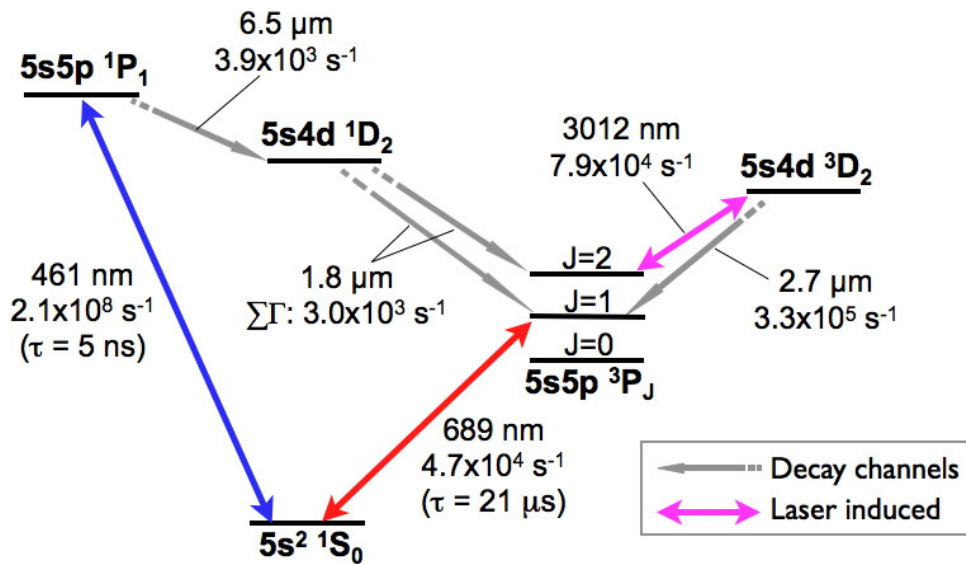


Figure 2.2 : Simplified energy level diagram for ^{88}Sr . Relevant transitions for the PAS and BEC experiments are shown, along with their vacuum wavelengths. Decay channels are shown with black arrows. The total angular momentum J of the state is specified to the right of the state for the triplet groups. The 461 nm and 689 nm (intercombination line) transitions are used for laser cooling, while the 3012 nm transition is a repumping transition. Adapted from [70].

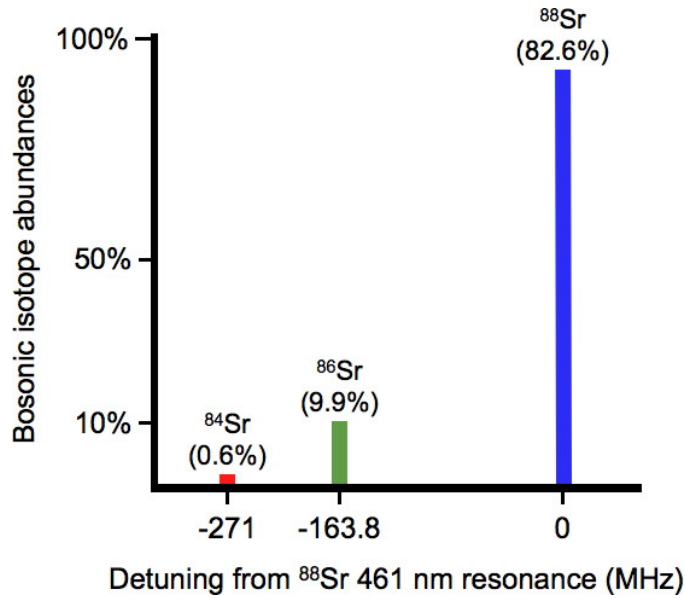


Figure 2.3 : Naturally abundant bosonic isotopes for Sr. The ^{84}Sr isotope is used in the BEC experiment, while ^{88}Sr is used for PAS experiments. Also shown are the isotope shifts for the 461 nm transition.

fore an electric dipole transition occurs between the ground state and the 3P_1 state, although its transition rate is considerably lower than it would be if this “intercombination” transition were strictly allowed. The narrow linewidths of intercombination transitions make them very useful for optical frequency standards (as seen in Chapter 1) as well as for laser cooling techniques, as will be discussed in Section 2.1.2.

When trapping different Sr isotopes, one has to consider the isotope shift of the trapping transition. These shifts come about because of differences between the mass and nuclear volume of the two isotopes [54]. Figure 2.3 also shows the isotope shifts in the 1S_0 - 1P_1 transition for the naturally abundant Sr bosons. The 1S_0 - 3P_1 transition also undergoes an isotope shift between ^{84}Sr and ^{88}Sr (presented in Section 2).

2.1.2 Limits on laser cooling

The discussion of Section 2.1 pointed out that atoms slow down as they absorb and spontaneously emit photons. An efficient cooling transition, therefore, is one in which the scattering rate is large. The maximum rate of photon scatter is, from Eq. 2.1, $\Gamma/2$ for very high beam intensities. This maximum rate translates into 10^8 photons per second per atom for the 461 nm transition with a lifetime of 5 ns. We therefore use this transition as our primary cooling transition.

Laser cooling has two well known temperature limits that are set by the transition linewidth (the Doppler limit) and by the recoil energy an atom gains when absorbing and emitting photons (recoil limit). For the 461 nm transition the Doppler temperature limit,

$$T_D = \hbar\Gamma/2k_B,$$

gives a minimum temperature attainable of $T_D \approx 760 \mu\text{K}$. This is many times greater than the photon recoil temperature [71, 72],

$$T_R \equiv 2E_R/k_B,$$

where $E_R = \hbar^2k^2/2m$. $T_R \approx 1 \mu\text{K}$ for the $^1S_0\text{-}^1P_1$ transition. Therefore, using the 461 nm transition when cooling atoms can produce samples with temperatures only about 1 mK cold.

For the intercombination line, however, the reverse is true and the temperature limit for laser cooling with the $^1S_0\text{-}^3P_1$ transition is the recoil limit ($T_R \approx 460 \text{ nK}$

$> T_D \approx 180$ nK). However, this transition has the potential to cool our samples 1000 times colder than the 461 nm transition does. With these considerations in mind, we prepare cold samples for our experiments by first cooling the atoms with the 461 nm transition and then with the 689 nm transition [73].

Low sample temperatures are necessary when performing PAS and BEC experiments like those described in this thesis. Long interrogation times and high densities are also important, as will be motivated in the following chapters. To this end we transfer the atom sample to an ODT and continue the experiments there. For the remainder of this chapter, we expound on our procedures for sample preparation and diagnosis. Previously published research articles ([63], [70], [30]) and theses ([74], [75]) also describe the cooling and trapping phases of our experiments.

2.2 Cooling with the 1S_0 - 1P_1 transition

All our experiments are done in a vacuum chamber with 10^{-10} Torr background pressure. Atoms from a heated reservoir travel along a tube that restricts their direction of travel toward the region where experiments will take place[†]. Opposing the atoms' motion is a 461 nm laser beam that slows the hot atom vapor down in a process called Zeeman slowing. The atom beam is also collimated upon exiting the heated reservoir by a 2-dimensional (2D) configuration of counterpropagating 461 nm

[†]The details of these initial pre-cooling stages will not be described further here, and the reader is referred to other published material for more information [74, 75, 68].

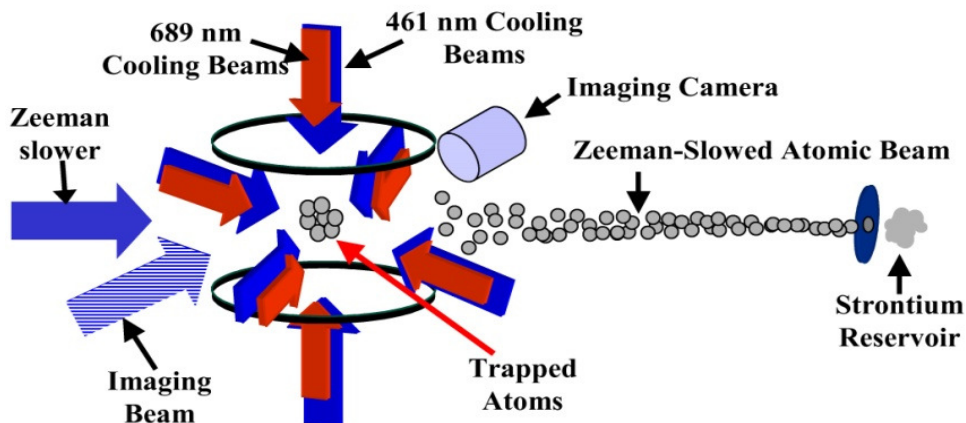


Figure 2.4 : Schematic drawing of the experimental setup. Sr atoms produced by heating solid Sr exit the heating chamber and are slowed by the Zeeman laser. The atoms enter a region of six counter-propagating laser cooling beams. Two current-carrying wire loops produce a magnetic field minimum at the center of the beam-crossing region. Two-stage cooling occurs (using 461 nm and 689 nm light). We count the number of atoms and measure the sample size with absorption imaging techniques: atoms resonantly scatter photons from an incident image beam and cast a shadow on the CCD camera. Adapted from [76].

beams that are perpendicular to the atoms' direction of travel. Both of these pre-cooling components precede the MOT cooling stage in order to slow down the atomic vapor enough so that the atoms can be trapped by the MOT beams as they enter the MOT region.

The first MOT using the strong 1S_0 - 1P_1 cycling transition produces atom samples of up to 60×10^6 ^{88}Sr atoms after 1 s of cooling time in an axial quadrupole magnetic field gradient of 60 G/cm. The MOT beams have a peak intensity in each beam of 3.6 mW/cm^2 and are red-detuned from the atomic resonance by 60 MHz. Figure 2.4 shows a schematic drawing of the physical setup for our experiments.

As seen in Fig. 2.2, the 1P_1 state has a decay channel to the 3P_2 and 3P_1 states

via the 1D_2 state, with a branching ratio

$$\frac{\Gamma_i}{\sum_n \Gamma_n} = \frac{\Gamma_{^1P_1-^1D_2}}{\Gamma_{^1P_1-^1D_2} + \Gamma_{^1P_1-^1S_0}}$$

of about 2×10^{-5} , where Γ_{a-b} is the decay rate from state a to b . 3P_1 atoms have a 21 μs lifetime and return to the 1S_0 state to continue the cooling process. Atoms in the 3P_2 state (8.3 min. lifetime [77]), however, can be trapped by the quadrupole field of the MOT [78, 79, 80, 65] where they do not scatter 461 nm light. As the 461 nm MOT cooling stage continues, atoms keep accumulating in the 3P_2 dark state.

We use this atom accumulation to our advantage when trapping ^{84}Sr atoms, where atom number enhancing techniques are crucial due to its extremely low natural abundance (0.6%). For the BEC experiment we accumulated 25×10^6 ^{84}Sr atoms in the 3P_2 after 30 s of 461 nm MOT cooling time (see Fig. 2.5). We then excite the $(5s5p)^3P_2$ - $(5s4d)^3D_2$ transition with 3 W/cm² of light at 3012 nm [70] for 35 ms to repump the magnetically trapped 3P_2 atoms to the ground state via the 3P_1 state (Fig. 2.2). In the experiments involving ^{88}Sr , we typically keep the 3012 nm light on during the 461 nm MOT cooling time of about 1 s and obtain sample of about 250×10^6 atoms in the 1S_0 state. The 3012 nm laser light when repumping ^{84}Sr is detuned about -600 MHz from the ^{88}Sr 3P_2 - 3D_2 resonance frequency [70].

After recapturing the repumped atoms from the 3P_2 state in the 461 nm MOT, we subsequently reduce the beam intensities to about 0.36 mW/cm² for 6.5 ms to reduce the sample temperature to about 2 mK. The measured lifetime of 3P_2 atoms in the quadrupole field is about 25 s, limited by background gas collisions [75].

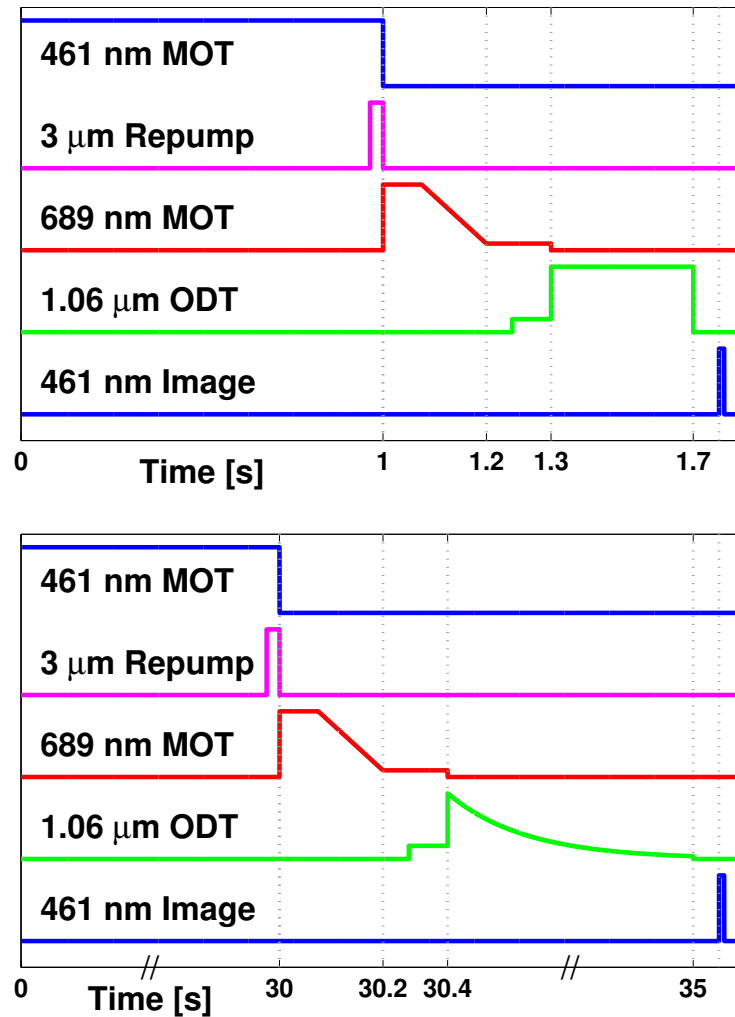


Figure 2.5 : Timing diagrams for PAS (top panel) and BEC (bottom panel) experiments. $3\ \mu\text{m}$ laser repumps Sr atoms from the 3P_2 state back to the 1S_0 state. 461 nm image beam turns on after a time-of-flight period after ODT turns off. The traces are offset for clarity and the heights indicate variation in beam power. Note the brake in the time axis.).

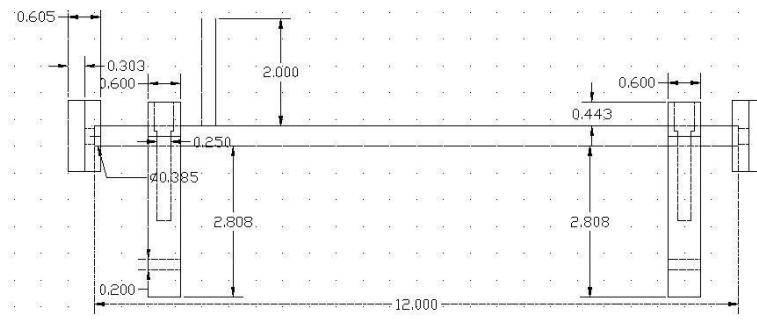


Figure 2.6 : AutoCAD drawing of 461 nm saturation-absorption cell. Details of its construction are found in Section 2.2.1.

2.2.1 Blue frequency control (magnetic cell)

For our experiments, we generate 461 nm light by frequency-doubling 922 nm light with a KNbO_3 crystal in a linear enhancement cavity [81, 82]. Our original 922 nm light source is a diode laser (Sacher), whose output is amplified by 922 nm tapered amplifier (TA) diodes (Eagle Yard) that we assemble in the laboratory. The generated 461 nm light then gets distributed among all the different beams necessary to make the 461 nm MOT work. References [74, 75] give more details on the 922 nm and 461 nm beam setups.

We use a saturation absorption signal [83, 84] to reference our 461 nm light to the $^{88}\text{Sr } ^1S_0\text{-}^1P_1$ resonance frequency f_0 . The saturation absorption cell we use was designed to allow us to tune the 461 nm light frequency by the Zeeman effect. It was built by Aditya Shashi, and I include details here about its design and construction for documentation purposes. Figure 2.6 gives an AutoCAD drawing of the dimensions of the cell.

We constructed the cell using commercially available parts and machined raw material. The cell body was made from a stainless steel (SS) tube 12" long, with an outer diameter (OD) of 0.374" and an inner diameter (ID) of 0.276". Two SS flanges (MDC Vacuum) with an OD of 4/3" were machined to accommodate the tube exactly. Furthermore, we bored a hole through them of diameter 0.276" to allow a path for the laser beams. These flanges were hard-soldered onto the ends of the cell body. We also machined a hole on the top of the cell tube, where we hard-soldered a 2" pipe fitted with a diaphragm valve (Swagelok DPS series 6LVV-DPHBW4). This pipe allows us to evacuate the cell with an external vacuum system.

A resistive, rigid coaxial cable (Nichrome wire, rated at 1.6 ohms/ft. of resistance) that would serve as the cell heater was wrapped around the cell body in pairs. This was done so as to have counter-propagating currents that would produce a net-zero magnetic field within the cell because of the coax cable. We then hard-soldered the coax cable onto the outside of the cell body. The entire apparatus was wrapped with a 2" layer of fiberglass for heat insulation and then encased by two SS half cylinders. The half cylinders were securely clamped together by wrapping a coil of copper wire (OD of 0.04") around them. This wire produces a magnetic field with current flowing through it. The copper wire was wrapped in electrical insulation.

We inserted solid Sr pieces in the cell through one of the ends and placed them roughly in the middle of the tube. Two glass view ports (Duniway P/N VP-133-075) screwed onto the cell body flanges served as the cell's end caps. We evacuated the

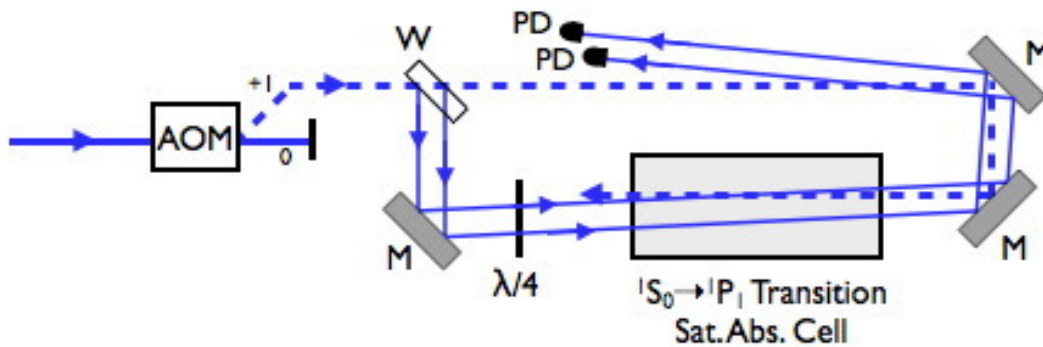


Figure 2.7 : Schematic of 461 nm saturation absorption setup. The direction of laser beam propagation through the functional elements of the setup is shown. The AOM diffracted order is +1. Other elements not crucial to the function of the setup are not shown. W: window, PD: photodiode, M: mirror, $\lambda/4$: quarter-wave plate.

cell to 10 μ Torr pressure and back filled with Argon gas.

Figure 2.7 shows a schematic drawing of the cell and the necessary optical layout for its implementation. The underlying principle of how it works is straightforward. A pump-probe beam pair intercept near the middle of the saturation cell as in a traditional Doppler-free absorption setup. Because the pump beam has much more power than the probe beam (probe 1), it saturates the transition rate for atoms that are on resonance with both the pump and probe 1 beams. Probe 1 therefore is not absorbed for these atoms, and monitoring this beam's power with a photodiode displays the normal "Lamb dip" feature on top of a Doppler-broadened absorption profile. A second probe beam (probe 2) also traverses the absorption cell, but since it does not counterpropagate a strong pump beam, its absorption is strictly Doppler-broadened absorption. We use the Doppler-broadened profile of probe 2 to subtract it from the signal from probe 1, thus isolating the Lamb dip for error signal generation.

To determine at what frequency our incident laser f_{laser} will be locked to, we can analyze the pump-probe beams that are in Doppler-free configuration. Both the pump and probe lasers come from the same beam diffracted from the incident laser by a saturated-absorption acousto-optic modulator (AOM). The AOM shifts the diffracted beam's frequency from f_{laser} by an amount δ_{AOM} , such that $f_{probe} = f_{pump} = f_{laser} + \delta_{AOM}$. Therefore, our laser will be locked to the frequency determined by

$$\begin{aligned}
 2\pi f_{probe} - \vec{k} \cdot \vec{v} &= 2\pi f_0 \\
 2\pi f_{pump} + \vec{k} \cdot \vec{v} &= 2\pi f_0 \\
 &\Downarrow \\
 2\pi f_{probe} + 2\pi f_{pump} &= 4\pi f_0 \\
 f_{laser} + \delta_{AOM} &= f_0 \\
 f_{laser} &= f_0 - \delta_{AOM}.
 \end{aligned}$$

As mentioned above, we are able to tune the 461 nm laser's frequency with this cell by the Zeeman effect. The cell is wrapped with a wire that produces a magnetic field B when current flows through it. This field splits the 1P_1 level into three levels spaced by the Zeeman energy splitting $\Delta E_B = g_J \mu_B B = \mu_B B$ ($g_J = 1$ for 1P_1 level). If we circularly polarize (σ^\pm) the light that interacts with the cell's atom vapor, it drives a specific $\Delta m = \pm 1$ transition from the 1S_0 to the 1P_1 states. Tuning B

therefore tunes the atom's transition frequency f'_0 by Zeeman energy splitting:

$$f'_0 = f_0 + \Delta E_B/h,$$

where h is Planck's constant. The original laser frequency f_{laser} in turn shifts with B as

$$f_{laser} = f'_0 - \delta_{AOM} = f_0 + \Delta E_B/h - \delta_{AOM}.$$

Figure 2.8 shows the frequency shift of the ^{88}Sr saturated absorption error signal as a function of applied voltage V_{satabs} to the current driver for the cell's magnetic coil. The laser's servo electronics lock to the zero crossing of the error signal. Applying a negative voltage to the current driver red-shifts the error locking point. This frequency reference setup allows us to scan our 461 nm laser frequency about 100 MHz by changing V_{satabs} . The conversion factor from V_{satabs} to frequency is 8.5 MHz/V.

The 461 nm light is always locked to the ^{88}Sr error signal (Fig. 2.8) in both the PAS and BEC experiments because it is large due to the isotope's large abundance. To detune the 461 nm laser by the $\Delta_{84-88} = -271$ MHz isotope shift [85], we detune f_{laser} by $\delta_{AOM} = +271.83$ MHz, and use the magnetic field B to optimize the frequency we use to trap ^{84}Sr . This is done by maximizing the atom number we image, as will be discussed in Section 2.5.

2.3 Narrow line MOT

The ~ 2 mK samples we prepared in the 461 nm MOT undergo a second cooling phase with 689 nm light [73] (see timing diagram in Fig. 2.5 for this transfer process). After

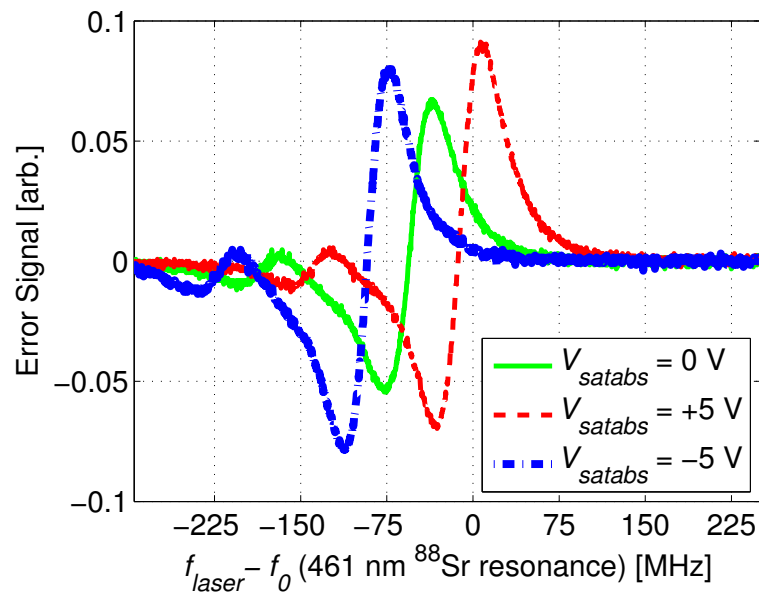


Figure 2.8 : 461 nm saturated absorption error signals. Varying V_{satabs} shifts the zero-crossing lock point of the error signal, thereby shifting the 461 nm laser frequency f_{laser} . This saturated absorption is produced when the saturated-absorption AOM frequency is $\delta_{AOM} \sim +56$ MHz (when trapping ^{86}Sr , ^{87}Sr , and ^{88}Sr). The conversion factor for V_{satabs} is 8.5 MHz/V.

the 461 nm MOT cooling time, we turn off the 461 nm beams, turn on the 689 nm light and simultaneously decrease the quadrupole magnetic field gradient to 0.1 G/cm. The velocity-capture range $\sim \Gamma/k$ for the 689 nm transition is small due to its narrow linewidth $\gamma = \Gamma/2\pi = 7.5$ kHz. Therefore, we increase it by broadening the laser frequency to increase the capture range to cool a significant amount of 2 mK atoms. The 689 nm laser frequency is coincidentally red-detuned from the resonance frequency [73].

The 689 nm beams are initially detuned 1 MHz red of resonance and frequency broadened by 700 kHz (peak-to-peak dither amplitude). Each beam has a peak intensity of 0.75 mW/cm². Over the next 150 ms, we increase the field gradient to 0.8 G/cm, reduce the laser spectrum to nearly single frequency (~ 10 kHz) and detune by only ~ 30 kHz, and reduce the beam power to 0.15 mW/cm². We then hold the final settings for about 150 ms to further cool the atoms. Figure 2.9 schematically shows how we change all the parameters of our 689 nm MOT laser cooling.

This cooling cycle results in atom samples at a temperatures of about 1-2 μ K and transfers of about 50 % or greater from 461 nm to 689 nm MOTs. The transfer efficiency depends on how much we optimize the 689 nm MOT's trapping characteristics (beam power, laser detuning, and field gradient) plus on the 461 nm MOT sample temperature. For ⁸⁴Sr, we ended with 1.6×10^7 atoms at a peak density of $\sim 10^{11}$ cm⁻³. Our ⁸⁸Sr samples have nearly 10 times as many atoms.

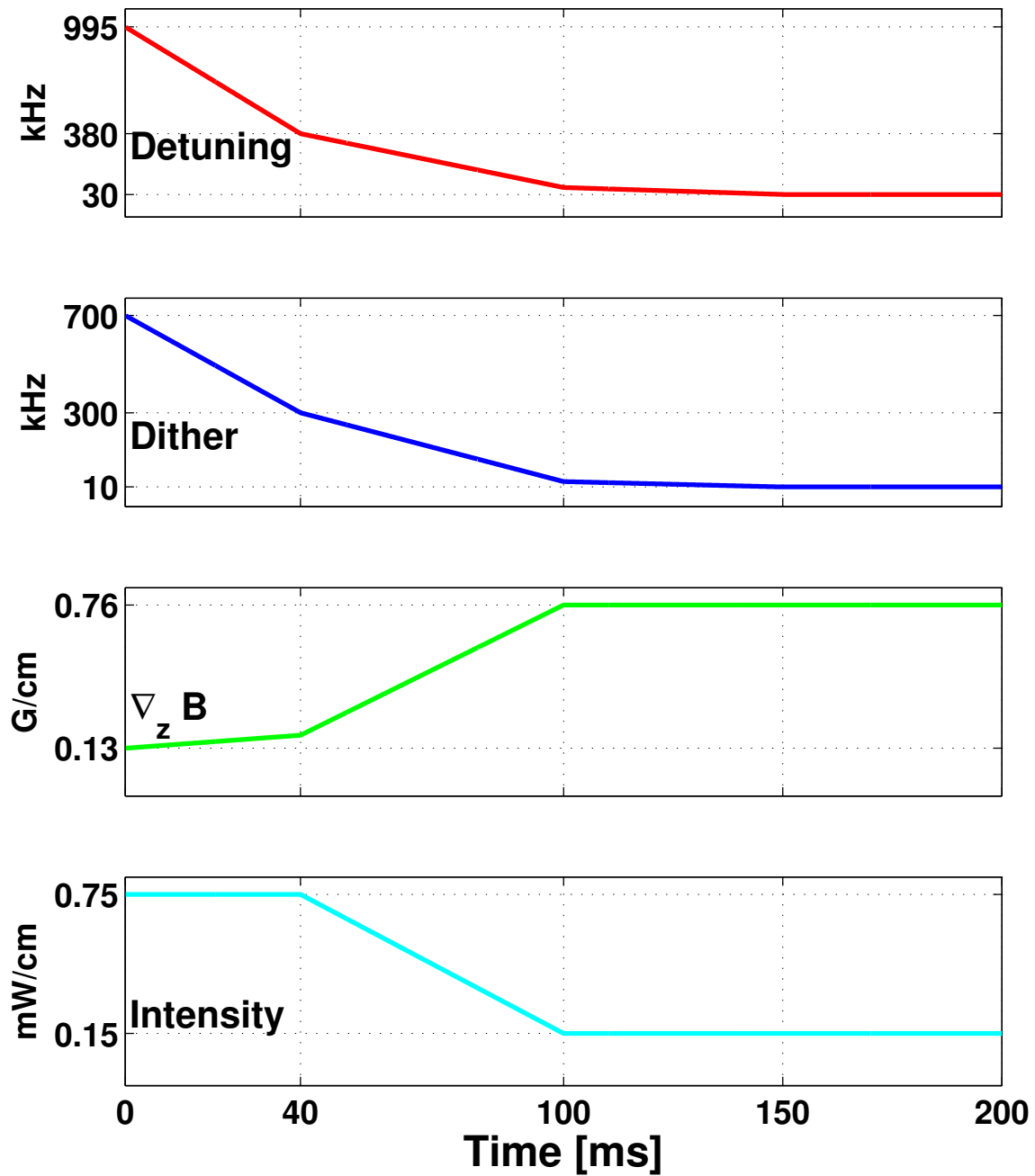


Figure 2.9 : Timing diagram for experimental components in 689 nm MOT operation. The 689 nm MOT components change the same for both ^{84}Sr and ^{88}Sr isotopes. Figure courtesy of B. J. DeSalvo.

2.3.1 689 nm light

We create all of our 689 nm light with home-made diode lasers systems. Figure 2.10 shows a schematic of the 689 nm laser setup for reference. The main laser is in Littman-Metcalf extended-cavity configuration [86], and details of its assembly and optical setup can be found in S. B. Nagel’s thesis [74]. This master laser is frequency-narrowed by servo-locking it to a high-finesse optical cavity with the Pound-Drever Hall method to produce a laser linewidth of ~ 50 kHz [87]. We reference the laser to the $^{88}\text{Sr } ^1S_0\text{-}^3P_1$ transition with a saturated-absorption cell for long-term stability.

After splitting the laser’s power into different beams to diagnose its performance and narrow its frequency, there is not enough power left for the actual experiment itself. We therefore use this main laser as a master laser for a first slave laser (^{88}Sr slave in Fig. 2.10) that provides the MOT beams to trap ^{88}Sr , ^{86}Sr or ^{84}Sr atoms. We use beam combiners (Sinocera) to combine the 689 nm and 461 nm MOT beams in the experimental setup.

Appendix A and Pascal Mickelson’s Ph.D. dissertation [75] gives further details of the additional 689 nm slave lasers (mainly used for trapping ^{87}Sr) in our experimental setup.

2.3.2 Doppler-free saturated absorption

To reference the 689 nm light to the ^{88}Sr atomic transition we use Doppler-free saturated absorption as we did in the 461 nm system (Section 2.2.1), but the setups differ

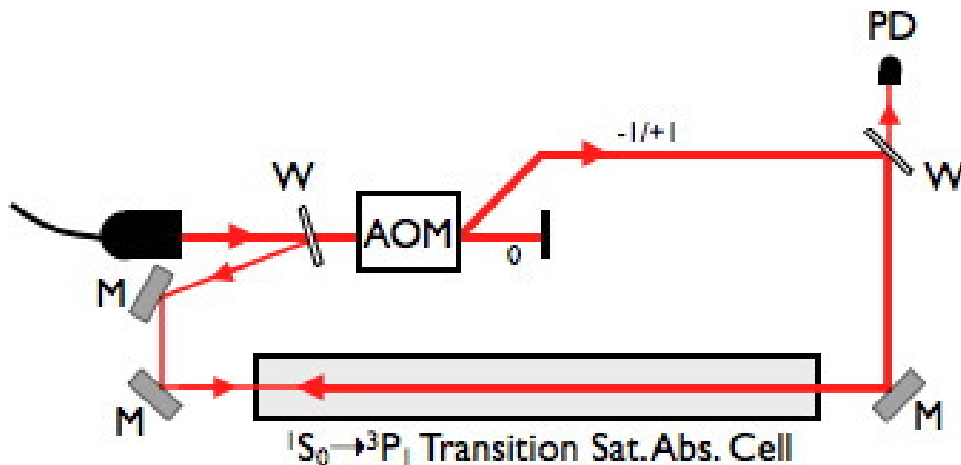


Figure 2.11 : Schematic of 689 nm saturation absorption setup. The direction of laser beam propagation through the functional elements of the setup is shown. The AOM diffracted order is -1 when trapping ^{84}Sr and ^{88}Sr . Other elements not crucial to the function of the setup are not shown. W: window, PD: photodiode, M: mirror.

somewhat. We only have one probe beam for the 689 nm saturated absorption setup. Another major difference is that the pump and probe beams are not from the same beam. Figure 2.11 shows a schematic drawing of the optical setup.

When trapping ^{88}Sr , the laser beam going to the saturated-absorption setup from the ^{88}Sr slave laser is at the main master laser frequency f_L (see Fig. 2.10). For the 689 nm configuration, the condition for on-resonance absorption of both the pump and probe lasers is (probe beam frequency is f_L and pump beam frequency is $f_L + \delta_{satabs}$):

$$2\pi f_L - \vec{k} \cdot \vec{v} = 2\pi f_0$$

$$2\pi (f_L + \delta_{satabs}) + \vec{k} \cdot \vec{v} = 2\pi f_0$$

From this relationship we get the laser frequency f_L with respect to the ^{88}Sr atomic

transition frequency, which serves as our absolute frequency reference:

$$f_L = f_0^{88} - \frac{\delta_{satabs}}{2}.$$

When we trap ^{84}Sr we actually detune the beam going to the saturated absorption setup by an additional $2\delta_{cat} \approx 2 \times 175.76$ MHz because the beam at frequency f_L (from the ^{87}Sr laser in Fig. 2.10) traverses an AOM in cat's eye configuration before going to the saturated absorption setup. The beam going to the saturated-absorption cell is at $f_L + 2\delta_{cat}$, so that the resonance condition for this situation gives us

$$f_L = f_0^{88} - \frac{\delta_{satabs}}{2} - 2\delta_{cat}.$$

With $\delta_{cat} \approx +175.76$ MHz, f_L gets detuned by

$$\begin{aligned} f_L &= f_0^{88} - \frac{\delta_{satabs}}{2} - 351.52 \\ &= f_0^{84} - \frac{\delta_{satabs}}{2}, \end{aligned}$$

where the isotope shift for the 689 nm transition $\Delta_{88-84} = f_0^{88} - f_0^{84} \approx 351.52$ MHz.

The MOT beams at a frequency $f_{MOT} = f_L + \delta_{MOT}$, with the MOT beams shifted by $\delta_{MOT} \approx \frac{\delta_{satabs}}{2}$, are then at the right frequency to trap ^{84}Sr atoms.

2.4 Multimode optical dipole trap (ODT)

The ultracold samples prepared with the 461 and 689 nm MOTs are finally transferred into our crossed-beam configuration ODT, which considerably increases both our atom density and sample lifetimes for the PAS and BEC experiments. A schematic

drawing of the ODT setup is shown in Fig. 2.12. We generate our ODT from a 21 W, 1064 nm, linearly-polarized, single-transverse-mode fiber laser[‡] (IPG Photonics) by using the first order deflection of an AOM at 110 MHz (Crystal Technology). The AOM allows fast turn on/off times and the ability to power control the trap beam. In our PAS experiments we did not have active servo control of the beam powers, and the highest powers attainable were 13 W. For the BEC experiment we did power control the ODT beams and the highest power was about 10 W.

The deflected beam from the AOM actually traverses our vacuum chamber and then is recycled through the chamber to intersect the first beam nearly perpendicularly. The plane of both ODT laser beams is inclined by about 10.5° from horizontal. Both beams have a waist (minimum e^{-2} intensity radius) of approximately $w = 90 \mu\text{m}$ in the trapping region. In this sense our ODT trap differs from traps utilized up to now by other groups that realized quantum degenerate gases with two-electron atoms, where one of the ODT beams had a significantly smaller waist [27, 88, 26, 28, 29].

We transfer up to 15% of the atoms from the 689 nm MOT to the ODT for an overlap time ranging from 80-115 ms. The transfer into the ODT works best if the trap begins shallow (about 2.5 to 5 W per beam) and then is ramped up quickly (in about 20 ms) to high powers. We also ramp down to low beam powers (around 2.5 W) if what we desire is a shallow trap to perform the experiment. The large amount of atoms (up to 20×10^6 ^{88}Sr atom for 13 W beams) yields peak densities on the

[‡]We actually run the fiber laser at 18 W instead of 21 W.

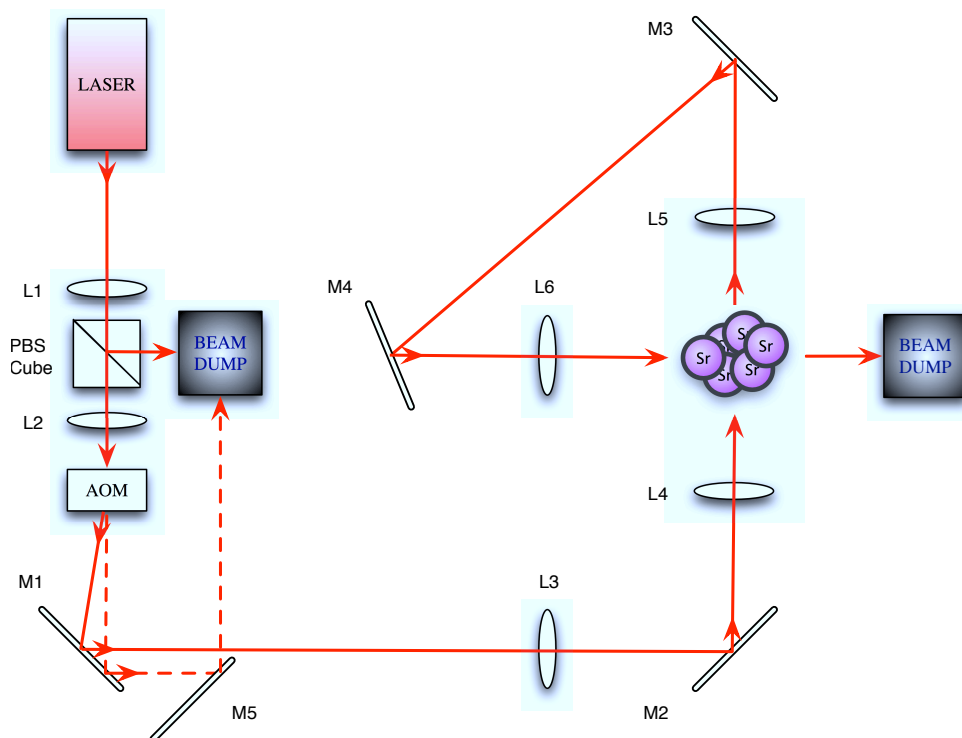


Figure 2.12 : Schematic drawing of 1064 nm ODT setup. The ODT beam traverses the experimental chamber to form a second beam for a crossed-beam setup. The direction of laser beam propagation through the functional elements of the setup is shown. A $\lambda/2$ quarter-wave plate in the second beam's path is missing. Other elements not crucial to the function of the setup are not shown. L: lens, M: mirror, PBS: polarization beam splitter cube. Figure courtesy of P. G. Mickelson [75].

order of 10^{14} cm^{-3} and peak PSD that can approach 10^{-1} . For the BEC experiment we trapped $\sim 3 \times 10^6$ atoms in 10 W ODT beams. Resulting sample temperatures for our ODT range from 3 – 15 μK , depending on the final trap used. Optimized transfer efficiency and stability depend strongly on the alignment of the FORT beams with the 689 nm MOT and the overlap between the two ODT beams.

After loading the atoms into the ODT, they are now ready for the particular experiment to be performed.

2.4.1 Profiling the ODT beams

A very important task left when working with the ODT is to characterize the beams' waist. Knowing the geometry of the trap is necessary when determining sample density and trap effective volumes (Chapter 3) when analyzing experimental measurements. We use a couple of methods to accomplish this, the first of which is profiling the ODT beams. Figure 2.13 shows a typical ODT beam profile before it traverses the vacuum chamber, with a measured mean beam waist of $\sim 69 \mu\text{m}$. The beam waists are actually slightly misaligned from the physical atom's position. In the figure, the atom's physical location is at zero. Therefore, the beam at the atoms has a size more like $\sim 90 \mu\text{m}$. Beam profile measurements similar to this one of the ODT beams after traversing the chamber windows show that the windows cause beam astigmatism. The astigmatism can displace the beam waists by up to $\sim 3 \text{ mm}$ from their original positions before traversing the chamber windows.

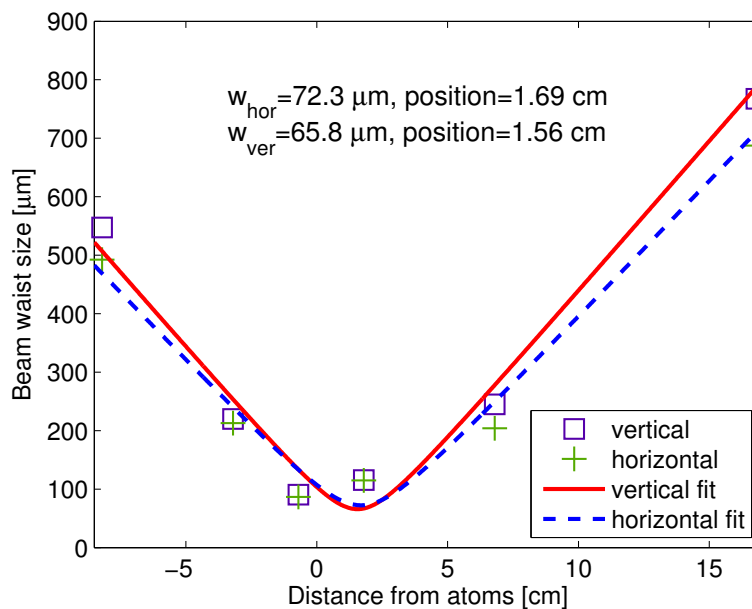


Figure 2.13 : Typical ODT beam profile before traversing the vacuum chamber. Although the beam’s mean waist is $69 \mu\text{m}$, the size of the beam near the atoms is $\sim 90 \mu\text{m}$. The atoms’ position is near 0 cm.

This distortion limits our ability to measure the beam waists precisely via beam profiling, so we resort to measure our trap’s frequency, as discussed in Section 2.4.2. However, our beam profiling measurements guide the way we assign our beam’s waist size when we model the trap’s characteristics, as explained in Section 2.4.3. We should be able to solve the beam astigmatism by using laser-grade vacuum viewports for the entrance and exit windows of the ODT beams.

2.4.2 Measuring trap frequencies

To aid us in correctly determining our ODT waists, we measure the trap oscillation frequencies by the parametric resonance technique [89]. The parametric resonance

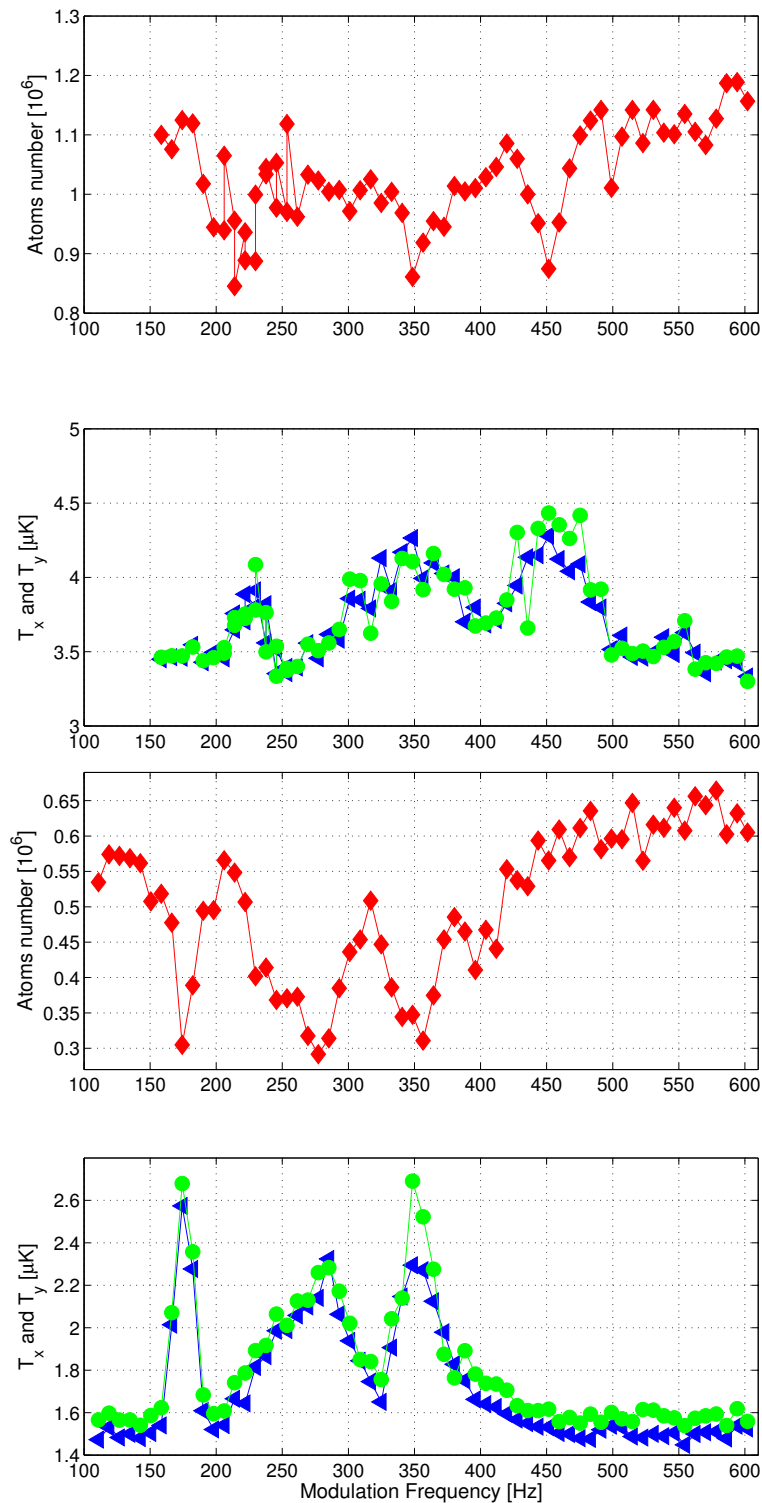


Figure 2.14 : Trap frequency measurements for 9.8 W (top two plots) and 5.3 W (bottom two plots) traps. Our trap frequency model gave us the following trap frequencies (f_x , f_y , f_z) for the best-fit waist sizes ($95 \mu\text{m}$, $80 \mu\text{m}$, $95 \mu\text{m}$): for 9.8 W trap (158.7 Hz, 240.2 Hz, 114.1 Hz) and for 5.3 W trap (124 Hz, 193.6 Hz, 92.2 Hz). The second harmonic frequencies are at $2f_i$. The measured frequencies shift to lower frequencies with decreasing trap depth (Eqs. 2.2 and 2.3).

technique works by modulating the intensity of the ODT laser and thus the trap's potential depth. For the trap frequency measurements, we collect atoms in the ODT at some desired beam power and then apply a sinusoidal modulation to the beam power via the ODT AOM. The modulation is 10-15% of the fixed beam power and lasts for 3 s. We then turn off the ODT and measure atom number and temperature with absorption imaging after a time of flight period, as will be described in Section 2.5. We typically measure trap frequencies at several beam powers, as shown in Fig. 2.14 for a deep (9.8 W, 35 μ K) and shallower (5.3 W, 18 μ K) trap, respectively.

The modulation frequency excites atoms trapped in the potential when the modulation frequency coincides with a harmonic of a trap's vibration frequency [89]. The excitation signals are seen in both atom losses and sample temperature spikes. Signals in the temperature measurements complement the atom loss spectrum well because our number loss spectra are usually very broad. We attribute this behavior to coupling between the radial and axial excitations due to our ODT setup. The trap's 10.5° incline and the potential caused by gravity couple any oscillations along the beam axial direction to oscillations in the beam's radial dimension. Furthermore, the trap's inclination and gravity also slightly couple the individual excitations of both crossed beams together.

By taking trap frequency measurements at different beam powers, we recognize a pattern in the way the resonance frequencies shift with trap power. By modeling the trap potential by a harmonic-oscillator potential (to be discussed in Section 2.4.3)

and using the observed trends in our measured frequencies, we are able to determine the ODT beam waists.

2.4.3 Modeling the ODT trap

We can numerically model the expected ODT trap frequencies for a certain set of trap parameters (trap beam power and waist sizes). Each trap beam forms a trapping potential of the form

$$U(x, y, z, P) = \alpha_{1S_0} \times \frac{2P}{\pi w_x w_y} U(x, y, z), \quad (2.2)$$

where α_{1S_0} is the polarizability of the 1S_0 state [90], w_i is the trap beam waists along the direction i , and P is the beam power ($\frac{2P}{\pi w_x w_y}$ is the beam's peak intensity). The position-dependent shape of the beam is

$$U(x, y, z) = \left[\left(1 + \left(\frac{\lambda z}{\pi w_x^2} \right)^2 \right) \left(1 + \left(\frac{\lambda z}{\pi w_y^2} \right)^2 \right) \right]^{-1/2} \times \exp \left(- \frac{2x^2}{w_x^2 \left(1 + \left(\frac{\lambda z}{\pi w_x^2} \right)^2 \right)} - \frac{2y^2}{w_y^2 \left(1 + \left(\frac{\lambda z}{\pi w_y^2} \right)^2 \right)} \right),$$

where z is along the beam's axis and $\lambda = 1064$ nm is the wavelength of the ODT beams. The crossed beam has the same position dependent shape but with beam waists w_y and w_z since it is nearly perpendicular to the first beam. The resulting trapping potential is the sum of the individual beam potentials. We include the effect of gravity by adding a potential term equal to $U_g = m g y$ to the trapping potential, where m equals the Sr mass, and $g = 9.8$ m/s². This defines the gravitational direction

along y . We also allow for the 10.5° tilt from horizontal by parametrizing the position variables with an angle θ .

By approximating the trapping potential U by a harmonic-oscillator potential, we obtain the trapping frequencies (when the other coordinates are zero) $\omega_i = 2\pi f_i$ from

$$U(i) = \frac{1}{2} m \omega_i^2 \sigma_i^2. \quad (2.3)$$

σ_i is chosen to account for the trapped atom's spatial excursion from the trap minimum due to their thermal energy. To determine the beam waists from modeling our trap frequencies, we vary the input trap waist sizes of the model until the model results ω_i match our measured trap frequencies for a given beam power P . Another criterion for our frequency modeling is that the model can reproduce the frequency shift expected when modeling the different trap depths.

We calibrate our beam power directly by measuring it with a power meter, and its uncertainty is within 5%. By modeling the measured trap frequencies in this way, we determine that the trap waists are $w_x = w_z = 95 \mu\text{m}$ and $w_y = 80 \mu\text{m}$. These waists are in good agreement with our trap beam profiles, from where we expected w_x and w_y to be approximately 80-100 μm , as discussed in Section 2.4.1.

With a fairly well-established value for the trap waists, we can determine the trap depth and mean oscillation frequency as a function of P (Eq. 2.2 and 2.3). The power dependence of both the trap depth and oscillation frequency is plotted in Fig. 2.15.

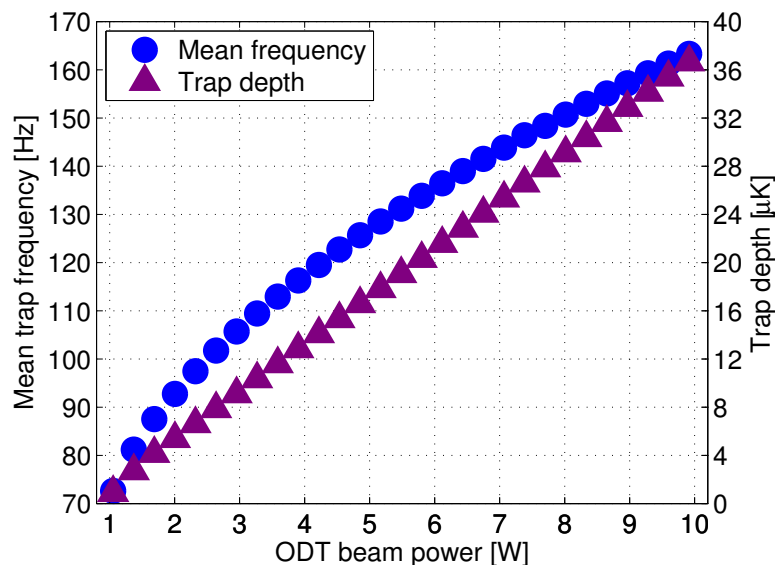


Figure 2.15 : Calculated trap depth and mean oscillation frequency versus ODT beam power. The waists used to calculate these parameters are $w_x = w_z = 95 \mu\text{m}$ and $w_y = 80 \mu\text{m}$.

2.5 Imaging techniques

We determine the number of atoms and sample temperatures with time-of-flight absorption imaging using the $^1S_0 \rightarrow ^1P_1$ transition. The drop time is chosen in order to decrease the sample's optical depth $OD(x, y)$, which is related to the density $n(x, y, z)$ of the atom cloud by

$$OD(x, y) = \int_{-\infty}^{\infty} n(x, y, z) \alpha_{abs} dz.$$

α_{abs} is the photon absorption cross section of the atoms,

$$\alpha_{abs} = \frac{3\lambda^2}{2\pi} \frac{1}{1 + (I/I_{sat}) + (2\pi\Delta_{image}/\Gamma)^2}, \quad (2.4)$$

and Δ_{image} is the image beam detuning from the resonance frequency. What we actually measure is the transmitted laser intensity I_{trans} after traversing the atom

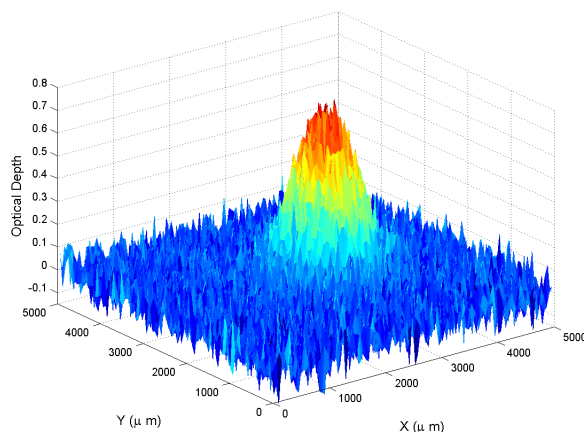


Figure 2.16 : A sample absorption image, showing the optical depth of an atom sample.

cloud. We relate I_{trans} to the incident laser beam intensity I_{inc} with the optical depth

$$I_{trans} = I_{inc}e^{[-OD(x,y)]}.$$

To measure I_{inc} , we take an absorption image of the image beam falling on the camera without atoms. From both the background and absorption images, we determine OD with

$$OD(x, y) = \ln[I_{inc}(x, y)/I_{trans}(x, y)].$$

Figure 2.16 shows a typical absorption image.

We determine the atom number from our absorption images using two methods. The first method includes numerically integrating OD over the entire region of interest. The atom number is then equal to

$$N_{OD} = \frac{\iint OD(x, y) dx dy}{\alpha_{abs}}$$

where α_{abs} is determined through Eq. 2.4. We can also fit the absorption image with

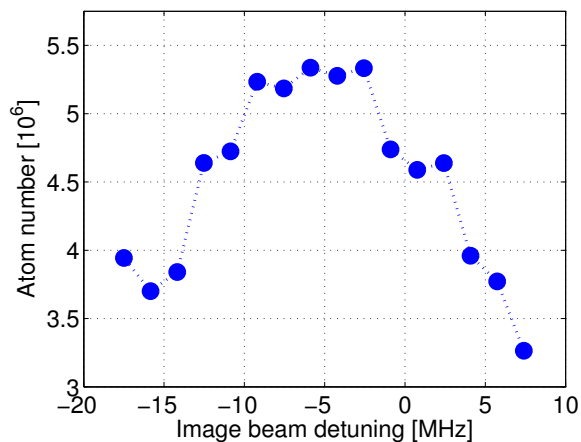


Figure 2.17 : 461 nm image beam spectrum of ^{84}Sr atoms. The image beam frequency is nearly resonant to the atomic transition of ^{84}Sr .

a function of the form

$$OD = \frac{\alpha_{abs} N_{fit}}{2\pi\sigma_x\sigma_y} \exp\left[-\frac{x^2}{2\sigma_x^2} - \frac{y^2}{2\sigma_y^2}\right],$$

where σ_i is the width of the absorption gaussian fit. A fit to the optical depth yields N_{fit} .

Since the detuning of our 461 nm light from resonance is a function of the saturated absorption cell's magnetic field B , it sometimes becomes necessary to optimize the magnetic field due to any current changes in daily operation. We use the image beam detuning for this purpose. Two AOMs produce the image beam from the main 461 nm laser at frequency f_L . These AOMs shift the image beam frequency f_{image} to be nearly resonant to the 461 nm transition frequency in order to make α_{abs} (Eq. 2.4) maximum, for a given image beam intensity I . We can therefore optimize B by taking a spectrum of the number of atoms imaged versus B . The measured atom number should peak when f_{image} is nearly resonant to the 461 nm transition, all other

parameters staying fixed. Figure 2.17 shows one such image frequency scan.

With the techniques presented in this chapter, we prepare ultracold, dense samples for the PAS and BEC experiments described in the following chapters.

Chapter 3

PAS of Sr using an intercombination transition

The next two chapters describe a series of experiments aimed at determining the s -wave scattering length a of Sr through photoassociative spectroscopy (PAS). Recalling the discussion of Chapter 1, PAS and its two-photon version, deal with accurately measuring the position of bound states of molecular potentials. Our goal was to locate the position of the least-bound level in the ground molecular potential of Sr with two-photon PAS since a is very sensitive to its binding energy.

In this experiment, we keep track of the frequencies necessary to bring the PAS lasers on resonance with the two-photon transition from the two-free-atom state to the bound level in the ground molecular potential. This is illustrated in Fig. 3.1, where f_1 and f_2 are the frequencies of these two lasers. The binding energy of the least-bound level b_2 is equal to the difference $f_1 - f_2$ of the laser frequencies when they are on resonance with the two-photon transition. Since our intermediate state b_1 is the metastable 3P_1 state with an inherent narrow linewidth, accounting for significant lineshifts to its unperturbed resonance frequency due to the ODT, laser and thermal broadening is required to understand the lineshape for this transition. Any frequency shifts should be included for an accurate determination of the b_2 bound state's binding energy. Performing one-photon PAS of b_1 allows us to measure these

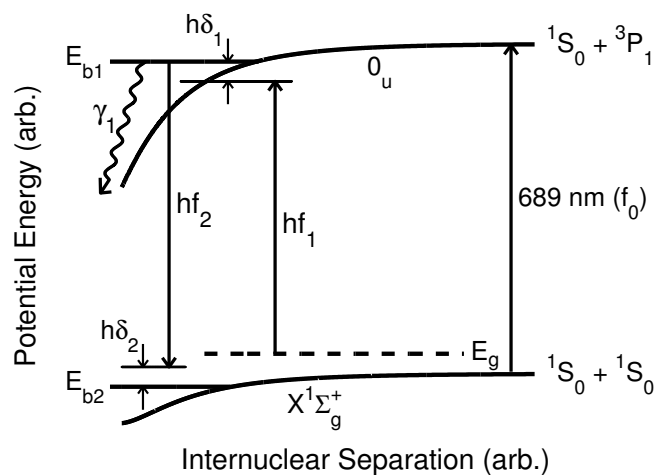


Figure 3.1 : Two-photon PAS diagram. E_g equals the energy of a colliding atom pair (zero energy is equal to when the atoms are far apart). E_{b1} is the unperturbed energy of a bound state (with decay rate γ_1) in the 1S_0 - 3P_1 molecular potential, while E_{b2} is the binding energy of the highest-lying state in the 1S_0 - 1S_0 potential. The photon energy $h f_1$ of laser 1 is detuned from E_{b1} by $h\delta_1$. Laser 2 is nearly resonant with the bound-bound transition between states E_{b1} and E_{b2} , and its photon energy $h f_2$ is detuned from E_{b2} by $h\delta_2$. The unperturbed resonance frequency of the atom at zero collisional energy is f_0 . Energy shifts due to the ODT are neglected in the diagram. Adapted from [63].

contributing lineshifts.

This chapter first presents the connection between ultracold collisions and the scattering length. It then describes the theoretical framework necessary to model the PAS spectrum for the one- and two-photon scenarios. By measuring PAS spectra of the metastable intermediate state, we determine the stimulated linewidth due to the PAS laser and the relative light shift on the ground and excited states because of the ODT. These measurements are preparatory to accurately measure the position of b_2 as described in Chapter 4.

3.1 Ultracold collision theory

A complete description of scattering theory can be found in standard textbooks ([91, 55, 92]) and is followed here to motivate the study of ultracold collisions with PAS. Because of the low thermal energy of colliding atoms in our experiments, their interactions are localized and elastic, such that their internal states do not change. Our task is to study the effect the collision has on the center-of-mass wave function and relate the collisional phase shift to the scattering length.

The appropriate wave function describing the center-of-mass motion of unbound, colliding atoms is a plane wave e^{ikz} traveling in the z direction, as shown in Fig. 3.2. Here, the energy of the state defines the wave vector k by the collision energy

$$E = \frac{\hbar^2 k^2}{2\mu},$$

where μ is the reduced mass of the colliding atoms. A collision between the incoming

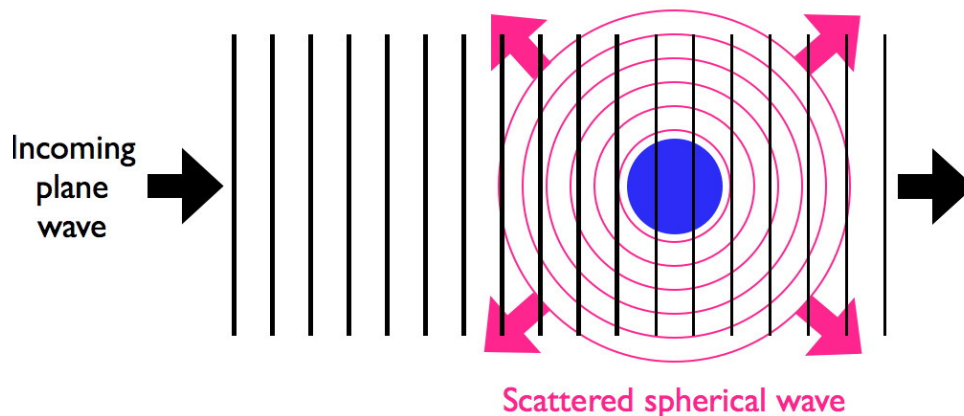


Figure 3.2 : Schematic of a scattering event. An incoming plane wave (representing two colliding, unbound atoms) interacts with a scattering potential that has spherical symmetry (blue circle). The collision with the potential results in a scattered spherical wave (pink wave). If the resulting wave is observed from far away, the entire waveform would be the incoming plane wave (e^{ikz}) plus a scattered part ($f(\theta) \frac{e^{ikr}}{r}$), where the plane wave travels in the $+z$ direction.

wave and a scattering potential results in a scattered wave ψ_{sc} that, far away from the interaction region, looks like an outgoing spherical wave. The resultant wave function at great distances, therefore, must have the form

$$\psi(\vec{r}) \rightarrow e^{ikz} + f(\theta) \frac{e^{ikr}}{r}, \quad (3.1)$$

with a scattering amplitude $f(\theta)$ (for spherically symmetric potentials) for an angle θ between the z -axis and the direction of the scattered particle. What is actually “measured” in an atom collision experiment is the amount of scattered particles that pass through a differential solid angle $d\Omega$, known as the cross section $d\sigma$:

$$d\sigma = |f(\theta)|^2 d\Omega.$$

The total scattering cross section is the integral of $d\sigma$ over all solid angles:

$$\sigma = 2\pi \int_0^\pi |f(\theta)|^2 \sin \theta d\theta. \quad (3.2)$$

$f(\theta)$ therefore contains all the information about the collision and an expression for this function would allow us to evaluate this integral.

To get $f(\theta)$ we can solve Schrödinger's equation for a central potential $U(r)$ in the asymptotic limit such that the resulting solution has the form of Eq. 3.1. A suitable center-of-mass wave function would display conservation of angular momentum and axial symmetry due to the way we defined the scattering particle's direction by θ . These conditions are met by the Legendre polynomials $P_l(\cos \theta)$ and the radial wave function $R_{kl}(r)$. In terms of these functions we get

$$\psi(r) = \sum_{l=0}^{\infty} A_l P_l(\cos \theta) R_{kl}(r) \quad (3.3)$$

for a satisfactory center-of-mass wave function to use. Using $\psi(r)$ in the Schrödinger equation $H\psi = E\psi$ results in the equation for the radial wave function:

$$\frac{\hbar^2}{2\mu} R''_{kl}(r) + \frac{\hbar^2}{\mu} \frac{1}{r} R'_{kl}(r) + \left[E - \frac{\hbar^2}{2\mu} \frac{l(l+1)}{r^2} - U(r) \right] R_{kl}(r) = 0. \quad (3.4)$$

The effective potential $\frac{\hbar^2}{2\mu} \frac{l(l+1)}{r^2} + U(r)$ has important implications for collisions at low energy E : the centrifugal barrier $\frac{\hbar^2}{2\mu} \frac{l(l+1)}{r^2}$ increases for partial waves* with angular momentum $l > 0$, blocking them from entering the region where $U(r)$ is significant when the energy E is low. Therefore, only $l = 0$ (s -wave) partial waves contribute to

*The partial wave functions would be ψ_l for the sum $\psi(r) = \sum_{l=0}^{\infty} \psi_l(r)$.

ψ during collisions at ultracold temperatures (low E). This concept will be important later.

Although we need the correct form of $U(r)$ to solve Eq. 3.4, knowing what the asymptotic form of $R_{kl}(r)$ allows us to continue. At large r we get a solution for Eq. 3.4 that can be used in Eq. 3.3 [92] (with the constant $A_l = \frac{1}{2k}(2l+1)i^l e^{i\delta_l}$):

$$R_{kl}(r) \approx \frac{2}{r} \sin(kr - \frac{\pi}{2}l + \delta_l), \quad (3.5)$$

where δ_l is a phase and l is the orbital angular momentum quantum number. Comparing Eqs. 3.1 and 3.3 eventually gives us[†]

$$f(\theta) = \frac{1}{2ik} \sum_{l=0}^{\infty} (2l+1)(e^{i2\delta_l} - 1)P_l(\cos\theta). \quad (3.6)$$

With Eq. 3.6 for $f(\theta)$, we can now evaluate Eq. 3.2. The total cross section becomes, in terms of δ_l ,

$$\sigma = \frac{4\pi}{k^2} \sum_{l=0}^{\infty} (2l+1) \sin^2 \delta_l. \quad (3.7)$$

In the limit of low-energy ($k \rightarrow 0$) scattering where only $l = 0$ terms are significant, $f(\theta) \approx \frac{1}{2ik}(e^{i2\delta_0} - 1) = \delta_0/k$ becomes constant for small δ_0 . We give that constant a symbol “ a ”, and Eq. 3.2 gives us the total cross-section $\sigma = 4\pi a^2$.

For the preceding derivation we have assumed that the particles are distinguishable, which is not the case for identical bosons. Taking into account the symmetrization of the wave function for bosons, the scattering state $\psi(\vec{r})$ in (3.1) becomes

[†]The plane wave e^{ikz} in Eq. 3.1 can also be expanded in terms of $P_l(\cos\theta)$ and $R_{kl}(r)$. Taking the difference $\psi - e^{ikz}$ gives us the desired expression for $f(\theta)$.

$\psi_{tot}(\vec{r}) = \frac{1}{\sqrt{2}} [\psi(\vec{r}) + \psi(-\vec{r})]$ [93], the total cross section for identical boson becomes

$$\sigma = \frac{8\pi}{k^2} \sum_{l \text{ even}}^{\infty} (2l + 1) \sin^2 \delta_l, \quad (3.8)$$

and for low-energy scattering ($l = 0$) it also approaches a constant value

$$\sigma = 8\pi a^2. \quad (3.9)$$

The constant a is called the s -wave scattering length, and it parametrizes low-energy collisional properties. It is related to the phase shift (δ_0) the scattering wave function experiences during a collision (see Eqs. 3.3 and 3.5).

3.1.1 Scattering length theory

As alluded to in Chapter 1, the scattering length a is most sensitive to the position of the least-bound state in the ground molecular potential. We can model this behavior by considering a 1D square well for the potential $U(r)$ in Eq. 3.4 when $k \rightarrow 0$ [93].

The solution to the Schödinger equation for $U(r)$ defined as

$$U(r) = \begin{cases} 0 & \text{for } r > b \\ -U_0 & \text{for } r \leq b \end{cases}$$

(where U_0 is positive) is

$$R(r) \propto \begin{cases} r - a & \text{for } r > b \\ \sin(k_0 r) & \text{for } r \leq b \end{cases}$$

with $k_0 = \sqrt{2\mu U_0}/\hbar$. Taking into account the continuity of $R(r)$ and $R'(r)$ at $r = b$ gives

$$a = b - \frac{\tan k_0 b}{k_0}. \quad (3.10)$$

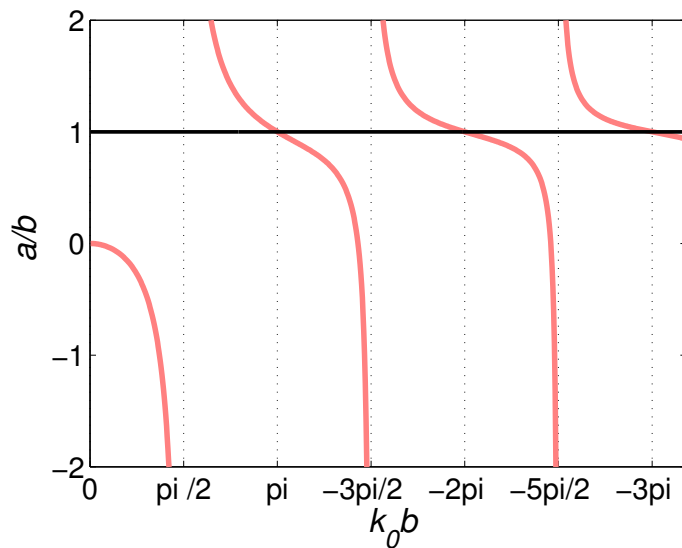


Figure 3.3 : Scattering length a as a function of square potential well energy parameter $k_0 b = b\sqrt{2\mu U_0}/\hbar$. The divergences for a occur when the parameter $k_0 b$ corresponds to the emergence of a new bound state in the potential $U(r)$ (Eq. 3.10). Adapted from [93].

Figure 3.3 displays the behavior of a from Eq. 3.10. When $k_0 b < \pi/2$, the potential $U(r)$ is too small to support a bound state in the well, making the scattering length a negative. As the potential deepens, a undergoes oscillatory behavior with regular divergences. These divergences occur at the point where a bound state appears in the potential well, corresponding to when $k_0 b$ is a multiple of $\pi/2$. Near the vicinity of the singularities, a is large and negative slightly before a bound state appears, and large and positive with each newly appeared bound state. The solution is more complex for a realistic molecular potential, but the qualitative behavior is the same [94].

Because of the sensitivity of a to the position of the least-bound state in the

potential, measuring its binding energy leads to a very accurate description of a and an understanding of the ultracold collisional properties of Sr.

3.2 Molecular potentials and levels

The transition between b_1 and b_2 (see Fig. 3.1) is between two molecular potentials, so we first consider the selection rules for transitions between them. The ground state of Sr atoms is 1S_0 , with orbital angular momentum $L = 0$ and spin $S = 0$. When two ground-state atoms are very far apart (interatomic distance $R \rightarrow \infty$), the total energy of the molecule ($^1S_0 + ^1S_0$) equals that of two isolated atoms. As the atoms draw near to each other (large R), they interact through the van der Waals interaction and approach along an attractive potential of the form C_6/R^6 [95, 55]. When $R \rightarrow 0$ the overlapping of the atoms' electron clouds causes a strong repulsion between the atoms. In between these two distance extremes the potential forms a minimum that can support rotational-vibrational eigenstates for the Sr_2 molecule [96].

When a ground-state atom interacts with another atom that differs in orbital angular momentum $|L|$ by 1, the dipole-dipole forces has a leading term of the form C_3/R^3 , where the interaction can be either attractive or repulsive [92]. These molecular potentials would correspond to when an atom in the 1S_0 state interacts with an excited atom in a P state. The attractive potentials could also support rotational-vibrational eigenstates, as in the $^1S_0 + ^1S_0$ case.

The molecular entity possesses cylindrical symmetry, which is in sharp contrast

to the spherical symmetry of individual atoms. The cylindrical axis of the molecule coincides with the line-of-sight between the two nuclei [96]. This symmetry line turns out to be the preferred projection axis for the molecule, and the orbital angular momentum \vec{L} of the individual atoms are quantized with respect to it. Similarly to the atomic quantum number L , the quantization axis results in a quantum number Λ for the molecule, with values $\Lambda = 0, 1, 2, \dots$. The corresponding molecular state labels (for each Λ value respectively) are Σ, Π, Δ , etc.

Rotational-vibrational eigenstates of the potentials can be approximately determined by solving the Schrödinger equation of the molecular system, with the nuclei vibrational motion decoupled from the rotational motion (the Born-Oppenheimer approximation). This simplified result, which works well near the molecular potential's minimum, describes each vibrational state in the potential as accompanied by a ladder of rotational states enumerated by the molecule's rotational angular momentum quantum number J [96].

Particular selection rules determine which molecular transitions are allowed when electronic transitions occur within the atoms forming the molecule, as in the case of PAS. For our PA experiment, the selection rules include $\Delta\Lambda = 0, \pm 1$ and $\Delta J = \pm 1$ [96, 97]. The electronic selection rules can be met for the transition from the ground molecular state to the $^1S_0 + ^3P_1$ potential [98]. Transitions will occur between rotational levels that change by 1. A last consideration (for homonuclear molecules) is a consequence of the electronic transition that the PA laser induces. In the transition

between 1S_0 to 3P_1 , the molecule must change symmetry due to the fact that the electric dipole connects states of different parity [96, 97]. This restricts the electronic transition to between ‘ g ’ (gerade, or symmetric) and ‘ u ’ (ungerade) symmetry states.

3.3 PA loss theory

Photoassociation (PA) with a laser nearly resonant with a transition between two atom-colliding states induces atom loss from our sample by promoting a colliding pair from one state to the other (see Fig. 3.1). The photoassociated molecule eventually spontaneously dissociates and the individual atoms generally acquire enough kinetic energy to escape the trap. PAS loss is then a two-body loss process, characterized by the collision event rate constant[‡] K . The purpose of using PAS is to locate the position of the molecular potential bound states in order to map out the molecular potential.

In analyzing PA loss, we model the sample’s density evolution with the equation

$$\dot{n} = -2Kn^2 - \Gamma n, \quad (3.11)$$

where n is the atomic density and Γ is the one-body loss rate. The laser-frequency dependence of the collision event rate constant $K(f)$ determines the spectrum of the PA loss, which for our experiments is comparably simple due to the lack of hyperfine structure for the Sr bosonic isotopes.

[‡]Two atoms are lost in each collision, so $\beta(n) = 2K$ defines the two-body loss rate β .

The transition energy depends upon the kinetic energy of the free atoms. Therefore, the PA line shapes are thermal averages over the energy distribution of the trapped atoms. For transitions with natural linewidths on the order of the sample's thermal energy $k_B T$ the spectrum's thermal broadening is slight, while broadening is significant when the transition is an intercombination line like those available in Sr. In any case, a detailed treatment of the thermally averaged spectrum is necessary to accurately determine bound level energies and other molecular potential characteristics.

We model PA resonances with theory developed in [99, 100], assuming only s -wave collisions and a Boltzmann energy distribution for the trapped atoms. We also neglect Doppler shift and photon recoil effects [101] because $T > T_R$, $T_R = h^2/(2k_B \lambda)$ being the recoil temperature for photons with wavelength λ . Trap confinement effects [98] are negligible for our sample temperatures since the thermal energy is much larger than the trap zero-point energy ($T \gg h \nu_{trap}/k_B$).

With all these considerations, the collision event rate constant for the PA process that produces a product p from colliding atoms becomes

$$K = \frac{1}{h Q_T} \int_0^\infty |S(E_g, f_1, f_2)|^2 e^{-E_g/k_B T} dE, \quad (3.12)$$

where $Q_T = \left(\frac{2\pi k_B T \mu}{h^2}\right)^{3/2}$ is the partition function for reduced mass μ and $|S|^2$ is the scattering probability for loss. The form of $|S|^2$ depends on whether the bound state b_2 in the ground molecular potential has a comparable decay rate γ_2 to that of the excited state b_1 . Since b_1 is metastable, this is a reasonable consideration. As we

will see in Chapter 4, the complete vanishing of the PA loss when the lasers are on two-photon resonance implies that decay from b_1 dominates [100], and the scattering probability is given by

$$|S_{1g}|^2 = \frac{(\delta_1 - \delta_2)^2 \gamma_1 \gamma_s / (2\pi)^2}{\left\{ \left[\delta_1 - \frac{\delta_2}{2} \right]^2 - \frac{1}{4} \left[\delta_2^2 + \frac{\Omega_{12}^2}{(2\pi)^2} \right] \right\}^2 + \left(\frac{\gamma_1 + \gamma_s}{4\pi} \right)^2 (\delta_1 - \delta_2)^2}. \quad (3.13)$$

For our notation, δ_i is the detuning of f_i from the transition frequency (Fig. 3.1), $\gamma_1 = 2\gamma_{atomic}$ is the decay rate of b_1 (γ_{atomic} is the decay rate of the atomic 3P_1 level), and $\gamma_s(E_g)$ is the stimulated linewidth of the transition to b_1 due to radiative coupling to the energy-normalized colliding state $|E_g\rangle$:

$$\gamma_s(E_g) = \frac{2\pi V^2 |\langle b_1 | E_g \rangle|^2}{\hbar}. \quad (3.14)$$

The Franck-Condon factor for the free-bound transition is $|\langle b_1 | E_g \rangle|^2$ and $V = d \left(\frac{I_1}{2\epsilon_0 c} \right)^{1/2}$ for a free-bound laser intensity I_1 and molecular dipole matrix element d . We define the splitting of the Autler-Townes doublet by Ω_{12} (to be discussed in Chapter 4), which differs from the definition of the molecular Rabi coupling of Reference [100].

Because we lack an ODT at the magic wavelength of 914 nm [98], the ODT causes ac Stark shifts of b_1 and b_2 . These frequency shifts must be taken into account when defining the laser detunings δ_1 and δ_2 . The situation is further complicated by the spatially-varying atom density produced by the ODT intensity profile. The spatially-varying atom density results in energy level shifts that vary with position.

Accounting for relative energy level shifts can be simplified somewhat when the shift of the incoming state of two colliding atoms g and that of the bound state b_2 are

regarded as equal (Fig. 3.1). This approximation is reasonable because b_2 is weakly bound and close to the energy of state g , making the polarizability of the molecule about twice that of a free atom and implying that both energy levels shift roughly the same magnitude in the same direction. However, the ground and excited molecular levels (b_1) do not shift by the same amount. We therefore treat the ac Stark shift as a position-dependent shift of the excited level b_1 . With these considerations, we define the laser detunings as

$$\delta_1 = f_1 - (E_{b_1} - E_g)/h - \chi I_{ODT}(\vec{r}) \quad (3.15)$$

$$\delta_2 = f_2 - (E_{b_1} - E_{b_2})/h - \chi I_{ODT}(\vec{r}), \quad (3.16)$$

where $I_{ODT}(\vec{r})$ is the intensity profile of the ODT and χ can be related to the differences in polarizabilities for 1S_0 and 3P_1 atoms for $1.06 \mu\text{m}$ laser light. A discussion of the ODT ac Stark shifts to the atomic energy levels can be found in P. Mickelson's thesis [75]. Defining the laser detunings δ_1 and δ_2 according to Eqs. 3.15 and 3.16 makes K (Eq. 3.12) position-dependent.

What we measure in our experiment is the number of trapped atoms left over after an atom-laser interaction time t . Integrating Eq. 3.11 over the trap volume gives us

$N(t)$:

$$\begin{aligned}
\dot{N} &= \int_V d^3r \dot{n} \\
&= -\Gamma N - \int_V d^3r 2K(r) n^2 \\
&= -\Gamma N - 2n_0^2 \int_V d^3r K(r) e^{-2U(r)/k_B T} \\
&= -\Gamma N - 2N^2 \frac{V_2}{V_1^2} \times \frac{1}{V_2} \int_V d^3r K(r) e^{-2U(r)/k_B T}, \\
&= -\Gamma N - 2N^2 \frac{V_2}{V_1^2} K_{\text{eff}}, \tag{3.17}
\end{aligned}$$

where we integrated the density $n = n_0 e^{-U(r)/k_B T}$ to determine the total number of atoms

$$\begin{aligned}
N &= \int_V d^3r n \\
&= n_0 \int_V d^3r e^{-U(r)/k_B T} \\
&= n_0 V_1
\end{aligned}$$

with V_q being the effective volume for the loss involving q number of particles:

$$V_q = \int_V d^3r e^{-qU(r)/k_B T}. \tag{3.18}$$

Solving the differential equation 3.17 results in

$$N(t) = \frac{N_0 e^{-\Gamma t}}{1 + \frac{2N_0 K_{\text{eff}} V_2}{\Gamma V_1^2} (1 - e^{-\Gamma t})} \tag{3.19}$$

for the time evolution of the trapped atom number. In evaluating the effective volumes for Eq. 3.19, we assume a constant sample temperature since atom temperatures varied by no more than 25% during an atom-laser interaction time. Since an atom

with energy greater than the trap depth $U_{max} - U(r)$ escapes the trap, the local trap depth truncates the energy integral for $K(r)$ in Eq. 3.12 and the effective collision event rate constant K_{eff} becomes

$$K_{\text{eff}} = \frac{1}{V_2} \int_V d^3r e^{-\frac{2U(\vec{r})}{k_B T}} \times \frac{1}{h Q_T} \int_0^{U_{max}-U(r)} dE_g |S_{1g}|^2 e^{-E_g/k_B T}. \quad (3.20)$$

To compare our PA data with this loss model, it is necessary to solve the integral (3.20) for K_{eff} numerically.

3.3.1 One-photon PAS limit

Since we are interested first in measuring the lineshifts to the unperturbed resonance frequency of the free-bound transition, we set all parameters pertaining to the second PAS beam in Eq. 3.13 to zero, recovering the one-photon PAS scattering probability for loss through b_1 [99]

$$|S_{1g}|^2 = \frac{\gamma_1 \gamma_s / (2\pi)^2}{\delta_1^2 + \frac{1}{(2\pi)^2} \left(\frac{\gamma_1 + \gamma_s}{2} \right)^2}. \quad (3.21)$$

The following sections describe experiments performed to determine $\gamma_s(I_1)$ in Eq. 3.21 and χ in the laser detuning δ_1 (see Eq. 3.15).

3.4 The PAS lasers

We derive both PAS lasers from the main 689 nm master laser setup[§] that produces our 689 nm MOT beams (see Chapter 1), so they have the same frequency stability

[§]This is a master-slave laser setup.

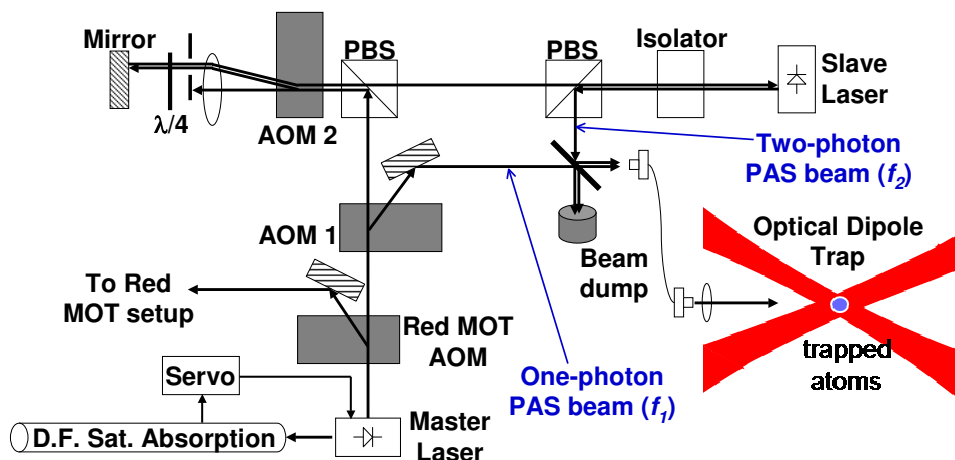


Figure 3.4 : Schematic of photoassociation lasers. The master-slave laser pair that provides light for the intercombination-line MOT is frequency-stabilized via saturated absorption spectroscopy to the atomic transition, and it also provides the photoassociation lasers. Laser 1 with frequency f_1 , is generated directly from the master with an AOM, while laser 2 (frequency f_2) is formed by injection-locking a slave diode with a double-passed deflected beam from an AOM in a cat's eye configuration. The direction of laser beam propagation through the functional elements of the setup is shown. Other elements not crucial to the function of the setup are not shown. PBS: polarizing beam splitter cube, $\lambda/4$: quarter-wave plate. Adapted from [63]

and linewidth. Although we use the same beam that produces the MOT beams, the setup works well because the MOT beams are off during the ODT cycle when the PAS lasers interact with the atoms. The main master laser is at frequency[¶] $f_{main} = f_0 - \delta_{satabs}/2 = f_0 + 75$ MHz, where f_0 is the ^{88}Sr 689 nm transition frequency. By using AOMs we detune f_{main} to the correct frequencies f_1 and f_2 necessary. Figure 3.4 shows a schematic drawing of the setup being discussed.

An AOM with a 200 MHz center frequency (Isomet P/N 1250c) generated the first beam at f_1 ($f_1 = f_{main} + \delta_{PAS}$ with $\delta_{PAS} \approx -297$ MHz) that we use for the

[¶] $\delta_{satabs} = 149.944$ MHz for this experiment.

first PAS laser. The remaining beam double-passed an AOM (Isomet P/N 1205C-2) in cat's eye configuration and served as the injection-locking beam for a slave laser that was used as the second PAS laser. The deflected beam is at $f_2 = f_{main} + 2\delta_{cat}$ with $\delta_{cat} \approx -78.5$ MHz. After their generation, we combine both PAS lasers with the same linear polarization and couple them into an optical fiber (Thorlabs P/N 630HP (FT030)). These beams focused to a beam waist of $w = 200 \mu\text{m}$ at the location of the atom sample with a combination of the fiber output coupler (OZ-Optics P/N HPUC-23AF-400/700-S-6AC-11) and a 750 mm lens placed about 15 mm after the output coupler.

We used a cat's eye setup to provide the injection-locking beam for the second PAS slave laser because this permits us to scan f_2 without misaligning the injection locking beam of the slave laser. The injection-locking beam had about $250 \mu\text{W}$ of power. This beam seeds a laser diode (Hitachi P/N HL6738MG) that delivered about 4.8 mW power at the fiber input coupler with a drive current of around 850 mA and a set control temperature of around 0.803 V . We inspected the performance of the slave's injection lock by monitoring on a Fabry-Perot cavity whether the slave laser followed the master laser.

A photodiode after the fiber monitors the output power of either PAS beam from the fiber, whose calibration was 0.562 mW per 1 V on the monitor photodiode. To vary the powers of either PAS beams, we placed fixed optical-depth attenuators in the desired laser beam path before the fiber. We used a beam shutter on the second PAS

beam to turn it on and off, while the first beam easily turned on and off because of the AOM. The power stability was not actively controlled, but was stable within 10%. More than 85% of the power of either output beams is linearly polarized vertically, perpendicular to the horizontal polarization of the ODT beams. However, we did not monitor nor explore the polarization stability of the output PAS beams.

Initial alignment of lasers f_1 and f_2 begins by copropagating the beams with a 461 nm beam derived from the main 461 nm image beam. The 461 nm guide beam is easily aligned on the ODT sample by absorption imaging using a CCD camera independent of the primary imaging camera used for data taking. We further optimize the alignment of the PAS beams by bringing laser f_1 on resonance with the free-bound transition and aligning to maximize the atom loss.

3.5 The one-photon PAS experiment

We prepare samples in the ODT following the same procedure outlined in Chapter 2. For this spectroscopy experiment, we choose ODT beam powers between 2.5 and 13 W, which yield about $4 - 15 \times 10^6$ atoms at equilibrium temperatures between 3 and 15 μK , depending on the beam power. These sample numbers produce peak densities on the order of 10^{14} cm^{-3} . Background atom pressure and photon scattering from stray 461 nm light limit the sample lifetime to about 2 s^{||}

^{||}After shielding the experimental chamber from all possible stray 461 nm light, the ODT sample lifetime increased to about 25 s. A long lifetime (~ 25 s) was the situation for our BEC experiment.

After a brief 250 ms of equilibration hold time, we turn laser 1 on, step its frequency f_1 near the free-bound resonance frequency and measure the remaining atoms after an atom-laser interaction time T_{int} to obtain a loss spectrum like in Fig. 3.5. Figure 3.6 diagrams the timing for this experiment. In some instances we included a short ODT hold time T_h after T_{int} before we measured the remaining atoms. Locating the third least-bound vibrational level b_1 of the 1S_0 - 3P_1 excited molecular potential at $f \approx f_0 - 222.2$ MHz was relatively straight forward thanks to previous measurements [98] of these bound vibrational levels. We took PAS spectrum at different ODT trap depths and PAS laser beam intensities to allow us to determine $\gamma_s(I_1)$ and χ .

From the spectra in Fig. 3.5 we notice a couple of features. The lineshape taken at higher ODT trap powers shifts to the blue compared to that at lower ODT trap power. This suggests that the polarizability of the 3P_1 state is less than that of the 1S_0 state by analyzing Eq. 3.15: the PA transition (when $\delta_1 = 0$) occurs at a blue-shifted f_1 because the position-dependent shift $\chi I_{ODT}(\vec{r})$ is positive. This will be described more quantitatively in Section 3.5.3. Another interesting feature of the spectra deals with its red spectral tail. If there would only be one collision energy, the spectrum observed would be a Lorentzian centered at the laser detuning corresponding to that collision energy. Due to the thermal distribution of collision energies, the resulting spectrum is actually a convolution of single-energy Lorentzians with a Maxwell-Boltzmann distribution of collision energies [102, 98].

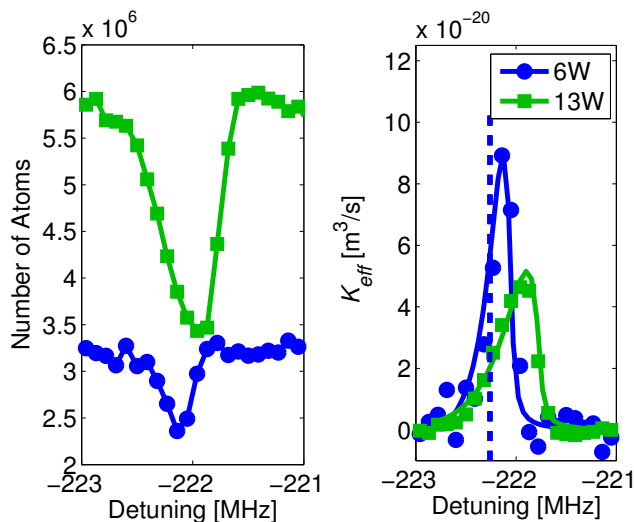


Figure 3.5 : One-photon PA spectra. Left: Atom number versus free-bound laser detuning from the 1S_0 - 3P_1 atomic transition. Spectra shown here are for 6 W and 13 W ODT single-beam powers with sample temperatures of 6 μK and 13 μK , respectively. Right: Collision-event rate constant K_{eff} derived from the atom loss. The ODT at 1064 nm causes an AC Stark shift of the excited molecular state compared to the ground state, which shifts and broadens the line. The solid lines are fits using Eqs. 3.20 and 3.21. We measure a peak shift of 480 kHz for a single-beam power of 13 W. The dashed line marks the position of our measured unperturbed resonance frequency at -222.25(15) MHz, which is in reasonable agreement with a previous measurement of -222.161(35) MHz [98]. Adapted from [63].

3.5.1 Determining K_{eff} from one-photon measurements

To derive K_{eff} from our measurements, we invert $N(t)$ from Eq. 3.19 to get K_{eff} as a function of N . We accounted for any one-body losses present during T_h (see Fig. 3.6) by determining N in the following way ($C = \frac{2K_{\text{eff}}V_2}{V_1^2}$):

$$N_1 = \frac{N_0 e^{-\Gamma T_{\text{int}}}}{1 + \frac{N_0 C}{\Gamma} (1 - e^{-\Gamma T_{\text{int}}})} \quad (3.22)$$

$$N = N_1 e^{-\Gamma T_h} = \frac{N_0 e^{-\Gamma (T_{\text{int}} + T_h)}}{1 + \frac{N_0 C}{\Gamma} (1 - e^{-\Gamma T_{\text{int}}})}. \quad (3.23)$$

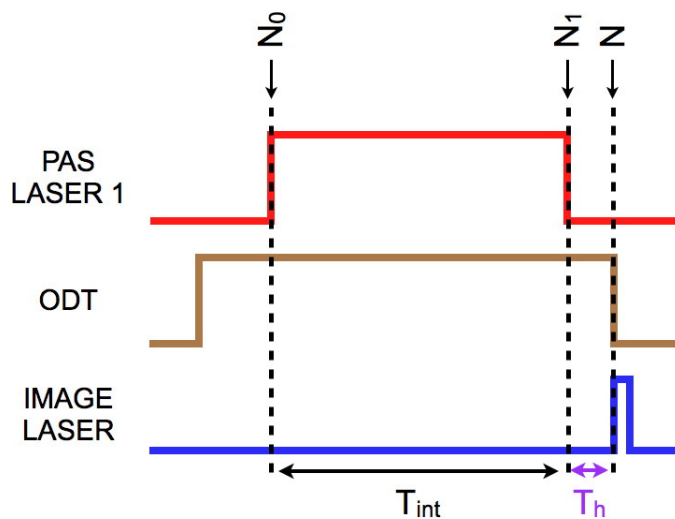


Figure 3.6 : Timing diagram for one-photon PAS. The traces are offset for clarity and the heights indicate turn on/off. We determine the initial number of atoms N_0 at the beginning of the atom-laser interaction time as described in Section 3.5.1. T_{int} : atom-laser interaction time, T_h : post-interaction ODT hold time.

Γ is the background loss rate for the ODT depth we made the measurement in. By inverting Eq. 3.23 for K_{eff} , we get:

$$K_{\text{eff}} = -\frac{V_1^2}{2V_2} \frac{\Gamma e^{-\Gamma T_h} (N e^{\Gamma(T_{int}+T_h)} - N_0)}{N_0 N (e^{\Gamma T_{int}} - 1)}. \quad (3.24)$$

We determined N_0 from an average of 4 number measurements taken with the PAS beam ~ 1 MHz detuned off resonance from the PAS transition. By assuming that the dominant loss mechanism was background gas collisions, extrapolating the off-resonance measurement average $N_{0,\text{off}}$ back in time resulted in $N_0 = N_{0,\text{off}} e^{\Gamma(T_{int}+T_h)}$. This assumption is satisfactory because the PAS laser detuning here is about 100 linewidths away from resonance.

3.5.2 Determining the stimulated width γ_s

The area under a PAS spectral line, which is related to molecular and experimental parameters, is determined by integrating K_{eff} by frequency:

$$A_\nu = \int d\nu K_{\text{eff}} = \frac{1}{h Q_T} \int dE_g e^{-E_g/k_B T} \frac{\gamma_s(E_g)\gamma_1}{\gamma_s(E_g) + \gamma_1}, \quad (3.25)$$

where we disregarded the truncation of the energy integral since it is a small correction. The Wigner threshold law implies that $\gamma_s = BI_1\sqrt{E_g}$ [102, 103], which gives A_ν as (for low light intensities such that $\gamma_s \ll \gamma_1$)

$$\begin{aligned} A_\nu &= \frac{1}{h Q_T} \int dE_g e^{-E_g/k_B T} \gamma_s(E_g) \\ &= \frac{1}{h Q_T} \int dE_g e^{-E_g/k_B T} B I_1 \sqrt{E_g} \\ &= \frac{(k_B T)^{3/2}}{h Q_T} B I_1 \frac{\sqrt{\pi}}{2}. \end{aligned} \quad (3.26)$$

The function Q_T depends on the temperature as $T^{3/2}$, making A_ν temperature independent. Our approach for determining the stimulated linewidth $\gamma_s = BI\sqrt{E_g}$ is to fit the one-photon spectra with a spectral lineshape, determine the spectral area A_ν and find a linear fit to the data to extract B (since $A_\nu \propto I_1$).

Experimentally, we took PA spectrum for different PAS beam intensities and interaction times in two different ODT traps (6 W and 13 W). The two different trap depths give us two different temperatures: 7 μK for the 6 W trap, and 13 μK for the 13 W trap. This allowed us to test the validity of the temperature independence of A_ν .

We fit each spectra with a gaussian profile $S_\nu = G_\nu e^{-\frac{(\nu-\nu_0)^2}{2\sigma_\nu^2}}$, from which we extract the spectral width and amplitude. We used a gaussian profile because the intrinsic

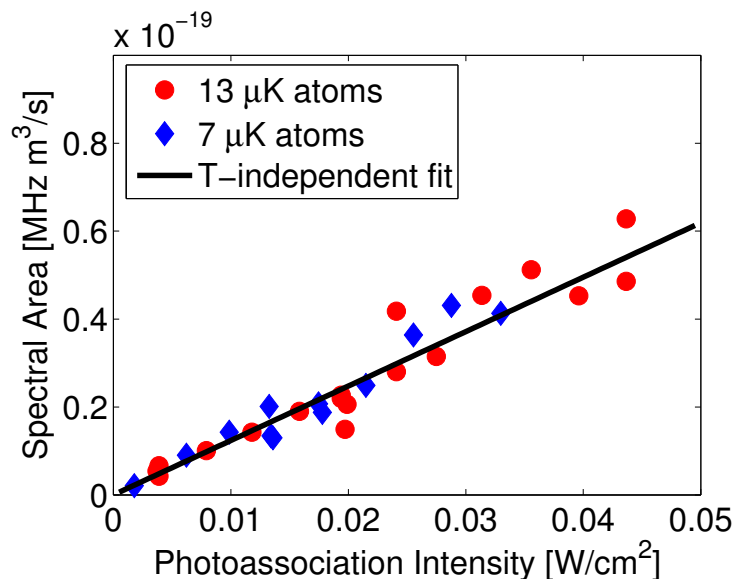


Figure 3.7 : One-photon PA spectral area. Spectral area under one-photon PA spectra versus free-bound laser intensity I_1 . The area can be related to molecular and experimental parameters to determine the stimulated linewidth $\gamma_s(E_g)$ of the PAS transition due to I_1 . For low I_1 the area is independent of temperature and linearly dependent on I_1 . Adapted from [63].

small linewidth of the unperturbed free-bound transition $\gamma_{atomic}/2\pi = 7.5$ kHz is much narrower than the observed linewidth ~ 1 MHz. Due to broadening effects because of ODT stark shifts and thermal broadening of the transition, a pure Lorentzian lineshape would not be satisfactory. The correct fit for the spectra, however, would be a gaussian summed over the collision energy [102].

Determining the spectral area from the fit amounts to multiplying the width and amplitude extracted from the fit:

$$\begin{aligned}
 A_{exper} &= \int_0^\infty d\nu G_\nu e^{-\frac{(\nu-\nu_0)^2}{2\sigma_\nu^2}} \\
 &= G_\nu \sigma_\nu \sqrt{2\pi}.
 \end{aligned} \tag{3.27}$$

Figure 3.7 shows the experimental spectral area A_{exper} versus laser intensity I_1 . A_ν depends linearly on I_1 (Eq. 3.26) and a straight-line fit to the measured spectral area gives the value for $B = 1 \times 10^{14}$. Since A_ν is temperature independent, we expect that the fit be general for either sample temperature, which it is.

We can express the stimulated linewidth γ_s as a saturated intensity for the free-bound transition. The saturation intensity is defined when the (thermally averaged) $\langle \gamma_s \rangle = \gamma_1$, where we determine $\langle \gamma_s \rangle$ from Eq. 3.26:

$$\begin{aligned} \langle \gamma_s \rangle &= \frac{1}{k_B T} \int dE_g e^{-E_g/k_B T} \gamma_s(E_g) \\ &= \frac{1}{k_B T} \int dE_g e^{-E_g/k_B T} B I_1 \sqrt{E_g} \\ &= \frac{B I_1}{2} \sqrt{\pi k_B T}. \end{aligned} \quad (3.28)$$

Equating $\langle \gamma_s \rangle = \gamma_1$ gives

$$I_{sat,PAS} = \frac{2\gamma_1}{B\sqrt{\pi k_B T}} = \frac{4\gamma_{atomic}}{B\sqrt{\pi k_B T}}. \quad (3.29)$$

For $T = 13 \mu\text{K}$, this gives $I_{sat,PAS} = 8 \text{ W/cm}^2$. In terms of an optical length $l_{opt} = \frac{\gamma_s}{2k_r\gamma_1}$, where $k_r = \sqrt{2\mu E_g}/\hbar$ [44] for this transition, we get $l_{opt} = 28 a_0$ for $I_1=1 \text{ W/cm}^2$. The optical length parametrizes the effect I_1 has on manipulating the collisional properties of the atom via this transition. To briefly put this transition's optical length magnitude into perspective, the free-bound transition to the least-bound level in the excited molecular 1S_0 - 3P_1 potential (bounded by only -400 kHz) has a theoretical $l_{opt} = 8.9 \times 10^5 a_0$ for $I_1=1 \text{ W/cm}^2$ [44, 98].

3.5.3 Determining the relative ac Stark shift χ

Having correctly accounted for linewidth broadening effects due to the PAS laser, we can now model the PAS spectra according to Eqs. 3.20 and 3.21 and vary χ to fit the data. PAS spectra at different trap depths demonstrate the ac Stark shift, as seen in Fig. 3.5. This data was taken at 6 and 13 W ODT beam powers and nearly the same PAS laser intensity of 20 mW/cm². The observed free-bound resonance transition frequency clearly experiences the largest shift with the strongest ODT beam power.

To determine the Stark shift we modeled one-photon spectra by numerically solving K_{eff} with the detuning $\delta_1 = f + \chi \times 2I_{ODT}$, where χ is equal to the frequency shift per beam intensity due to the ODT. We account for the Stark shift due to both ODT beams by including the factor of two in the detuning, as shown above. To model the spectra it is important to account for any saturation effects due to the PAS laser, which was determined through γ_s as described in Section 3.5.2. All other parameters are experimental (e.g., the PA laser's intensity, the sample's temperature, the ODT trap beam powers, etc.) and are readily accounted for.

Figure 3.5 also shows our fits, obtained through numerical integration of K_{eff} . We find $\chi = 160 \pm 30$ kHz/(100 kW/cm²), in good agreement with published measurements of the different state's polarizabilities from Reference [90]. Our measurement of the unperturbed resonance frequency for the free-bound transition is -222.25 MHz (shown in Fig. 3.5 as a dashed line), which is in reasonable agreement to that of Reference [98].

Having traced down the important perturbations in determining the free-bound transition resonance frequency, we are ready to use the second PAS laser to locate the bound levels in the ground molecular potential. This is the goal of Chapter 4.

Chapter 4

Measuring the binding energy of the least-bound state b_2

Chapter 3 presented the theoretical treatment of two-photon spectroscopy and the experimental results of the one-photon limit. From these measurements we accounted correctly for broadening effects and line shifting of the free-bound resonance frequency due to the PA laser and the ODT.

Here we incorporate a second PAS laser to measure the binding energy of the least-bound level b_2 in the ground molecular potential. To accomplish this, we tune the first PAS laser to the free-bound transition resonance frequency (see Chapter 3) and scan f_2 such that it becomes on resonance with the bound-bound transition between b_1 and b_2 , as shown in Fig. 3.1. The difference between their frequencies equals the frequency position of the least-bound state. Having quantified the important perturbations to the free-bound transition, we can accurately determine the binding energy of b_2 .

4.1 Quantum optical effect due to two laser beams

Adding a second PAS laser introduces intriguing quantum optical effects due to the coupling of b_1 and b_2 it induces. The Λ system that forms between the three states

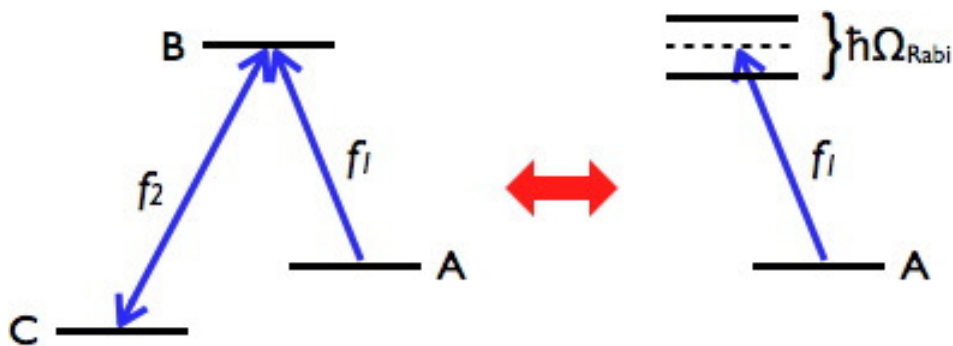


Figure 4.1 : Dressed atom picture of coupled atom states by bound-bound laser. Laser 2 couples states B and C when nearly on resonance with the B - C transition. The coupling creates a pair of states that are separated by the generalized Rabi frequency $\Omega_{Rabi} \propto |\langle B|C\rangle|\sqrt{I_2}$. Laser 1, originally on resonance with the A - B transition, no longer promotes PA loss because the energy level splitting produced by the coupling shifts the energy levels. We use the Autler-Townes doublet splitting to determine the Franck-Condon factor $|\langle B|C\rangle|$.

due to the two lasers produces either PA loss suppression or Autler-Townes splitting of the PA loss, depending on which laser is scanned [100].

Figure 4.1 shows* what occurs when a laser field at frequency f_2 is on resonance with the transition between two states B and C . In the dressed-state picture of the atom, the coupling creates a pair of states that are separated by the generalized Rabi frequency

$$\Omega_{Rabi} \propto |\langle B|C\rangle|\sqrt{I_2} \quad (4.1)$$

of this transition. If laser 2 was off, the weaker laser at f_1 would be on resonance with the A - B PA transition. With laser 2 on, laser 1 finds itself off resonance with any transition at the same frequency where it previously was on resonance with the

*This schematic depicts the real atomic states g , b_1 and b_2 as in Fig. 3.1.

PA transition.

We witness this phenomenon in two different ways. With laser 2 on resonance with the B - C transition, we scan f_1 across the PA resonance. The outcome is that PA loss does occur, but not until f_1 becomes on resonance with one or the other of the two dressed states. These are the well known Autler-Townes doublets. Their frequency splitting can be related to the strength of the bound-bound Franck-Condon factor $|\langle B|C\rangle|^2$ which will be necessary when modeling K_{eff} with Eqs. 3.13 and 3.20.

In the second scenario, we keep laser 1 on resonance with the A - B PA transition and expect PA loss with f_2 off resonance from the B - C transition. As we scan f_2 and it approaches the resonance frequency for the B - C transition, once again, the coupling between B and C due to laser 2 becomes important, so that when f_2 is on resonance with the B - C transition, laser 1 is off resonance with the dressed states. The PA loss originally present when f_2 was off resonance with the B - C transition is suppressed, until f_2 becomes off resonance again. Quantum interference of the multiple possible paths to state B cause these two situations when the system is in two-photon resonance. We use both types of spectra to determine molecular parameters such as the bound-bound Franck-Condon factor and the binding energy of the least bound state in the ground molecular potential.

4.2 Experimental details

Here, we prepare and use samples like those described in Chapter 3 to continue PAS experiments with the two PAS lasers. Both lasers need to be nearly on resonance to their respective transition frequency. Coupling the two lasers into an optical fiber facilitates both beam's overlap on the atoms. A beam shutter on laser 2 along with a fast rf switch on the AOM producing laser 1 controlled their on/off times independently, as mentioned in Chapter 3.

We needed to search for the correct laser frequency f_2 that brought the second laser on resonance with the bound-bound transition. To guide our frequency search our collaborators, Dr. Robin Côté and Dr. Phillip Pellegrini, supplied us with theoretical predictions for f_{b_2} based on a range of possible scattering length values. Previous PAS measurements [104, 62, 105] narrowed the possible magnitude of a_{88} close to zero. Their theoretical input significantly narrowed our experimental search.

To measure the binding energy of b_2 , our experiment proceeded as follows. After loading atoms in the ODT, we held the trap at a fixed trap beam power for a brief equilibration time (235 ms) before we turned on the two PAS lasers for a 100 ms interaction time. The free-bound laser intensity of 50 mW/cm² gave ~50% atom loss when on resonance. We then scanned f_2 and looked for the PA loss suppression expected when f_2 is on resonance with the bound-bound transition, as discussed in Section 4.1. Our initial choice of large bound-bound laser intensity made it easy to find peculiar behavior of the PA loss spectrum. We found a promising signal near

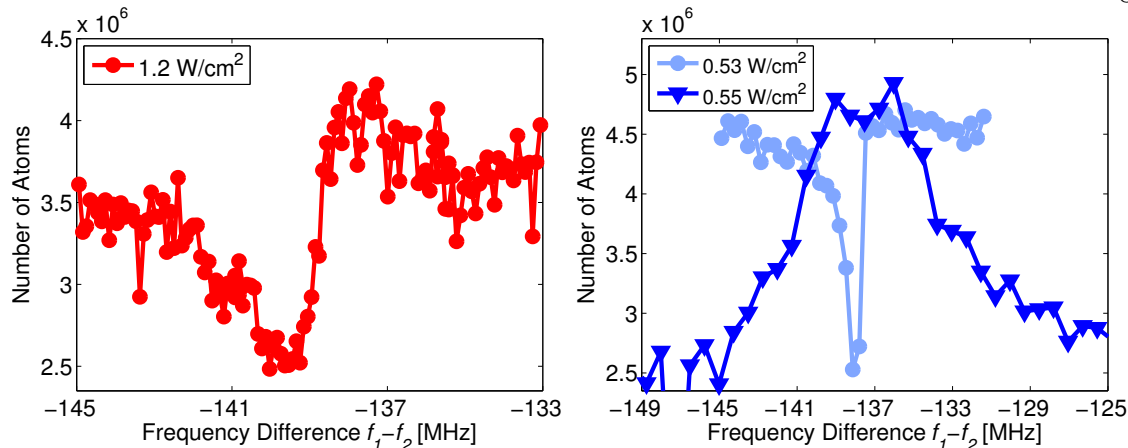


Figure 4.2 : Initial two-photon PAS scans. Left: This was the first signal observed when the two-photon PAS scans began. Its asymmetry is due to an incorrect frequency chosen for the free-bound laser ($\delta_1 \approx -500$ kHz). Right: Two-photon spectra of equal laser powers for both PAS lasers. The blue-triangle trace has laser 1 nearly resonant ($\delta_1 \approx 0$ kHz) to the free-bound transition, while the light blue-circle trace has $\delta_1 \approx -500$ kHz.

$f_1 - f_2 = -140$ MHz as we scanned f_2 , shown in Fig. 4.2(a)).

Our initial observations had distorted spectral shapes because the frequency of laser 1 was not chosen correctly (Fig. 4.2(a)). After slightly adjusting f_1 to optimize our choice of the free-bound resonance frequency and scanning f_2 with our optimal f_1 frequency, we obtained suppression spectra like that shown in Fig. 4.3. The different spectra are for different I_2 but equal I_1 . As expected, the suppression region gets narrower with lower I_2 due to the decreasing coupling strength of laser 2, and the reduction in the coupled states' frequency splitting (see Section 4.1).

We saw complete PA loss suppression in our experiment, as can be seen in Fig. 4.2 for the -137 MHz signal. This strongly suggests that decay from state b_1 is the dominant decay channel. If the decay rate for the final state b_2 were comparable to that

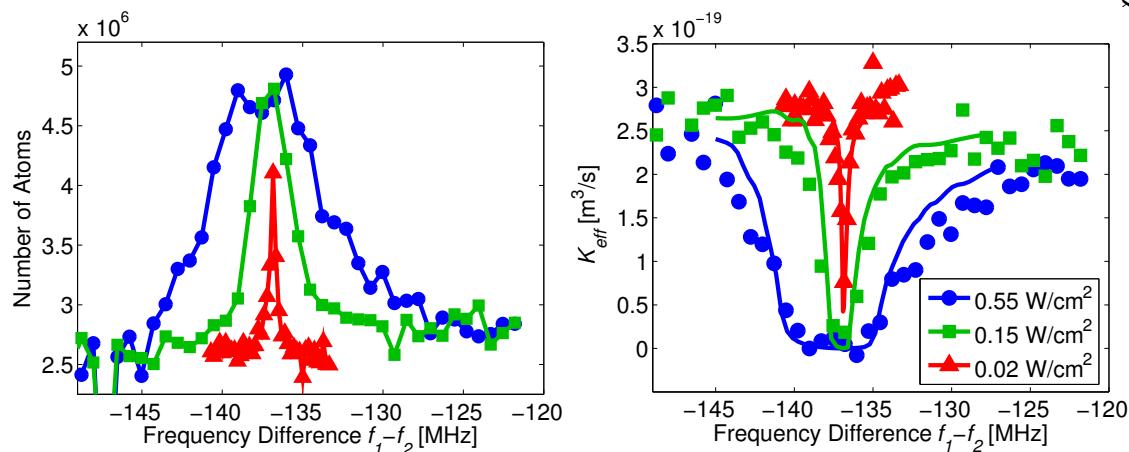


Figure 4.3 : Number of atoms (left) and collision-event rate constant K_{eff} (right) versus frequency difference between laser 1 and laser 2 for spectroscopy of the $J = 0$, $v = 62$ level of the $X^1\Sigma_g^+$ potential. The free-bound laser frequency is fixed close to the one-photon PAS resonance and the intensity is $I_1 = 0.05 \text{ W/cm}^2$. The bound-bound laser frequency is scanned, and its intensity is indicated in the legend. On two-photon resonance, PAS loss is suppressed due to quantum interference. The left plot connects the measurements by lines to guide the eye. The solid lines in the right plot are fits using Eqs. 3.20 and 3.13, which yield $E_{b2}/h = -136.7(2) \text{ MHz}$. The atom temperature is $8 \mu\text{K}$. Adapted from [63].

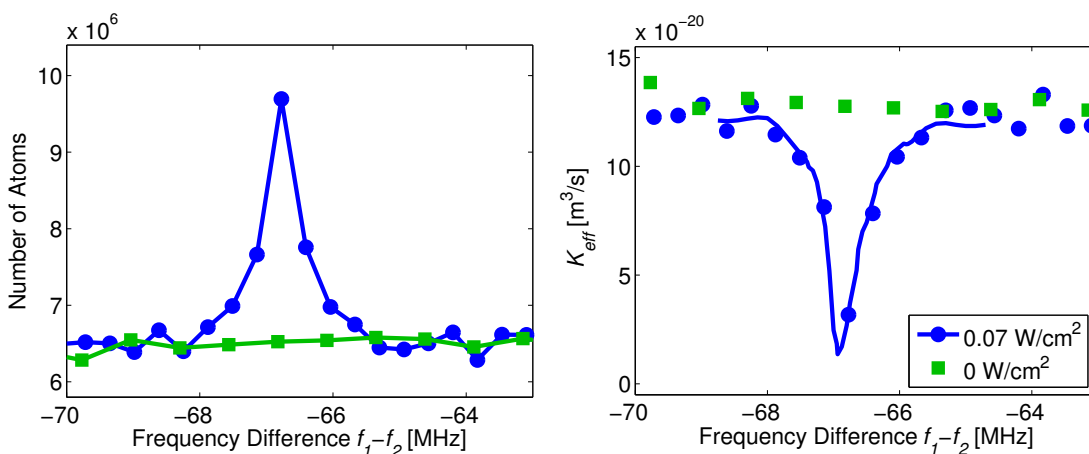


Figure 4.4 : PAS suppression spectra for the $J = 2$, $v = 62$ ro-vibrational bound level of the ground molecular potential, as described in Fig. 4.3. The sample temperature is $9 \mu\text{K}$. The free-bound laser intensity is $I_1 = 0.04 \text{ W/cm}^2$, and the bound-bound intensity is indicated in the legend. Left: Number of atoms measured, with measurements connected by lines to guide the eye. Right: Corresponding collision-event rate constants K_{eff} . The solid line is a fit using Eqs. 3.20 and 3.13, which yields $E_{b2}/h = -66.6(2) \text{ MHz}$. Adapted from [63].

of b_1 , then the PA suppression would only be partial, and the scattering probability $|S_{1g}|^2$ would only have a minimum, as opposed to having a zero in amplitude [100].

Once we knew the frequency necessary to bring f_2 on resonance to the bound-bound transition, we can study the Autler-Townes spectra described in Section 4.1. We kept f_2 on resonance to the bound-bound transition and scanned f_1 to obtain spectra shown in Fig. 4.5. The presence of laser f_2 couples b_1 and b_2 to form two “dressed” states separated by the coupling strength

$$\Omega_{12} = \alpha |\langle b_1 | b_2 \rangle| \gamma_1 \sqrt{\frac{I_2}{4I_{sat,atom}}}, \quad (4.2)$$

where $I_{sat,atom} \equiv \pi \hbar c \gamma_{atomic} / (3\lambda^3) = 3 \mu\text{W}/\text{cm}^2$, and $\alpha = \sqrt{2/3}$ [61] is the rotational line strength factor that accounts for the change in dipole moment from single atoms to molecule. The spectra offsets in Fig. 4.5 are proportional to $\sqrt{I_2}$, and the linear relationship between their spacing shows that the splitting presents the correct dependence on I_2 .

From the Autler-Townes spectra we can extract the bound-bound Franck-Condon factor $F = |\langle b_1 | b_2 \rangle|^2$, which is the overlap between the ground and excited states’ wave functions. This overlap integral governs the strength of transitions between the two states, and has important consequences for producing molecules in the bound levels of molecular potentials with PAS [106, 107]. Modeling the Autler-Townes spectra with Eqs. 3.20 and 3.13 and manually changing the value of \sqrt{F} in Eq. 4.2 allowed us to determine the frequency separation of the doublets. The splitting turns out to be $\Omega_{12}/2\pi = 1 \text{ MHz}$ for an intensity of $I_2 = 0.35 \text{ W}/\text{cm}^2$, which gives $F = 0.28$ for

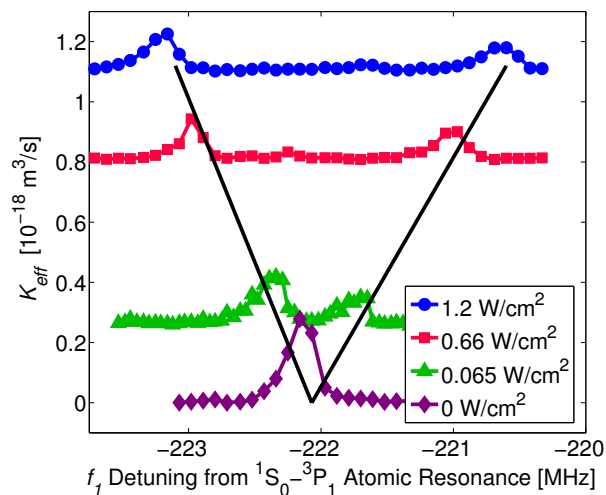


Figure 4.5 : Autler-Townes doublet spectra. Collision-event rate constant K_{eff} versus free-bound laser detuning from 1S_0 - 3P_1 atomic resonance for different bound-bound laser intensities I_2 (indicated in the legend). These Autler-Townes doublets are measured with laser 2 frequency f_2 fixed such that $\delta_2 \approx 0$ while scanning f_1 . The spectra offset is proportional to $\sqrt{I_2}$ as shown by the lines. The splitting of the spectra is given by the Rabi frequency $\Omega_{12}/2\pi$ and varies as $\sqrt{I_2}$. The asymmetry in the lineshapes arises from f_2 being slightly off resonance from the bound-bound transition. Laser 1 intensity I_1 is constant for all four spectra at 0.05 W/cm^2 . The sample temperature is $8 \mu\text{K}$.

the bound-bound Franck-Condon factor from the 3P_1 to 1S_0 molecular potentials.

With a knowledge of F and all other significant frequency shifts discussed in Chapter 3, we model the two-photon spectra according to Eqs. 3.20 and 3.13 to determine the bound energy of b_2 . When the system is in two-photon resonance, $f_1 - f_2 = (E_{b_2} - E_g)/h$ and one can extract E_{b_2} . The measured binding energy for this ro-vibrational level ($J = 0$, $v = 62$ state) is $E_{b_2}/h = -136.7 \text{ MHz}$ (Fig. 4.3). A similar transition was found for the $J = 2$, $v = 62$ state with a binding energy $E_{b_2}/h = -66.6 \text{ MHz}$, as shown in Fig. 4.4.

4.2.1 Determining K_{eff}

One important complication that needs to be addressed when deriving K_{eff} from our measurements is the turn-on/turn-off time of the beam shutter on laser 2 (Chapter 3.4). This shutter lagged by about 15 ms in either its turn-on or turn-off from when the shutter received a trigger[†]. We accounted for the shutter lag times when determining the atom number evolution as explained in this section.

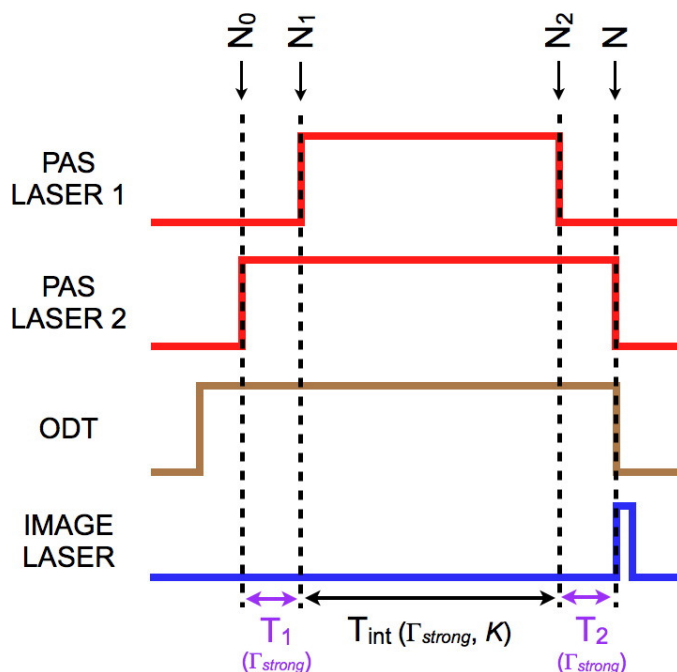


Figure 4.6 : Timing diagram for two-photon PAS scans. The traces are offset for clarity and the heights indicate turn on/off. We determine the initial number of atoms N_0 at the beginning of the atom-laser interaction time as described in Section 4.2.1. Only laser 2 was on during time T_1 , causing one-body atom loss (together with background gas collisions) with a rate of Γ_{strong} . During T_{int} , both PAS lasers interact with the atoms, and promote one- and two-body losses (with loss rate Γ_{strong} and rate constant $K_{\text{eff}}(f)$). By time T_2 , only laser 2 interacts with the atoms again.

[†]We constructed these shutters from computer hard drives. Their operation was not optimized for the shortest off-time possible.

The timing for the two-photon and Autler-Townes spectra is diagrammed in Fig. 4.6. The AOM that produced laser 1 had a very rapid turn on/off time ($\sim 3 \mu\text{s}$) and the limitation was the shutter on laser 2. We therefore gave it time to fully turn on and off before measuring the atom number[‡] (times signified by T_1 and T_2 in Fig. 4.6). T_{int} corresponds to the time when both lasers interacted with the atoms. We determine our atom number by accounting for any one-body losses present during any hold times in a similar fashion to Section 3.5.1. We determined N in the following way ($C = \frac{2K_{\text{eff}}V_2}{V_1^2}$):

$$N_1 = N_0 e^{-\Gamma_{strong} T_1} \quad (4.3)$$

$$N_2 = \frac{N_1 e^{-\Gamma_{strong} T_{int}}}{1 + \frac{N_1 C}{\Gamma_{strong}} (1 - e^{-\Gamma_{strong} T_{int}})} \quad (4.4)$$

$$\begin{aligned} N &= N_2 e^{-\Gamma_{strong} T_2} \\ &= \frac{N_0 e^{-\Gamma_{strong}(T_1+T_2+T_{int})}}{1 + \frac{N_0 e^{-\Gamma_{strong} T_1} C}{\Gamma_{strong}} (1 - e^{-\Gamma_{strong} T_{int}})}, \end{aligned} \quad (4.5)$$

with Γ_{strong} described by

$$\Gamma_{strong}(I) = \Gamma_{bg} + \Gamma_{max} \frac{P}{P_{max}}. \quad (4.6)$$

Γ_{strong} is an effective one-body loss rate that includes the background gas collision loss rate Γ_{bg} and the contribution due to laser 2 (the factor $\Gamma_{max} \frac{P_2}{P_{max}}$). Γ_{max} equals

[‡]In some scans $T_1 = 0$ due to how we fixed the timing of laser 1 to turn on directly when laser 2 was fully on.

the maximum loss rate of atoms[§] due to laser 2 when its power P_2 is equal to P_{max} , such that $\Gamma_{max} \frac{P}{P_{max}} \rightarrow \Gamma_{max} \frac{P_{max}}{P_{max}} = \Gamma_{max}$. By inverting Eq. 4.5 for K_{eff} , we get:

$$K_{eff} = \frac{V_1^2 \Gamma_{strong} e^{-\Gamma_{strong} T_2} (N e^{\Gamma_{strong}(T_1+T_2+T_{int})} - N_0)}{2V_2 N_0 N (1 - e^{\Gamma_{strong} T_{int}})}. \quad (4.7)$$

Determining N_0 is a different process for both types of spectra because of which lasers interact with the atoms. In resolving N_0 for the two-photon spectrum, we utilized a scan with the same timing as a two-photon scan but with only laser 2 on. These measurements allowed us to independently determine how much atom loss laser 2 produced. This allows us to determine N_0 from the relationship $N_0 = N' e^{\Gamma_{strong}(T_1+T_2+T_{int})}$, where N' is the atom number resulting from atom loss due solely to I_2 . Since laser 1 is off during this scan, the losses promoted by laser 2 and background gas collisions (total loss rate Γ_{strong}) are only one-body losses since it is very far-detuned from any transition resonance.

The situation is different for the Autler-Townes spectra. The first number measurements for each spectra are always with laser 2 on and laser 1 detuned from the PA and dressed-atom transitions by at least 1 MHz. This scenario is similar to that of one-photon PAS discussed in Section 3.5.1, where we expect losses due to laser 1 are negligible due to it being so far-detuned from a PA resonance. The dominant loss processes here are one-body losses due to background gas collisions and laser 2. We

[§]We obtained Γ_{max} by taking a lifetime measurement of a sample in the ODT with laser 2 on at maximum power (equal to 0.85 mW). From the fitted loss rate Γ_{total} we subtracted the known one-body loss rate Γ_{bg} to get $\Gamma_{max} = \Gamma_{total} - \Gamma_{bg}$.

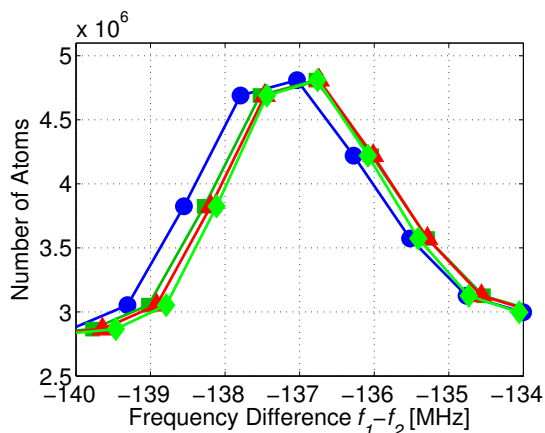


Figure 4.7 : VCO frequency calibration uncertainty. Number of atoms versus frequency difference between laser 1 and laser 2 for spectroscopy of the $J = 0, v = 62$ level of the $X^1\Sigma_g^+$ potential. Four different VCO frequency calibrations are used with the same data in this figure. The maximum spectral frequency difference is ~ 500 kHz between the spectra.

obtain N_0 by the relationship $N_0 = N' e^{\Gamma_{strong}(T_1+T_2+T_{int})}$, where N' now is the first number measurement of the actual Autler-Townes spectra.

4.2.2 Frequency uncertainties

Our largest experimental error comes from the frequency determination of our equipment. We utilized voltage-controlled oscillators (VCO) to produce rf voltage signals that controlled the AOMs detuning frequency when generating the two PAS laser frequencies. These devices accept an input control voltage V_{dac} that controls the frequency which the output rf signal will have. For most of the experimental scans we made sure to calibrate the VCO frequencies versus V_{dac} . In keeping track of the calibrations, we became aware of the VCO frequency drifts from day to day.

Figure 4.7 plots a two-photon signal recorded for the $J = 0, v = 2$ state with

a binding energy near -137 MHz. The same signal has been plotted using four different VCO V_{dac} -to-frequency calibrations. The uncertainty in which calibration is the correct one is the largest uncertainty for our experiment. We typically used the frequency calibration that corresponded to that particular experimental run, or made an educated guess as to which calibration to use by comparing the expected resonance positions to another measurement where we did know what the correct calibration was.

4.3 The scattering length a

After experimentally measuring E_{b2} , our theoretical collaborators were able to determine the scattering length a for the ground molecular potential. The binding energy of these high-lying states also help constrain the van der Waals coefficients C_n (see Section 3.2). Table 4.1 compares our measured binding energies with those calculated from theory.

To obtain values for a , the theoretical procedure includes calculating molecular potentials that reflect the measured bound level energies. Our collaborators made use of various available measurements, including our own described in this chapter, to determine the ground molecular potential and the scattering length. Published results of measurements of the inner part of the potential performed with Fourier-transform spectroscopy of Sr_2 [108] help restrict the shape of the calculation in that region. Information about the long range of the molecular potential came from previous

Isotopes	ν	J	Exper. [MHz]	Theory [MHz]	Diff. [MHz]
88	62	0	-136.7(2)	-136.7	0.0
88	62	2	-66.6(2)	-66.5	-0.1

Table 4.1 : Experimental and theoretical level energies for ground molecular potential. Energies given in frequency units (E_{b2}/h).

one-photon PAS measurements [62, 105] and our measurements here [63]. Further guidance in the form of the potential curve at long range came from precise relativistic calculations of the C_n coefficients. Putting these different components together allows our collaborators to model the ground molecular potential curve and assign to our measurements the correct ro-vibrational state labels.

Unfortunately, our binding energy measurements and those of PAS and Fourier-transform spectroscopy are insufficient to independently fit all the van der Waals coefficients and improve the currently calculated C_n coefficients. Nevertheless, by using the available information to obtain as best a model for the ground state as possible, we state the results of the theoretical analysis in Table 4.2. The scattering length a_{88} of ^{88}Sr turns out to be very close to zero, as previously determined with PAS experiments [62]. By mass scaling the potential energy curve obtained as described above, the analysis also derived the scattering lengths for all the stable-isotope collisional combinations, as shown in Table 4.2. Mass scaling the potential is possible because Sr is a heavy molecule, as was the case of rubidium (Rb), where successfully using mass scaling lead to precise determination of scattering lengths and Feshbach

resonances for ^{87}Rb [109].

The scattering lengths for the most abundant bosonic isotopes (^{88}Sr and ^{86}Sr) turn out to be non-ideal for thermalization purposes. Due to its small scattering length, ^{88}Sr will not thermalize fast enough given our ODT lifetimes (~ 25 s for the BEC experiment) without significant sample loss during evaporative cooling. We were finally successful at producing a ^{88}Sr BEC by sympathetically cooling it with the ^{87}Sr isotope [31, 75]. The ^{86}Sr isotope suffers from large three-body losses due to a scattering resonance produced by its very shallow least bound state in the ground molecular potential [91]. Previous evaporation experiments showed that the three-body losses limited the production of a BEC [65].

4.3.1 Collisional cross section vs. energy (^{88}Sr)

The small magnitude for a_{88} causes the elastic collision cross section to be energy-dependent, as shown in Fig. 4.8. The cross section is determined by the expression

$$\sigma = (8\pi/k^2) \sum_{l=0,2,\dots}^{\infty} (2l+1) \sin^2 \delta_l(k) \xrightarrow{k \rightarrow 0} 8\pi a^2 \quad (4.8)$$

for identical bosons. Figure 4.8 displays the resulting cross section (solid line) after including partial waves up to $l = 4$. Previous thermalization measurements [65] that measured the collisional cross section can be compared to our cross section calculation. The agreement between the measurements and our cross section is reasonable, as can be seen in Fig. 4.8.

The variation in the collisional cross section for ^{88}Sr complicates any thermaliza-

	2-phot. PAS [this study]	Fourier- transform [108]	1-phot. PAS [62]	1-phot. PAS [105]	Thermal- ization [65]
Isotopes	a	a	a	a	$ a $
88-88	-1.4(6)	0(5)	10^{+3}_{-11}	-40^{+40}_{-100}	21^{+3}_{-4}
87-87	96.2(1)	97(2)	-	-	-
86-86	823(24)	1050(380)	1000^{+1300}_{-400}	-	430^{+80}_{-90}
84-84	122.7(3)	124(3)	-	-	-
88-87	55.0(2)	56(2)	-	-	-
88-86	97.4(1)	99(2)	-	-	110^{+10}_{-20}
88-84	1790(130)	> 1170 or < -1900	-	-	-
87-86	162.5(5)	165.5(5.5)	-	-	-
87-84	-56(1)	-55(10)	-	-	-
86-84	31.9(3)	33(3)	-	-	-

Table 4.2 : Published values of scattering lengths given in units of $a_0 = 0.053$ nm

tion studies. To treat the variation in an approximate manner, we assume the system can be described with an effective, temperature-dependent cross section, which is an average of the collision-energy dependent cross section. This averaging is taken into account in an evaporation model we developed when modeling ^{88}Sr thermalization and evaporation behavior in our ODT [110]. Chapter 5 discusses evaporation in general.

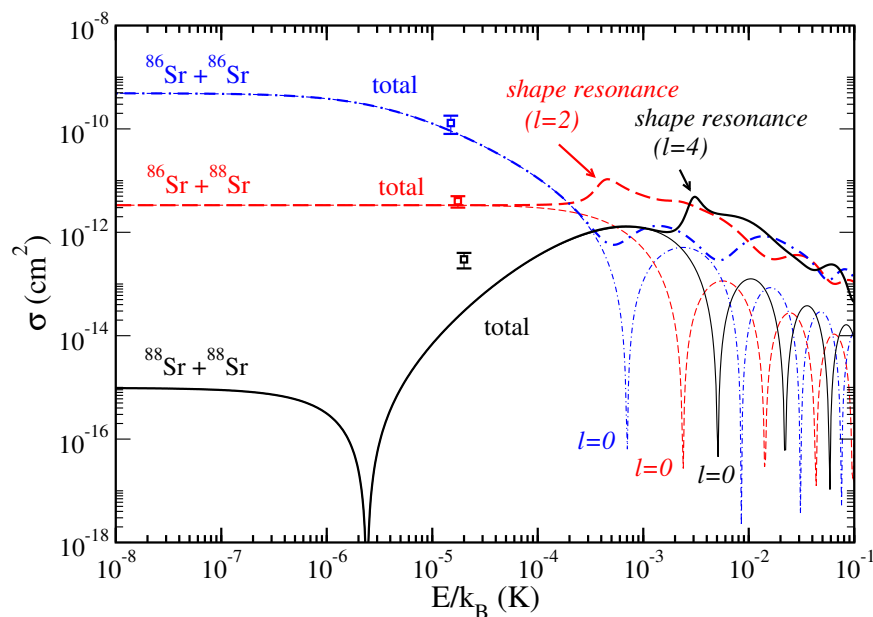


Figure 4.8 : Energy dependence of elastic collisional cross section for Sr . The cross section significantly varies with collision energy for ^{88}Sr , even at energies below $1\ \mu\text{K}$, due its very small scattering length a_{88} . The ^{86}Sr also experiences a varying cross section due to its very large a_{86} (see Table 4.2). The thick lines are cross sections including partial waves up to $l = 4$ by using Eq. 4.8. Shape resonances are indicated. Thin lines indicate cross section contributions from $l = 0$ only. The data symbols are cross section measurements from thermalization experiments [65], and the respective collision energies are set to $E = k_B T$, where T is the sample temperature.

Chapter 5

Evaporative Cooling Of ^{84}Sr

The experiments described in Chapter 4 allowed a precise determination of the elastic scattering properties of ^{88}Sr and the remaining isotopes through mass scaling. From Table 4.2, we determine that both ^{84}Sr and ^{87}Sr have favorable interatomic scattering lengths for efficient thermalization. Studies of fermionic ^{87}Sr thermalization (both unpolarized and polarized samples) can be found in Pascal Mickelson's Ph.D. dissertation [75].

Most of the characteristics of bosonic ^{84}Sr atoms are favorable for quantum degenerate gases except for one: it is the least naturally abundant Sr isotope. However, implementing the techniques described in Chapter 2 provided excellent initial conditions to achieve BEC with ^{84}Sr with forced evaporative cooling in an ODT. This chapter introduces a model for the evaporation process and discusses forced evaporation up to the onset of the BEC phase transition. It then presents the evaporation characteristics of ^{84}Sr up to the BEC transition.

5.1 The BEC phase transition for a nonuniform ideal gas

All experiments with dilute Bose gases to date rely on evaporative cooling in conservative traps to reach quantum degeneracy. At temperatures comparable to those

at the beginning of the evaporation process, the effects of the quantum statistics of particles is negligible. The sample temperature decreases and the PSD increases as the evaporation process ejects the most energetic atoms out of the trap. As the temperature lowers, the individual quantum mechanical wavepackets, with an extent on the order of the deBroglie wavelength $\lambda_{dB} = (2\pi\hbar^2/mk_B T)^{1/2}$, begin to increase in size. When λ_{dB} becomes on the order of the interparticle spacing $n^{-1/3}$ (n is the number density), the indistinguishability of particles becomes important and bosonic particles inherently begin to occupy the same quantum state [55]. We are therefore concerned with the process of producing a BEC from a thermal gas.

Our dilute gas of particles is confined in a trap, where it can be a magnetic or optical trap, as discussed in Chapter 1. These traps are well approximated by a harmonic shape near the bottom where the dense atom sample resides, so the potential is safely described with the quadratic form

$$V_{ext}(r) = \frac{m}{2}(\omega_x^2 x^2 + \omega_y^2 y^2 + \omega_z^2 z^2). \quad (5.1)$$

Here, ω_k are the oscillator frequencies in the three cartesian directions and m is the atom mass. Because of the gas' diluteness it is considered to be an "ideal" gas, where the atom-atom interactions are weak enough so as to be negligible. Although real experiments are done with interacting bosons, studying the non-interacting system is valuable because it allows an almost analytic derivation of relevant thermodynamic quantities and its solutions have guided experimentalist to actual properties belonging to weakly-interacting Bose gases. The ideal gas is studied in many standard textbooks

[55, 92] and their discussion is followed here to highlight important details of quantum degeneracy in harmonic traps necessary later in this document.

When interactions are negligible, the quantum-mechanical problem of determining the energy levels E_n of the whole gas is reduced to that of determining the energy levels ϵ_i of the single-particle Hamiltonian $H_i = \frac{p^2}{2m} + V_{ext}$. The gas' energies E_n are then determined by the sums of the energies of the individual particles. Furthermore, the many-body wavefunction $\Phi(r)$ can also be determined by the single-particle wavefunctions $\phi_i(r)$. The eigenvalues to the single-particle Hamiltonian H_i with V_{ext} defined in 5.1 turn out to be

$$\epsilon_{n_x n_y n_z} = (n_x + \frac{1}{2})\hbar\omega_x + (n_y + \frac{1}{2})\hbar\omega_y + (n_z + \frac{1}{2})\hbar\omega_z,$$

where n_k are non-negative integers numbering the eigenstate solutions to the Schrodinger equation ϕ_i . We will disregard the lowest state energy $\epsilon_{000} = \frac{1}{2}\hbar(\omega_x + \omega_y + \omega_z)$ for the remainder of the discussion in this section. This is a reasonable approximation because for energies large compared to $\hbar\omega_k$ (which is the situation for the gas above the BEC phase transition temperature), the energy states can be treated as continuous and the offset ϵ_{000} is insignificant. Therefore, the energy of the lowest state for the harmonic trap will be taken as $\epsilon_{000} = 0$.

As mentioned in Chapter 1, bosonic particles occupy energy states according to an average occupation number \bar{n}_i , described as

$$\bar{n}_i = \frac{1}{e^{(\epsilon_i - \mu)/k_B T} - 1},$$

and restricted by the condition that the total number of bosons equals the sum of all the average occupation numbers

$$N = \sum_i \bar{n}_i(\epsilon_i) = \sum_i \frac{1}{e^{(\epsilon_i - \mu)/k_B T} - 1}. \quad (5.2)$$

This relationship defines the chemical potential μ . An important consequence due to Eq. 5.2 is that the chemical potential is always less than the energy of the lowest energy state ϵ_{000} . If this were not the case the occupation number $\bar{n}_0 = \frac{1}{e^{(\epsilon_{000} - \mu)/k_B T} - 1}$ of the ground state would be negative and unphysical [55].

At temperatures T above the phase transition temperature the sum in Eq. 5.2 can be replaced by an integral as

$$N \approx \int_0^\infty d\epsilon g(\epsilon) \bar{n}(\epsilon). \quad (5.3)$$

The density of states $g(\epsilon)$ describes how the energy states are distributed in the system between energy ϵ and $\epsilon + d\epsilon$ and becomes, for a harmonic oscillator potential

$$g(\epsilon) = \frac{\epsilon^2}{2\hbar^3 \omega_x \omega_y \omega_z}.$$

Note that for the lowest energy state $\epsilon_{000} = 0$, $g(0) = 0$, implying that there is no atoms occupying the ground state. However, from Eq. 5.2 we find $N_0 \equiv \bar{n}_0 \neq 0$. Therefore, Eq. 5.3 accounts only for occupation in the excited states of the trap, and we introduce the term N_{BEC} to include the ground state occupation: $N = N_{BEC} + N_T$, where

$$N_T = \int_0^\infty \frac{d\epsilon g(\epsilon)}{e^{(\epsilon - \mu)/k_B T} - 1}. \quad (5.4)$$

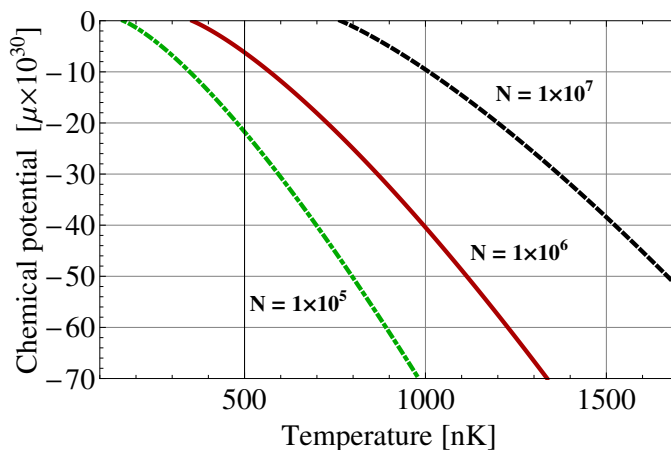


Figure 5.1 : Behavior of chemical potential. By numerically solving Eq. 5.4, one notices important trends about the behavior of μ . As the temperature of the sample decreases, μ increases. However, it is always less than the energy of the lowest energy state, which is zero here. Trap parameters chosen for numerical solution: $\omega_x = \omega_y = \omega_z = 2\pi \times 90$ Hz.

Figure 5.1 plots the behavior of μ as a function of temperature, which we obtained from the numerical solution to Eq. 5.4. Two important trends need to be pointed out. First, for a constant number of atoms in the gas, μ increases as the temperature of the sample decreases [55]. This is what occurs in our experiment as we evaporatively cool our sample. Another important aspect of μ is that the solution to N_T restricts its value to be below ϵ_{000} , which in this case is equal to zero (see Fig. 5.1). Therefore the chemical potential never exceeds the energy of the ground state, as we had rationalized earlier.

When μ takes on its maximum value (in this case it is zero) as the temperature decreases, the solution to Eq. 5.4 gives the maximum number that occupy the excited states for a given temperature. This maximum number can only be the total

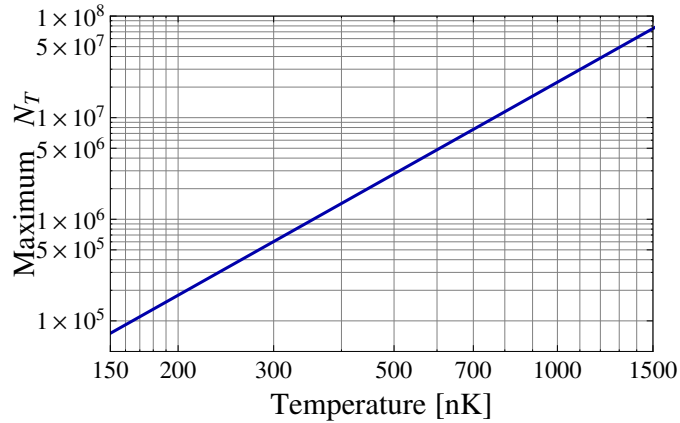


Figure 5.2 : Maximum number in thermal cloud at T_c . The plot is the solution to Eq. 5.4. Trap parameters chosen for numerical solution: $\omega_x = \omega_y = \omega_z = 2\pi \times 90$ Hz.

number of particles N in the sample. This condition, therefore, defines the critical temperature T_c for a given number of atoms N :

$$N = N_T(T_c) = \int_0^\infty \frac{d\epsilon g(\epsilon)}{e^{\epsilon/k_B T_c} - 1}. \quad (5.5)$$

Figure 5.2 plots the results for Eq. 5.5 for trap parameters common in our experiments.

Evaluating Eq. 5.5 gives us the expression for T_c :

$$k_B T_c = \hbar \omega_{ho} \left(\frac{N}{\zeta(3)} \right)^{1/3} = 0.94 \hbar \omega_{ho} N^{1/3}. \quad (5.6)$$

Here, $\omega_{ho} = (\omega_x \omega_y \omega_z)^{1/3}$ is the geometric mean harmonic oscillator frequency and $\zeta(n)$ is the Riemann function. For a fixed number of particles in the gas, if the temperature drops below T_c , no more atoms can be accommodated in the excited states, and a macroscopic number of atoms must enter the ground state to form a condensate.

The number of particles in the condensate is given by $N_0 = N - N_T$. This expression,

together with the solution to Eq. 5.5, gives the temperature dependence of the condensate fraction as

$$\frac{N_0}{N} = 1 - \left(\frac{T}{T_c}\right)^3.$$

It is interesting to notice that (for a harmonic potential) the atoms occupy many levels of the trap at T_c . From Eq. 5.6 we get

$$k_B T_c \sim \hbar \omega_{ho} N^{1/3} = \hbar \omega_{ho} \times 100.$$

for a suitable Bose gas of $N = 1 \times 10^6$ atoms undergoing the BEC phase transition. Near the phase transition's temperature, atoms are occupying many levels of the trap. Therefore, it is quantum statistics that causes the atoms to avalanche into the lowest-energy state of the trap.

5.2 Theory of forced evaporative cooling in an ODT

Dropping the temperature of a dilute Bose gas to reach quantum degeneracy was the main drive for developing evaporative cooling, as discussed in Chapter 1. Using this tool in the final stages of atom cooling is appealing because it does not involve density-limiting interactions with light. In this section, we briefly discuss and present a kinetic theory model to describe evaporative cooling. Many review articles discuss this topic at length (e.g., [52, 53]) and that will not be done here.

Evaporative cooling is a classical process whereby the most energetic atoms escape an atom sample and elastic collisions among the remaining atoms redistribute the remaining energy. Since the atoms removed had more than the sample's average

energy, the sample's new average energy is smaller than before. For a trapped gas, this process will slow down if the remaining atoms do not have sufficient energy to leave the trap depth. Therefore, by lowering the trap depth, one forces the evaporation to continue.

Several models have been proposed to describe the evaporative cooling process (e.g., [111, 112, 113, 114]). The one summarized in this section and utilized in developing the evaporation trajectory we used in producing our BEC [114, 115, 116] applies the Boltzmann transport equation [117] for a classical gas to model forced evaporation from an ODT. In this treatment, the gas is described by a distribution function $f(\vec{r}, \vec{p}, t)$ and allowed to evolve according to the Boltzmann transport equation. The distribution function f is defined such that

$$\begin{aligned} N(t) &= \int \frac{d^3r d^3p}{(2\pi\hbar)^3} f(\vec{r}, \vec{p}, t) \\ &\equiv \int d\epsilon g(\epsilon) f(\epsilon), \end{aligned}$$

$N(t)$ being the number of atoms in the trap at time t and $g(\epsilon)$ being the density of states. Assigning f to describe the gas is valid if sufficient thermalization, or “ergodicity”, exists in the system such that all energy states corresponding to the total energy of the atoms are sampled with equal probability.

An important assumption made in developing the evaporation model is that the gas is dilute enough such that only binary collisions occur. Furthermore, atoms with energy ϵ greater than the trap depth U_0 are assumed to leave the trap before interacting with another atom. Therefore, we can use a Boltzmann distribution truncated

at the trap depth for f :

$$f(\epsilon) = n_0 \Lambda^3 e^{-\epsilon/k_B T} \Theta(U_0 - \epsilon), \quad (5.7)$$

where n_0 is the particle density at the trap minimum, $\Lambda = \left(\frac{2\pi\hbar^2}{mk_B T}\right)^{1/2}$, and $\Theta(x)$ is the Heaviside step function ($n_0 \Lambda^3$ is the PSD). Comparing the numerical solution of the Boltzmann transport equation to the truncated Boltzmann distribution Eq. 5.7 demonstrates that the distribution function actually accurately describes the expected distribution of an evaporating gas for various types of trapping potentials [114, 116]. A comment worth stating is that both the ground state occupation number $n_0 \Lambda^3$ and the thermal energy $k_B T$ change with time. Due to the time dependence of the distribution function f , n_0 and T characterize a non-equilibrated system.

Using Eq. 5.7 as the sample's distribution function greatly simplifies the solution to the Boltzmann transport equation and permits explicit expressions for the evaporation rate and other dynamic properties of the gas (e.g., temperature). For evaporative cooling from a fixed trap depth (no forced evaporation), both the numerical solution to the Boltzmann transport equation and the analytical expression for the rate of change of T show that the temperature of the sample falls rapidly and eventually reaches a value of about $U_0/10$ with time [116] (assuming no excessive loss mechanisms exist). The rate at which free evaporation occurs eventually stagnates due to a combination of competing heating processes and fewer atoms having the required energy to escape the trap. This stagnation can be avoided when evaporation is "forced" to continue by lowering the threshold energy U_0 . The expression for total

number of atoms lost per unit time for a fixed trap depth

$$\dot{N}_{ev} \propto -n_0^2 \sigma e^{-\eta}$$

also demonstrates that the evaporation rate is exponentially suppressed by a factor $e^{-\eta}$. Here, $\eta = U_0/k_B T$, $\sigma = 8\pi a^2$ and a is the s -wave scattering length.

References [115] and [116] extend the kinetic theory model [114] to time-dependent traps that take the form of

$$U(r, t) = -U(t)g(r), \quad (5.8)$$

where $g(r)$ encapsulates the trap shape. This is the situation when evaporatively cooling in an ODT: energetic atoms escape over the potential barrier established by the intensity of the ODT laser. To continuously evaporate one lowers the trap depth by decreasing the trapping laser intensity. In the process, the trap strength decreases as the potential barrier decreases in the evaporation process [115]. When modeling the evaporation process, the effect of decreasing trap strength appears in time-varying energies of the trap eigenstates, which have significant consequences on the evaporation process. The treatment in References [115, 116] of a time-dependent gaussian potential to model a changing focused laser beam differs from the approach of considering a time-dependent truncation energy [118, 119]. Forced evaporation in a magnetic trap falls under the second description because the trap strength stays constant while rf radiation chooses the “height” of the potential barrier when promoting energetic atoms to unbound states. Using a time-dependent truncation depth when modeling evaporative cooling had a negligible effect on the process [115, 116, 119].

With this treatment References [115, 116] derive simple scaling laws for the atom number, PSD and elastic collision rate during the forced evaporation process with a potential like Eq. 5.8. This is the focus of Section 5.2.1. Since our ODT fits into this class of time-dependent traps, we choose to use these scaling laws to help us model our sample's evaporation during the ^{84}Sr BEC experiment.

5.2.1 Forced evaporation trajectory

This section presents the scaling laws for forced evaporation in a continuously lowered potential [115, 116] that we employed during our BEC experiment. The scaling laws follow from using the truncated Boltzmann distribution (Eq. 5.7) to solve the Boltzmann transport equation for the trap energy-loss and number-loss rates (\dot{E} and \dot{N} , respectively) of the evaporating gas. The derivation neglects background gas collisions and other heating processes and assumes that only evaporative losses contribute to the change in energy and number. For the derivation, the collision rate γ is assumed to be large enough to keep $\eta \approx 10$ such that the atoms reside near the bottom of the trap. This allows one to approximate the trap potential of a gaussian laser beam as a parabola near the bottom.

From the Boltzmann transport equation, one determines that the rate of energy loss from the trap becomes

$$\dot{E} = E_{ev} + \langle \dot{H} \rangle. \quad (5.9)$$

E_{ev} specifies the rate associated with the average energy carried away by evaporating

atoms, while $\langle \dot{H} \rangle$ describes the rate of change in potential energy. Using the Boltzmann distribution function Eq. 5.7, the average energy removed by an evaporating atom turns out to be between U and $U + k_B T$. By solving Eq. 5.9 under the assumption that the trap depth is determined by the relation $U = \eta = 10 k_B T$ to the temperature T , we get that the number of atoms varies with the trap depth as

$$\frac{N}{N_i} = \left(\frac{U}{U_i} \right)^{3/[2(\eta'-3)]}, \quad (5.10)$$

where $\eta' = \eta + (\eta - 5)/(\eta - 4)$. The subscript i in Eq. 5.10 denotes the initial condition at $t = 0$, $N = N(t)$, and $U = U(t)$.

The second scaling law comes from the definition of PSD for a harmonic trap $\rho = N \left(\frac{h\nu}{k_B T} \right)^3$, where the trap oscillator frequency $\nu \propto \sqrt{U}$. Rearranging Eq. 5.10 gives the scaling law for PSD as a function of either U or N

$$\frac{\rho}{\rho_i} = \left(\frac{U_i}{U} \right)^{3(\eta'-4)/[2(\eta'-3)]} = \left(\frac{N_i}{N} \right)^{(\eta'-4)}. \quad (5.11)$$

To find how the elastic collision rate $\gamma(t) \propto n_0 \sigma \bar{v}$ scales with the trap depth U , we use the relationship $n_0 \simeq \rho/\Lambda^3$ for the peak density and $\bar{v} = \sqrt{8k_B T/\pi m}$ for the average velocity. From Eq. 5.11, one gets the scaling law for γ

$$\frac{\gamma}{\gamma_i} = \left(\frac{U}{U_i} \right)^{\eta'/[2(\eta'-3)]}. \quad (5.12)$$

References [115, 116] show that the agreement between the three scaling laws (Eqs. (5.10), (5.11), and (5.12)) and the numerical solution of the Boltzmann transport equation is very good for the situation when $\eta = 10$. They also obtain the optical

trapping potential $U(t)$ from the rate of change of N from Eq. 5.10 and by combining it with Eq. 5.12, conclude

$$U(t) = U_i \left(1 + \frac{t}{\tau}\right)^{-\beta}, \quad (5.13)$$

where the time constant τ is

$$\frac{1}{\tau} = \frac{2}{3}\eta'(\eta - 4)\exp(-\eta)\gamma_i, \quad (5.14)$$

the initial elastic collision rate for a Bose gas in a harmonic potential is

$$\gamma_i = 4\pi N_i m \sigma \nu_i^3 / (k_B T_i), \quad (5.15)$$

and the parameter β is given by

$$\beta = \frac{2(\eta' - 3)}{\eta'}. \quad (5.16)$$

τ sets the timescale of how fast to lower the trap depth U : if the decrease occurs too fast (τ is small), the sample loses atoms without ample time to thermalize. If τ is too large then the evaporation competes with other heating processes in the system. We lower our trapping laser power using the form of Eq. 5.13 in our BEC experiment.

5.3 Evaporation characteristics of ^{84}Sr

In this section we analyze the evaporative attributes of ^{84}Sr , both in a fixed-height and time-varying trapping potential. A scattering length of $123 a_0$ provides this isotope with ideal thermalization characteristics, making it a suitable system to obtain BEC as will be seen.

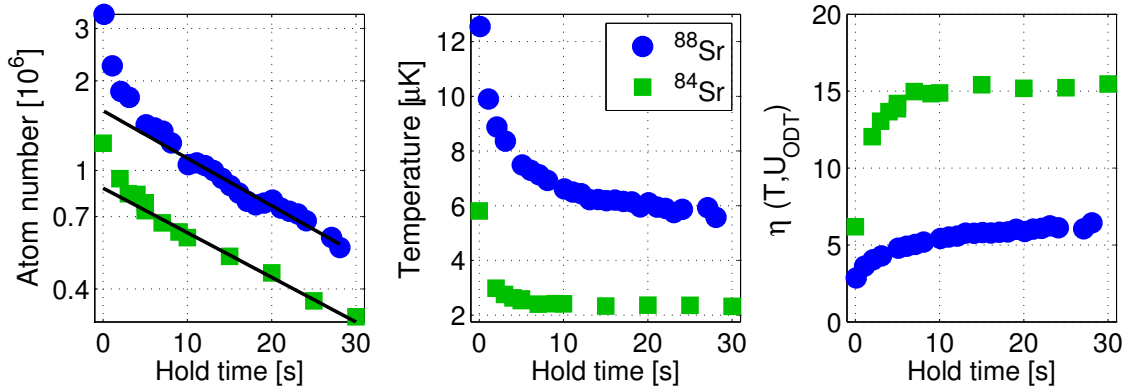


Figure 5.3 : Comparing thermalization behavior of ⁸⁴Sr and ⁸⁸Sr. The straight line through the data in the left-most panel is a one-body decay fit to extract the lifetime of the sample. The fit for both ⁸⁴Sr and ⁸⁸Sr scans is ~ 28 s. Due to a s -wave scattering length of $123 a_0$, the ⁸⁴Sr isotope thermalizes much faster than the ⁸⁸Sr isotope. Although the zero-energy $a_{88} = -2 a_0$, for the sample temperatures here, the energy dependent cross section for ⁸⁸Sr yields $a_{88} \approx 6 a_0$. The ODT trap depth is $35 \mu\text{K}$.

5.3.1 Free evaporation (thermalization)

It is instructive to see the effect of an ideal scattering length a when the thermalization rate of ⁸⁴Sr is compared to that of ⁸⁸Sr, whose $a = -2 a_0$. We prepare atom samples of either isotope type in the ODT as described in Chapter 2. Since we desire to examine the thermalization behavior of either isotope, we hold the atoms in a fixed depth ODT and allow free evaporation to occur. After a specific hold time, we turn off the trap to drop the atom sample and take absorption images after a 6-8 ms time of flight period for diagnostic purposes.

Figure 5.3 show typical thermalization data for both Sr isotopes in a $35 \mu\text{K}$ trap depth (9.5 W ODT beam power). Up to 1.2×10^6 ⁸⁴Sr atoms transfer into the ODT for this study compared to 3.4×10^6 ⁸⁸Sr atoms. The initial peak densities

for both samples are roughly equal ($n_{84} \sim 2 \times 10^{13} \text{ cm}^{-3}$ while $n_{88} \sim 3 \times 10^{13} \text{ cm}^{-3}$) for the previously mentioned atom numbers and initial temperatures of $T_{84} = 6 \mu\text{K}$ and $T_{88} = 12 \mu\text{K}$. The favorable transfer of ^{84}Sr atoms into the ODT despite its small abundance attests to the effectiveness of the number enhancement techniques discussed in Chapter 2.

A speedy reduction in the sample's temperature (seen in Fig. 5.3b) for ^{84}Sr atoms implies very fast thermalization times, which is in contrast to the ^{88}Sr sample. The ^{84}Sr sample reaches its equilibrium temperature of $\sim 2 \mu\text{K}$ after only about 5 seconds, compared to more than 30 seconds for ^{88}Sr . The corresponding initial average collision rates* from Eq. 5.15 are $\Gamma_{84} \sim 150 \text{ s}^{-1}$ and $\Gamma_{88} \sim 1 \text{ s}^{-1}$. Figure 5.3c displays the behavior of $\eta = U_{ODT}/k_B T$ which can be thought of as parametrizing how effective the thermalization process is. ^{84}Sr evaporation produced very cold samples such that $\eta \sim 15$, in sharp contrast to ^{88}Sr with $\eta \sim 6$.

We can use a numerical model [110] (based on the work of Ref. [114]) developed in the Killian lab to model collisional dynamics in our fixed-depth ODT. This model is particularly suited for the ^{88}Sr case, because thermalization is inefficient due to its small scattering length. Figure 5.4 shows our model results. By reproducing the sample evolution, the numerical model outputs a value for the expected scattering length of the sample. The model fit well to both lifetime curves, yielding a scattering

*The scattering length for ^{88}Sr utilized was $6 a_0$ due to the energy dependence of the cross section for this isotope. See Chapter 4 for a discussion of this behavior.

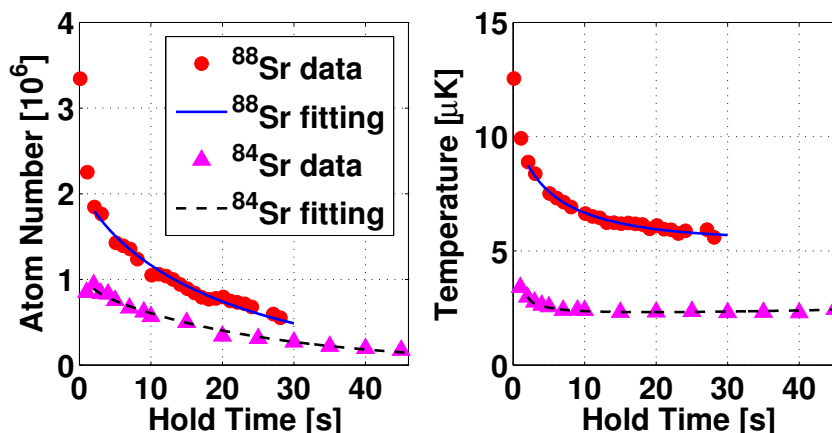


Figure 5.4 : Modeling thermalization data from Fig. 5.3 for ^{84}Sr and ^{88}Sr . The model fits well to both lifetime curves. The evaporation model [114] yields $a_{84} = 130 \pm 20 a_0$ for ^{84}Sr and $a_{88} = 5.4 \pm 1 a_0$ for ^{88}Sr .

length of $a_{84} = 130 \pm 20 a_0$ for a background gas collision loss rate of $\Gamma_{bg} = 0.04 \text{ s}^{-1}$, which is close to the measured value of $123 a_0$. Using the same Γ_{bg} in the case of ^{88}Sr , the model gave $a_{88} = 5.4 \pm 1 a_0$. This is a reasonable result considering the energy dependence of the elastic cross section for ^{88}Sr (see Chapter 4).

5.3.2 Forced evaporation

As discussed in Section 5.2.1, we utilize the evaporation trajectory described in Eq. 5.13 to ramp down the ODT beam powers to reach quantum degeneracy with ^{84}Sr [120]. Following the experimental procedure described in Chapter 2, we trap 3×10^6 atoms at $5 \mu\text{K}$ in the crossed-beam ODT by transferring atoms from the 689 nm MOT at low (2.5 W) ODT beam power and then ramping the power up to 10 W in 20 ms . With 3×10^6 atoms, this translates to a peak density of $6 \times 10^{13} \text{ cm}^{-3}$ in an ODT trap with a mean oscillation trap frequency of 167 Hz . The average collision

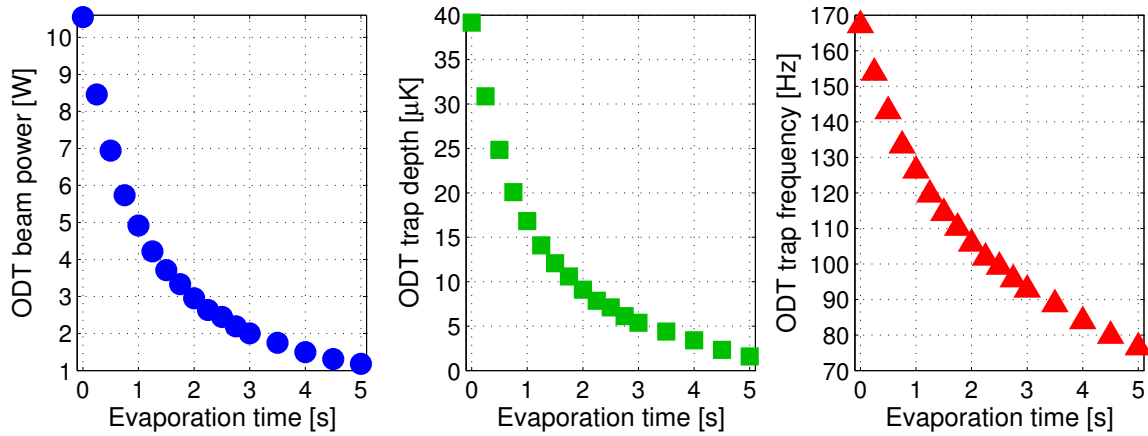


Figure 5.5 : Trap model calculations (Section 2.4.3) for ODT beam power, trap depth, and mean oscillator frequency during the forced evaporation trajectory.

rate[†] for these parameters is 1000 s^{-1} and the peak initial PSD is 10^{-2} .

With these as our initial conditions, we ramp down the power in the ODT beams according to Eq. 5.13, where t is the evaporation time. From Eqs. 5.14 and 5.16 we calculate $\tau = 1.33 \text{ s}$ and $\beta = 1.45$ from our initial conditions and assuming $\eta = 10$, which is a reasonable assumption for ^{84}Sr . We choose to use $\tau = \beta = 1.5$ during our forced evaporation process. Our ODT power calculated using our trap model varied as shown in Fig. 5.5. The figure also displays the ODT trap depth and mean oscillator frequency, since these two parameters also change with power as discussed in Chapter 2.

For each data point, we evaporated for a specific amount of time before turning off the ODT to measure the atom number after a delay time varying between 10 and 40 ms. Our experimental results are summarized in Fig. 5.6. With the evaporation

[†]The elastic collision rate was calculated using Eq. 56 from Reference [110].

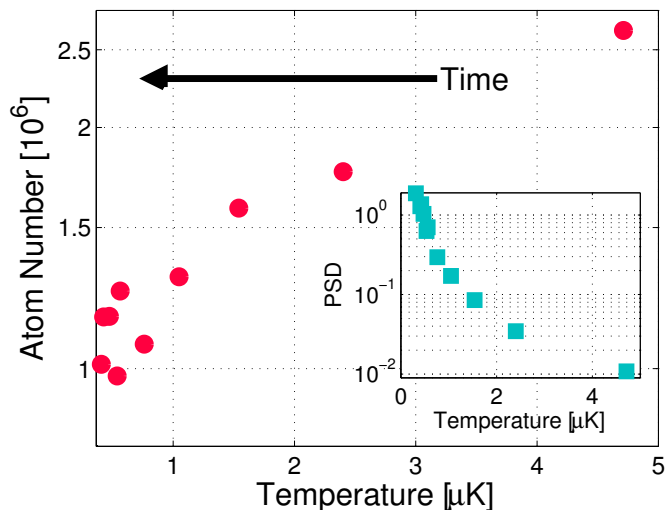


Figure 5.6 : N , T , and PSD along a typical evaporation trajectory for the ^{84}Sr BEC experiment. The measurements are taken from 200 ms after the completion of loading of the ODT and commencement of evaporation, until quantum degeneracy is reached 3 s later. The phase space density increases by a factor of 100 for a reduction of atom number by a factor of 3. Adapted from [30].

trajectory chosen, it took 3 s to reach a PSD on the order of 1, at the onset of quantum degeneracy. By losing a factor of 3 in the atom number for the duration of forced evaporation, the PSD increased by about a factor of 100. Our evaporation trajectory is very efficient due to our excellent initial PSD of 10^{-2} . These initial conditions are possible because of the available intercombination-line cooling in Sr.

We can use the scaling laws described in Section 5.2.1 to see if they describe our evaporation results. Using Eq. 5.10 to model the evolution of atom number with trap depth, we get the results shown in Fig. 5.7. The figure shows that the change of atom number aligns fairly well with the expected trajectory with trap depth. With the scaling laws, we can also model the number trajectory and adjust different variables

to get a sense for the sensitivity of the number to these experimental parameters. The largest changes to the expected number came by varying η by ± 1 . We conclude that η was about 6 for the evaporation trajectory.

A similar study is done with the peak PSD as a function of atom number, as shown in Fig. 5.8. We calculate the peak PSD for a classical gas in a harmonic potential as $\rho = N \left(\frac{h\nu}{k_B T} \right)^3$. This equation is valid for our system except very close to T_c when Bose-Einstein effects become important. Our analysis of the evolution of the PSD with Eq. 5.11 gives the same conclusion about the sensitivity to η , with a preferred $\eta = 7$. We checked the sensitivity of the model output to the initial mean oscillator frequency of the trap, which is an experimental variable that has a large uncertainty. By varying the frequency by 10% from the original trap frequency of ~ 210 Hz we found that the expected PSD evolution is fairly robust to a varying frequency. In these analyses, we determined our mean oscillator frequency by extrapolating a fixed frequency of 93 Hz to any desired frequency ν with the function $\nu = 93\sqrt{P/P_{93\text{Hz}}}$. This technique is valid since $\nu \propto \sqrt{U_{ODT}}$ and facilitated our scaling law comparisons.

We were able to model the trajectory of the elastics collision rate $\gamma = 4\pi N m \sigma \nu^3 / (k_B T)$ versus power fairly well using the scaling law from Eq. 5.12. A substantial response was evident as we varied the mean oscillator frequency for the model.

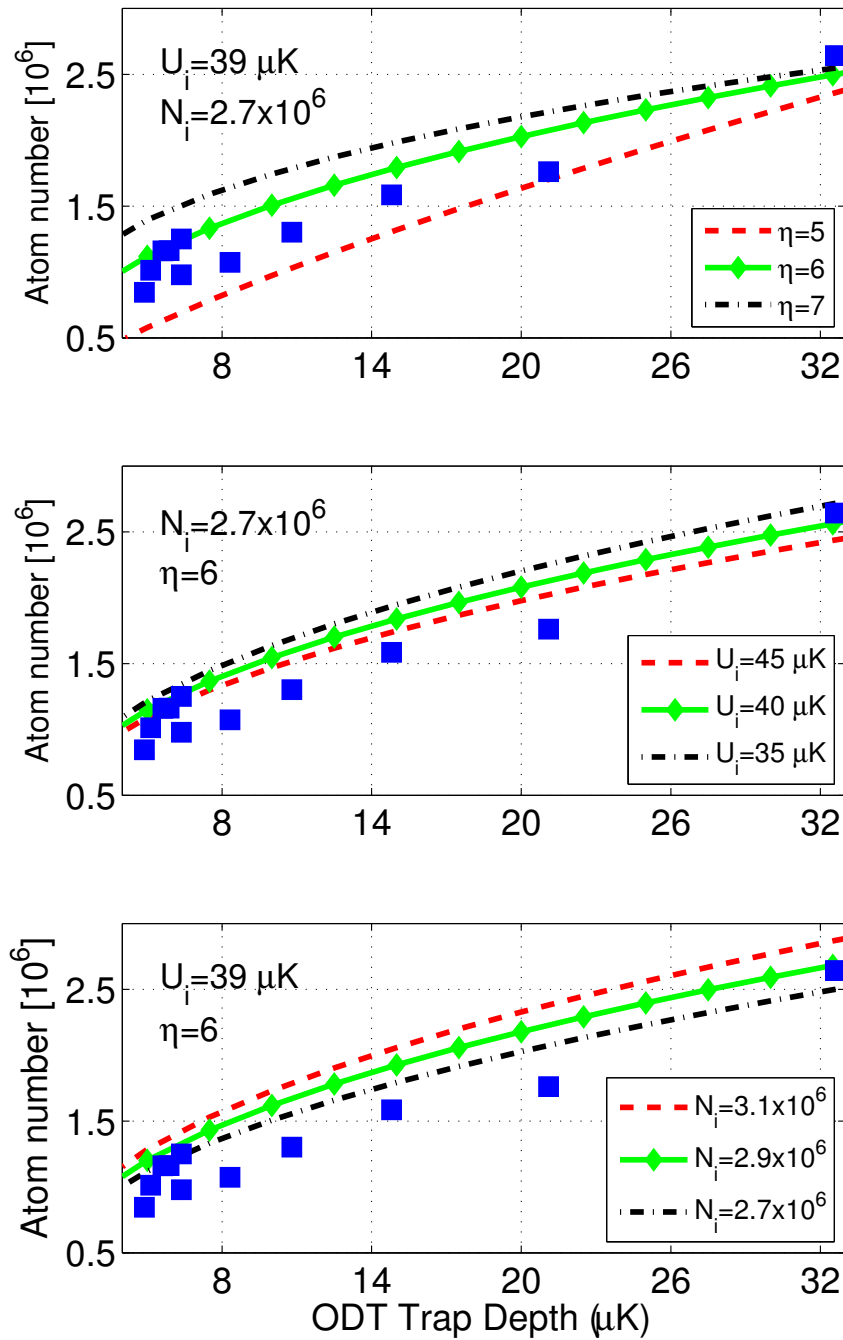


Figure 5.7 : Comparing scaling law for atom number as a function of ODT trap depth (Eq. 5.10) to experimental measurements along a typical BEC evaporation trajectory.

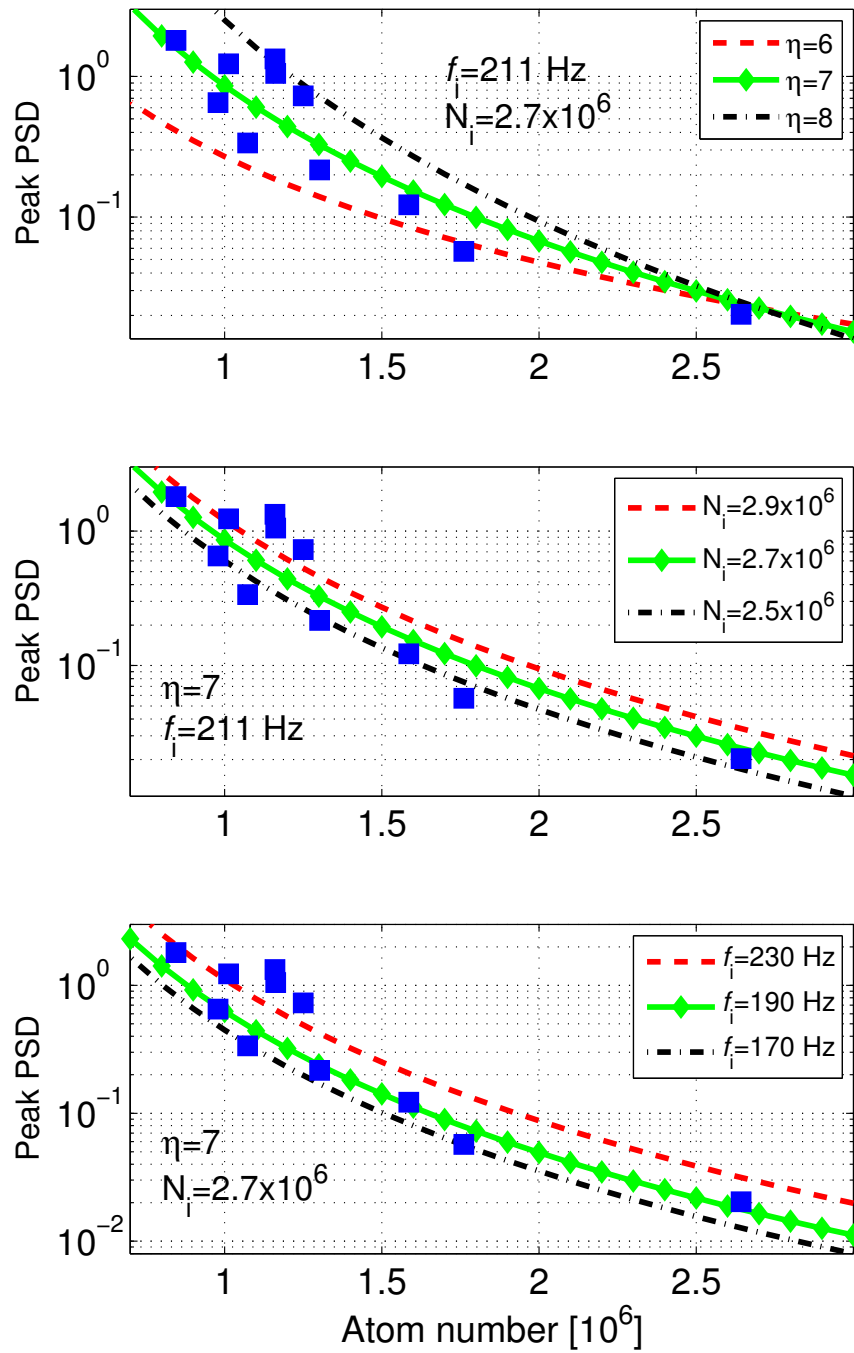


Figure 5.8 : Comparing scaling law for PSD as a function of atom number (Eq. 5.11) to experimental measurements along a typical BEC evaporation trajectory.

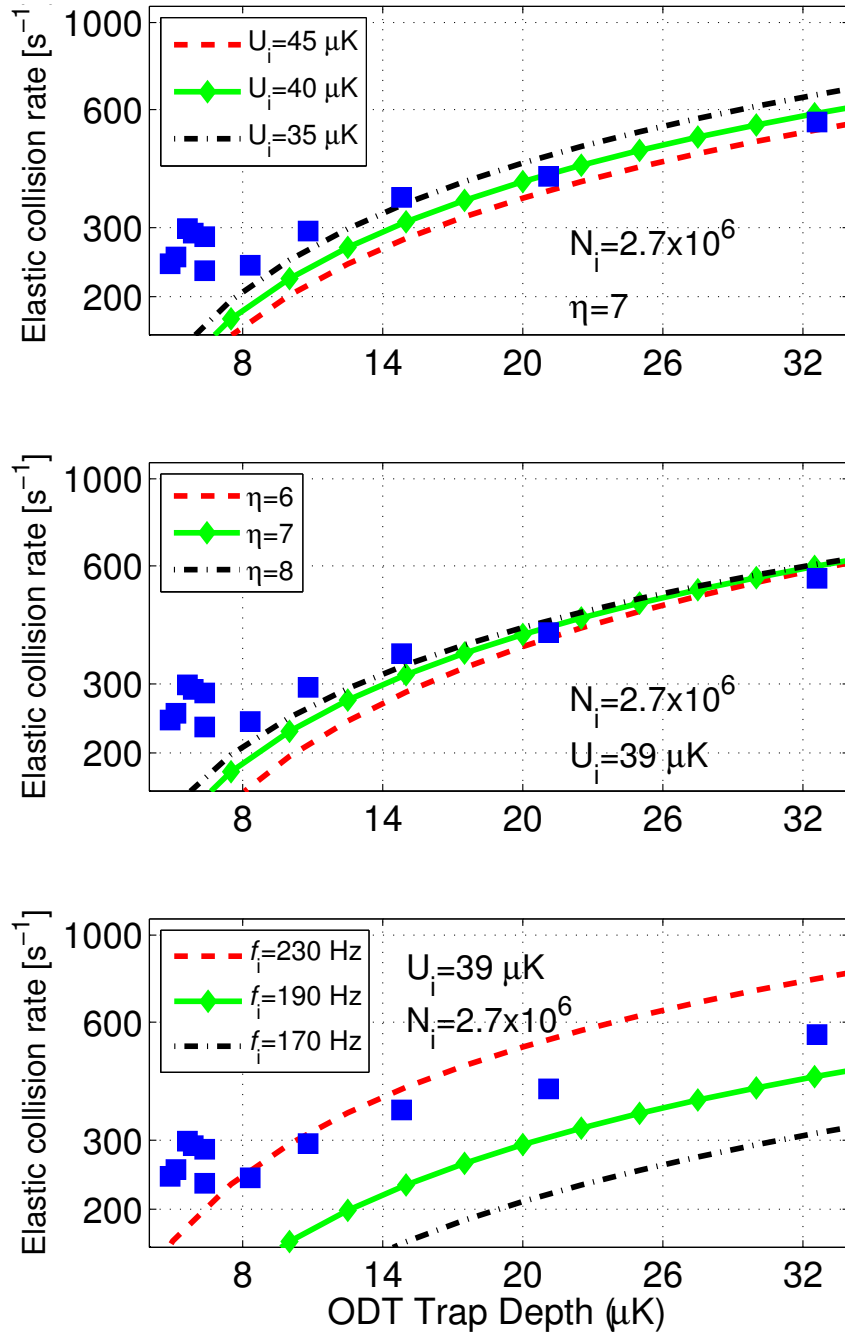


Figure 5.9 : Comparing scaling law for elastic collision rate γ as a function of ODT trap depth (Eq. 5.12) to measurements along a typical BEC evaporation trajectory.

Chapter 6

Determining T_c

In the present chapter, we continue the evaporative cooling process of the samples described in Chapter 5 to increase the sample's PSD further. At the critical temperature T_c , the PSD = 2.6 [121] and the atoms begin to condense to the lowest energy state of the trap. Both non-condensed and condensed atoms coexist in this temperature regime, until further evaporative cooling yields a condensate with negligible thermal population. It is therefore important to develop reliable models to determine the cloud's density distribution and their physical properties such as number and temperature for the coexisting phases.

This chapter describes our procedure for determining T_c and the functional form necessary to analyze the thermal portion of the cloud to determine its characteristics correctly. Our first approximate approach neglects the effects of quantum statistics by using standard Boltzmann statistics in our fitting routine. Then we present the correct investigation using a "Bose-enhanced" fit function and compare it to the classical results.

6.1 Analyzing the thermal component

In this section we will develop the tools to describe the atoms in the system that are not in the condensate. In a semiclassical approximation [122, 123, 121], bosonic particles obey the distribution function

$$f_0(\vec{r}, \vec{p}) = \frac{1}{e^{[\epsilon(\vec{r}, \vec{p}) - \mu]/k_B T} - 1}, \quad (6.1)$$

with

$$\epsilon(\vec{r}, \vec{p}) = \frac{p^2}{2m} + V_{ext}(\vec{r}) \quad (6.2)$$

being the energy of a classical free particle at point \vec{r} , and $V_{ext}(\vec{r})$ the external harmonic trapping potential. Here we have neglected quantization of the particle energy levels, which is valid since the thermal energy of the atoms $k_B T$ is larger than the level spacing $\hbar\omega$.

As described in [55, 124], to find the density $n_{th}(\vec{r})$ of the thermal component in the trap, we integrate* the number distribution over the particle momenta \vec{p} :

$$\begin{aligned} n_{th}(\vec{r}) &= \frac{1}{(2\pi\hbar)^3} \int d\vec{p} f_0(\vec{r}, \vec{p}) \\ &= \frac{1}{(2\pi\hbar)^3} \int 4\pi p^2 dp f_0(\vec{r}, \vec{p}) \\ &= \frac{g_{3/2}(z(\vec{r}))}{\lambda_{dB}^3} \end{aligned} \quad (6.3)$$

*The function $g_\gamma(r) = \sum_{n=1}^{\infty} \frac{r^n}{n^\gamma}$ is a solution to integrals of the form

$$\int_0^{\infty} dx \frac{x^{\gamma-1}}{r^{-1}e^x - 1} = \Gamma(\gamma) g_\gamma(r),$$

where $\Gamma(\gamma)$ is the Euler gamma function. For the case of Eq. 6.3, $\gamma = \frac{3}{2}$ and $\Gamma(\frac{3}{2}) = \sqrt{\pi}/2 = 0.886$.

with the thermal de Broglie wavelength $\lambda_{dB} = \sqrt{2\pi\hbar^2/mk_B T}$ and

$$z(\vec{r}) = e^{[\mu - V_{ext}(\vec{r})]/k_B T}. \quad (6.4)$$

The function $z(\vec{r})$ reduces to the fugacity $\zeta = \exp(\mu/k_B T)$ when the trap's ground state energy is taken to be zero, a valid limit if $k_B T \gg \hbar\omega$.

However, we actually drop the cloud and take absorption images after a time-of-flight period for quantitative analysis of the sample. Using the same semiclassical approach, we determine the atom's density distribution after the time-of-flight period. The distribution function 6.1 and the energy 6.2 describes the distribution of the gas before turning off the trap. After turning the trap off, the atoms move from their initial positions \vec{r}_0 in the trap before the drop time to a point \vec{r} according to their velocity. At long times ($t \gg \omega_y^{-1}, \omega_x^{-1}, \omega_z^{-1}$) the resulting distribution is [55]

$$n_{th,tof}(\vec{r}, t) = \frac{1}{\omega_x \omega_y \omega_z t^3 \lambda_{dB}^3} g_{3/2} \left(e^{(\mu - \frac{mr^2}{2t^2})/k_B T} \right) \quad (6.5)$$

$$= n_{0,tof} g_{3/2} \left(\zeta e^{(-\frac{mr^2}{2t^2})/k_B T} \right) \quad (6.6)$$

where ζ is the fugacity and $r^2 = x^2 + y^2 + z^2$.

In reality, absorption imaging measures the density profile of the cloud along the imaging axis (column density). The correct function to fit the 2D images then becomes

$$\begin{aligned} OD(x, y) &= \sigma_{abs} \int_{-\infty}^{\infty} dz n_{th,tof}(\vec{r}, t) \\ &= \sigma_{abs} \int_{-\infty}^{\infty} dz n_{0,tof} g_{3/2} \left(\zeta \exp \left[-\frac{x^2}{2\sigma_x^2} - \frac{y^2}{2\sigma_y^2} - \frac{z^2}{2\sigma_z^2} \right] \right) \\ &= \sqrt{2\pi} \sigma_{abs} \sigma_z n_{0,tof} g_2 \left(\zeta \exp \left[-\frac{x^2}{2\sigma_x^2} - \frac{y^2}{2\sigma_y^2} \right] \right), \end{aligned} \quad (6.7)$$

where $OD(x, y)$ is the optical depth (OD) and σ_{abs} is the absorption cross section. Determining the peak OD of the image helps one relate σ_z and $n_{0,tof}$ to observed cloud parameters [55],

$$OD(0, 0) = \sqrt{2\pi} \sigma_{abs} \sigma_z n_{0,tof} g_2(\zeta) \quad (6.8)$$

such that 6.7 becomes

$$OD(x, y) = OD(0, 0) \frac{g_2 \left(\zeta \exp \left[-\frac{x^2}{2\sigma_x^2} - \frac{y^2}{2\sigma_y^2} \right] \right)}{g_2(\zeta)}. \quad (6.9)$$

To get a count of the atom number one utilizes the density's normalization condition with number:

$$\begin{aligned} N_{total} &= \int_{-\infty}^{\infty} d^3\vec{r} n_{0,tof} g_{3/2} \left(\zeta \exp \left[-\frac{x^2}{2\sigma_x^2} - \frac{y^2}{2\sigma_y^2} - \frac{z^2}{2\sigma_z^2} \right] \right) \\ &= n_{0,tof} (2\pi)^{3/2} \sigma_x \sigma_y \sigma_z \sum_{k=1}^{\infty} \frac{\zeta^k}{k^3} \\ &= n_{0,tof} (2\pi)^{3/2} \sigma_x \sigma_y \sigma_z g_3(\zeta) \\ &= \frac{2\pi OD(0, 0) \sigma_x \sigma_y g_3(\zeta)}{\sigma_{abs} g_2(\zeta)}. \end{aligned} \quad (6.10)$$

For small ζ , which corresponds to a gas far from quantum degeneracy, we can approximate the sum $g_2 \left(\zeta \exp \left[-\frac{x^2}{2\sigma_x^2} - \frac{y^2}{2\sigma_y^2} \right] \right)$ from Eq. 6.9 by its first term. This yields a 2D Gaussian function that corresponds to a classical Maxwell-Boltzmann gas:

$$OD(x, y) = OD'(0, 0) \exp \left[-\frac{x^2}{2\sigma_x^2} - \frac{y^2}{2\sigma_y^2} \right], \quad (6.11)$$

where $OD'(0, 0)$ contains information on ζ . Our first analysis procedure used this form of fitting function to determine the critical temperature of the BEC phase transition.

Its results give a good approximation, and the functional form is much easier to work with. But quantum statistics as included in Eq. 6.9 give more accurate results.

6.2 Experiment with Gaussian fitting (classical)

We continue the experiment described in Chapter 5, where forced evaporation cooled the Bose cloud until the PDS was on the order of 1. This results in a high density sample in the center of the trapped gas due to atoms with low thermal energy. Time-of-flight images confirm that as the evaporation time increased the cloud temperature decreases. Our next task was quantifying the sample’s characteristics such as atom number and temperature, and we chose a classical Maxwell-Boltzmann approach for our first pass of analysis, as discussed in Section 6.1.

Anticipating the presence of a condensed fraction in our sample, we excluded the central portion of the time-of-flight 2D images of the cloud in our analysis. This was accomplished by determining the position of the central portion of the cloud and assigning the data points in this region a large error (1×10^6) such that the fitting procedure would disregard that section of the cloud and only fit the external parts (“wings”) of the data. Our approach works because our fitting procedure fits weighted data (weighted by a calculated error[†]) with the function of our choice (in

[†]To calculate the error of our signal we first determine the root-mean-square deviation of the signal of a 5-pixel by 5-pixel square from the 4 corners of the region of interest (ROI) being analyzed without the background and then average these 4 noise levels. The error becomes the averaged noise level normalized by the amount of pixels in the ROI.

this case it is a 2D Gaussian). We always manually determined the position of the central portion of the cloud in both directions of the image's 2D coordinate system (which we will specify as \mathbf{x} and \mathbf{y}) and kept the exclusion region square. The ROI for the data analysis was also always kept square. Finally, the length of the exclusion region was chosen manually and was around 30 to 40 pixels long.

With this procedure of excluding the central region of the cloud, we were successful at fitting the thermal population of atoms with a 2D Gaussian fitting function of the form

$$OD(x, y) = BG + m_x(x - x_0) + m_y(y - y_0) + A \exp \left[-\frac{(x - x_0)^2}{2\sigma_x^2} - \frac{(y - y_0)^2}{2\sigma_y^2} \right] \quad (6.12)$$

to obtain information about the cloud's size (σ_x and σ_y), peak OD (A), and coordinate position (x_0 and y_0). The parameters BG , m_x , and m_y characterize the background signal, which we subtract from the original measurements for our further analysis. In Fig. 6.1 we plot 1D "slices" of the data obtained by either fixing the x or y position of the data through the center. We also plot the corresponding Gaussian fit of the data, fixing one dimension in the same fashion as the data and plotting it against the other dimension. These figures show the exclusion region chosen to ensure that the Gaussian fit function would only fit the wings of the data. In Fig. 6.2 we also plot the 2D false color rendering of the corresponding time-of-flight images.

At times before 3 s of evaporation time, the time-of-flight images are fit well by the Boltzmann distribution (2D Gaussian). The first indication of a bimodal distribution is seen at 3 s of evaporation (Fig. 6.1) where a narrow peak at the center of the

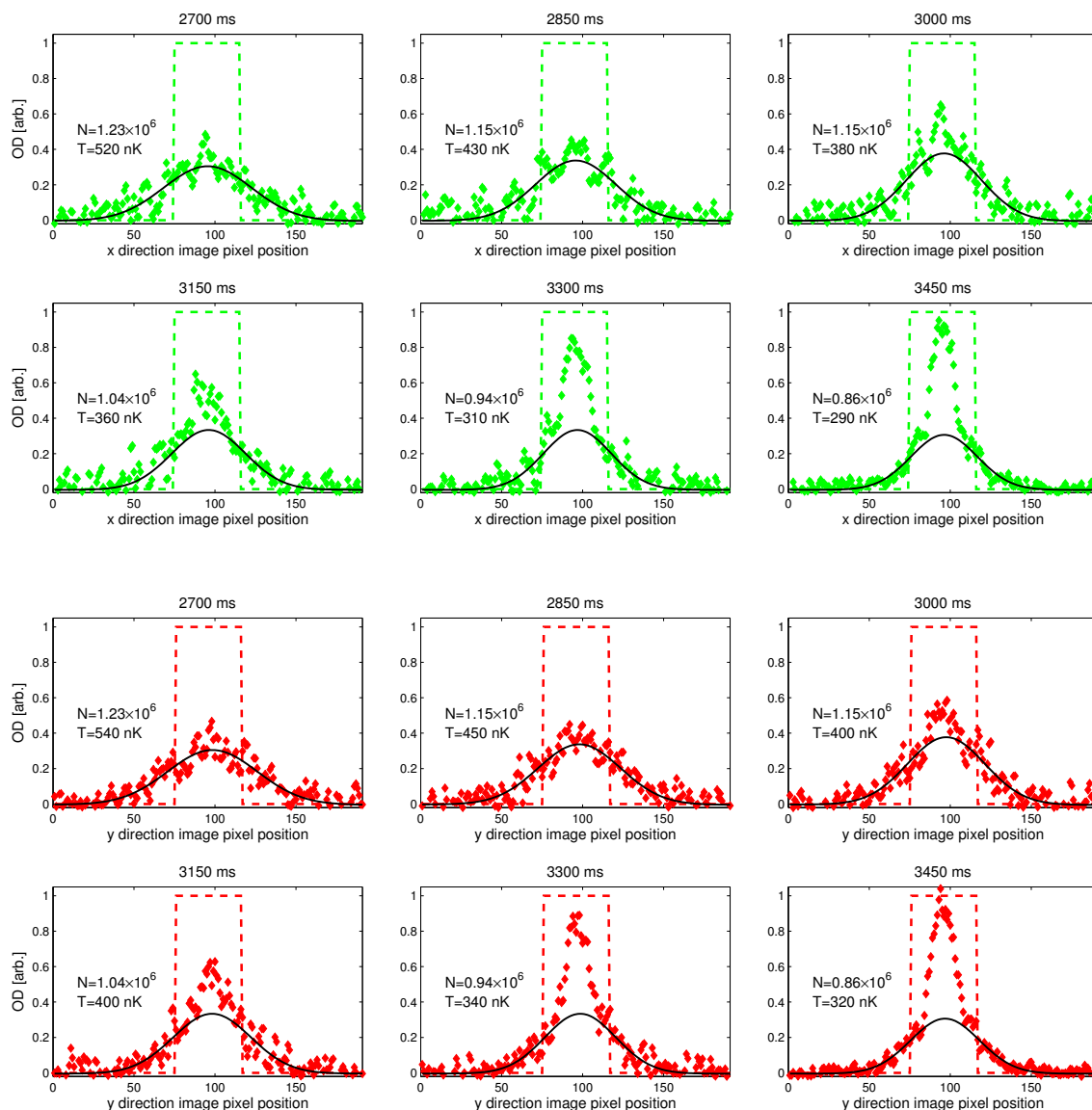


Figure 6.1 : Column density profiles of 2D absorption images fitted with a gaussian function (6.11). Data corresponds to 35 ms of free expansion after indicated evaporation times (above data panel). The top(bottom) panel in green(red) corresponds to an x(y) vertical cut through the center of the atom cloud. Temperatures are extracted from 2D gaussian fits to the thermal component. At 3.0 s, the beginning of a bimodal distribution indicates the presence of a BEC, which becomes increasingly clear with longer evaporation time.

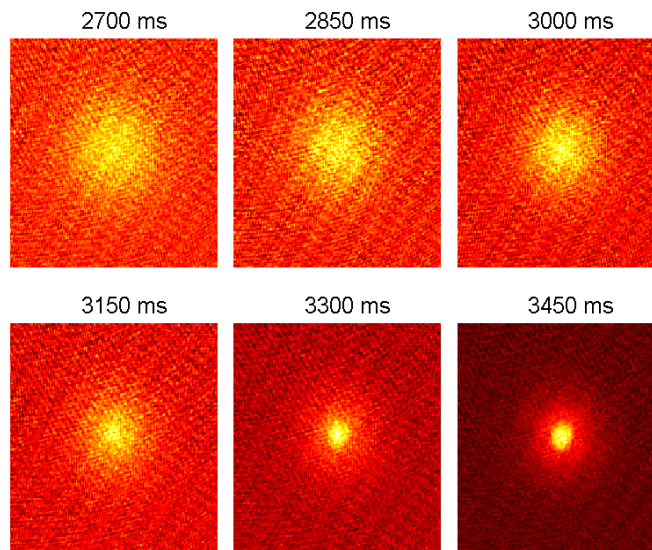


Figure 6.2 : False color rendering of time-of-flight images corresponding to those in Fig. 6.1.

image indicates the initial formation of a BEC. Since the images are taken after a time-of-flight period, the spatial distribution of the atoms from the center of the cloud indicates the magnitude of their initial velocity at the beginning of the drop time. Those atoms with the greatest kinetic energy (thermal energy) when the trap turns off will be farthest away spatially from the center of the cloud after a given drop time τ due to their large initial velocity. Atoms condensed to the ground state of the system have smaller initial kinetic energy at the beginning of the time-of-flight period and very low initial velocity. After the same time τ they travel much less away from the center of the cloud and form a narrow peak near the center of the image. After 3 s of evaporation, the bimodal structure becomes increasingly clear.

Subtracting the 2D Gaussian fit from the data also indicates that the onset of

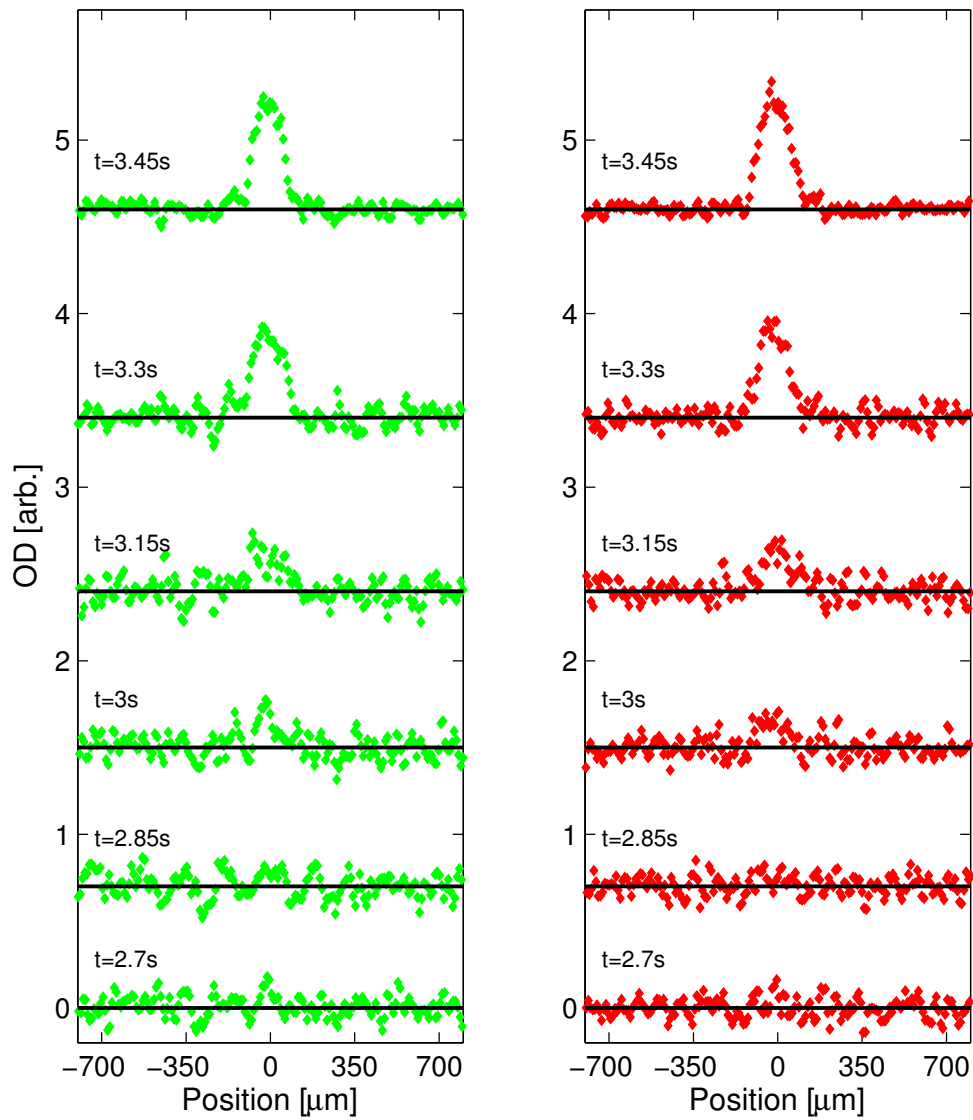


Figure 6.3 : Remaining atom distribution after subtracting 2D gaussian fit from data in Fig. 6.1. At 3.0 s and later, the nucleation near zero indicates a BEC.

the phase transition occurs at 3 s of evaporation time, as shown in Fig. 6.3. The remaining distribution after taking the difference between the 2D fit and the data is approximately equal to the BEC population. To accurately determine the BEC population, it is necessary to use the correct functional form (6.9) to fit the thermal portion of the cloud. We discuss how to analyze the BEC portion of the cloud in Chapter 7.

Using the 2D gaussian function for data analysis, we determine that the BEC transition, where atoms begin to occupy the ground state of the trap, occurred at a critical temperature of $T_c \approx 400$ nK after 3 seconds of evaporation and with 1.2×10^6 atoms. This transition temperature and number of atoms in the cloud indicate that the optical trap has a characteristic trap frequency

$$f_{ho} = \frac{\omega_{ho}}{2\pi} = \frac{k_B T_c}{0.94 h N^{1/3}} \quad (6.13)$$

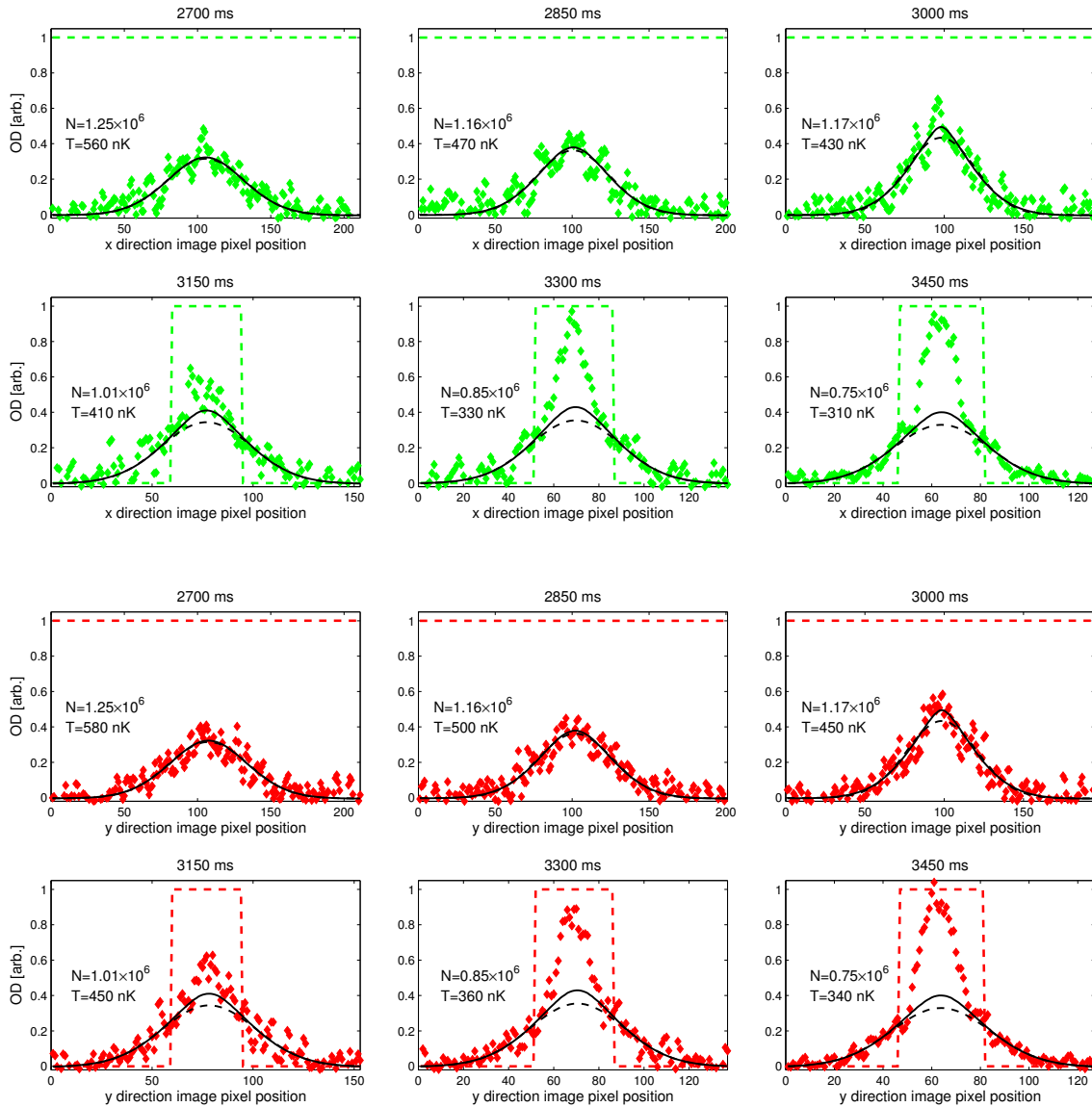
of $f_{ho} = 83$ Hz, where $\omega_{ho} = (\omega_x \omega_y \omega_z)^{1/3}$ is the geometric mean of the oscillator frequencies of the ODT. We can also determine the ODT oscillator frequencies by directly measuring the trap frequencies and modeling the trap potential (discussed in Chapter 2) to assess whether the result from the critical temperature is reasonable. For a 2 W trap beam power, which is the beam power at the phase transition, our modeled mean trap frequency $\bar{f} = (f_x f_y f_z)^{1/3} = 93$ Hz. The agreement of the expected trap frequency at T_c to our model calculation is reasonable, and we are safe in using our model results (given in Chapter 2) when describing our trap characteristics (e.g., the trap depth and volume) for analyzing our entire evaporation trajectory, as

in Chapter 5.

6.3 Experiment with Bose-enhanced fitting

In reality, the correct way to analyze the thermal component of the cloud is by using Eq. 6.9, as discussed in Section 6.1. Figure 6.4 shows the results of this type of fit. The procedure is somewhat different from when analyzing the thermal portion of the cloud with the gaussian fitting function. When we fit data that had no condensate fraction with Bose-enhanced statistics (Eq. 6.9), we did not exclude any part of the data from the fitting routine as we did when fitting with a gaussian. This is seen in Fig. 6.4, with the dashed colored lines indicating what region of the cloud we chose to exclude in the fitting routine. A straight horizontal line at 1 indicates that the error in the exclusion region equals the error in the full image (as discussed in Section 6.2), and hence there was no weighing of the data for the fit. We did this because the fitting routine with the Bose-enhanced distribution function included fitting the parameter ζ , since ζ is sensitive to the shape of the atom distribution when a BEC appeared. Therefore, when it was clear from our data that there was no BEC present, we allowed our fitting function to fit ζ . As the evaporation process brought the sample closer to the BEC phase transition, the parameter ζ fitted closer to one until $\zeta = 1$, where the chemical potential μ of the sample equaled the lowest state energy for our trap.

If we tried to fit ζ in the presence of a condensate fraction, our fitting procedure



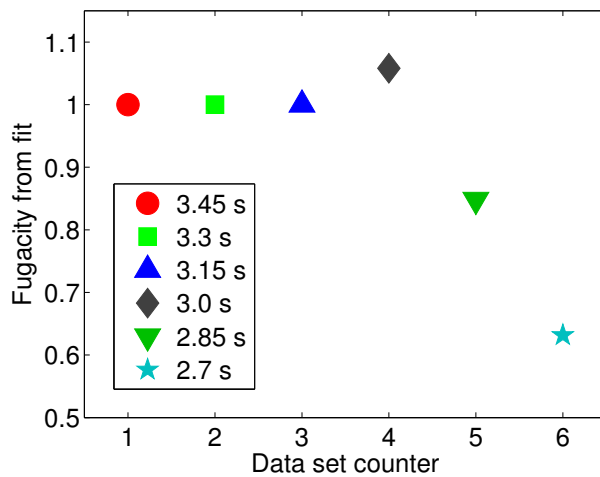


Figure 6.5 : Fugacity values from data fits, with the evaporation time found on the legend. When there is no BEC present, our fitting routine fits the value for ζ while fitting the entire Bose cloud profile. The fugacity's proximity to one indicates how close the sample is from reaching quantum degeneracy. Once there was condensate present, a fit to ζ was not needed and we fixed it to 1.

never converged until we fixed $\zeta = 1$ to continue fitting the thermal portion with the Bose-enhanced distribution function. Since the behavior of ζ indicated that there indeed was a BEC present we excluded the central area of the data in a similar fashion to our analysis with the gaussian distribution, as seen in Fig. 6.4, where the data exclusion regions we chose when fixing $\zeta = 1$ are shown. Figure 6.5 demonstrates the behavior of ζ for the data sets shown in Fig. 6.4. By implementing this complete analysis routine we fit the cloud images to obtain quantitative information about the thermal portion in and without the presence of a condensate fraction. All of the solid-line fits shown in Fig. 6.4 are using the fugacity fitting function. To visually compare the difference between the results of the fugacity fit function to the gaussian fit function, we also plotted the gaussian fit for the corresponding data set.

Our indicator for quantum degeneracy is now the behavior of ζ , since the fugacity's proximity to 1 indicates how close the sample is from quantum degeneracy. From this new analysis we determine that the BEC phase transition occurs at $T_c \sim 430$ nK at an evaporation time of 3 s (see Fig. 6.5). This is the same evaporation time we ascribed to as the onset of quantum degeneracy in our first pass of analysis with the simple gaussian, although the transition temperature using the gaussian fit is lower. A transition temperature of 430 nK and atom number of 1.2×10^6 implies that the mean harmonic trap frequency at the transition temperature was $f_{ho} = \frac{k_B T_c}{0.94 h N^{1/3}} = 90$ Hz. This is very consistent with the trap model results.

Chapter 7

BEC in ^{84}Sr

The previous chapter described how a fit to the fugacity ζ of the sample helps one determine when the sample undergoes the BEC phase transition during the evaporation trajectory. This chapter continues the cooling path until the sample becomes a pure BEC, and presents our analysis of the condensate along this trajectory. It is therefore necessary to develop tools to correctly analyze only the condensate portion of the cloud.

Chapter 5 introduced the BEC phase transitions with noninteracting atoms. Real systems, however, have interacting atoms. The interactions modify the transition very little, but they modify the density distribution of the condensate significantly, as mentioned in Chapter 1. The first part of this chapter introduces the concept of mean-field theory to treat interactions and describes the large- N limit for systems with repulsive interactions, which is the case for ^{84}Sr . This leads to the Thomas-Fermi (TF) limit, where one obtains analytical equations to study the condensate. We then analyze our experimental results using the TF limit to describe its characteristics such as condensate fraction, expansion behavior and loss rates.

7.1 Mean-field Gross-Pitaevskii equation

The following discussion is adapted from References [49, 125, 126]. The method of second quantization is utilized to formulate the mean-field description of a dilute Bose gas with interactions. This approach is powerful when dealing with a macroscopic number of particles, where it is impractical to explicitly write the wave function for the many-body system, let alone to solve the time-dependent Schrodinger equation for this wave function. The many-body Hamiltonian for N interacting bosons in an external potential V_{ext} becomes (in second quantization)

$$\begin{aligned} \hat{H} = & \int d\vec{r} \hat{\Psi}^\dagger(\vec{r}) \left[-\frac{\hbar^2}{2m} \nabla^2 + V_{ext}(\vec{r}) \right] \hat{\Psi}(\vec{r}) \\ & + \frac{1}{2} \int d\vec{r} d\vec{r}' \hat{\Psi}^\dagger(\vec{r}) \hat{\Psi}^\dagger(\vec{r}') V(\vec{r} - \vec{r}') \hat{\Psi}(\vec{r}') \hat{\Psi}(\vec{r}), \end{aligned} \quad (7.1)$$

$V(\vec{r} - \vec{r}')$ being the particle-particle interaction term. Equation 7.1 is comprised in terms of the boson field operators $\hat{\Psi}^\dagger(r)$ and $\hat{\Psi}(r)$ that create and annihilate a particle at the position \vec{r} , respectively.

The mean-field treatment comes about by decomposing the field operator into a mean condensate contribution and a component that accounts for quantum fluctuations in the particle number around the mean value. This description, developed by N. Bogoliubov [127], is valid for large single-particle state occupation (large N). The field operator separates as

$$\hat{\Psi}(r, t) \equiv \Phi(r, t) + \hat{\Psi}'(r, t)$$

where the function $\Phi(r, t)$ is defined as the expectation value of the field operator

($\Phi(r, t) \equiv \langle \hat{\Psi} \rangle$) and the operator $\hat{\Psi}'$ represents the excitations of the interacting Bose gas. The classical field $\Phi(r, t)$ is defined as the wave function of the condensate possessing a well-defined phase.

For strongly interacting systems $\hat{\Psi}'$ is significant and must be included for an accurate description of $\hat{\Psi}$. However, when $\hat{\Psi}'$ is small, $\hat{\Psi}$ is well defined by its mean value $\Phi(r, t)$ and its evolution determines the behavior of the Bose gas in a mean-field description. Strictly speaking, the condition that $\hat{\Psi}' = 0$ is valid only at zero temperature where all atoms are in the condensate, making the following discussion true for a gas at $T = 0$ K. Corrections due to finite temperature, which are on the order of 1% or less [49], exist but will not be considered here.

To determine the evolution of the condensate wave function Φ , one determines the evolution of the field operator $\hat{\Psi}(r, t)$ (using the Heisenberg representation) and then replaces the operator Ψ with the field Φ . With the Hamiltonian 7.1, this becomes:

$$\begin{aligned} i\hbar \frac{\partial}{\partial t} \hat{\Psi} &= [\hat{\Psi}, \hat{H}] \\ &= \left[-\frac{\hbar^2 \nabla^2}{2m} + V_{ext}(\vec{r}) + \int d\vec{r}' \hat{\Psi}^\dagger(\vec{r}', t) V(\vec{r}' - \vec{r}) \hat{\Psi}(\vec{r}', t) \right] \hat{\Psi}(\vec{r}, t). \end{aligned} \quad (7.2)$$

Replacing $\hat{\Psi}$ with $\Phi(r, t)$ amounts to saying that the effect of the scattering potential $V(\vec{r} - \vec{r}')$ is not very strong to distort an incoming wave much (the Born approximation) and its effect is local. This situation is well satisfied in the ultracold collisions occurring in a dilute-gas BEC, where collisions are characterized by the s -wave scattering length a (introduced in Chapter 3) that sets the typical length scale of a scattering event. Therefore, one chooses a potential $V(\vec{r} - \vec{r}')$ that will describe the low energy

scattering properties of the system correctly. The specific form of the representative potential does not matter (cf. [126]) and a convenient choice is the contact potential

$$V(\vec{r} - \vec{r}') = g\delta(\vec{r} - \vec{r}'), \quad (7.3)$$

where $g = \frac{4\pi\hbar^2 a}{m}$ and a is the scattering length. Utilizing Eq. 7.3 in Eq. 7.2 makes the integration simple and results in the following evolution equation for the order parameter Φ , known as the Gross-Pitaevskii (GP) equation [128, 129, 130]:

$$i\hbar\frac{\partial}{\partial t}\Phi(\vec{r}, t) = \left(-\frac{\hbar^2\nabla^2}{2m} + V_{ext}(\vec{r}) + g|\Phi(\vec{r}, t)|^2 \right) \Phi(\vec{r}, t). \quad (7.4)$$

To describe a gas with Eq. 7.4, the atom number in the condensate is much larger than 1. It also requires that the Bose gas be dilute enough that the scattering length a be much smaller than the average particle spacing $n^{-1/3}$. But, as Section 7.2 points out, the importance of the interactions is determined by comparing it with the kinetic energy of the gas.

The state with lowest energy can be easily obtained by considering the stationary states of Φ . By expressing the wave function $\Phi(\vec{r}, t) = \phi(\vec{r})\exp(-i\mu t/\hbar)$, the GP equation 7.4 takes the form

$$\left(-\frac{\hbar^2\nabla^2}{2m} + V_{ext}(\vec{r}) + g|\phi(\vec{r})|^2 \right) \phi(\vec{r}) = \mu\phi(\vec{r}), \quad (7.5)$$

where μ is the chemical potential and the wave function is normalized such that the total condensate number N is $N = \int d\vec{r} |\phi(\vec{r})|^2$. The first term on the left side of Eq. 7.5 is known as the quantum pressure term, while the third term is the mean-field

interaction term. $V_{ext}(\vec{r}) = \frac{m}{2}(\omega_x^2 x^2 + \omega_y^2 y^2 + \omega_z^2 z^2)$ is the harmonic oscillator potential confining the Bose gas.

7.2 Effect of interactions: Thomas-Fermi limit

To quantify whether interaction effects are significant, one compares them with the kinetic energy E_{kin} of the atoms in the trap. The interaction term in Eq. 7.5 is $E_{int} = gN|\phi(\vec{r})|^2 = gNn$ where $n \sim N/a_{ho}^3$ is the average particle density and $g \propto |a|$. The trap harmonic oscillator length $a_{ho} = \sqrt{\hbar/(m\omega_{ho})}$ gives the size of a non-interacting cloud in the lowest energy state. E_{kin} represents the quantum pressure term of the gas and is on the order of $N\hbar\omega_{ho}$, so that $E_{kin} \propto Na_{ho}^{-2}$. The ratio of these two terms gives the parameter

$$\frac{E_{int}}{E_{kin}} \propto \frac{N|a|}{a_{ho}}, \quad (7.6)$$

parametrizing the importance of the interactions to the kinetic energy. Although one typically defines a dilute gas to be when $n|a|^3 \ll 1$, the parameter Eq. 7.6 can be easily larger than 1, implying that very dilute gases can have significant non-ideal gas behavior if interactions exist [49].

For gases with repulsive interactions ($a > 0$) and large N , the interaction term in the GP equation dominates over the quantum pressure ($\frac{N|a|}{a_{ho}} \gg 1$). In this case, one can completely neglect the quantum pressure term in Eq. 7.5 and the GP equation reduces to a simple analytic form,

$$\phi^2(\vec{r}) = n(\vec{r}) = g^{-1} [\mu - V_{ext}(\vec{r})], \quad (7.7)$$

referred to as the Thomas-Fermi (TF) approximation. The particle number N and chemical potential μ are related by

$$\mu = \frac{\hbar\omega_{ho}}{2} \left(\frac{15Na}{a_{ho}} \right)^{2/5}. \quad (7.8)$$

The density distribution $n(\vec{r})$ from Eq. 7.7 takes the form of an inverted paraboloid

$$\begin{aligned} n(\vec{r}) &= \frac{\mu}{g} \left[1 - \frac{x^2}{R_x^2} - \frac{y^2}{R_y^2} - \frac{z^2}{R_z^2} \right] \\ &= n_{TF}(0) \left[1 - \frac{x^2}{R_x^2} - \frac{y^2}{R_y^2} - \frac{z^2}{R_z^2} \right] \end{aligned} \quad (7.9)$$

that goes to zero at the radius \vec{R} where $\mu = V_{ext}(\vec{R})$. This implies that $\mu = m\omega_{ho}^2 R^2/2$ and (together with Eq. 7.8) the radii R of the condensate becomes

$$R_i = \sqrt{\frac{2\mu}{m\omega_i^2}}, \quad (7.10)$$

with the index $i = x, y, z$. The relatively large value of the scattering length for ^{84}Sr ($a \sim 123 a_0$) suggests that the TF approximation is the correct profile to analyze our condensates clouds.

Figure 7.1 shows a representative 1D slice through the center of a condensate absorption image and the fitting function Eq. 7.9 along the same central line, demonstrating that this functional form is valid. One remarkable result is that the 1D profile of Fig. 7.1 is of a condensate after a time-of-flight period, whereas we have considered a Bose gas in a potential V_{ext} . It is important to notice, then, that the condensate radii in Eq. 7.10 correspond to $t = 0$, for a trapped BEC in a harmonic potential before subjected to a drop time. As we will see in Section 7.3.1, the condensate retains

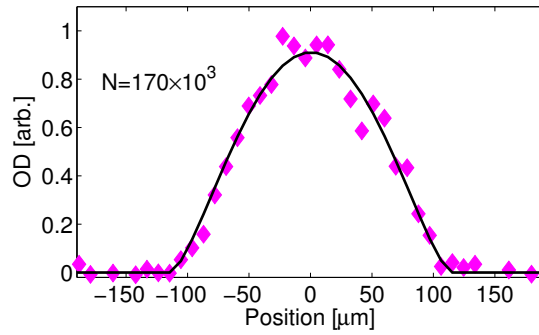


Figure 7.1 : A representative 1D slice of the condensate column density together with TF (Eq. 7.11) fit profile on top.

its shape. The new condensate radii after a time-of-flight period are a rescaling of $R_i(0)$ (Eq. 7.10).

7.3 Making and analyzing the BEC

Experimentally, we finish the evaporation trajectory from Chapter 6 until we produce pure BECs. Our sample is, therefore, near or below the critical temperature, where both thermal and condensate atoms exist at the same time. This allows us to fix the fugacity $\zeta = e^{\mu/k_B T} = 1$ (discussed in Chapter 6) when fitting our images, since the chemical potential $\mu = 0$ at $T \leq T_c$. By using the fitting function Eq. 6.9 with $\zeta = 1$, we correctly quantify the thermal cloud and extract the condensate profile. Then we subtracted the thermal profile fit from the data, which leaves behind the atom distribution that is in the condensate as discussed in Chapter 6.

We fit the column density of the expanded condensates with the functional form

$$n(x, y) = \frac{5N_0}{2\pi} \left(1 - \frac{x^2}{[R_x(t)]^2} - \frac{y^2}{[R_y(t)]^2} \right)^{3/2} \theta \left(1 - \frac{x^2}{[R_x(t)]^2} - \frac{y^2}{[R_y(t)]^2} \right), \quad (7.11)$$

where θ is the Heaviside function, and $R_x(t)$ and $R_y(t)$ are the condensate radii (after a drop time). Figure 7.2 presents the results of this analysis in the form of 1D slices of data through the center of the condensate and the corresponding slice of the fitting function, similar to that done in Chapter 6.

Using the TF limit to analyze the condensate empowers us to quantify the BEC's characteristics easily. In Fig. 7.3 we plot the chemical potential (Eq. 7.8) as a function of atom number for three different mean oscillation frequencies. The harmonic oscillator length a_{ho} for our trap ranges from $1.1 \mu\text{m}$ to $1.4 \mu\text{m}$ for expected experimental oscillator frequencies (from 75 to 105 Hz). Comparing μ to a typical harmonic oscillator energy scale of $3\hbar\bar{\omega}/2k_B \sim 5 \text{ nK}$ vastly shows that atomic interactions are the dominant energy scale for our experiment (see Fig. 7.3).

We can also examine the parameter $(Na)/a_{ho}$ from Eq. 7.6 for similar trap parameters, with N equaling the condensate number. Figure 7.4 shows the magnitude of this parameter as a function of condensate number N_{bec} . The magnitude of this parameter is greater than 1 for $N_{bec} > 1 \times 10^3$ and is about 1000 for our pure BECs. This result implies that the condensate is strongly interacting and is appropriately described by the TF distribution.

Due to the importance of the interaction energy, the pure condensate's wavefunction is sensitive to the chemical potential and the potential confinement (optical trap) it is subject to. This can become evident in the free expansion of the condensate and its size evolution. As discussed in Section 7.2, one expects that the condensate shape

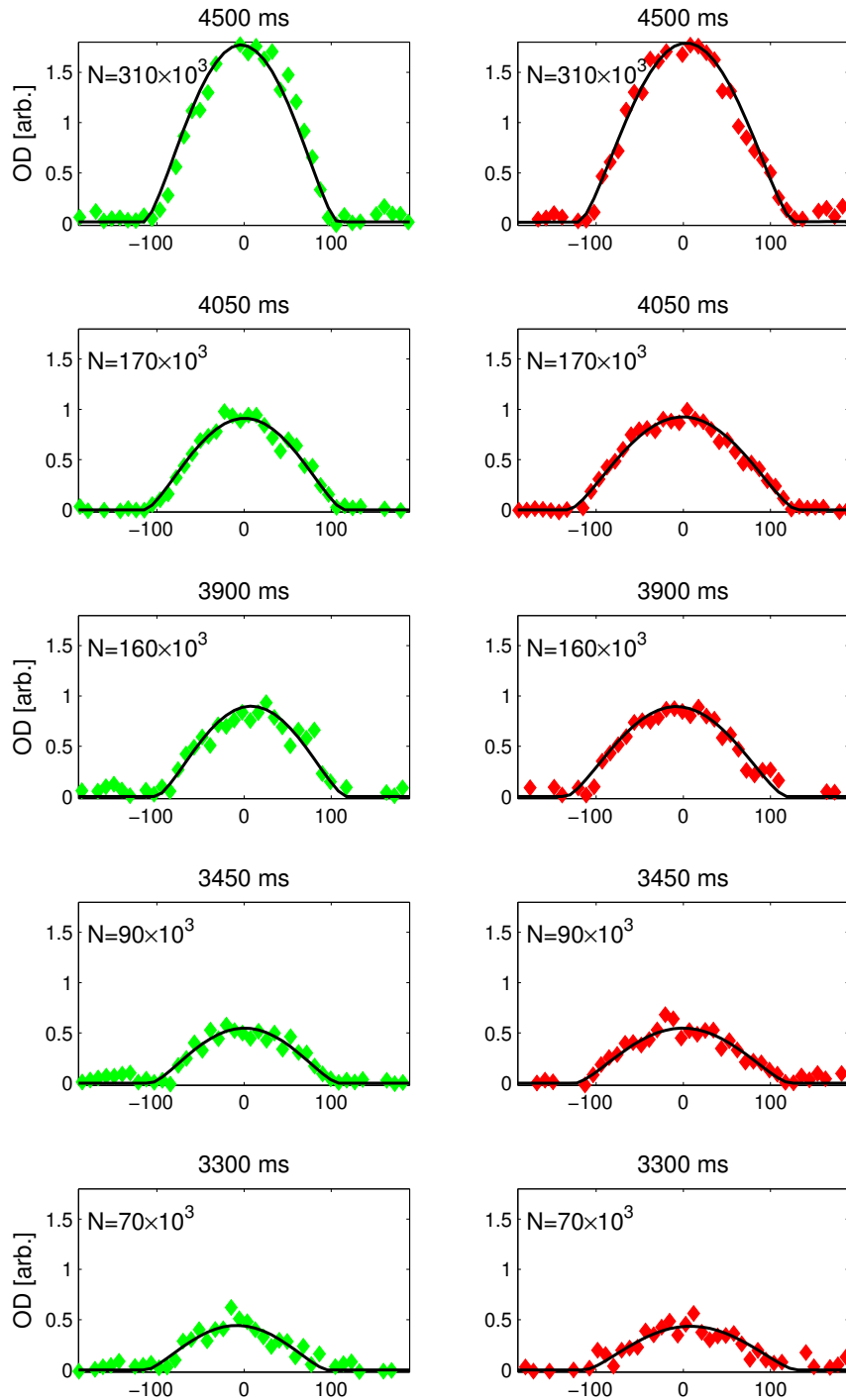


Figure 7.2 : X (left) and Y (right) 1D slices of condensate column density. Plotted on top of the data is the corresponding TF (7.11) fit profile. The plot shows the evaporation time above the data frame. The condensate number extracted from the TF fit is shown in the data frame.

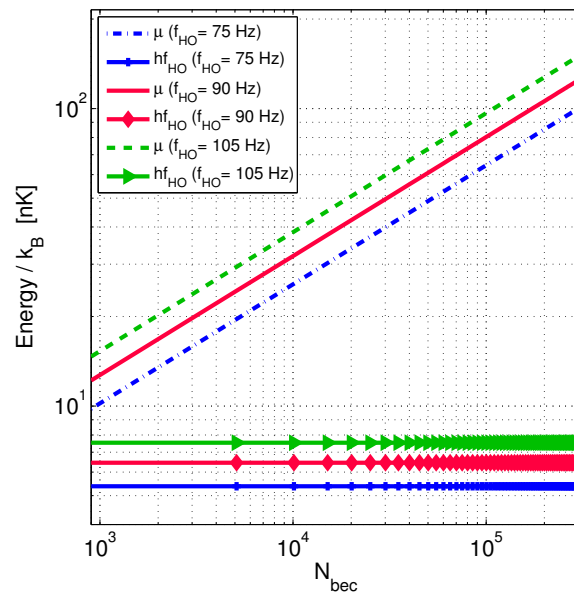


Figure 7.3 : The chemical potential (Eq. 7.8) for typical experimental mean trap oscillator frequencies (75 Hz, 90 Hz and 105 Hz). The trap harmonic oscillator energy scale ($3 \hbar \omega_{ho}/2$) is also plotted for comparison.

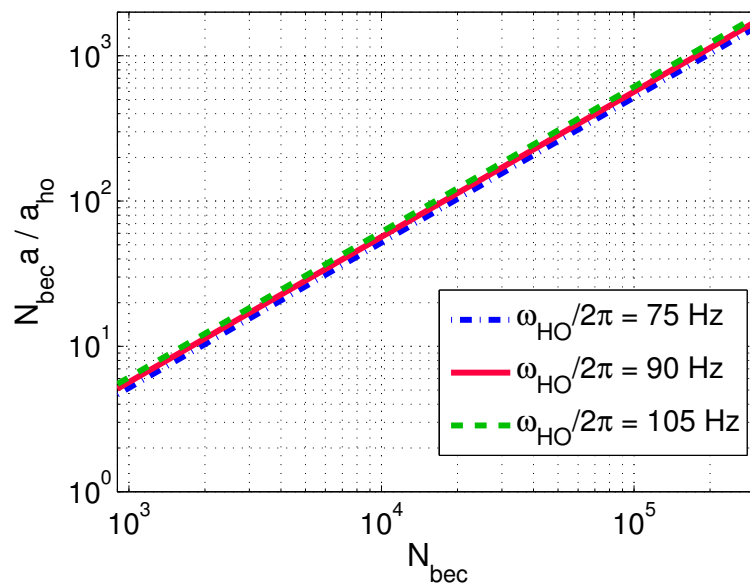


Figure 7.4 : The parameter $(N_0 a)/a_{ho}$ for typical experimental mean trap oscillator frequencies (75 Hz, 90 Hz and 105 Hz). The Bose gas is in the strongly interacting regime when this parameter is much greater than one. The TF profile is valid in this strong-interaction regime.

be preserved during ballistic expansion. We will consider this behavior in Section 7.3.1.

7.3.1 Castin-Dum model

One can extract information about the interactions in a BEC from the shape of the expanded cloud after a time-of-flight period. For a falling cloud having been trapped by an anisotropic harmonic potential, the tighter the confinement in a given direction was, the faster the expansion velocity in that direction will be during the drop period. But the expansion preserves the original shape of the condensate [49]. Therefore, the condensate evolves with a parabolic shape, and its radii scale in time according to [131]

$$R_i(t) = R_i(0)b_i(t) = \sqrt{\frac{2\mu}{m(2\pi f_i)^2}}b_i(t) \quad (7.12)$$

for $i = x, y, z$, where the scaling parameters obey

$$\ddot{b}_i(t) = (2\pi f_i)^2/(b_x b_y b_z). \quad (7.13)$$

To study the expansion behavior of a pure BEC, we evaporatively cool our Bose gas for 4.5 s until no discernible thermal population is present, turn the ODT off suddenly and allow the condensate to fall for variable drop times before taking an image. We then fit the optical depth with the TF density distribution Eq. 7.11 and obtain condensate size information from the fit parameters R_x and R_y . Since our ODT is slightly asymmetric with respect to gravity due to the nearly 10.5° tilt of the trap beams from the horizontal plane, we expect that the principle axes of the

condensate's expansion will be at an angle with respect to the direction of gravity.

In order to improve the fit to the radial sizes of the condensate during the free expansion, we rotate the coordinate system in which we analyze the images by an angle θ . The absorption images taken are in the *lab coordinate system* with coordinates \mathbf{x} and \mathbf{y} . The BEC fitting function is of the form

$$n(x, y) = n_0 \left(1 - \frac{x'^2}{R_x^2} - \frac{y'^2}{R_y^2} \right)^{3/2}, \quad (7.14)$$

with the density going to zero outside the extend of R_i . We are only concerned in rotating two coordinates because our absorption images are in 2 dimensions.

We then relate a position vector $\mathbf{X} = \begin{pmatrix} x \\ y \end{pmatrix}$ in the BEC axes frame to the position vector $\mathbf{X}' = \begin{pmatrix} x' \\ y' \end{pmatrix}$ in the lab by

$$\begin{pmatrix} x' \\ y' \end{pmatrix} = R_\theta \begin{pmatrix} x \\ y \end{pmatrix},$$

where

$$R_\theta = \begin{pmatrix} \cos \theta & \sin \theta \\ -\sin \theta & \cos \theta \end{pmatrix}$$

for rotations in a clockwise direction. This yields

$$x'^2 = x^2 \cos^2 \theta + y^2 \sin^2 \theta + 2xy \cos \theta \sin \theta$$

$$y'^2 = x^2 \sin^2 \theta + y^2 \cos^2 \theta - 2xy \cos \theta \sin \theta.$$

Using these definitions for coordinates in a rotated frame, we find $\theta = 45^\circ$ to give us the best fit.

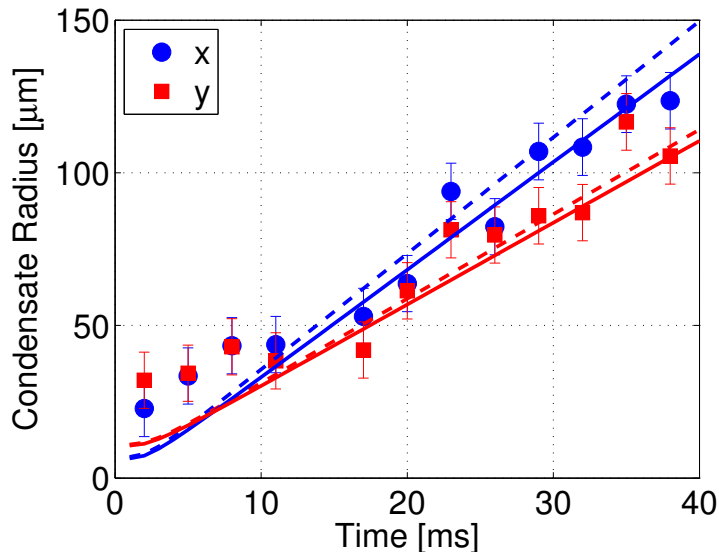


Figure 7.5 : Condensate radius after release from the trap. The expansion of the condensate is fit by the Castin-Dum model [131]. Deviations at early times most likely reflect limitations of the optical imaging system and large optical depths of the condensate.

We do not attempt to make a precise model for rotating our BEC into the lab frame. The effect of the condensate not expanding in the principal axes of our imaging system should turn out to be small because our trap is close to spherical. Furthermore, the details of the principal axes of the expansion depend on a knowledge of the independent waists of our two trap beams that is more accurate than what we know. However, this approach is reasonable for the level of accuracy we are looking for in this analysis.

Figure 7.5 shows the evolution of condensate radii as a function of expansion time by fitting the absorption images with Eq. 7.14 with the substitutions for x' and y' . We model the condensate expansion using a numerical solution to Eq. 7.12 with $b_i(t)$

evolving according to Eq. 7.13. Figure 7.5 shows our results (dashed line) obtained by using the known value of the scattering length a and the estimated trap parameters from trap frequency measurements. By decreasing the trap frequencies by about 5%, we obtain an improved fit to the data, shown by the solid line. This variation in the trap frequencies is within our uncertainty in the trap parameters. We therefore conclude that the Castin-Dum model [131] describes the expected expansion behavior.

We also measured the lifetime of the condensate by holding it in the ODT after 4.5 s of evaporation and measuring the number decay. Studying the loss processes of a condensate determines what limits the density and lifetime of the sample. This knowledge becomes particularly relevant when one desires to tune the atomic interactions (as with a Feshbach resonance) or determine the time available to perform useful experiments with the BEC. Two- and three-body loss processes become increasingly important in samples near zero temperature where BEC occurs because the density becomes very high. Typically, two-body loss comes about by collisions between atoms that promote atoms to a non-trapped state (particularly in magnetic traps). For our system, this type of loss should not be relevant due to our non-degenerate ground state. Therefore, we quantify the magnitude of three-body losses in our system here.

Because no discernible thermal fraction was evident in these samples, we fit the complete absorption image with a TF profile (Eq. 7.11). Figure 7.6 shows one- and three-body decay fit curves to our lifetime measurement. We use the three-body decay curve found in Reference [132] when fitting the data. This curve is described

by

$$\frac{1}{N} \frac{dN}{dt} = -K_1 - K_3 \langle n^2 \rangle,$$

where N is the condensate number, K_1 is the one-body loss rate, and K_3 is the loss rate constant for three-body decay. The mean squared density $\langle n^2 \rangle$ is defined as $\langle n^2 \rangle = 8/21 n_0^2$ for a harmonic potential, where n_0^2 is the measured peak density. In the TF regime, the peak condensate density equals [133, 132]

$$n_0 = 0.118 \left(\frac{N m^3 \bar{\omega}^3}{\hbar^3 a^{3/2}} \right)^{2/5}. \quad (7.15)$$

The corresponding mean oscillator frequency for the trap after 4.5 s of evaporation is (calculated from our trap model) $\bar{\omega} = 2\pi \times 81$ Hz. In Eq. 7.15, m is the atom mass and a is the scattering length, which we took to equal $123 a_0$. The one-body loss rate fit was a normal fit to an exponential and yielded a loss rate of 8 s.

Higher quality measurements are needed for a more rigorous measurement of the three-body decay. However, the fits to the data are satisfactory and yield a three-body loss rate constant $K_3 = 7 \times 10^{-30} \text{ cm}^6 \text{ s}^{-1}$ for the curve shown in Fig. 7.6. For the three-body fit, we fixed the one-body loss rate K_1 at $1/\tau$ with $\tau = 30$ s, based on lifetime measurements in our ODT of non-condensed clouds. Our fitted K_3 is comparable to systems with a similar scattering length such as ^{87}Rb [134, 135], which has a scattering length $a = 106 a_0$. Two different experiments reported K_3 at $5.8 \times 10^{-30} \text{ cm}^6 \text{ s}^{-1}$ ($F = 1$, $m_F = -1$ state) [135] and $1.8 \times 10^{-29} \text{ cm}^6 \text{ s}^{-1}$ ($F = m_F = 2$ state) [134] for condensed atoms.

Theoretical predictions show that the three-body loss rate scales universally as a^4

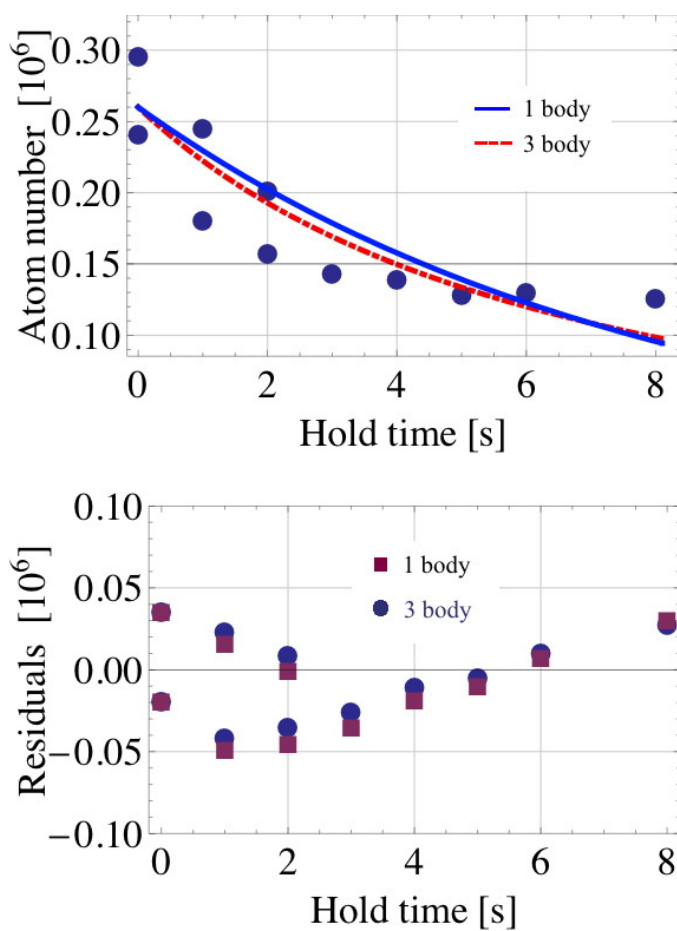


Figure 7.6 : BEC one- and three-body loss rate fits. The resulting three-body loss rate constant $K_3 = 7 \times 10^{-30} \text{ cm}^6 \text{ s}^{-1}$, with the one-body loss rate fixed at $1/\tau$ with $\tau = 30 \text{ s}$. For the one-body loss fit, the resulting loss rate constant $K_1 = (8 \text{ s})^{-1}$.

[136, 137]. This relationship seems to hold well for other experiments, including those of Rb mentioned before*. We therefore infer that our fitted value of $K_3 = 7 \times 10^{-30}$ $\text{cm}^6 \text{s}^{-1}$ is a reasonable value for experiment.

*Note that Reference [137] quotes the event rate constant for three-body recombination, which is twice as large as our K_3 . In addition, they calculate the event rate constant for a spin-polarized Bose gas near zero temperature and not for a BEC. This increases their theoretically calculated rates by another factor of 3! [138, 135].

Chapter 8

Conclusion

Strontium BEC had been a quest of various experimental groups for almost two decades (e.g., [64]) because of this atom's important role as an optical frequency standard and its potential applications in quantum information. Previous attempts at reaching this goal were not successful due in large part to the lack of accurate understanding of the collisional properties of Sr. The experiments presented in this thesis play a key role in both of these issues.

The results of two-photon PAS in ^{88}Sr allowed us to understand the different collisional properties of the Sr isotopes. Our one-photon PAS experiments [104, 62] preceding the two-photon experiment [63] concentrated on spectroscopic measurements at large interatomic separation. These long-range measurements were appropriate to determine a rough order-of-magnitude for the scattering length of ^{86}Sr and ^{88}Sr . Since these PAS results are for large interparticle separation, they aided in clarifying what the accurate lifetime of the 1P_1 state was. However, the powerful advantage that two-photon PAS has over the one-photon version is that it directly probes the ground molecular potential. Via these spectroscopic measurements, one gets information about the shape of the potential and can eventually reconstruct it for a full picture of the phase shifts experienced by the ground molecular potential wavefunc-

tion. At ultracold temperatures, the wavefunction's phase shift is directly related to the scattering length a .

The importance of understanding the interaction between atoms is evident in the experiments focused on producing quantum degenerate gases of Sr. Previous attempts to reach quantum degeneracy had concentrated on using the most abundant isotopes (^{86}Sr and ^{88}Sr). It became clear after the two-photon spectroscopic results that favorable collisional properties belonged to the least abundant one (^{84}Sr).

Our results on BEC came amid intense interest in quantum degenerate gases of alkaline-earth metal atoms. This experimental and theoretical activity attests to the timeliness and importance of our work. Although Yb and Ca BECs came before the first results in Sr [29, 30], the Sr systems proved to be more robust than the prior two. This potentially puts Sr at the forefront for tremendously fruitful experiments such as producing ultracold molecules for a new generation of frequency standards and demonstrating optical Feshbach resonances with low-loss tunability of atomic interactions.

Appendix A

Experimental details from Natali's notebooks

The contents of this appendix can be, at times, very scarce, due to the lack of importance of the subject being treated or to insufficient detail in my notebooks (the details are probably found in one of the lab notebooks, for instance). However I hope it provides enough explanations on the different experimental components I worked on in the Killian lab to enable their repair/discovery. **NOTE: All of the part numbers included in this appendix were the correct part numbers as of the date when the corresponding piece was used/built and could very likely have changed since then.**

A.1 Data taken with ^{86}Sr

During the course of the experiments performed in this dissertation, we performed spectroscopic measurements using the second most abundant isotope (^{86}Sr). In this section I include Table A.1 which catalogs where and when the data was taken (in case one wants to locate the data again).

From these experimental runs we found three ^{86}Sr One-photon PAS candidates, one at about -8.5 MHz, another at about -25 MHz (see Fig. A.1) and the last at about -112 MHz (all detuned from the 1S_0 - 3P_1 resonance). The -25 MHz line had the correct

Date of data sets	Notebook letter & Page #	Type of experiment
8 May 2008	Notebook F, pg. 3 (yellow)	One-photon PAS
12 May 2008	Notebook F, pg. 6 (yellow)	One-photon PAS
15 May 2008	Notebook F, pg. 10 (yellow)	One-photon PAS
23 June 2008	Notebook F, pg. 39 (white)	One-photon PAS
24 June 2008	Notebook F, pg. 40 (white)	One-photon PAS
30 June 2008	Notebook F, pg. 43 (white)	One-photon PAS
2 July 2008	Notebook F, pg. 45 (white)	One-photon PAS
24 June 2008	Notebook F, pg. 40 (white)	Two-photon PAS
2 July 2008	Notebook F, pg. 48 (white)	Two-photon PAS

Table A.1 : ^{86}Sr spectroscopic measurements.

asymmetric shape that we expect for this temperature, so we had high confidence that this is a PAS line. The line at -8 MHz is a little too broad and symmetric, so that is less certain. But taking into account the third line at -112 MHz, we believe that both this line and the -8 MHz line are on the 0_u potential (using JILA's notation in [98]). That would place the -25 MHz line on the 1_u molecular potential.

A.2 Calibrating pixel size with atom samples

In order to correctly analyze our BEC data, it was imperative to know the correct camera pixel size used in our images. This parameter changed at some points during the experiments because we found it necessary to sometimes change the camera

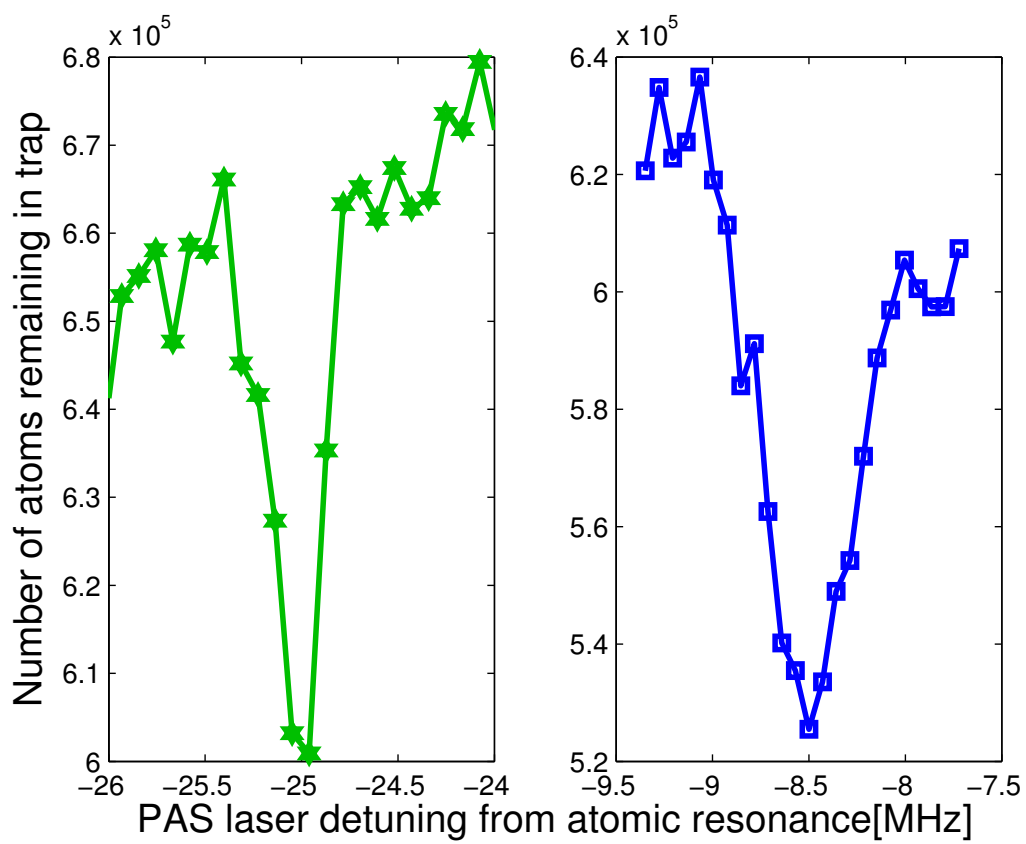


Figure A.1 : ^{86}Sr one-photon PAS candidates. These spectra were measured on May 8, 2008.

focusing lens position. However, we are capable of determining the correct pixel size for the data using the atoms' falling trajectory under the influence of gravity.

From the **kinematic** equation for position as a function of time, we have

$$y(t) - y_0 = -\frac{1}{2}g(t - t_0)^2 \quad (\text{A.1})$$

where $\vec{F} = m\vec{a} = -mg$ and $g = 9.8 \text{ m/s}^2$. The atom cloud's position as it falls ($y(t)$ in Eq. A.1) is a function of the time in which the cloud's image was taken (t in Eq. A.1). y_0 is the cloud's initial vertical position while t_0 is its corresponding image time. But, we will obtain $y(t)$ from the raw images only *after* analyzing the images, as described next.

The camera's raw absorption images are analyzed with "imagefit_binaryread", a Matlab program that fits an image with a 2D gaussian function. The output parameters from this fit include the 2D function x - and y -*position*, which come from the x and y pixel positions of the images. It is **this** fitted y -*position* that will be used for $y(t)$ in Eq. A.1. As of May 2010, the x -*position* output parameter from "imagefit_binaryread" was parameter #7 in the program's output file (ending with the suffix "2Dfitparams.txt"), while the y -*position* output parameter was #8. IT IS IMPORTANT TO NOTE that in the program "imagefit_binaryread" one (pre)decides what the pixel size *is* to analyze the raw image, while at the same time, sets how the image pixels will be "binned" so as to permit the fitting function routine (in "imagefit_binaryread") to converge in a timely manner. Specifically, the parameters determined before analyzing the raw image are *pixelsize*, *softwarebinsize*, *CCDbinsize*

ning, and *sampleinterleave* (as of May 2010). *CCDbinning* and *sampleinterleave* are typically 1 in the final level of data analysis. Therefore, the 2D function output *y-position* depends on the values of *pixelsize* and *softwarebinsize* used in the analysis - they are correlated, unfortunately. The parameter $\text{pixelsize} \times \text{prebinning}$ (where $\text{prebinning} = \text{softwarebinsize} \times \text{CCDbinning} \times \text{sampleinterleave}$) is output parameter #29 saved in the “2Dfitparams.txt” file.

Therefore, in order to determine the correct camera pixel size for that particular set of data, one fits the atoms’ falling trajectory while making *pixelsize* a variable. You will have to adjust $y(t)$ for the pixel size originally used to fit the raw data. Only the correct pixel size will make the cloud’s position fit the kinematic trajectory expected under gravity. By revisiting the pixel size calibration for our BEC data, I determined that:

Data sets (October 10, 2009 data)	$\mu\text{m}/\text{pixel}$
Before time stamp 2539	12.2
After time stamp 2539	9.2

A.3 Details about ^{87}Sr slave lasers setup

This section expands on the description given by Pascal Mickelson in his PhD dissertation [75] with details taken from Natali’s notes. As mentioned by Pascal, the ^{88}Sr master-slave laser setup provides a seed beam (from a window reflection) for an addi-

tional slave laser (named from here on ^{87}Sr slave #1) that becomes one of the lasers used for trapping ^{87}Sr in the 689 nm MOT. A diffracted beam from slave laser #1 by a 1.3 GHz AOM (centered at 1.251 GHz) further provides a second seed beam for ^{87}Sr slave #2; these particulars are depicted in Fig. A.2. Figure A.3 also shows laser powers measured at different positions along the laser setup (as of January 2009).

We used different diodes when assembling the two ^{87}Sr slave lasers. The laser diode placed inside ^{87}Sr slave #1 is a 50 mW diode (Hitachi P/N HL6750MG) without the diode cap. Similarly, a 35 mW laser diode (Hitachi P/N HL6738MG) is placed inside ^{87}Sr slave laser #2 without the diode cap. Each diode laser assembly has a 9-pin subminiature connector "feedthrough", to which the TEC, thermistor and diode connections are made. Its mating connector powers these three components through wires coming from their respective power supplies. Figure A.4(a) shows how the connections are distributed, and Fig. A.4(b) shows the connections of the diodes used for the slave lasers.

A typical current setpoint for the two slave laser is about 900 mV (where 1 V = 80 mA), although the current for each laser is independently optimized to ensure that the slave laser is injection-locked. We control the slave laser's diode temperature via the TEC and thermistor system with a Wavelength Electronics temperature controller (P/N HTC3000) and its PCB (P/N HTCEVALPCB). ^{87}Sr slave laser #1 has its diode temperature setpoint (for its temperature controller) at 0.942 V, while ^{87}Sr slave laser #2 has its diode temperature setpoint at 0.889 V (as of May 2010). These

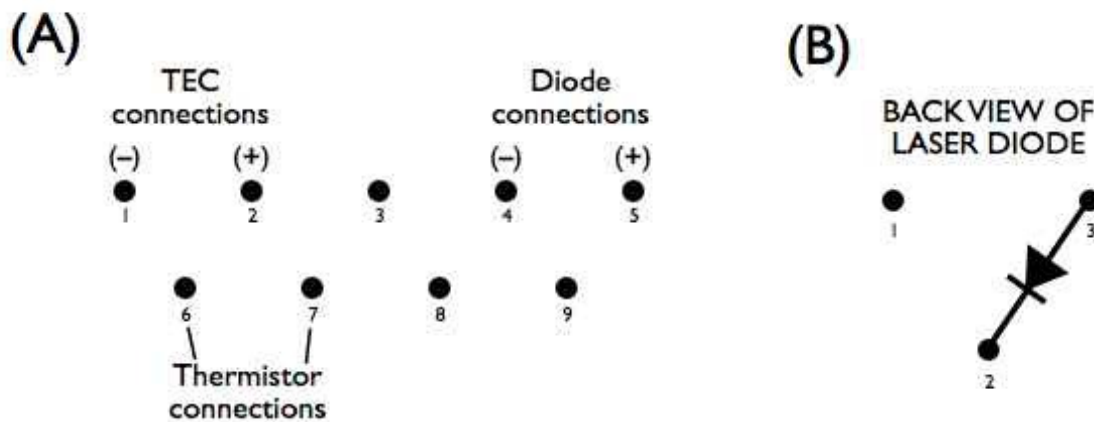


Figure A.4 : ^{87}Sr slave laser connections. Both ^{87}Sr slave laser have their internal components connected to 9-pin subminiature connectors as shown in the figure to the left. The figure to the right shows the pin designation for the HL6750MG (50 mW) and HL738MG (35 mW) laser diodes.

temperatures (near room temperature) are actually pretty typical for the 689 nm diode lasers in the lab, although independent tuning is necessary for correct mode selection.

Both ^{87}Sr slave lasers use a Melles Griot collimating lens (P/N 06GLC001) to collimate the output laser beam. Each slave laser also uses an optical isolator to reduce optical feedback back into the laser. These isolators were typically from Optics For Research (OFR) with P/N IO-5-690-LP/NONE. The “NONE” at the end of the isolator part number means that one of the beam polarizers typically found at the ends of the isolator was not supplied. This is because we used an external PBS cube in place of the missing polarizer, allowing us to separate the incoming seed beam from the outgoing laser light.



Figure A.5 : RF power delivered to 1.3 GHz AOM. In order to ensure that the RF power delivered to this AOM never exceeded its acceptable maximum power level, we set up its power system as shown in this schematic. The commercial RF signal generator (currently controlled with a LabVIEW VI) used for this AOM has the capability to set an attenuation level to its output signal. We worked with the attenuation level set to 0 dB (NO ATTENUATION) in order to avoid mistakenly overpowering the AOM. An attenuation level of 0 dB implied a +8 dB output signal power from the signal generator. Other fixed-power attenuation/amplification components were added to the RF power chain to ensure that the AOM received ~ 30 dB RF power and no more. The delivered RF power is estimated to be +29 dB, as shown in this schematic. The values in parenthesis indicate the amount of RF power expected at that stage in the setup.

The RF for the Brimrose 1.3 GHz AOM (in the path of slave laser #1 as shown in Fig. A.2) follows the sequence shown in Fig. A.5 (as of January 2009). We took care of this AOM because of how delicate/expensive it is, plus how hard it is to replace in the optical path. In September 2008, we measured the diffraction efficiency of this AOM to be 30%, equal to what the specification documents of the AOM quoted. To achieve high diffraction efficiency with these types of AOMs, it is necessary to get the input laser beam as close as possible to the RF signal transducer (i.e., to the edge of the AOM crystal where the RF transducer is attached). Also, driving the AOM near the maximum RF power level called for in the AOM specifications will optimize the diffraction efficiency possible. For this particular AOM, the maximum RF drive power is 1 Watt (+ 30 dB).

A.4 ECDL (master ^{88}Sr laser) and ^{88}Sr slave laser details

Our ^{88}Sr master laser is of the Littmann-Metcalf extended cavity type and the design was created in the Killian laboratory by Andrew Traverso and Tom Killian. We last replaced the laser diode in this laser on August 12, 2009 (as of May 2010) with a (Teledyne?) Eudyna (P/N FLD6A2TK) diode (the laser diode uncapped). The details of the diode change were documented in the Littman-Metcalf laser notebook found in the Killian laboratory. The ECDL worked incredibly well after changing the laser diode — the cavity was single-mode from 14503.6 cm^{-1} to 14504.6 cm^{-1} (the full 150 V range for the laser's PZT). Unfortunately, the extended-cavity lasing optimization deteriorates with time (on the order of a couple of days) because the cavity grating screws relax.

A good way to check the extended-cavity quality is to check the laser's output power after its optical isolator (P/N IO-5-689 from OFR) and lens. When the ECDL current is at normal levels (31.65 mA as of April 2010) and at the right frequency mode (14504.35 cm^{-1}), the laser power after the optical isolator should be about 1.4 mW. If this is not the case, then the grating angle needs to be adjusted with the external plastic screw on the ECDL housing until the output power is optimized (up to 1.4 mW).

There are two temperature controllers for the ^{88}Sr master ECDL: one controls the laser diode temperature and the other controls the ECDL base plate that holds all of the different components that make up the ECDL. These controllers are also

from Wavelength Electronics (see Sec. A.3). The setpoint for the diode temperature controller is 1.338 V, and the setpoint of the base plate temperature controller is 0.999 V (as of April 2010).

As for the ^{88}Sr slave laser, the diode temperature controller is set to 1.362 V, and its actual temperature was measured to be 1.358 V. The current driver is set to 947 mV, with which its power right after the laser's housing was measured to be 19.7 mW (14.9 mW after the PBS cube in front of the laser). 1.2 mW of beam power from the master ^{88}Sr laser goes to the slave laser as a seed beam. This laser's injection lock is pretty stable such that neither the seed beam's alignment, diode's temperature nor its current need be adjusted often, ensuring that the laser is ready for use pretty much right after switching it on.

A.5 689 nm saturated absorption system details

This section complements the information contained in Sec. 2.3.2 about the saturated absorption (sat. abs.) setup. Additional details about the 689 nm laser system may be included here because of their relation to the sat. abs. system.

Our 689 nm sat. abs. cell was designed by Ying Chen Cheng (a former postdoc) and Tom Killian. The cell's technical drawings (produced by Ying Chen) are shown in Fig. A.6 through A.9. Figures A.10 and A.11 show the technical drawings for the cell mounts and Swagelok connection mount, respectively, that were machined for this setup.

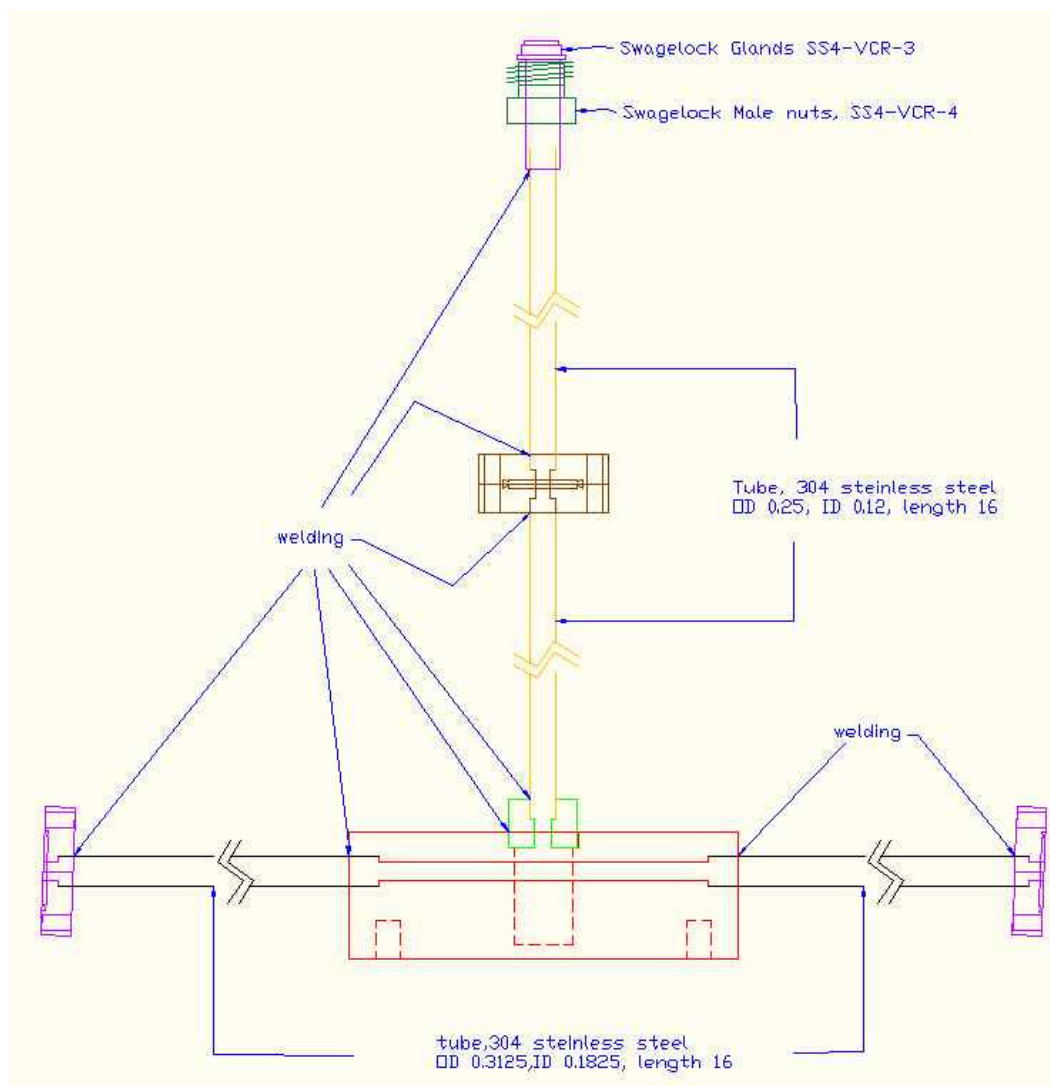
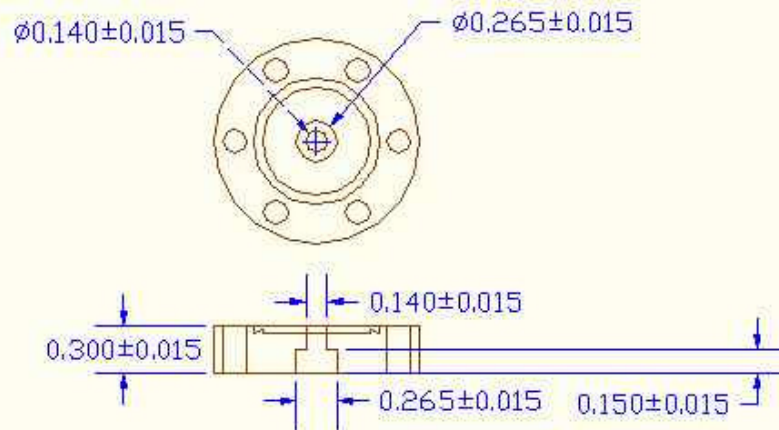
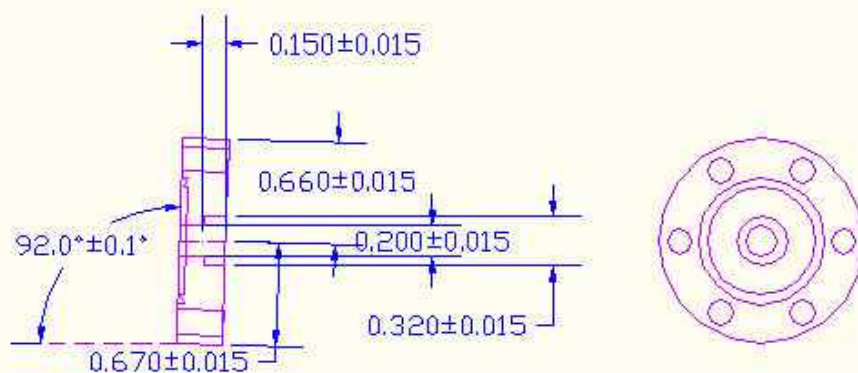


Figure A.6 : Drawing of assembled 689 nm sat. abs. cell.



A&N 133-000 ConFlat
Flange, 2pcs, Drill hole
only



A&N 133-000 ConFlat
Flange, 2pcs, Drill hole
only

Figure A.8 : Drawings of 689 nm sat. abs. cell flanges. See Fig. A.6 to reference the position of each flange. Note that the arm flanges are machined to have a 2° tilt.

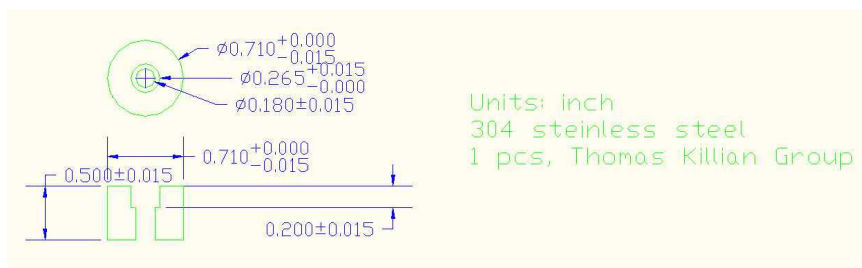


Figure A.9 : Drawing of 689 nm sat. abs. cell attachment piece. See Fig. A.6 for reference.

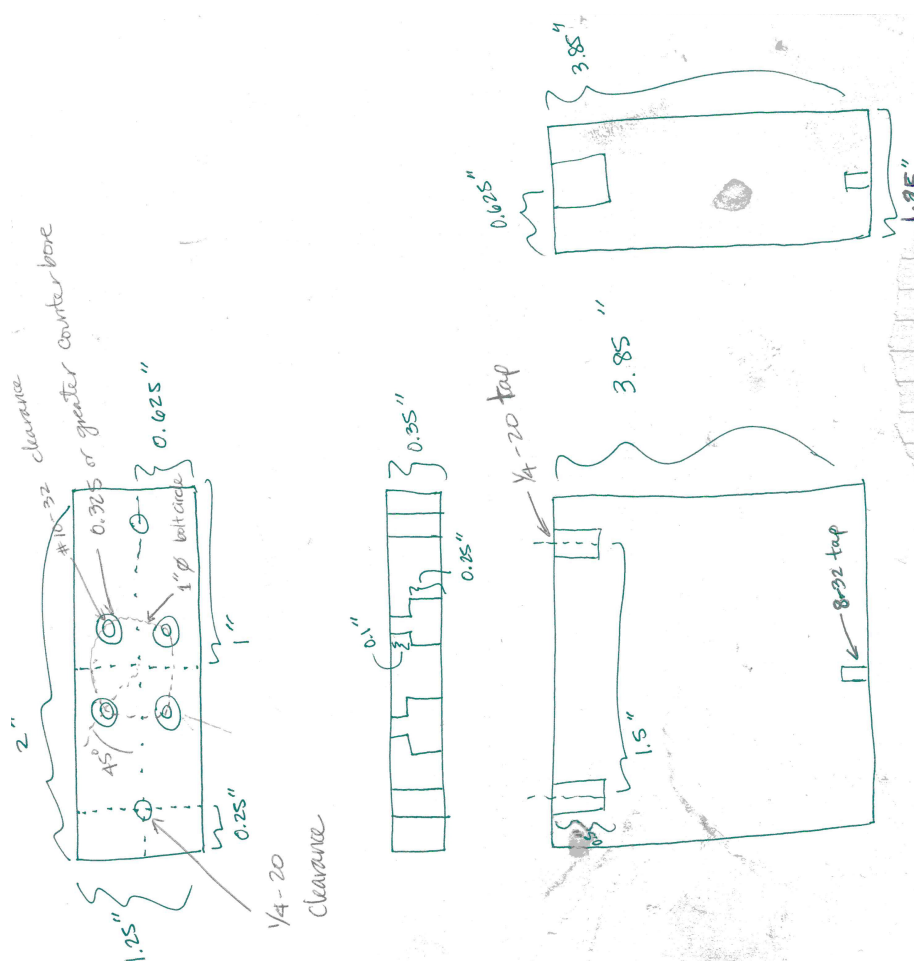


Figure A.10 : Drawing of 689 nm sat. abs. cell mount for the Swagelok connection. The top Swagelok joint of the sat. abs. cell is connected to a Swagelok extension that serves to translate its other end (a Swagelok valve) closer to the table. This valve is the one attached to the mount depicted in this drawing.

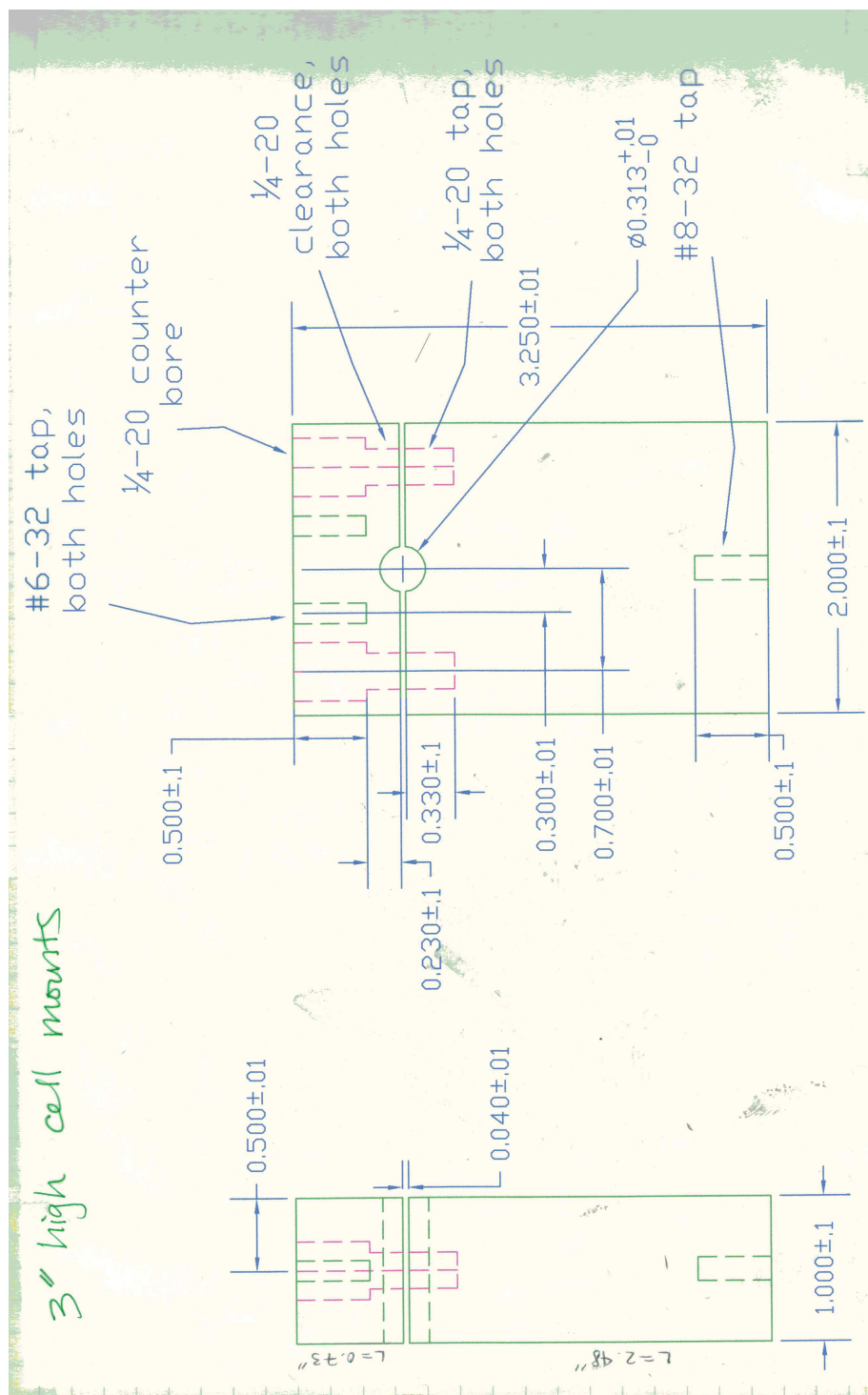


Figure A.11 : Drawing of 689 nm sat. abs. cell mounts for the cell horizontal arms. Two of these mounts were made from aluminum.

Figure A.12 shows a schematic of the thermocouple and heater placement for the 689 nm sat. abs. cell. As of February 2009, a large Variac served as the power supply for the cell heaters. The heaters are connected in a particular fashion, which I describe here (as of Feb. 2009).

The “Lime green + white” heater is in series with 2 4.8 Ω resistors (in total, measured resistance is 9.2 Ω). In addition, all of the cell heaters* (except for the “White” booster heater) are connected in parallel with each other, and the total measured parallel resistance is 9.2 Ω . The “White” booster heater is not connected to the power supply at all, while all the other heaters are. I also measured the temperature of the cell thermocouples when the Variac setting was at 46% (this is the low/off power supply position) and Table A.2 lists these values. As stated earlier, changing the Variac to the high/on position, along with sufficient time for the cell to heat up (about 2 hours) and the laser powers specified in Table A.4, produce an atomic error signal of about 3 V_{pp} .

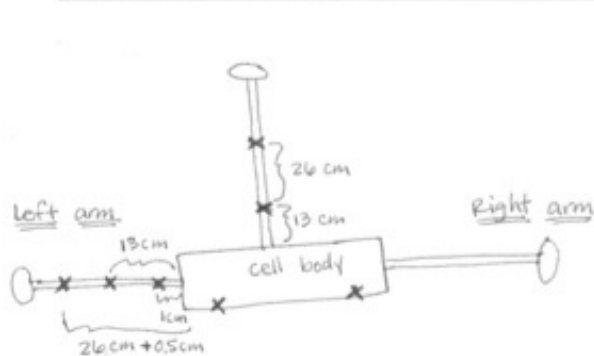
In Fig. A.13 through A.15 I include images of my lab notebook entries recorded during the period of the cell’s assembly, with the image found in Fig. A.13 explaining the cell heaters and thermocouples placement. Two thermocouples for the cell body

*Although all of the cell heaters are connected in parallel as mentioned here, be aware that the Cell body heater was once thought to be shorting due to the very high resistance measured at one point in January 2004. For a while this heater was not used and the system instead relied on the Arm and Booster heaters to heat the cell body. It is unclear from my notes when the Cell heater began to work/was connected in parallel with the other heaters.

HEATER AND THERMOCOUPLE CONFIGURATION

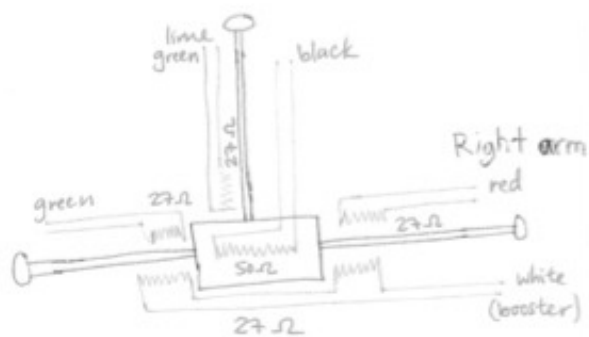
(Natali's notebook #2, pg. 55, 59, 76. Original subject to change)

Physical label	Description	Resistance (if applic.)
Lime green + white	Vertical arm heater	27 ohms
Black	Cell body heater	50 ohms
Green + white	Left arm heater	27 ohms
Red + white	Right arm heater	27 ohms
White	Booster heater across side arms	27 ohms
No knots (left)	Thermocouple at cell body	
1 knot (left)	Thermocouple at 1 cm from the cell body	
2 knots (left)	Thermocouple at 13 cm from the cell body	
3 knots (left)	Thermocouple at 26 cm from the cell body	
No knots (vertical)	Thermocouple at 13 cm from the cell body	
1 knot (vertical)	Thermocouple at 26 cm from the cell body	
No knots (right)	Thermocouple at cell body	



Thermocouples placed at the X

THERMOCOUPLE
PLACEMENT



HEATER
PLACEMENT

Figure A.12 : 689 nm sat. abs. cell thermocouple and heater placements.

Thermocouple position	Measured temperature
26 cm from cell body (vertical)	164°
13 cm from cell body (vertical)	233°
At cell body	153°
1 cm from cell body (left arm)	216°
13 cm from cell body (left arm)	262°
26 cm from cell body (left arm)	207°

Table A.2 : Measured sat. abs. cell temperatures. The Variac setting was set to the low/off position when these measurements where taken.

are hard-soldered onto their own small little plate and screwed into the bottom of the cell body via the plates; the other thermocouples were hard-soldered onto the cell itself at the positions shown at the bottom of Fig. A.13.

Fig. A.14 depicts how we wrapped fiberglass around the sat. abs. cell. Besides this notebook image, I noted in my notebook (pg. 61 of notebook 2) that an extra layer of insulation was wrapped around the center/cell body. On top of this insulation came a layer of Magnetic shielding alloy (CO-NECTIC AA Foil from Magnetic Shield Corporation, P/N CF010-15): 12" cylinders were placed on the arms and a 15" cylinder was placed on the vertical arm, all of which were fastened with steel wire. Another layer of fiberglass insulation came on top of this for the horizontal and vertical arms. On top of the insulation just mentioned, Fig. A.15 explains what comes next: more magnetic shielding alloy and fiberglass insulating layers was used, followed by

THE CELL IS DONE 4. Today, we wrapped the 25.2 heaters 6th of December, 2023
 25.2 heater wrapping:

We've wrapped part of this heater on the cell. (Want $\frac{2}{3}$ of arm wrapped)
 The heater

The wrapping, after accommodation & squeezing in, measured ~ 26 cm (marks arm)

* 6' + 1.5' want extra = 7.5'

We squeezed it down &

Left 6' 3" on 1st leg to 20 cm from end (measured the small wire for 6' 3")

Wrapped the remaining heater on top of the first layer (going backward)

Left ~ 2' (close to it) without wrapping. (In reality, we ~~left~~ left ~ 23" on one wire & ~ 28" on the other wire).

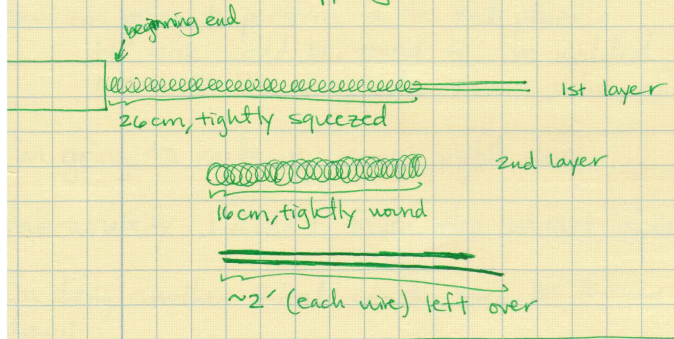
* BUT WE FORGOT TO HARD SOLDER THE THERMOCOUPLES ON THIS SIDE!

To hold the remaining heater down, after finishing the 2nd layer wrap & leaving the 2' extra on each wire, we went under the last two wraps with the remaining wires. Hopefully, this will hold this ~~remaining~~ remaining wire in place. (or "knot")

2nd layer measures (until last wrap): 16cm.

To fix the beginning end, we used a hose clamp on top of fiberglass insulation. The fiberglass was only of one layer

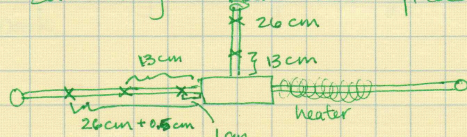
Therefore, the wrapping is like so:



* We're going to hard solder the thermocouples on the other arm since this arm is done already. Hopefully we will wrap the second arm symmetrically as well.

* We checked for continuity in the heaters. Both arms had a contact spot @ the cell body. We fixed by taking the end & bringing it over the heaters. The vertical bar had two contact spots: one @ cell body & another near the end of the first layer/beginning of second.

The hard solderings have been placed @



We fixed the first-layer-end contact by rotating the heater. The cell body contact was fixed by heater near the end of the first layer/beginning of second.

Figure A.13 : Image 1 from Natali's notebooks with information on the 689 nm sat. abs. cell assembly. This entry describes the placement and wrapping of the cell heaters and the thermocouples placement.

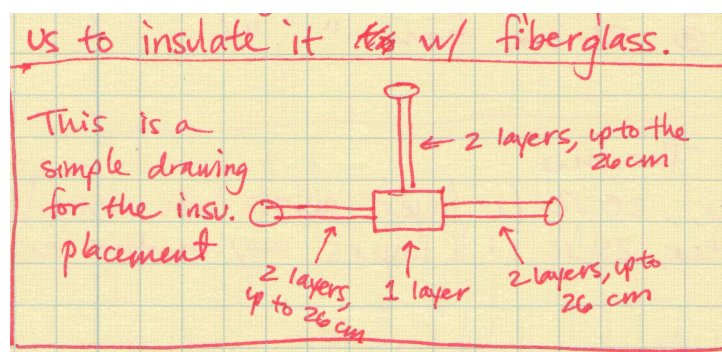


Figure A.14 : Image 2 from Natali's notebooks with information on the 689 nm sat. abs. cell assembly. This entry describes the first round of thermal insulation placed on the cell.

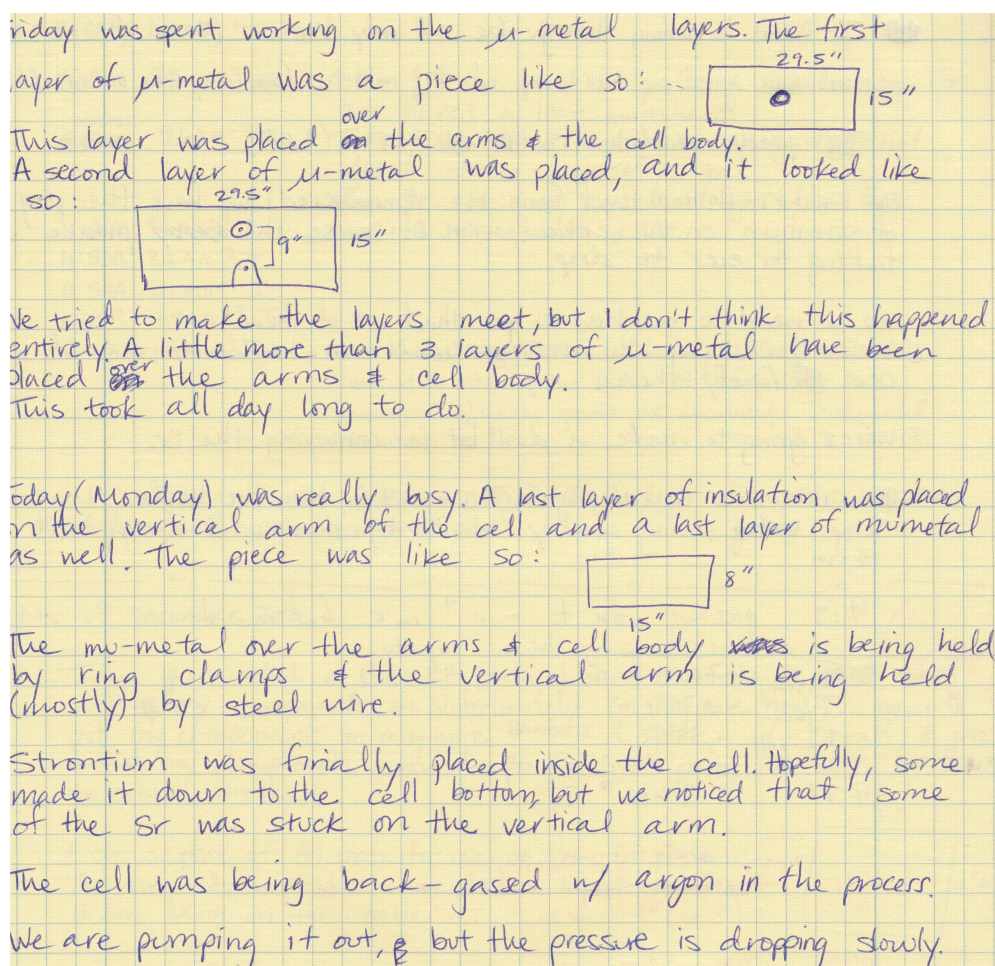


Figure A.15 : Image 3 from Natali's notebooks with information on the 689 nm sat. abs. cell assembly. This entry describes the final round magnetic shielding and fiberglass insulation wrapped on the cell.

AOM	FREQ.	ORDER	ISOTOPE
Sat. abs.	180 MHz	-1	^{88}Sr
Sat. abs.	147.64 MHz	1	^{86}Sr
red MOT	90 MHz (about)	-1	^{86}Sr and ^{88}Sr

Table A.3 : 689 nm saturated absorption and red MOT AOM frequencies (as of January 2009). The 689 nm AOM order and frequency is fixed near -90 MHz (-1 order for this AOM), while the sat. abs. AOM order and frequency change depending on which Sr isotope one wants to trap, as listed in this table.

loading it with Sr and back-filled with Argon gas.

The current frequencies (as of May 2010) for the sat. abs. beam AOM (Crystal Technology P/N 3200-124) and 689 nm MOT beam AOM (Isomet P/N 1205C-2) are listed in Table A.3 (see Sec. 2.3.2 and Fig. 2.10, 2.11 and A.2 for reference). That is, depending on what isotope we choose to trap (true only for ^{86}Sr and ^{88}Sr), we change the sat. abs. AOM frequency and diffraction order so that the 689 nm MOT beams frequency can shift accordingly and trap the desired isotope.

Recall the equation for the main master 689 nm laser frequency f_L with respect to the ^{88}Sr atomic transition frequency (see Sec. 2.3.2): $f_L = f_0^{88} - \frac{\delta_{satabs}}{2}$. When our

desire is to trap ^{86}Sr :

$$\begin{aligned}
 f_L &= f_0^{88} - \frac{\delta_{satabs}}{2} \\
 &= f_0^{88} - \frac{147.64}{2} \\
 &= f_0^{88} - 163.82 + 90 \\
 &= f_0^{86} + 90
 \end{aligned}$$

where the isotope shift between ^{86}Sr and ^{88}Sr for the 689 nm transition $\Delta_{88-86} = f_0^{88} - f_0^{86} = +163.817$ MHz. When trapping ^{88}Sr , $\delta_{satabs} = -180$, so that $f_L = f_0^{88} + 90$. The MOT beams are at a frequency $f_{MOT} = f_L + \delta_{MOT} \simeq f_L - 90$, such that both of these situations shift the 689 nm MOT beams to the right frequency to trap the desired isotope. The 689 nm sat. abs. AOM is driven with the corresponding voltage regulator circuit that produces the frequency needed to trap the desired isotope (each circuit has different voltage ranges, and hence, obtainable frequencies from the sat. abs. VCO (Minicircuits P/N ZOS-300)).

To trap ^{87}Sr , the sat. abs. system is locked to the ^{88}Sr error signal, and the laser frequencies for the ^{87}Sr trap and stir beams are shifted with AOMs (see [75] and Sec. A.3). When trapping ^{84}Sr , we actually send the output beam of ^{87}Sr slave #1 (i.a. Fig. A.2) to the cat's eye setup mentioned in Sec. 2.3.2. The cat's eye shifts this beam's frequency, which is then sent to the sat. abs. fiber, coupled in, and eventually serves as the sat. abs. cell beam. AS OF MAY 2010: The ^{84}Sr AOM frequency used to shift the aforementioned cat's eye AOM (shown in Fig. 2.10) is produced with a refurbished ZOS-300 VCO driven with a voltage regulator circuit (P/N LM7805).

Dither amplitude	$2.04 V_{pp}$
Dither frequency	7.69 kHz
Dither frequency offset	$0 V_{pp}$
Pump beam power	$53 \mu\text{W}$
Probe beam power	$8.7 \mu\text{W}$
Total power through fiber	$233 \mu\text{W}$
Total power before AOM	$224 \mu\text{W}$

Table A.4 : Characteristics of saturated absorption AOM setup (as of Sept. 2008). A frequency dither is added to the pump beam through the sat. abs. AOM and this table lists each component's different magnitudes. The dither frequency was measured with an oscilloscope while the function generator markings indicates that the frequency is close to 7 kHz. Both pump and probe beam powers measured right before traversing the absorption cell. Total power out of fiber measured after the 500 mm lens found about 1 in. in front of fiber output coupler. The fiber output's power was not optimized for this measurement.

This AOM has a 200 MHz center frequency.

In order to produce an absorption error signal, the sat. abs. optical/RF system modulates the sat. abs. laser light via an AC dither added to the DC voltage supplied to the ZOS-300 VCO. Since the pump beam becomes the diffracted beam of the sat. abs. AOM (Fig. 2.11) the frequency dither gets written on this beam's original frequency, according to the parameters in Table A.4. The probe beam, after having traversed the sat. abs. cell, falls on a photodiode (Thorlabs P/N DET110). This photodiode has a load resistance of $120 \text{ k}\Omega$ and its output goes to a lock-in amplifier (PerkinElmer 7265 DSP). The use of a lock-in makes changing between isotopes rather easy compared to how it would be if there was a mixer-low pass filter system, in my

AC gain	30 dB
Reference signal phase (^{88}Sr)	-162.98°
Reference signal phase (^{86}Sr)	17.02°
Sensitivity	1 mV
Time constant	640 μs

Table A.5 : PerkinElmer 7265 Lock-in amplifier settings. These settings, together with the magnitudes listed in Table A.4 and the bias magnetic field produced by the external wire coils (see text) produce an atomic error signal of about $3 V_{pp}$.

opinion.

The current settings (as of September 2008) of the lock-in amplifier used to produce our atomic error signal are found in Table A.5. It is common to change the phase of the error signal slightly to optimize the error signal size once in a while — the change is usually $< 2^\circ$. It is also important to change the polarity (change the error signal phase by 180°) of the ^{86}Sr error signal with respect to the ^{88}Sr signal (see Table A.5).

To separate the magnetic sublevels m_J of the 3P_1 state we apply a static magnetic field produced by wire coils running parallel to the long sat. abs. cell. 75 V is applied to the wire coils, requiring 238 mA of current. The 689 nm light polarization has to be aligned to the axis of this magnetic field (vertically polarized light coming out of the sat. abs. fiber) to avoid exciting “cross-over” transitions produced when the unaligned light polarization drives $\Delta m_J = \pm 1, 0$ transitions[†]. These settings along

[†]Mi Yan demonstrated this effect by changing the sat. abs. beam polarization before being

Cavity Characteristics	Theoretical	Measured
Free Spectral Range (FSR)	1 GHz	999.3 MHz
FWHM (Δf)	300 kHz	≤ 490 kHz
Finesse (F)	3000	≥ 2040
Mirror reflectance	N/A	$\geq 99.8\%$

Table A.6 : HF Fabry-Perot cavity theoretical and measured characteristics. The FSR “measured” value is determined from the mirror spacing via the relation $\text{FSR} = c/2d$, where $d = 15$ cm and c , the speed of light. See Sec. A.7 for the procedure for our cavity linewidth (Δf) measurement, and the footnote in the same Section that states that the latest linewidth measured was in fact ≤ 365 kHz. The cavity’s finesse F is related to Δf and FSR by $F = \text{FSR}/\Delta f$. If the cavity’s FWHM is taken to be ≤ 365 , then $F \geq 2740$.

with the pump and probe beam powers found in Table A.4 produce a ^{88}Sr atomic error signal of about $3 V_{pp}$.

A.6 High Finesse Fabry-Perot Cavity

We designed and built a high-finesse (HF) Fabry-Perot (FP) cavity in order to narrow the master 689 nm ECDL frequency. This section describes its design and fabrication, as well as other components prepared for its use. Table A.6 lists the characteristics of our HF cavity, and Sec. A.7 describes how we characterized some of its properties, including our procedure for measuring its spectrum full-width at half-maximum

coupled into the sat. abs. optical fiber. PDF scans of his notebook entries on this experiment are shown in Appendix C.

(FWHM).

To design the cavity, we initially calculated what cavity mirror spacing was required to obtain a desirable standing-wave mode distribution in the cavity (i.e., the length of the cavity was chosen such that the TEM₀₀ modes were as conveniently separated as possible from all other strong, higher-order cavity modes denoted by non-zero mode numbers m and n). The resonant frequency, ν , of a mode depends on the length of the cavity and the radius of curvature of the mirrors as [139]

$$\nu = \nu_0 \left[(q + 1) + \frac{1}{\pi} (m + n + 1) \arccos(1 - d/R) \right] \quad (\text{A.2})$$

where ν_0 is the FSR, d is the length of the cavity, R is the radius of curvature of the mirrors, and m , n , and q are integers. Figure A.16 shows the theoretical separation of the transverse modes versus frequency for one FSR of our cavity made with mirrors separated by $d = 15$ cm and $R = 25$ cm (the MatLab script necessary to produce this figure is found at the end of Sec. A.6). The mode amplitudes are plotted as $1/(m + n + 1)$ so that the TEM₀₀ ($m = 0$, $n = 0$) mode has an amplitude of 1.

The actual HF cavity consists of a low-expansion spacer and two mirrors, with a PZT behind each mirror to allow the cavity's length, and hence, the wavelengths that fit in the cavity, to change. This cavity is actually placed inside another can (the external vacuum can - MDC P/N 404053-2003) to separate it thermally from the environment by keeping the inside of the can under vacuum (on the order of 10^{-4} torr) and minimizing the cavity's thermal links to the can (using Viton gaskets). Details of the design and assembly of these components are found below, but technical

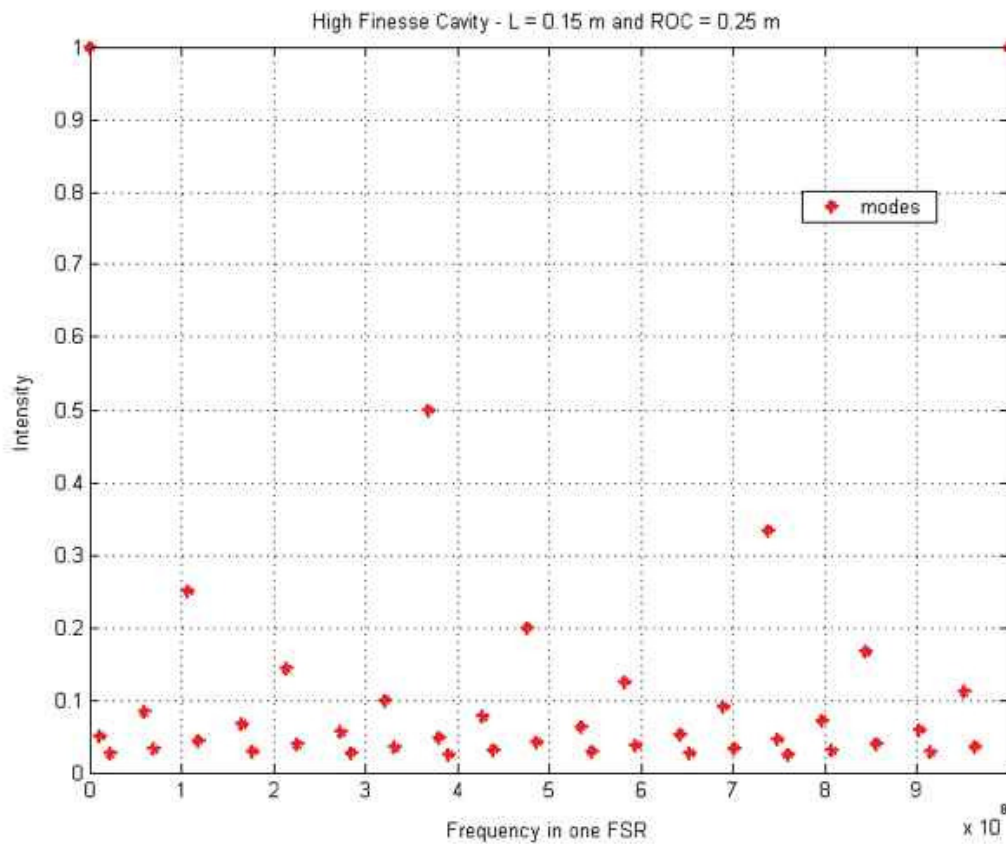


Figure A.16 : High finesse FP cavity calculated cavity modes for original design. A mirror separation of $d = 15$ cm and a mirror radius of curvature $R = 25$ cm were utilized with the MatLab code found at the end of this section to produce this plot. The mode amplitudes are plotted as $1/(m+n+1)$ so that the TEM_{00} ($m = 0, n = 0$) mode has an amplitude of 1, $TEM_{01}=TEM_{10} = 1/2$, etc. The TEM_{00} are separated by one free spectral range in the plot.

illustrations of individual pieces are shown in Fig. A.18 through A.24. Figure A.17 depicts the assembled cavity inside the vacuum can (minus the can's windows).

A 10 ft., 8.8Ω resistance heater (Omega Engineering P/N NI80-025) was wrapped around the vacuum can to enable its temperature control. The goal in temperature controlling the can was to sufficiently stabilize its temperature near room temperature since the internal FP cavity has a weak thermal link to the can through heat conduction via the Viton gaskets slipped onto the Invar spacer (see Fig. A.17). Two thermistors were externally attached to the vacuum can using thermally conductive epoxy (Emerson & Cuming P/N STYCAST 2762 with Catalyst 17M-1): one would be used in conjunction with the temperature controller (Wavelength Electronics P/N HTC-3000) to control the can's temperature and the other would be an additional monitor. At least 2 layers of thermal rubber insulation (from Orion Industries) were wrapped around the cylindrical body of the vacuum can, with 1 layer of the same insulation placed on the "end caps" of the can's cylindrical body. Unfortunately, the vacuum can became contaminated with oil in the summer of 2007 and was eventually opened to clean the internal parts. After this incident the insulation was not replaced entirely and the cavity modes drift slowly over the course of the day. It therefore becomes necessary to change the PZTs' voltage to center the cavity's mode near the desired 689 nm wavelength (at 14504.34 cm^{-1} if the wavemeter doesn't drift).

The external, vacuum can windows are custom-made, assembled from specially-cut $2 \frac{3}{4}$ " flanges (Fig. A.22), the window holder (Fig. A.23), a 0.03" thick washer

P/N	Qty.	Curvature (mm)	Diam. (in.)	Thick. (in.)	High R coat
SMC127-250	6	250 (concave)	0.5	0.25	yes
SMC128-250	2	250 (concave)	0.5	0.375	yes
SMC127-150	4	150 (concave)	0.5	0.25	yes
SMC254-250	2	250 (concave)	1	0.375	yes
SMC254-150	2	150 (concave)	1	0.375	yes
SMC128-300	2	300 (concave)	0.5	0.375	yes
FM127-095-1	2	Flat	0.5	0.375	no
FM254-095-1	2	Flat	1	0.375	no

Table A.7 : VLOC optics order for high-finesse FP cavity. The high reflectance coating for the optics noted as having one (“yes” for the last column) is $R = 99.8\% + 0.13\% - 0\%$ at 689 nm, 0 degrees incidence angle. ALL optics are anti-reflection (AR) coated on one side ($R < 0.25\%$ at 689 nm, 0 degrees incidence angle).

of Teflon sheet that acts as insulation between the 1” optic and window holder (Fig. A.24), the window optics themselves (1” dia., 3/8” thick flat windows from VLOC with P/N FM254-095-1; see Table A.7), and a vacuum seal made from 1 mm diameter Indium wire (Alfa Aesar P/N 11462). Our In circular “gasket”, with a gasket radius of 0.45”, makes a seal between the actual optic and the 2 3/4” flange.

Our FP cavity spacer was machined from a 6” long Invar cylinder (ESPI Stock #KNC8226) so that the mirror separation is $d = 15$ cm. Connections to the cavity’s temperature thermocouple and PZTs (APC P/N 855) to deliver high voltage were made via an electrical feedthrough using vacuum-safe crimp connectors (ISI P/N 9924074) and wires on the inside of the vacuum can, since the can is sealed. The

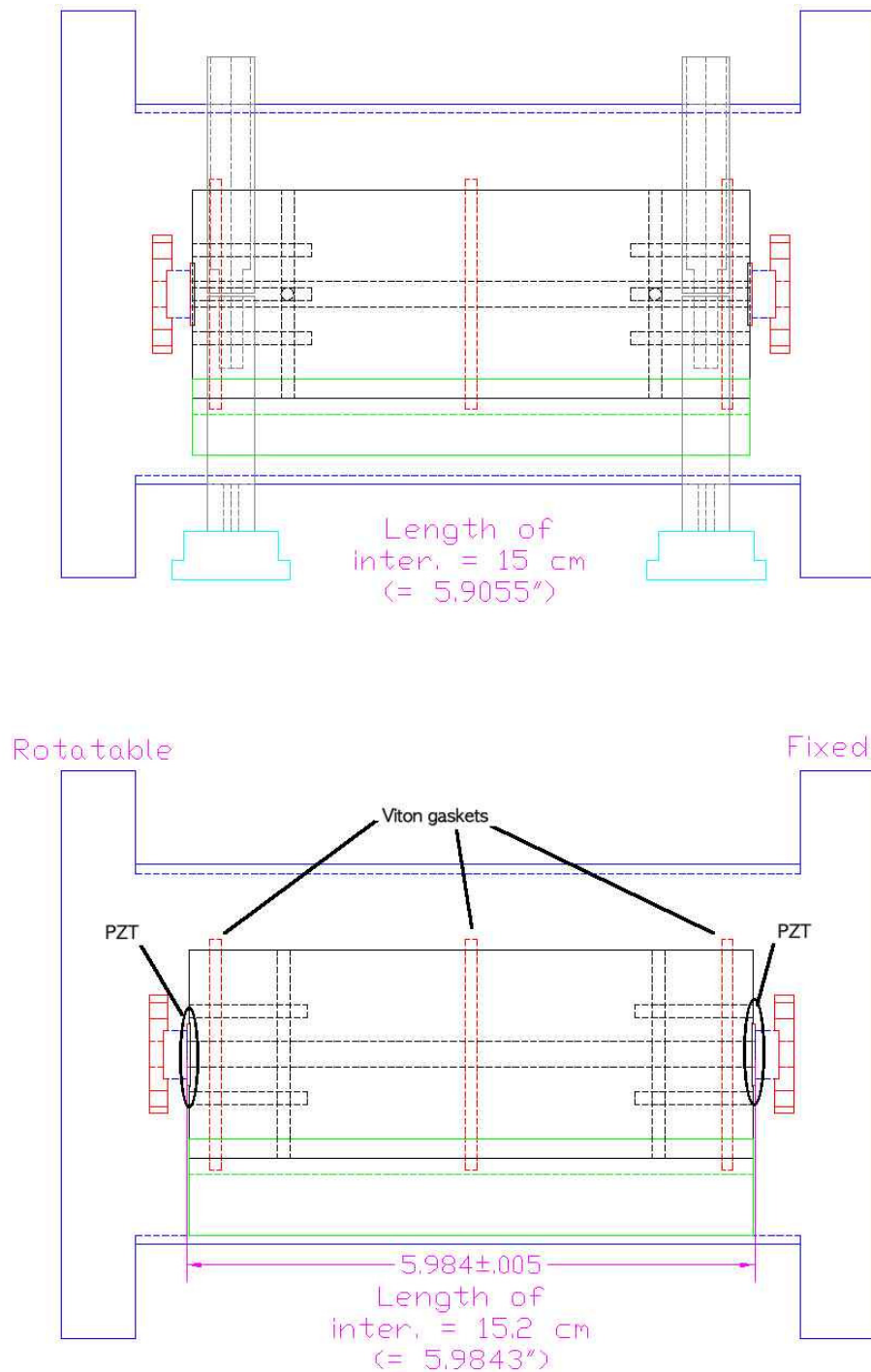


Figure A.17 : Drawing of assembled internal HF cavity. The Viton gaskets' and PZTs' position are pointed out in the version at the bottom of the figure. The version at the top of this figure shows how the vacuum can's external mounts are placed on the can. The sky blue pieces on the bottom of the external can mounts are ordinary optics pedestal posts. 1 1/2" posts were used in our cavity's assembly, although the ones drawn here are 1/2". The larger posts raise the beam height to 4".

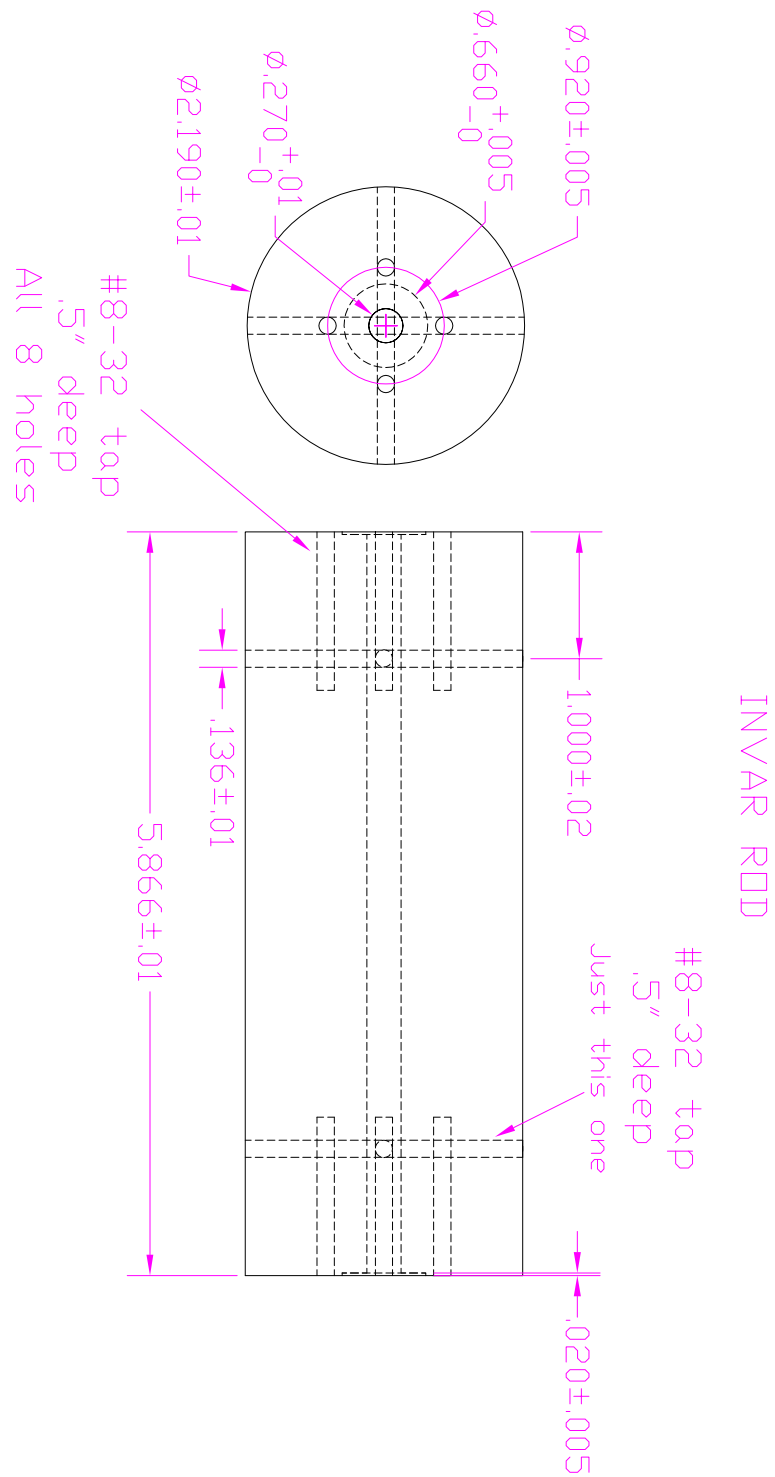


Figure A.18 : High finesse cavity Invar spacer. The Invar spacer served as the ground for the voltage supplied to the PZTs.

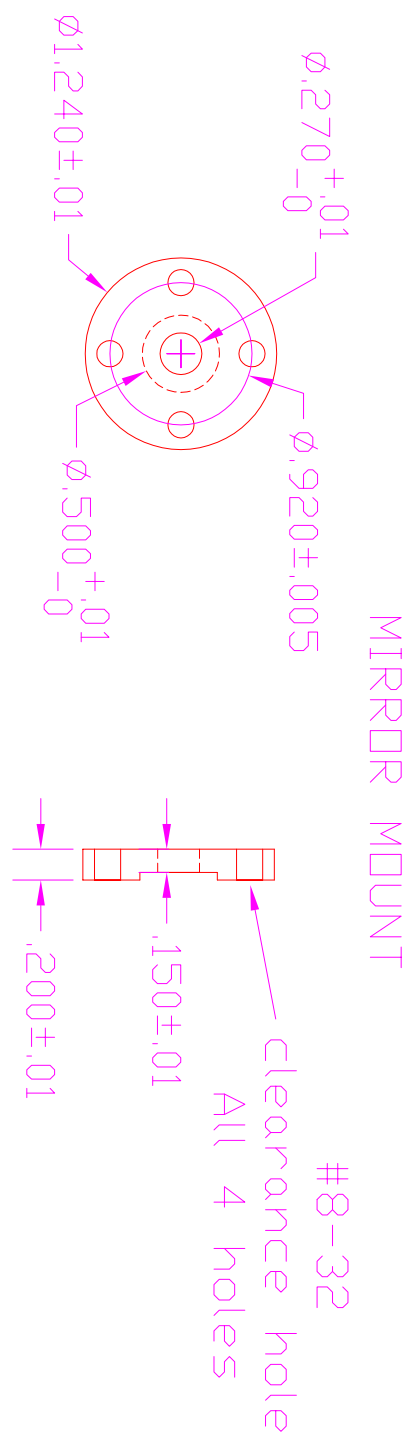


Figure A.19 : High finesse cavity internal mirror mounts. These pieces (2 in quantity) were made from stainless steel.

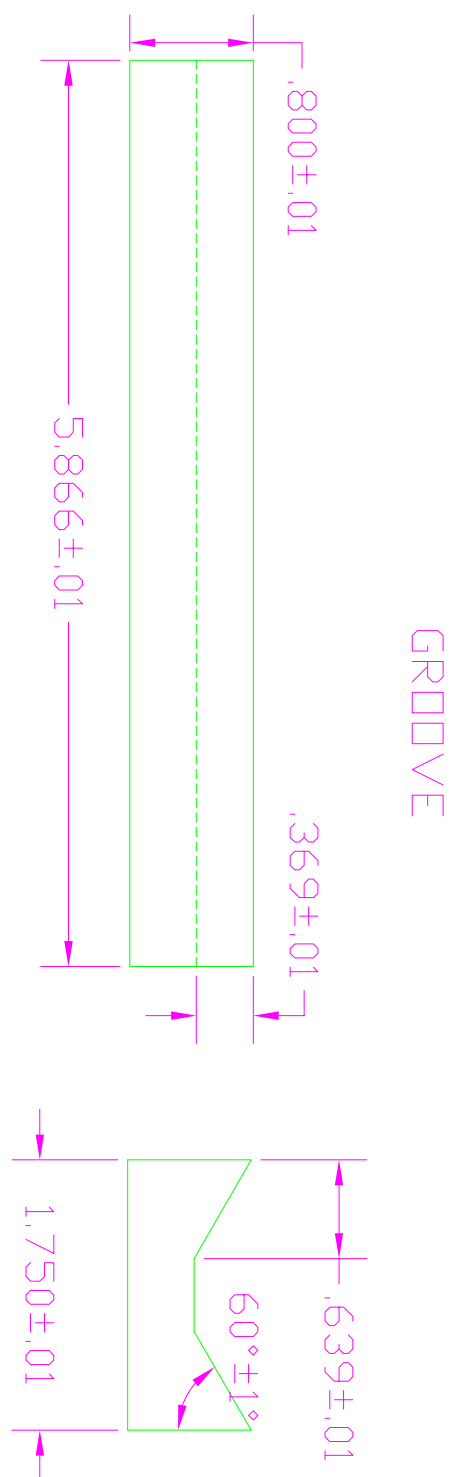


Figure A.20 : High finesse cavity “groove” piece. This piece goes inside the external vacuum can and serves to sustain the assembled FP cavity. One of these pieces was made out of stainless steel.

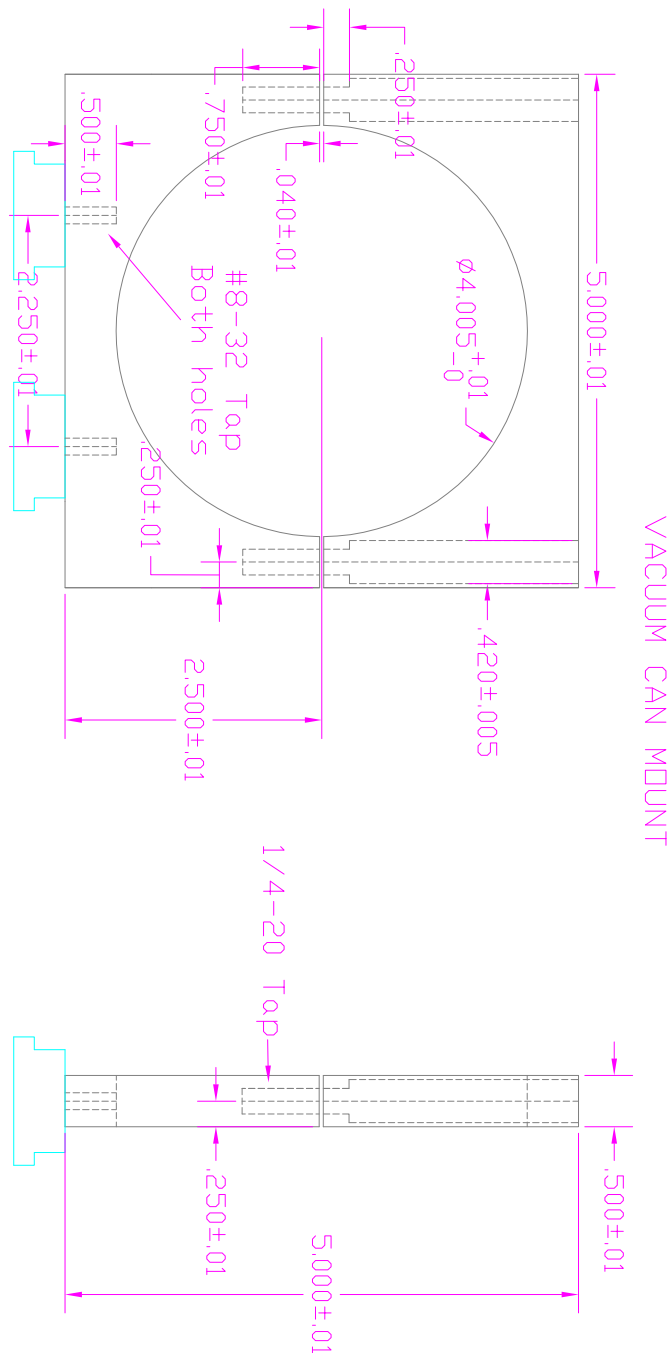


Figure A.21 : Vacuum can external mount. These pieces (2 in quantity) were made from stainless steel. The sky blue pieces on the bottom of the external can mounts are ordinary optics pedestal posts. 1 1/2" posts were used in our cavity's assembly, although the ones drawn here are 1/2". The larger posts raise the beam height to 4".

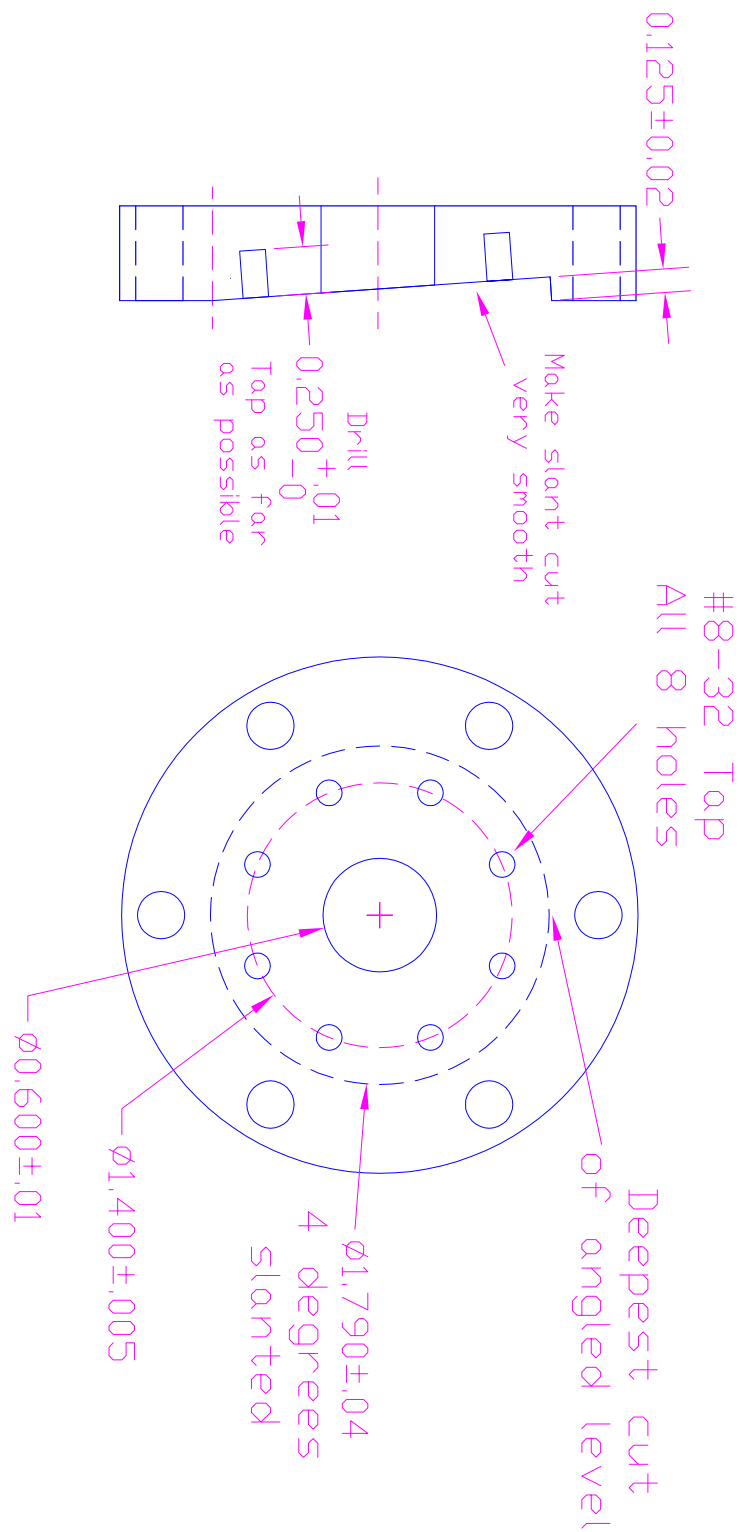


Figure A.22 : External vacuum can window flange. These window flanges (2 in quantity) were made from 2 3/4" blank conflat flanges.

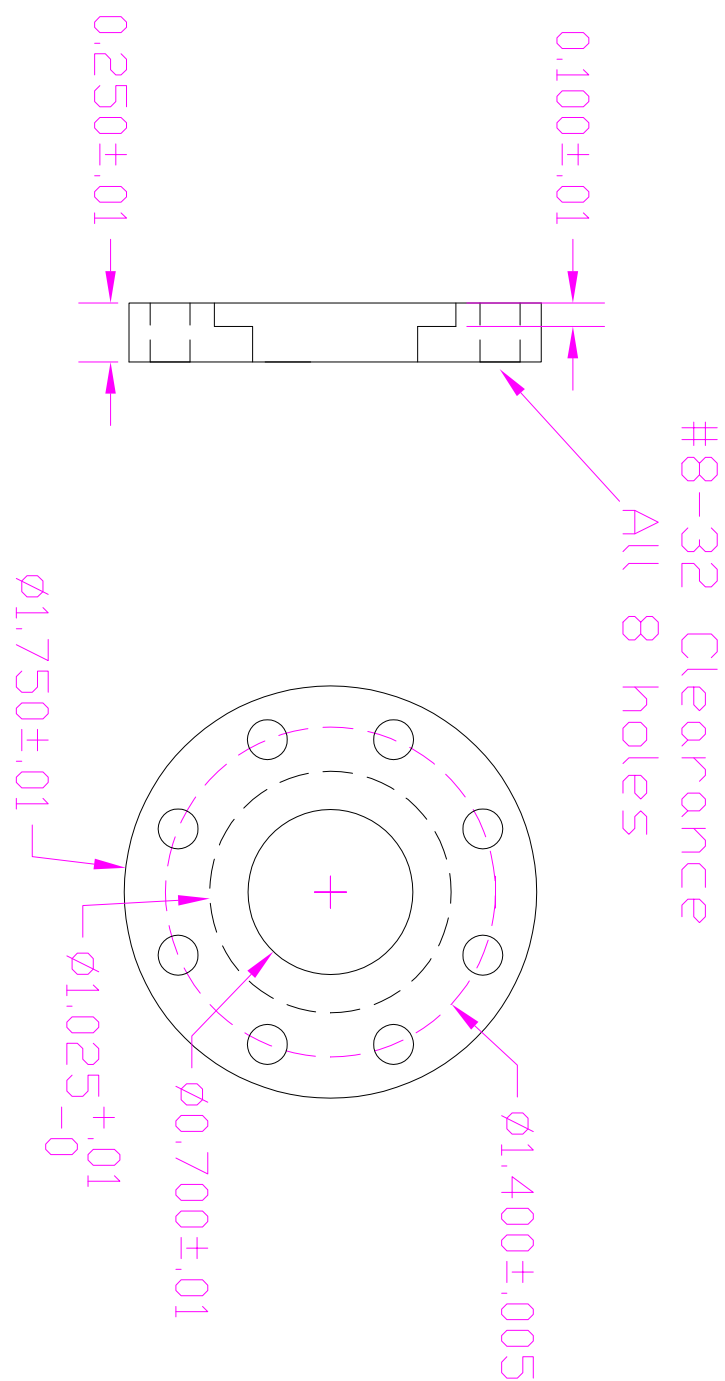


Figure A.23 : External vacuum can window holder. These window holders (2 in quantity) were made from brass.

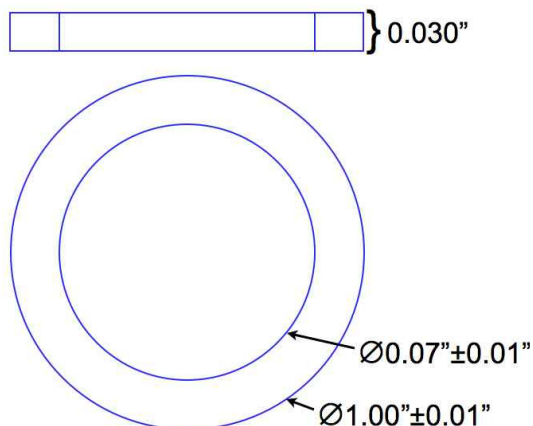


Figure A.24 : Teflon washers for external vacuum can windows. These washers are placed between the vacuum can's window and the window holder (Fig. A.23).

two PZTs allowed us to make very small spacial changes to the FP cavity's mirror spacing (on the order of 100 nm; the normal PZT thickness is 0.04"); they expand proportional to the voltage applied to them (on the order of 100 V). Each PZT is placed between the FP cavity optics and the Invar rod, making contact with both items (see Fig. A.17). We soldered one wire onto each PZT (the side of the PZT with a dot marking on it) to deliver high voltage to them. The other side of the PZT was grounded to the Invar cavity by their mutual contact. We distinguished the different pins of the electric feedthrough with the following markings made ON the feedthrough to keep track of what their wires were being used for:

Pin # 1	1 dot	Ground wire (attached to Invar rod)
Pin # 2	2 dots	PZT #1 (near ground wire attachment onto Invar rod)
Pin # 3	3 dot	PZT #2 (away from ground wire attachment onto Invar rod)

I cleaned all the washable parts that would go inside the vacuum chamber (this excludes the PZTs, Viton gaskets, and wires) before assembling the HF cavity. The cleaning procedure is as follows: 1) scrubbing with a detergent solution, 2) rinsing with distilled water, 3) rinsing with Acetone, and 4) rinsing with Methanol.

689 nm laser light from the ECDL comes to the high finesse FP cavity through a fiber (which currently is a polarization-maintaining fiber, OZ Optics P/N LPC-04-689-4/125-P-1.2-6.2AS-50-1A-3A-2 on both ends). The output coupler at the FP cavity optical setup is a Thorlabs F220FC-B fiber coupler (as of May 2010). This same output fiber coupler was used together with a Thorlabs single-mode fiber (P/N P3-630A-FC-5) when originally building and setting up the FP cavity. The beam profile of the output 689 nm light from this original fiber-output coupler setup informed me that the input light's waist ($w_1 = 257.5 \mu\text{m}$, which is an average of the vertical and horizontal waists measured) was about $d_{input} = 1.21 \text{ m}$ (an average of the two measured waists' positions) inside of the fiber, measured from the face of the output coupler's lens. From Ref. [139] we find that the FP cavity's virtual waist w_2 and waist position $d_{virtual}$ are determined by the following two equations (see Clayton Simien's [140] and Aaron Saenz's [82] masters thesis for more information on the process of coupling into a cavity):

$$w_2^2 = \frac{R\lambda}{\pi} \frac{\sqrt{d(2R-d)}}{2R+d(n^2-1)} \quad (\text{A.3})$$

$$d_{virtual} = \frac{ndR}{2R + d(n^2 - 1)} \quad (\text{A.4})$$

with the parameters becoming $w_2 = 137.2 \mu\text{m}$ and $d_{virtual} = 8.2 \text{ cm}$. The variables in Eqs. A.3 and A.4 are mostly FP cavity parameters: $R = 250 \text{ mm}$ is the cavity mirror's radius of curvature, $d = 15 \text{ cm}$ is the mirror's separation, $n = 1.45542$ is the index of refraction of fused silica (from which the mirror substrates are made of), and $\lambda = 689 \text{ nm}$. (NOTE: the calculations I originally made for the virtual waist and its position used $d = 16.271 \text{ cm}$ which equals the separation of the inner surfaces of the optics plus the mirror's thickness of the input optic. However, this is incorrect because the cavity modes resonate between the high-reflecting surfaces which are on the INNER surfaces of our substrates. Therefore, the thickness of the cavity's input coupler should not be included with the mirror's separation.) By determining w_2 and $d_{virtual}$ I was then able to determine the space needed for my FP cavity external optics, since this is determined by mode matching the light's waist w_1 to the cavity's virtual waist w_2 , as depicted in Fig. A.25. The mode matching equations needed to calculate d_1 and d_2 (Fig. A.25) are

$$d_1 = f \pm \frac{w_1}{w_2} \sqrt{f^2 - f_0^2} \quad (\text{A.5})$$

$$d_2 = f \pm \frac{w_2}{w_1} \sqrt{f^2 - f_0^2} \quad (\text{A.6})$$

where $f_0 = \pi w_1 w_2 / \lambda$. Choosing the mode matching lens $f = 500 \text{ mm}$, I calculated

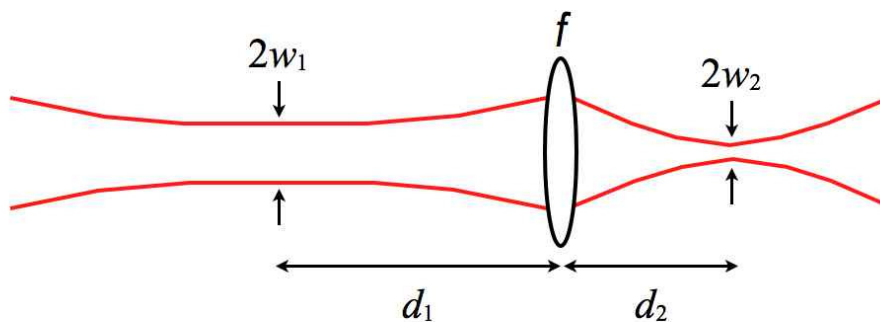


Figure A.25 : Principle of mode matching.

$d_1 = 1.388$ m and $d_2 = 75.23$ cm. With these numbers, I determined what size of optical breadboard I needed in order to place the FP cavity and its necessary external optics. I ordered a Thorlabs breadboard with $12'' \times 18'' \times \frac{1}{2}$ dimensions. Under this breadboard (which contains all the optical components necessary to lock the FP cavity) we placed rubber vibration insulation (McMaster-Carr Super-Soft Neoprene Rubber with 10A durometer) to dampen vibration noise.

I built a fast photodiode to monitor the transmission signal of the HF cavity. The speed of the photodiode need not be more than 10 times the cavity's FWHM, since $\tau = 1/\text{FWHM}$ is the lifetime of the photons inside the cavity (analogous to the lifetime of an atom's excited state). This means that the photodiode was designed to have a bandwidth of $f_{PD} = 10 \times \text{FWHM} = 3$ MHz. The photodiode's circuit diagram is shown in Fig. A.26. Figure A.27 contains a schematic of the HF cavity's optical and RF layout for reference.

In the summer of 2005, we desired to increase the bandwidth of the servo electronics used to lock the 689 nm laser to the HF cavity. To this end I set out to analyze

$C_f = 2.5 - 25 \text{ pF}$
 $R_f = 18 \text{ k}\Omega$
 $R_b = 18 \text{ k}\Omega$
 Op-amp: EL2044
 PD: UDT PIN 5D

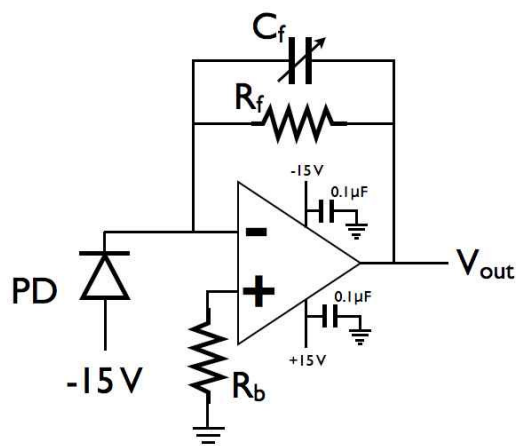


Figure A.26 : High bandwidth photodiode to measure HF cavity transmission signals. The op-amp used in this circuit is an Intersil EL2044 high speed op-amp. A UDT PIN 5D photodiode was used for this circuit. C_f : variable feedback capacitor, R_f : feedback resistor; R_b : non-inverting bias resistor; V_{out} : output photodiode voltage; PD: photodiode.

the gain profile of the fast[‡] path electronics and components, such as the laser's bias tee[§], the device we use to couple the DC laser current from the current supply (ILX Lightwave as of May 2010) to the faster, AC current correction signal supplied by the fast path of the servo electronics. The procedure used to analyze the fast path is simple: the response (output signal amplitude and phase) of the components being tested is measured as a function of the frequency of an input sinusoidal signal that is sent in through the components.

[‡]"Fast" meaning that the AC corrections from this section of the servo circuit are fed directly to the laser diode's current.

[§]Two different bias tees were used/purchased for the 689 nm system. The one currently used (as of May 2010) is from Picosecond Pulse Labs (P/N 5546-107) and the second one (unused yet) is from Thorlabs (a VERY small one; P/N T1G).

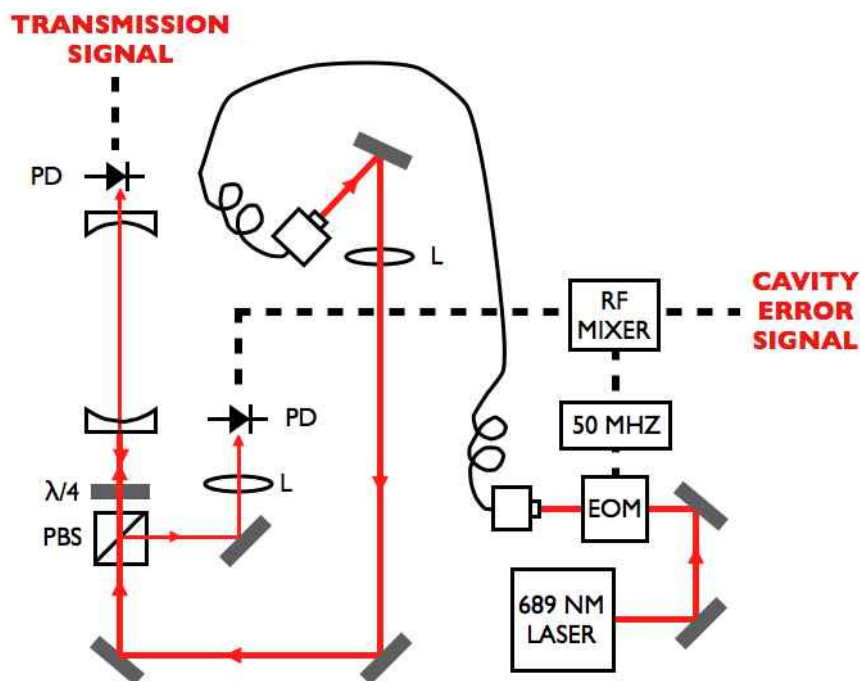


Figure A.27 : Schematic of HF cavity optical and electronic components layout. Dashed lines demonstrate electrical and RF signals, while solid red lines depict optical beam paths taken. A beam from the 689 nm master laser traverses an EOM and is coupled through a polarizing-maintaining fiber. The output beam from the fiber is guided by a series of mirrors to the HF cavity formed by two partially-reflecting mirrors (see text). The lens traversed by this lens serves as the cavity-coupling lens. A small amount of the input beam is reflected off the back face of the first partially-reflecting mirror and is rejected by the PBS cube in the original beam's path. The reflected beam's intensity depends on the length of the cavity, which changes due to the length change of the cavity PZTs. A photodiode translates this into a voltage, which then goes to a mixer system that produces an error signal eventually used to frequency-lock the 689 nm master laser to the cavity modes. The RF signal frequency applied to EOM/mixer is actually near 48.5 MHz (as opposed to 50 MHz as shown in the drawing). PD: photodiode, $\lambda/4$: quarter-wave plate, PBS: polarization beam splitter, L: lens, EOM: electro-optic modulator.

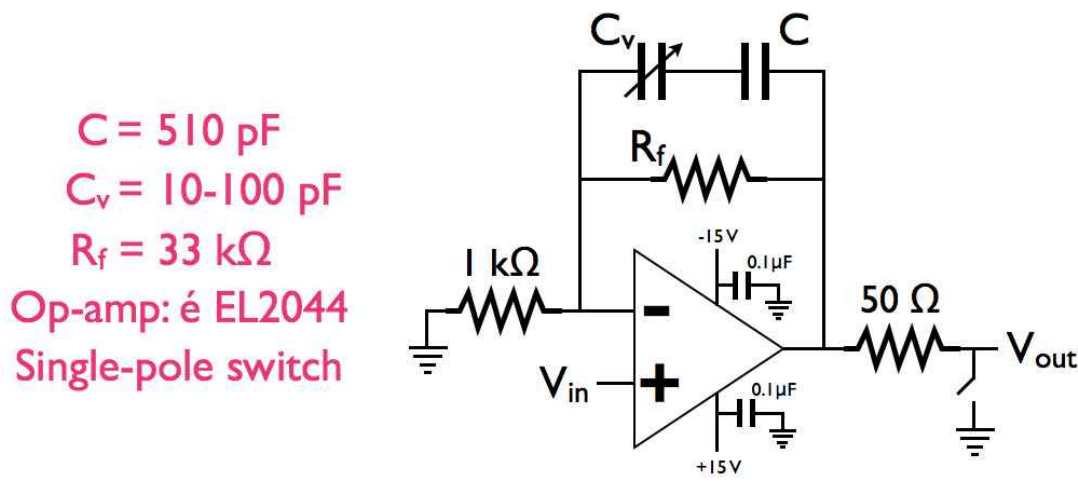


Figure A.28 : Stand-alone active fast path circuit schematic. C_v : variable feedback capacitor, C : feedback capacitor, R_f : feedback resistor; V_{in} : input error signal from HF cavity circuit, V_{out} : fast path output voltage (goes direct to laser diode bias tee).

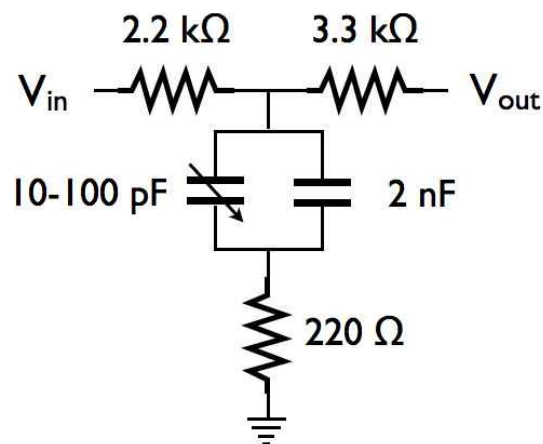


Figure A.29 : Stand-alone passive fast path circuit schematic. V_{in} : input error signal from HF cavity circuit, V_{out} : fast path output voltage (goes direct to laser diode bias tee). Two passive fast paths were built, with the larger one in size (currently used on the master 689 nm laser as of May 2010) lacking the variable capacitor shown in this diagram.

After phase and gain measurements, I built both active and (two) passive stand-alone fast paths[¶]. The circuit for the active fast path is shown in Fig. A.28, and the actual physical dimensions of the circuit board are about 2" × 1". Two passive fast path circuits were built because the smaller one's size was optimal to use with the Thorlabs bias tee. The passive circuit schematic is shown in Fig. A.29. We did not use the Thorlabs bias tee because a special cable (OSMT coaxial connector with characteristic 50 Ω impedance) was needed to use it.

For reference: a beam from the master ⁸⁸Sr laser is sent to the cavity's fiber, as shown in Fig. A.27. After traversing the EOM, this beam's power was measured to be about 100 μW, and the power out of the fiber is about 60 μW. This amount of power out of the fiber gives 29 mV on the DC monitor of the HF cavity's photodiode (used to produce the error signal — see Fig. A.27).

[¶]The two passive circuits differ in their size (the larger one is currently used on the 689 nm laser as of May 2010) and that the larger circuit lacks the variable capacitor shown in the circuit diagram of Fig. A.29.

```

%%%%%%%%%%%%%%%%%%%%%%%%%%%%%%%%%%%%%%%%%%%%%%%%%%%%%%%%%%%%%%%%%%%%%%%%MATLAB CODE%%%%%%%%%%%%%%%%%%%%%%%%%%%%%%%%%%%%%%%%%%%%%%%%%%%%%%%%%%%%%%%%%%%%%%%%
clear all;
%Necessary constants
c = 2.9979*10^8;
lambda = 689*10^(-9);
R = .99;

%Length and Radius of Curvature of cavity
L = 15*10^(-2);
%Rad = 400*(15/25)*10^(-3);
Rad = 25*10^(-2)

%Free Spectral Range of cavity
FSR = c/(2*L);
.5
%Num. of Nodes of Axial Standing Wave Pattern
q0 = (2*L)/lambda - 1;
q = q0;

%Starting #'s of the transverse integers
m = 0; n = 0;

%Num. of resonant frequencies of the mode (0,0) fit in the FSR
Num= ((q + 1) + (1/pi)*(m + n + 1)*acos(1 - (L/Rad)))
NUMBER = floor(Num)

%Frequency to start and end with
%START = NUMBER*FSR;
START = FSR*((q0 + 1) + (1/pi)*(1)*acos(1 - (L/Rad)));
S = START;
FINISH = START + FSR;

%Freq:= FSR*((q + 1) + (1/Pi)*(m + n + 1)*ArcCos[1 - (L/Rad)])
%Inten:= (1/(m + n + 1))

q = q0 - 10;
k=1;
%M=zeros(20,2);
%for q=q0-10:10 the original
for q=q0-20:q0+10
    for m=0:40
        for n=0:40
            if m + n < 41
                Inten(k,1)=(1/(m + n + 1));
                Freq(k,1)=FSR*((q+1)+(1/pi)*(m + n + 1)*acos(1 - (L/Rad)));
                k=k+1;
            end
        end
    end
end
end

%Plotting.....
figure(1)
subplot(1,1,1)
h = plot((Freq-S),Inten);
set(h, 'LineWidth',2,{'LineStyle'},{'*'})
set(h,{'Color'},{'r'})
axis([0 FSR 0 1])
grid on
xlabel('Frequency in one FSR')
ylabel('Intensity')
legend(h,'modes',0)
title(['High Finesse Cavity - L = ',num2str(L),' m and ROC = ',num2str(Rad),' m'])

```

A.7 Characteristics of our 689 nm HF FP cavity

Our desire was to measure the HF cavity’s FWHM, which gives us a measure of the lifetime of photons inside the cavity. The photon bounce number b equals the number of round trips the cavity photon makes before there is a $1/e$ probability of it being lost. The bounce number is, therefore, equal to the inverse of the losses of the cavity:

$$b = \frac{1}{2(1 - R)}, \quad (\text{A.7})$$

where R is the reflection of the cavity mirrors ($R = 0.998$). The lifetime of the photons inside the cavity (the round trip time) is therefore the amount of bounces the photon makes divided by the FSR:

$$\tau = b * \frac{2L}{c}. \quad (\text{A.8})$$

The cavity length is denoted L , $c = 2.998 \times 10^8$ m/s. This gives $\tau = 0.25 \mu\text{s}$.

In measuring the HF cavity FWHM, we chose to scan the 689 nm laser PZT^{||} around the correct laser/cavity mode so that the laser’s frequency ramp served as a “mechanical chopper” that swept over the photon buildup time of the cavity. Hence, monitoring the cavity’s light transmission gave us a measure of the buildup and decay of photons inside the cavity. We utilized the high bandwidth photodiode described in Sec. A.6 for this cavity ringdown measurement.

^{||}NOTE: A Littrow ECDL was used for this measurement — this type of laser was the only type available at the time (January 2004). See Sarah Nagel’s master’s thesis [141] for an explanation about this laser.

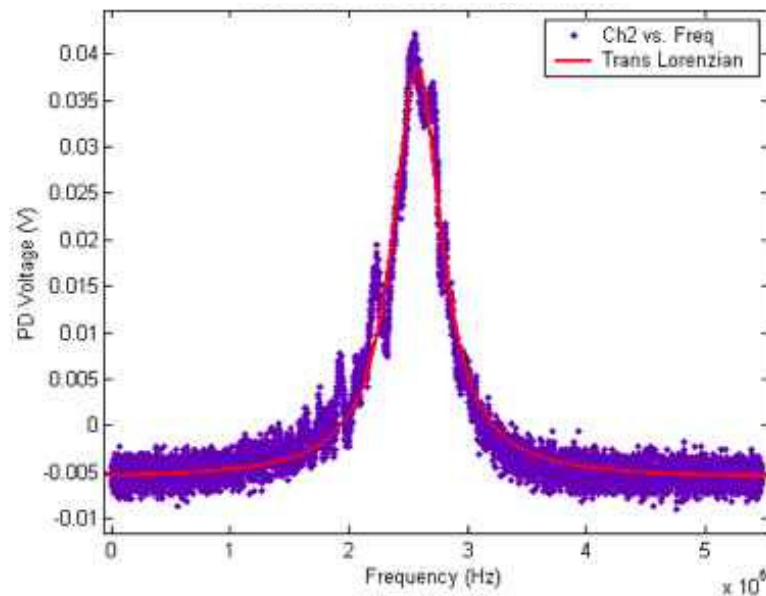


Figure A.30 : HF cavity ringdown measurement at 16 Hz frequency sweep. To perform this measurement, we swept the Littrow extended-cavity laser frequency (by ramping the grating's PZT) over a cavity transmission trace. A Lorentzian function fit to the trace gave $\text{FWHM} = 496.3 \text{ kHz}$.

We took light transmission measurements by ramping the laser's PZT at 16 and 200 Hz. Fitting the 16 Hz trace with a Lorentzian of the form

$$P(\nu) = \frac{P_0}{1 + 4\left(\frac{\nu - \nu_0}{\Gamma}\right)^2} \quad (\text{A.9})$$

gave the fit shown in Fig. A.30 and a value of $\text{FWHM} = 496.3 \text{ kHz}^{**}$, translating into

^{**}On pg. 61B of Natali's notebook #4, there is a note stating that the HF cavity's linewidth was measured with a Littman-Metcalf extended-cavity laser and the measurement gave a linewidth measurement of $\text{FWHM} \leq 365 \text{ kHz}$. This measurement entry in the notebook was written on August 5, 2005. No details on the measurement are given, but they might be recorded in the extended-cavity laser's notebook found in the laboratory. The ones that seemed to have performed the measurement were Andrew Traverso and Tom Killian.

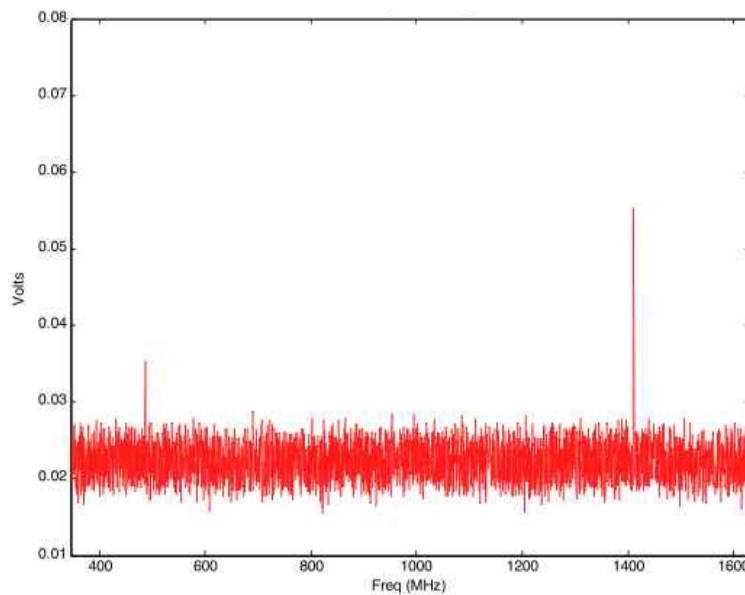


Figure A.31 : HF cavity Free Spectral Range (FSR) measurement. The original 689 nm Littrow extended-cavity laser and fast photodiode were used in this measurement.

a photon lifetime of $\tau = 1/(2\pi \times \text{FWHM}) = 0.32 \mu\text{s}$. This measurement is an upper limit on the cavity linewidth because the measurement depends on the properties of the measurement instruments (particularly the photodiode) and the stability of other components in the measurement loop (such as the laser), which can cause a broadening of the transmission signal.

To measure the cavity's FSR, one measures the frequency/voltage gain of the cavity's PZT voltage ramp and then determines what voltage is required for the cavity ramp to scan a full FSR. When originally built, the cavity PZTs were capable of ramping the cavity length to observe a full FSR. Unfortunately this capability has been disabled for a couple of years now, and the HF cavity is currently set up so that the PZTs (or is it only one of them?) receive a voltage that is the sum of a DC voltage

(from about -15 V to +350 V) and a ~ 20 V ramp. This voltage signal is enough to ramp the cavity about 50 MHz, enough to observe the main signal carrier of the error signal and lock the 689 nm laser to the HF cavity. Figure A.31 presents one of these measurements, which roughly puts the FSR around 950 MHz. This measurement was also made using the original Littrow extended-cavity laser and the high bandwidth photodiode. It also depends on the stability of components in the measurement loop, such as the laser and the cavity.

A.8 922 nm laser sources and 461 nm cavities

As briefly mentioned earlier (see Sec. 2.2.1), a 922 nm diode laser serves as our primary IR laser (we frequency-double 922 nm light to produce 461 nm light). Appendix B contains a Status Report of this laser when it failed in 2007. Fortunately, this diode laser has not failed since the incident recorded in this Status Report.

We amplify our 922 nm light by Tapered Amplifiers (TAs) to increase our available 461 nm power. I assembled a couple of our TAs^{††} and am including in this section details of their assembly that were unique to the Neutral Atom team's TAs. Relevant remarks about the 461 nm cavities for the neutral atoms setup are also included.

Our 922 nm TAs (as of May 2010) were purchased from EagleYard Photonics (P/N EYP-TPA-0915-01500-3006-CMT03-0000). The housing of the TA is the diode's AN-

^{††}The one for the Zeeman slower setup, named TA 2, and the TA once used to amplify the 922 nm seed beam from the Ti-Sapphire, named TA 0.

ODE, while the mounting wire is the diode's CATHODE. The physical assembly of the TAs is actually a design created in the Killian lab, along with the details of how to mount the TAs and the input and output coupling lenses. These techniques are described in Sarah Nagel's dissertation [74].

We use laser diode drivers from Wavelength Electronics (P/N MPL-2500) to power the TAs. A small muffin fan helps cool the TA diode drivers (it is mounted on top of the driver). We also include in the current path a semiconductor diode protective circuit, an arrangement of diodes that 1) limit the amount of forward-bias voltage across the TA diode and 2) provides any reverse-biased current a path to flow through without going through the TA diode itself. A schematic of the protective circuit is shown in Fig. A.32. The six forward-biased diodes clamp the forward-bias voltage at about 3.6 V (about 0.6 V voltage drop for each diode), while the reverse-biased diodes allow the reverse current to flow through THEM. The faster, lower-current rated 1N4148 diodes were used because of their quick response time during a potential current surge to protect the TA diode.

For reference (as of Dec. 2008): The diode driver for the Zeeman slower beam's TA was powered with 12 V for an ordinary power supply. When the TA was switched on, 2.06 A of current were used, and 0.53 A were used when the TA was switched off (the muffin fan also turned off).

The Zeeman slower 461 nm doubling cavity for the Neutral Atom setup has undergone a couple of overhauls. The latest one, where a home-made doubling cavity

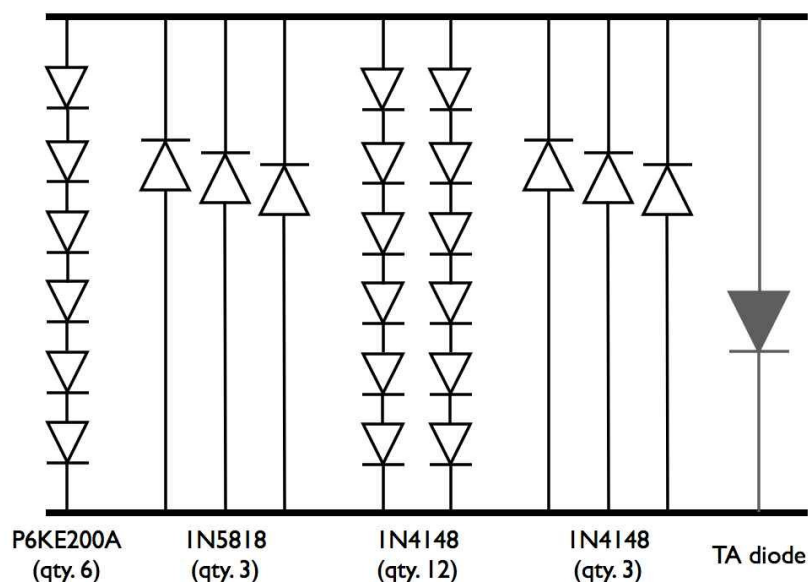


Figure A.32 : TA protective circuit. The six forward-biased diodes clamp the forward-bias voltage at about 3.6 V, while the reverse-biased diodes allow any reverse current a path to flow through without traversing the diode itself.

mount (designed by Tom Killian and Aaron Saenz) was replaced by a commercial two-axis motion mount (OptoSigma P/N 122-0090), occurred in December 2008 and accomplished mostly by Brian DeSalvo. A 40 mm input coupler lens couples the 922 nm light into the Zeeman cavity. The doubling cavity crystals for both the MOT and Zeeman slower doubling cavities are KNbO_3 crystals (purchased from VLOC), $3.0 \text{ mm} \times 3.0 \text{ mm} (\pm 0.1 \text{ mm}) \times 5.00 \text{ mm} (+ 0.5/- 0.2 \text{ mm})$ in dimensions, angle cut for doubling 922 nm light at room temperature. One end of the crystal is anti-reflection (AR) coated for both 922 and 461 nm. The other end has a high-reflection coating (HR) for both 922 and 461 nm. The 922 nm reflectivities are more crucial on both sides. The HR coating are the same as in VLOC order # 16390 and PO#

40823 of January 2001 so that the nodes of the 922 nm standing wave line up with nodes of the 461 nm standing wave in the crystal.

When Brian finished with this Zeeman slower assembly, he was successful at getting about 115 mW of 461 nm light out of the doubling cavity with about 260 mW of 922 nm in. This amount of 461 nm output power is possible most of the time, but the cavity/crystal seems to suffer from temperature instabilities over time while the cavity remains locked, making it necessary for the operator to move the crystal a bit so that the IR light interacts with a different part of the crystal after some time.

A.9 Details about the 1064 nm multimode laser ODT

This section includes details obtained from Natali's notes pertaining to the setup and details of the 1064 nm (multimode laser) ODT (IPG Photonics YLR-20-LP fiber laser) besides its every-day use, which is a well-known procedure in the lab. Designing our lab's first ODT was a learning experience, since its assembly had not been considered when the neutral atom's experimental chamber and components were set up. There were laser beams we needed to clear with the ODT optics and mounts, structures we needed to go over or under. In the end, the ODT setup was decent, as Tom Killian put it.

The mirror mounts used on the ODT pillars^{‡‡} are CVI 160 series, and they were

^{‡‡}Stainless steel and aluminum pillars were machined for the ODT because the ODT beam needed to rise and enter the experimental chamber at 10.5°.

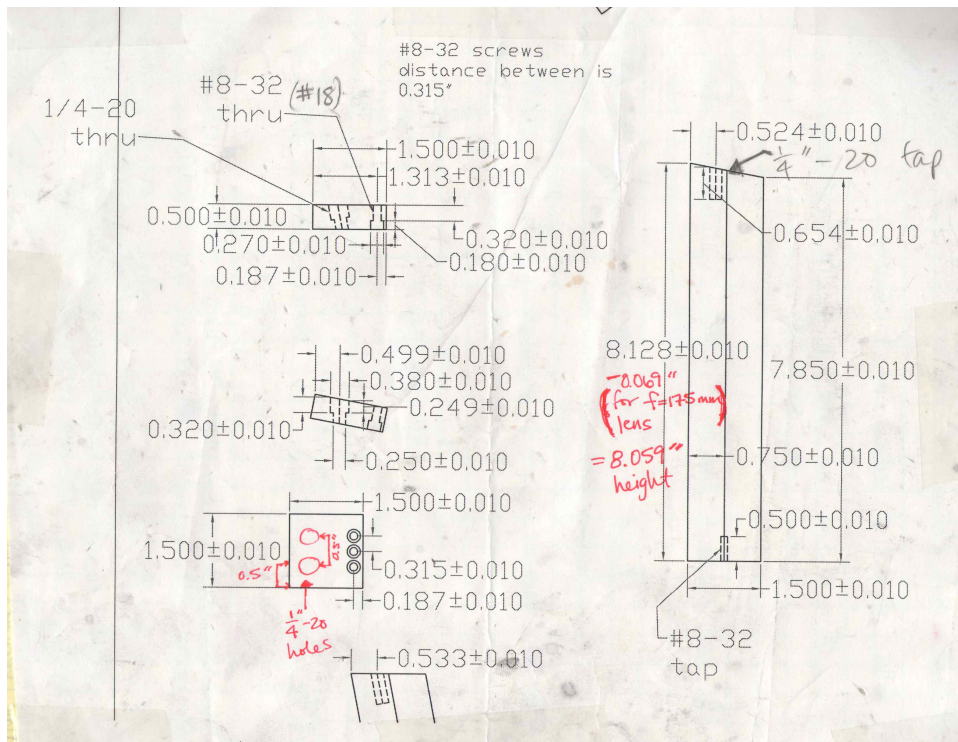


Figure A.33 : Pillar for first ODT beam focusing lens. Part of the post had to be milled off to allow the magnetic trim coils to remain in their place.

chosen because they were appreciably sturdier than common Thorlabs mounts found in the lab. The 1" focusing (qty. 2) ODT lenses were also mounted on CVI 2-axis translation mounts (P/N 2100). Figure A.33 shows the schematic for the pillar sustaining the first ODT beam focusing lens. The second lens ($f=400$ mm) encountered by the ODT beam collimates the beam while it traverses toward a third pillar that holds a re-focusing lens (also $f=400$ mm) and the beam is re-routed into the experimental chamber to form a crossed dipole trap. The pillars holding the second and third ODT lenses and mirrors are depicted in Fig. A.34 and A.35, respectively. The three lenses described here are achromatic doublet lenses.

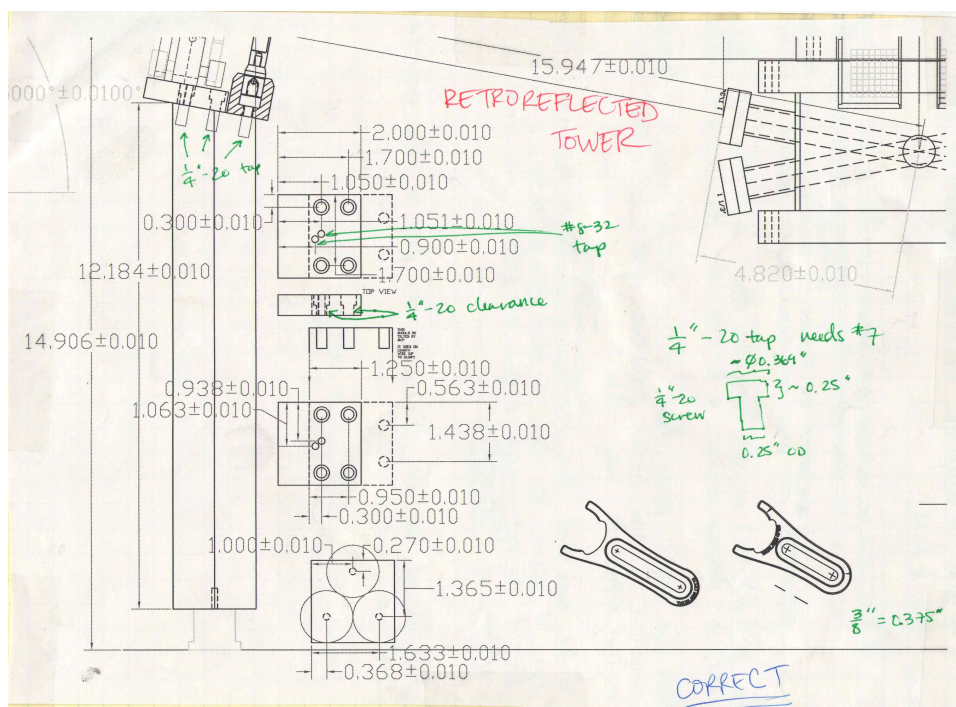


Figure A.34 : Pillar for collecting first pass of ODT beam. The CVI 160-10 mirror mount can be mounted in two different orientations.

While performing the BEC experiments in 2009, we began to insert a half-wave plate in the ODT's recycled beam's path because we obtained larger number of atoms for evaporation. This was crucial for the ^{84}Sr and ^{87}Sr experiments because of their very low natural abundance. The 1064 nm laser itself is linearly polarized, and it traverses a 1064 nm PBS cube (see Fig. 2.12) that shaves off a small amount of power off the main ODT beam to serve as a "dimple" beam. Due to this PBS cube, the main ODT beam starts off horizontally polarized (parallel to the experimental table surface). Table A.8 lists the part number of this half-wave plate. It also includes the part number of a 1064 nm high power harmonic separator window used in different ways on the ODT: when beam profiling the high power ODT beam, when combining

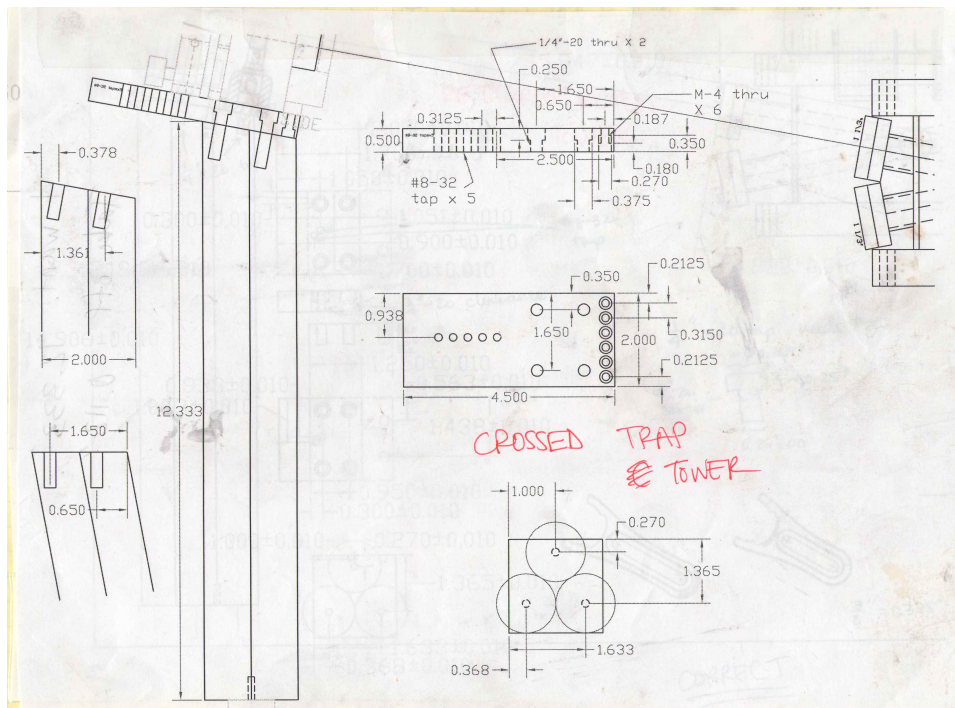


Figure A.35 : Pillar for crossed ODT. (PG. 12 WHITE) The CVI 160-10 mirror mount can be mounted in two different orientations.

$\lambda/2$ waveplate	WPH05M-1064
1064 nm high power window	BSR-51-2025

Table A.8 : 1064 nm optics used with ODT.

the dimple beam with the 461/689 nm MOT beams. A note on the laser's polarization: According to IPG Photonics, the laser is polarized along an arrow mark on the laser's output. If the arrow is parallel to the table, for instance, the polarization is VERTICAL. I personally found it very difficult to determine the laser's polarization from the manufacturer's marking, and found that using a PBS cube was much easier.

While performing the two-photon experiments (in late December 2007), we saw a

PAS-type feature that occurred when any 689 nm laser beam used for single-photon PAS was detuned by a multiple of 110 MHz from the 689 nm atomic resonance. This observation stumped us for a while, but it was a real occurrence: we tested the systematics by scanning a PAS beam that was detuned red and then blue of the atomic resonance by 110 MHz and saw the signal in both instances. One of the most plausible reasons for this involves our multimode (frequency-wise) ODT beam. From the manufacturer (IPG Photonics), we learned that the Fabry-Perot cavity formed by the laser's total fiber length would correspond to spectral modes spaced by 3-7 MHz due to the FP cavity length of 15-25 m. However, the total fiber length seems to be made up of spliced, shorter-length fibers of about 1 m long (a standard length for single-mode passive fiber pigtailed used in assembling the fiber laser, according to the company). Non-perfect splicing between these fiber pieces could lead to light reflection at the boundaries and result in additional FP etalons. Etaloning between 1 m fiber pieces would correspond to spectral modes spaced by $c/2nL \approx 103$ MHz, where c is the speed of light, n is the fiber's index of refraction (about 1.45), and L is the fiber's length. To give spectral mode spacings of 110 MHz, the fibers would be $L \approx 0.94$ m long. In conclusion, the fiber laser seems to be the culprit, such that, in conjunction with the 689 nm laser present at the right frequencies, it's promoting multi-photon transitions and a loss mechanism for the atoms. The experiment providing conclusive evidence of this phenomenon was performed on around February 6, 2007.

A.10 Specific details - Neutral Atoms experimental chamber

This section includes certain details about the Neutral Atoms (NA) experimental chamber and setup that may not be common knowledge. The latest NA experimental chamber AutoCAD drawing/file was named **strontiumvacuum23.dwg** (as of May 2010). Other important drawings about the experimental chamber that may be of importance (and that Natali has knowledge about) include **VacuumChamber-Housing.dwg** and **UHVHousingAtMOTChamber.dwg**. These two drawings are described later in this section.

The atom source heaters were ordered from the company Thermal Solutions. Pertinent information on these heaters (which were a custom-made part) is found in the following table:

HT Firerod (240 W, 120 V, 23 A max.)
Total length: 7.5"
Actual outer diameter: 0.58" \pm 0.004"
Heat concentrated in 1.25" at heater end
Thermocouple type J

Our chamber's Sr reservoir is also unique to our setup. Figure A.36 shows the assembled "nozzle" system and Fig. A.37 through A.41 show its separate parts. This nozzle system was in function until about August 2011, when Brian DeSalvo informed me that a new nozzle design was being implemented such that instead of having a

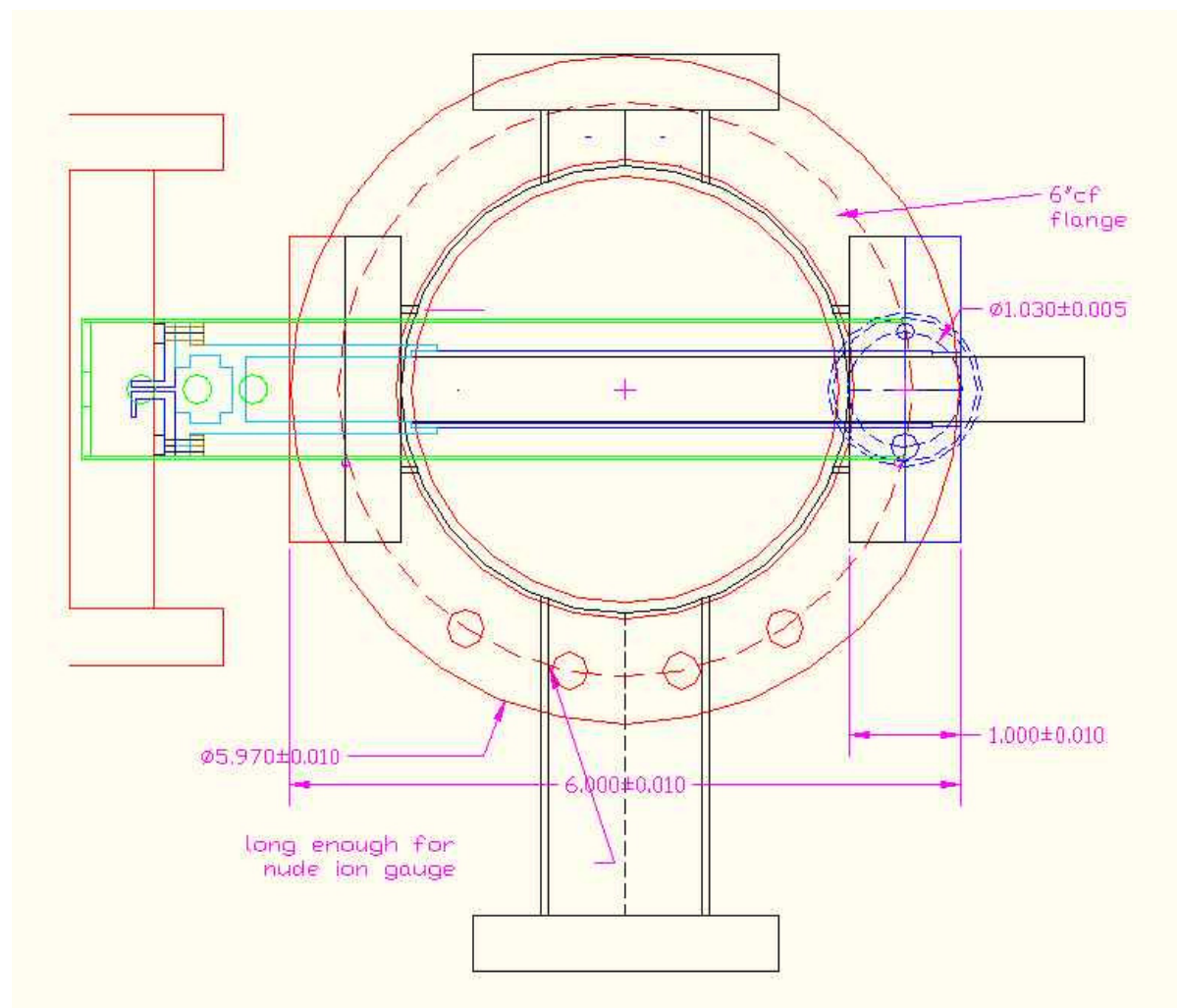


Figure A.36 : Assembled Sr atom beam source. The chamber this “nozzle” system is mounted to is the source chamber, originally designed by Pascal Mickelson. After the source chamber comes the cross that permits the 2D collimator to compress the Sr atom beam before it travels down the Zeeman slower towards the main experimental chamber.

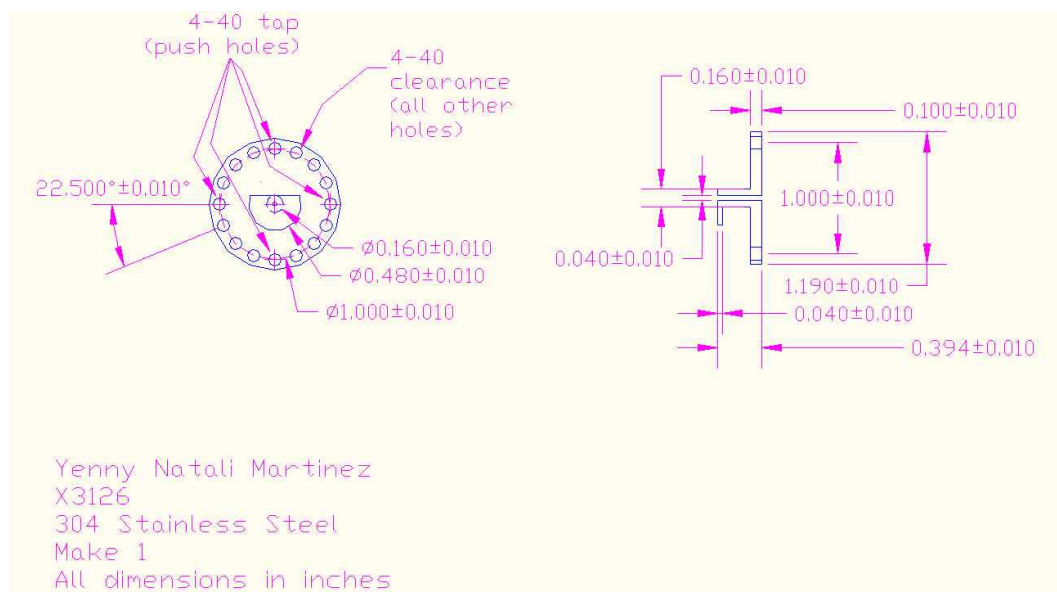


Figure A.37 : Nozzle cap for the Sr atom beam source. This piece was replaced in August 2011 by a newly designed nozzle which, according to Brian DeSalvo, has an array of thin tubes for an output port.

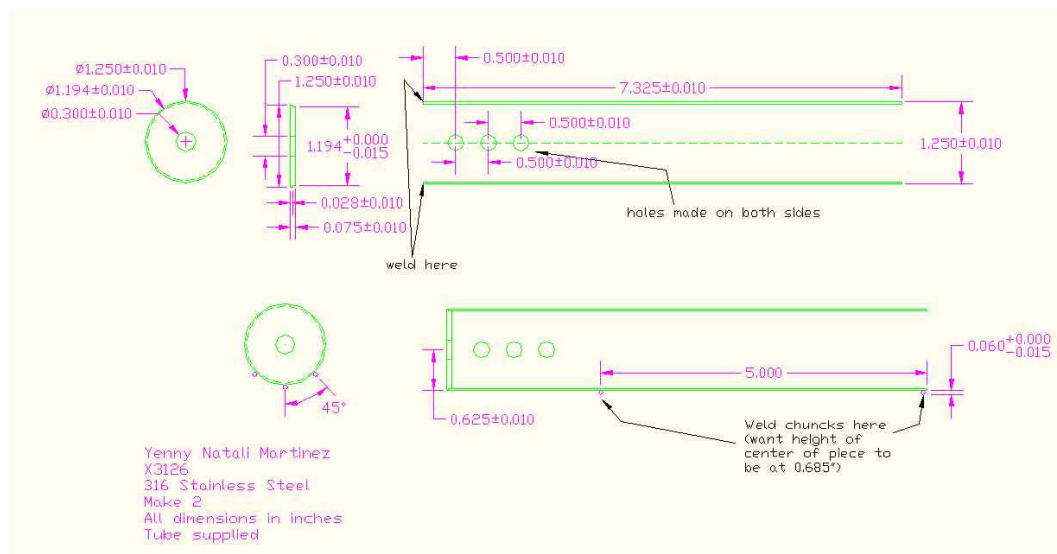


Figure A.38 : Heat shield for Sr atom beam source. The purpose of the heat shield was to help keep the MOT chamber pressure low compared to the Sr atom beam source pressure when it was on.

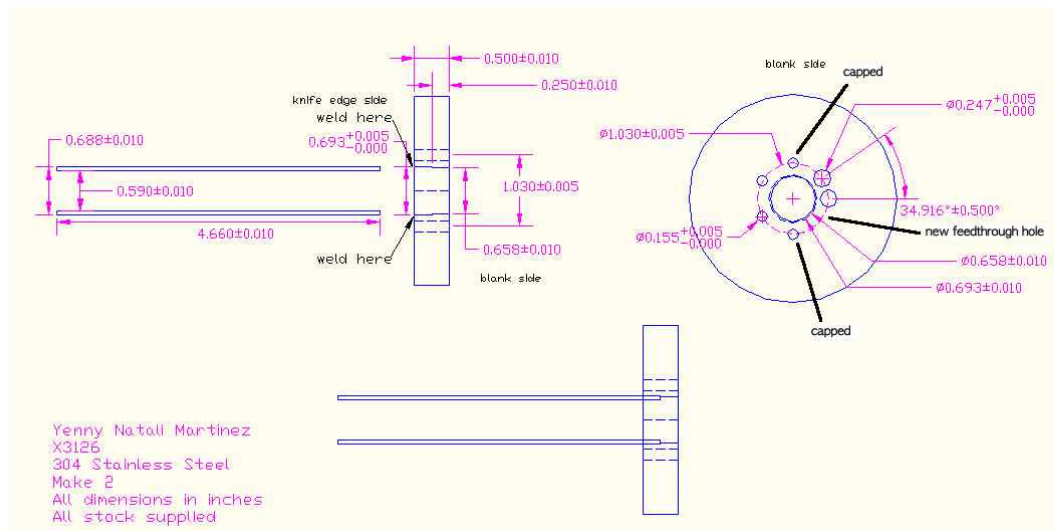


Figure A.39 : Sr atom beam source heater holder. The 7.5" long heater (see text) is inserted inside the tube (from the right side when looking at the bottom half of this drawing). The clearance holes drilled to the 2 3/4" flange served to allow feedthrough to be welded to the flange in order to drive current through the internal "nozzle heater" used to prevent the nozzle hole from becoming plugged (at the nozzle cap, Fig A.37). There are also two thermocouples attached to the assembly to read the nozzle's temperature. The small holes were difficult to weld correctly and couldn't sustain a vacuum seal. A new feedthrough hole (indicated on the drawing) was made to allow a power feedthrough to be welded (the feedthrough that delivers current to the nozzle heater).

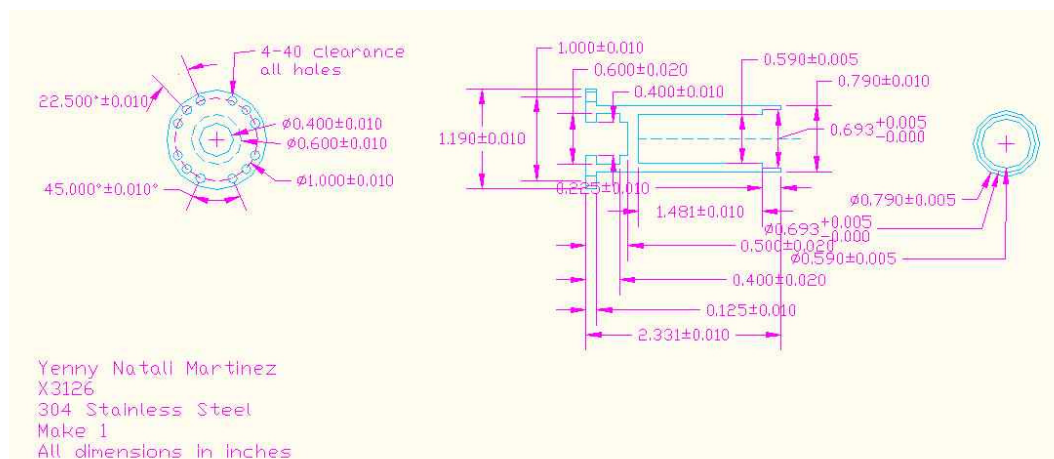


Figure A.40 : Sr atom beam source holder. Sr is loaded into the opening (from the left when looking at the middle component of this drawing). This piece then is welded onto the heater holder (Fig. A.39).

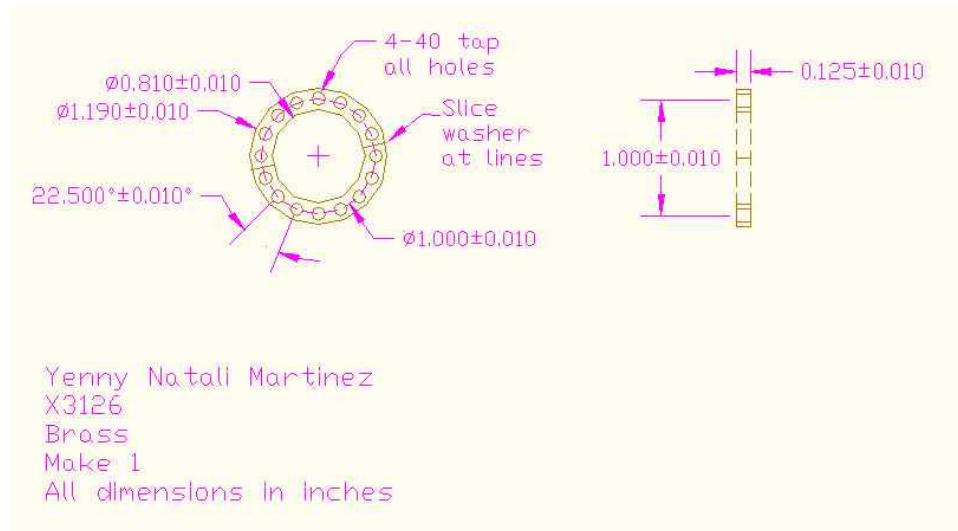
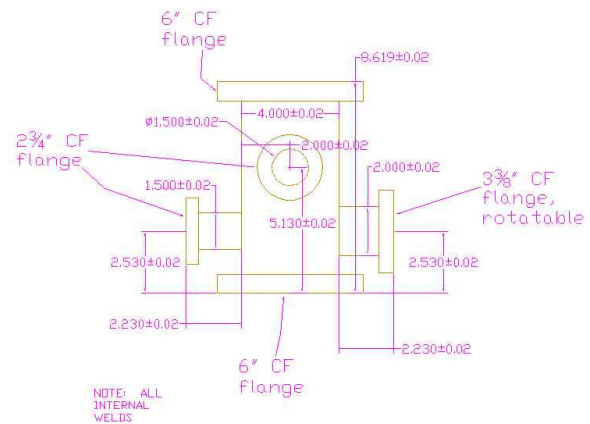
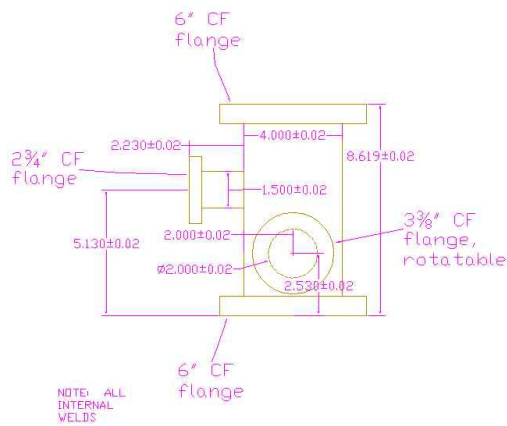


Figure A.41 : Sr atom beam source nozzle nut. This nut served to fasten the nozzle cap (Fig. A.37) to the Sr holder (Fig. A.40).

single hole at the end (see Fig. A.37) it has an array of thin tubes, giving them a lot more flux as well as better collimating the Sr atom beam from the start. In the original design, a “nozzle heater” was wrapped around the nozzle cap to deliver localized heat to the nozzle and prevent it from clogging. The heater used is coaxial heater wire from ARi Industries (P/N 1HN040B-16.3), the same heater used in the plasma team’s Sr source design.

Our experimental chamber was designed to have a high vacuum “chamber” next to the actual main chamber. This auxiliary chamber would give us the flexibility to attach a titanium sublimation (Ti-sub) pump to it and theoretically improve our MOT chamber vacuum. There are two versions of this HV chamber, with the original one shown in Fig. A.42 and A.43 (currently in use as of May 2010) and a second design shown in Fig. A.46 and A.47.



Natali Martinez
 Rice University
 Physics and Astronomy
 natali@rice.edu
 (713) 348-3126
 FAX (713) 348-2603
 316 Stainless Steel
 All measure, in inches

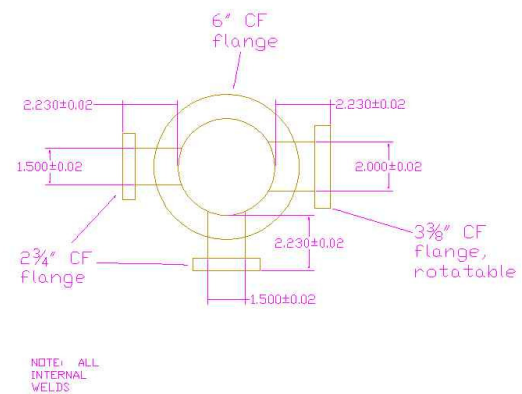
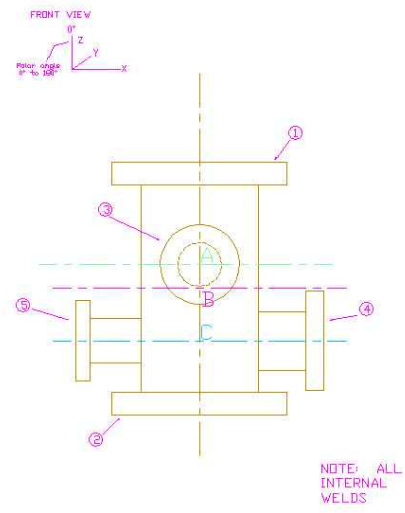
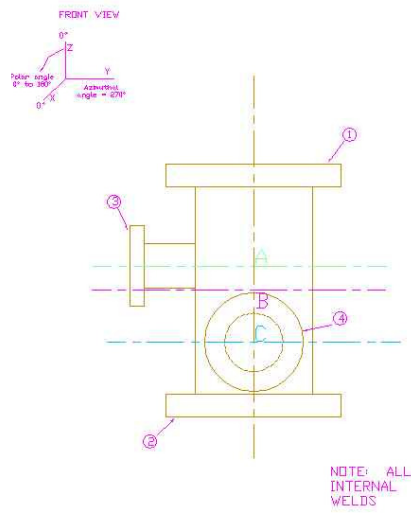


Figure A.42 : First version of HV chamber. This is the chamber originally installed in the experimental chamber (as of May 2010) along with the setup shown in the bottom half of Fig. A.45.



TOLERANCE ASSUMED:
±0.02 INCH

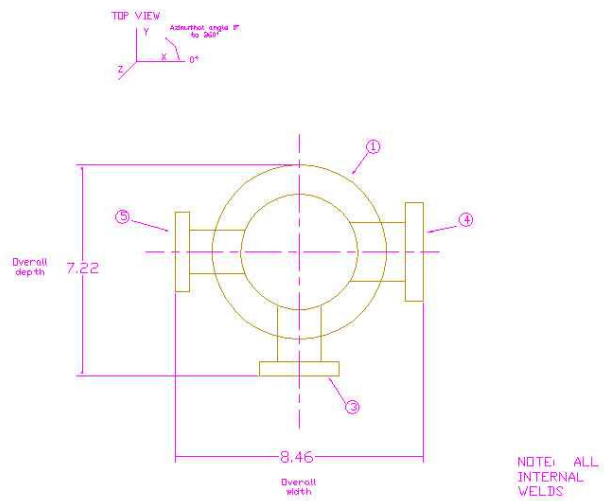


Figure A.43 : First version of HV chamber (view #2). Explanation about each port is found in Fig. A.44.

This is a list of the flanges necessary for my chamber. Please note the bold writing which indicates that there is a modification requested for that particular piece. Note: All internal welds.

PORT NO.	FLANGE SIZE	FLANGE TYPE	TUBE O.D.	FOCAL POINT	FOCAL LENGTH	AZIMUTHAL ANGLE	POLAR ANGLE
1	6"	CF	4"	B	4.310	0.00	0.00
2	6"	CF	4"	B	4.310	0.00	180.00
3	2 3/4"	CF	1.5"	A	4.230	270.00	90.00
4	3 3/8"	CF, R	2"	C	4.230	0.00	90.00
5	2 3/4"	CF	1.5"	C	4.230	180.00	90.00

LEGEND

CF = Conflat Flange ***Focal length is measure from the flange seal face to the focal point
 T = Tapped ***Focal point is the port's target point
 R = Rotatable

Figure A.44 : Information about chamber ports for first version of HV chamber (Fig. A.43).

The original HV chamber has our setup's ion pump (Varian P/N VacIon Plus 75) attached to its top. The Zeeman slower beam enters the chamber through the 2 3/4" port that is opposite the 3 3/8" port (port #5 in Fig. A.43). Figure A.45 shows the two plans we had to introduce the Ti-sub pump in our setup. The setup we chose when assembling the chamber is the one shown in the bottom half of Fig. A.45 (as of May 2010). The 4 1/2" elbow is attached to port #2 of Fig. A.43, and the Ti-sub pump is installed inside the nipple as shown. Figure A.44 shows information about the different ports of the chamber as shown in Fig. A.43. This chamber was manufactured by Huntington Vacuum Technologies, and as part of their ordering process request this second view (Fig. A.43) and the explanations found in Fig. A.44.

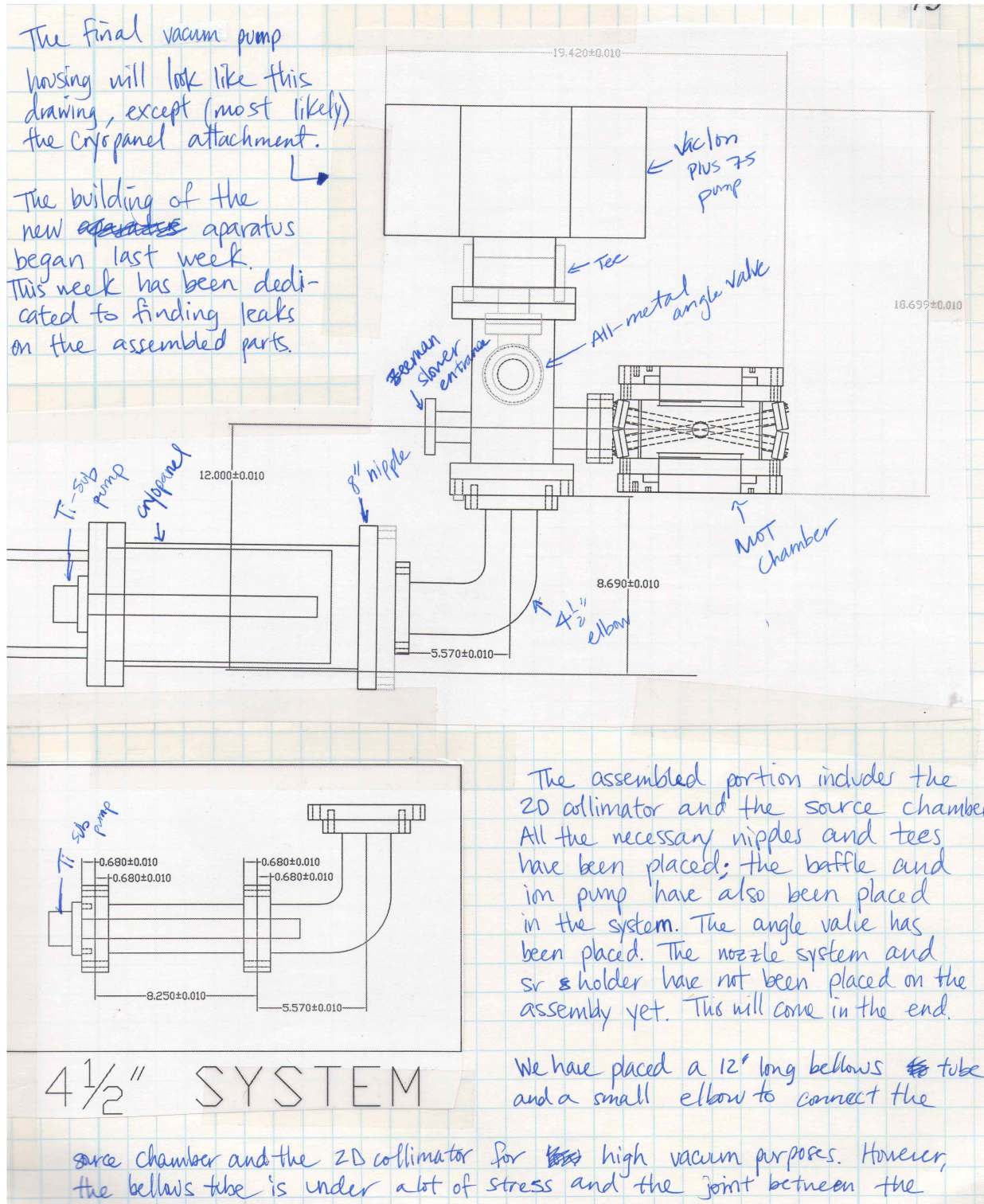


Figure A.45 : Two plans to introduce the Ti-sub pump in the first version of HV chamber (Fig. A.42 and A.43). The setup chosen when originally assembling the experimental chamber was the one shown in the bottom half of this figure.

Natali Martinez
 Rice University
 Physics and Astronomy
 natali@rice.edu
 (713) 348-3126
 FAX (713) 348-2603
 316 Stainless Steel
 All measure. in inches

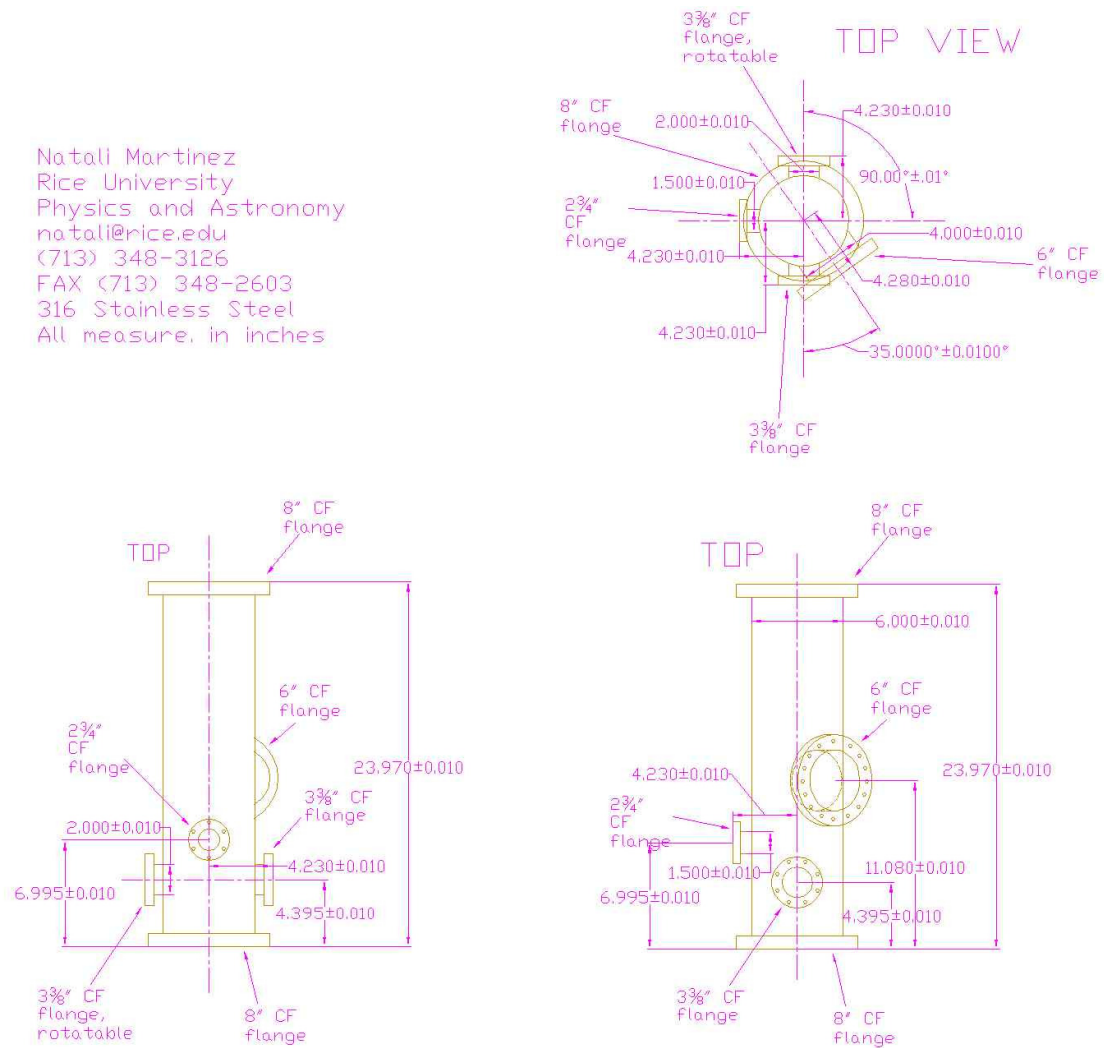


Figure A.46 : Second version of HV chamber (compare with Fig. A.42).

Natali Martinez
 Rice University
 Physics and Astronomy
 natali@rice.edu
 (713) 348-3126
 FAX (713) 348-2603
 316 Stainless Steel
 All measure. in inches

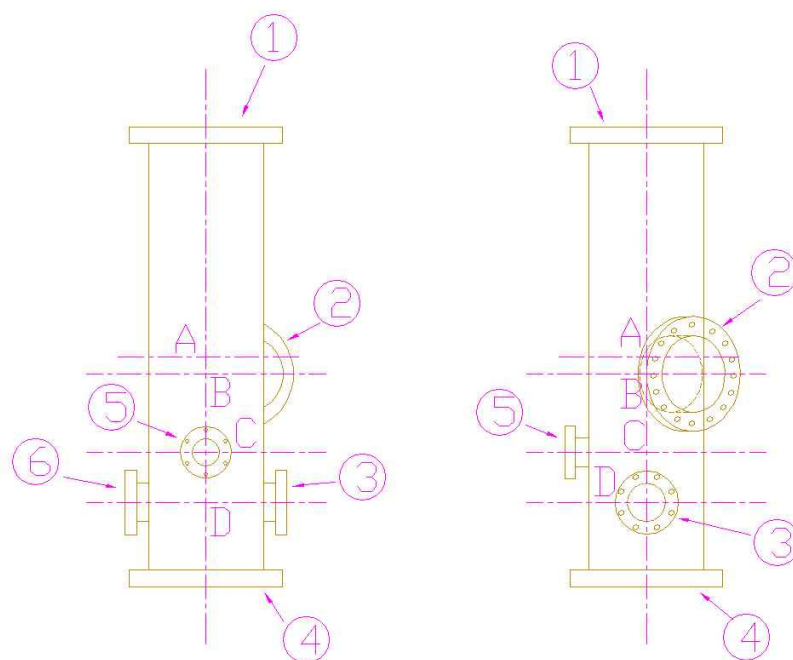
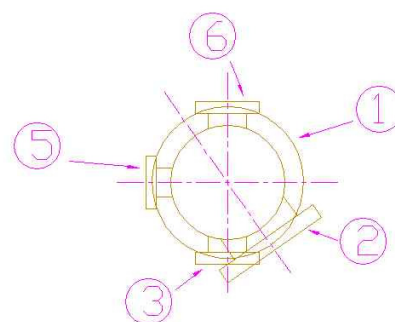


Figure A.47 : Second version (view #2) of HV chamber (compare with Fig. A.43).
 Explanation about each port is found in Fig. A.48.

This is a list of the flanges necessary for my chamber. NOTE: ALL INTERNAL WELDS

PORT NO.	FLANGE SIZE	FLANGE TYPE	TUBE O.D.	FOCAL POINT	FOCAL LENGTH	AZIMUTHAL ANGLE	POLAR ANGLE
1	8"	CF, T	6.00	A	11.985"	0.00	0.00
2	6"	CF, T	4.00	B	4.28"	35.00	90.00
3	3 3/8"	CF, T	2.00	D	4.23"	0.00	90.00
4	8"	CF, T	6.00	A	11.985"	0.00	180.00
5	2 3/4"	CF, T	1.50	C	4.23"	270.00	90.00
6	3 3/8"	CF, T, R	2.00	D	4.23"	180.00	90.00

LEGEND

CF = Conflat Flange

T = Tapped

R = Rotatable

***Focal length is measure from the flange seal face to the focal point

***Focal point is the port's target point

Figure A.48 : Information about chamber ports for second version of HV chamber (Fig. A.47).

The second design for the HV chamber is actually designed to house a Ti-sub cryopanel, which is attached to port #1 of Fig. A.47. The ion pump is attached to port #2 and the Zeeman slower beam enters the chamber through port #3. Figure A.48 shows information about the different ports of the chamber as shown in Fig. A.47. This chamber was ordered and delivered, but as of May 2010 was not installed.

While assembling the main experimental chamber (MOT chamber), we chose to use specifically-coated windows for each port. On the 28th of January 2005, I assisted with putting the MOT chamber windows on and performing a vacuum leak test. The windows used when originally assembling the chamber are listed in Table A.9 (along with their respective coating) and shown schematically in Fig. A.49. The coating job was made by Rocky Mountain Instrument (RMI), and according to my notes, it is a broadband anti-reflection coating from 450-700 nm. NOTE: Some of the chamber

MOT beam ports	4 qty.	Coated
Image beam ports	2 qty.	Coated
1 1/3" port #1	Top	Non-coated
1 1/3" port #1	Bottom	Coated
1 1/3" port #2	Top	Non-coated
1 1/3" port #2	Bottom	Coated
1 1/3" port #3	Top	Coated
1 1/3" port #3	Bottom	Non-coated
1 1/3" port #4	Top	Coated
1 1/3" port #4	Bottom	Non-coated

Table A.9 : MOT experimental chamber windows. The 1 1/3" ports are labeled according to their positions in Fig. A.49.

windows (particularly those used in the current Dipole trap ports) may have been replaced with differently-coated ones after this date.

The chamber underwent a long bakeout period with which we desired to improve the chamber's background pressure to perform our BEC experiments. Details of this bakeout cycle (which began in January 2009 and ended by May 2009) are registered beginning on pg. 17W of the Neutral Atom group's notebook G. This bakeout phase took a long time due to leaks springing out at different chamber fitting junctions and contamination from internal residual plastic from a previous bakeout period (at around 2005).

A.11 AutoCAD drawings

In this section I include other drawings made in the lab (while I was there) that could be useful to conserve. Relevant details are included in the captions when necessary.

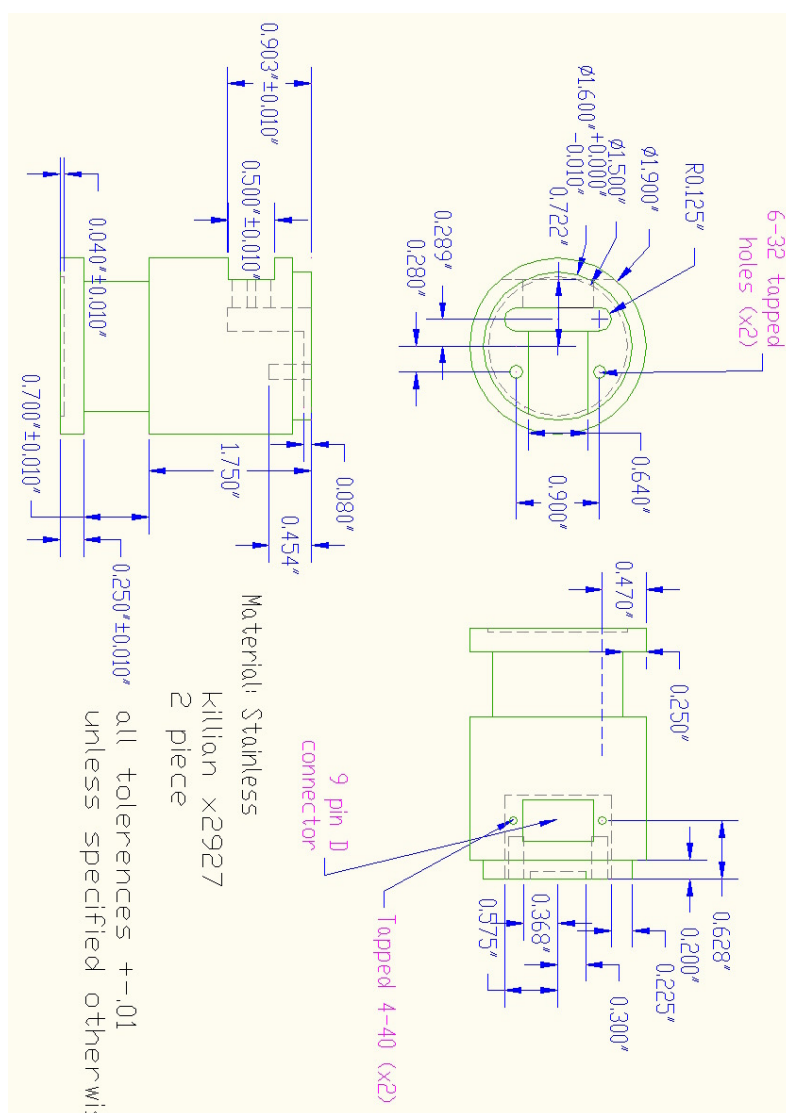


Figure A.50 : Base for 689 nm slave lasers (original lab design). This design was also used for ^{87}Sr slave laser #1. The base used for ^{87}Sr slave laser #2 is slightly different.

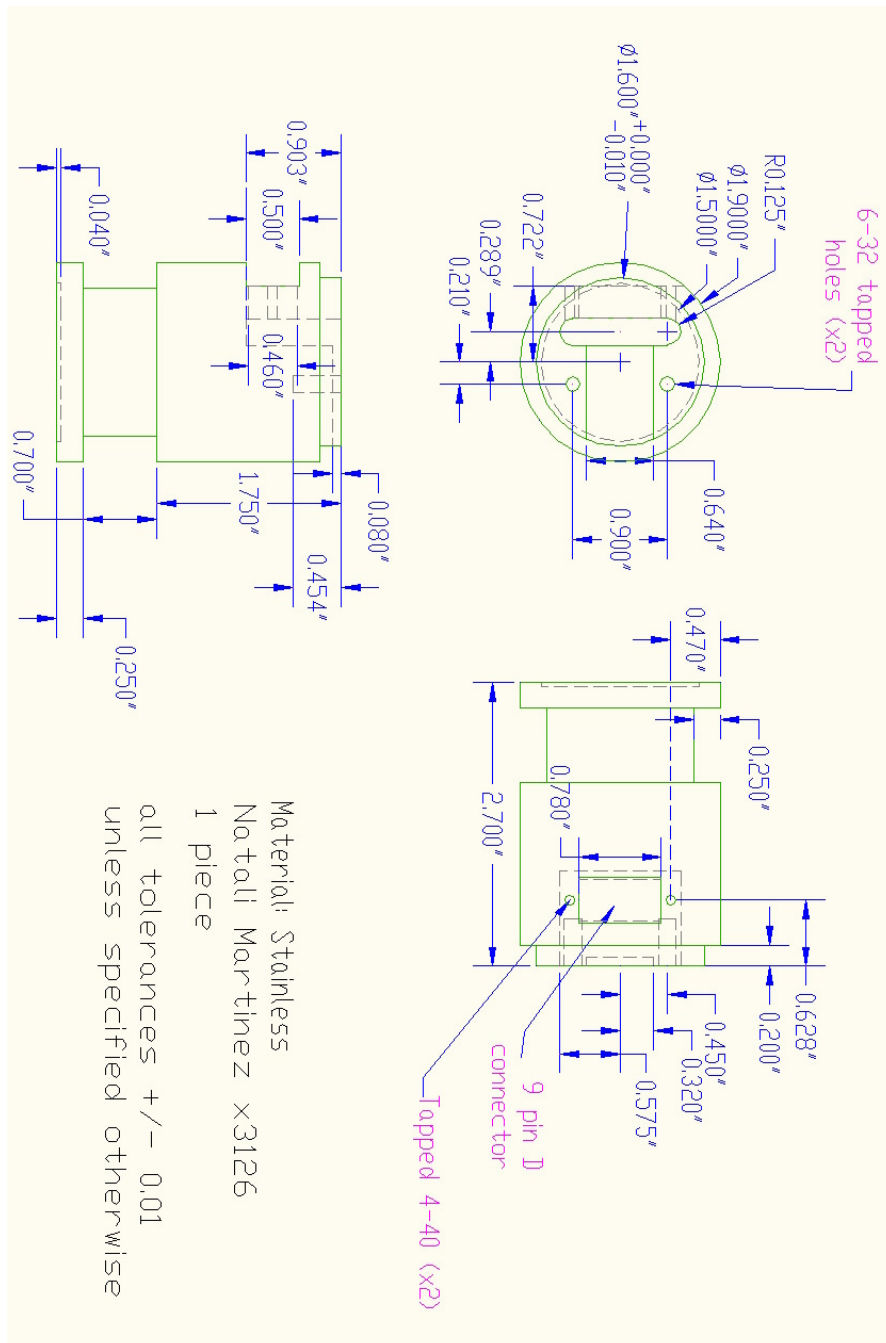


Figure A.51 : Base for ^{87}Sr slave laser #2 (second slave laser design). The material used for this piece was actually Brass. It was necessary to change the original slave laser design (Fig. A.50) in order to accommodate a top over the laser's lens and lens holder (Fig. A.52).

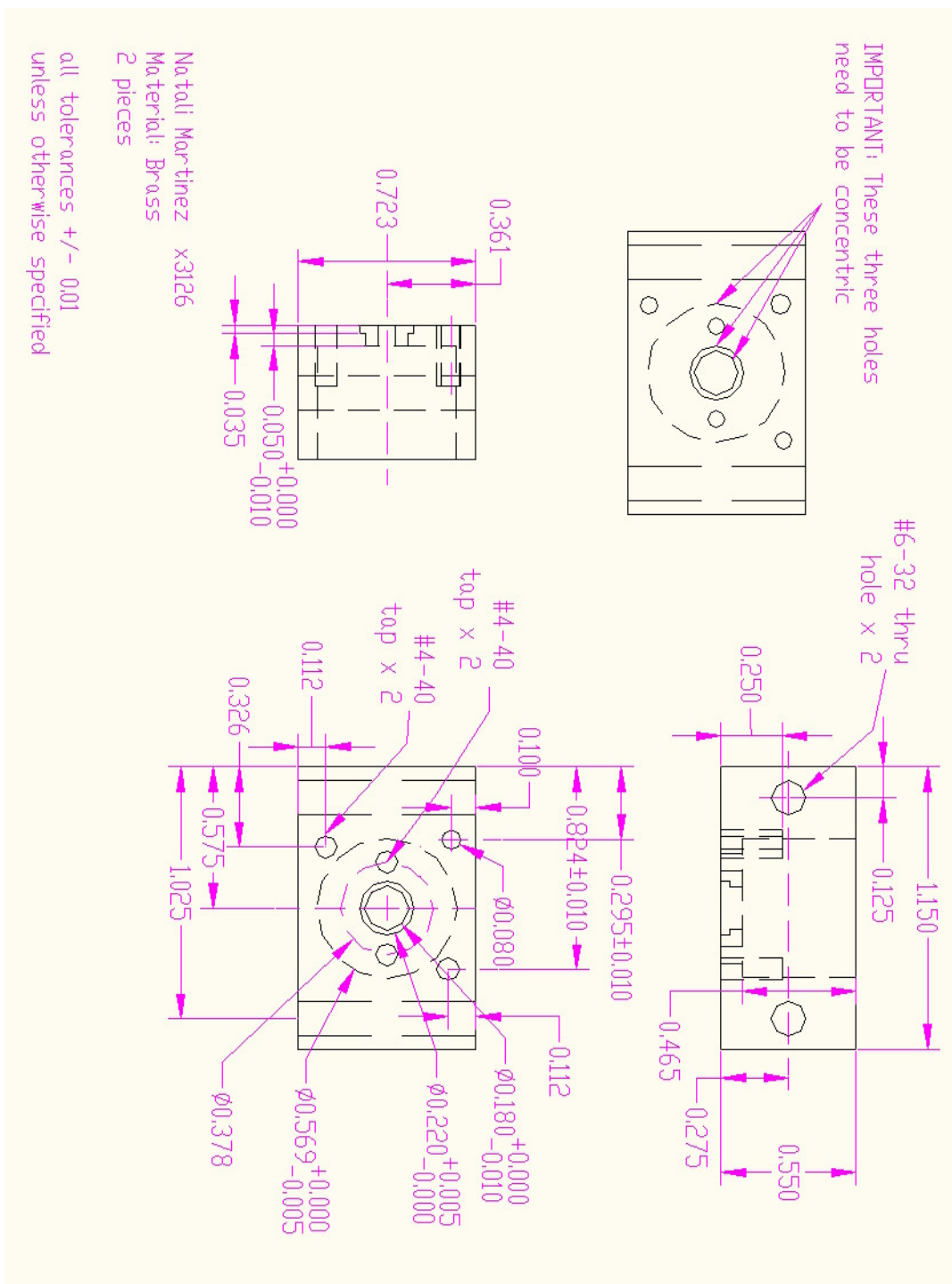


Figure A.52 : Melles Griot lens holder for 689 nm slave lasers. This seems to be a lab original design. It was used on both ^{87}Sr slave lasers.

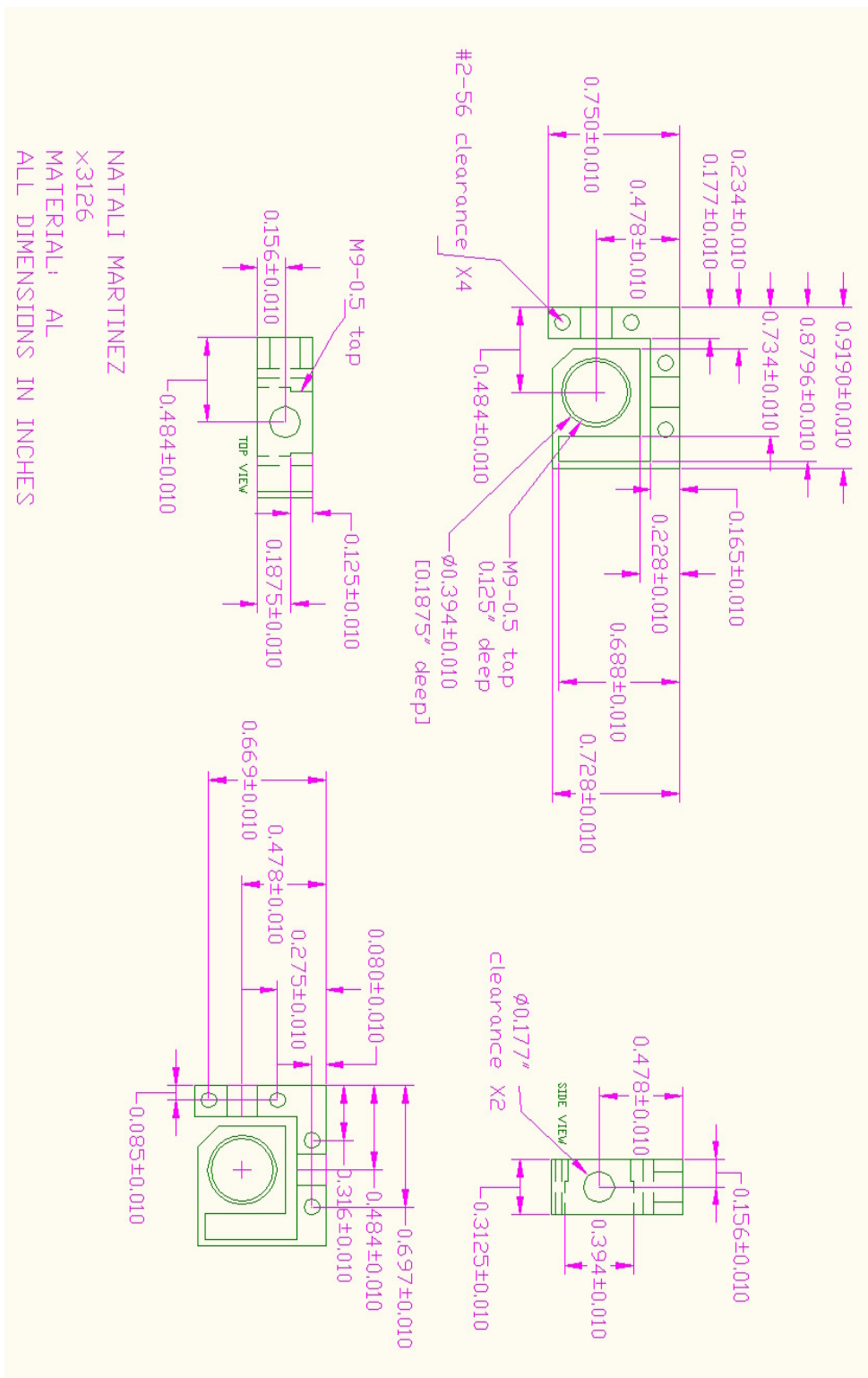


Figure A.54 : Second version of flexible collimating lens mount (compare to Fig. A.53).

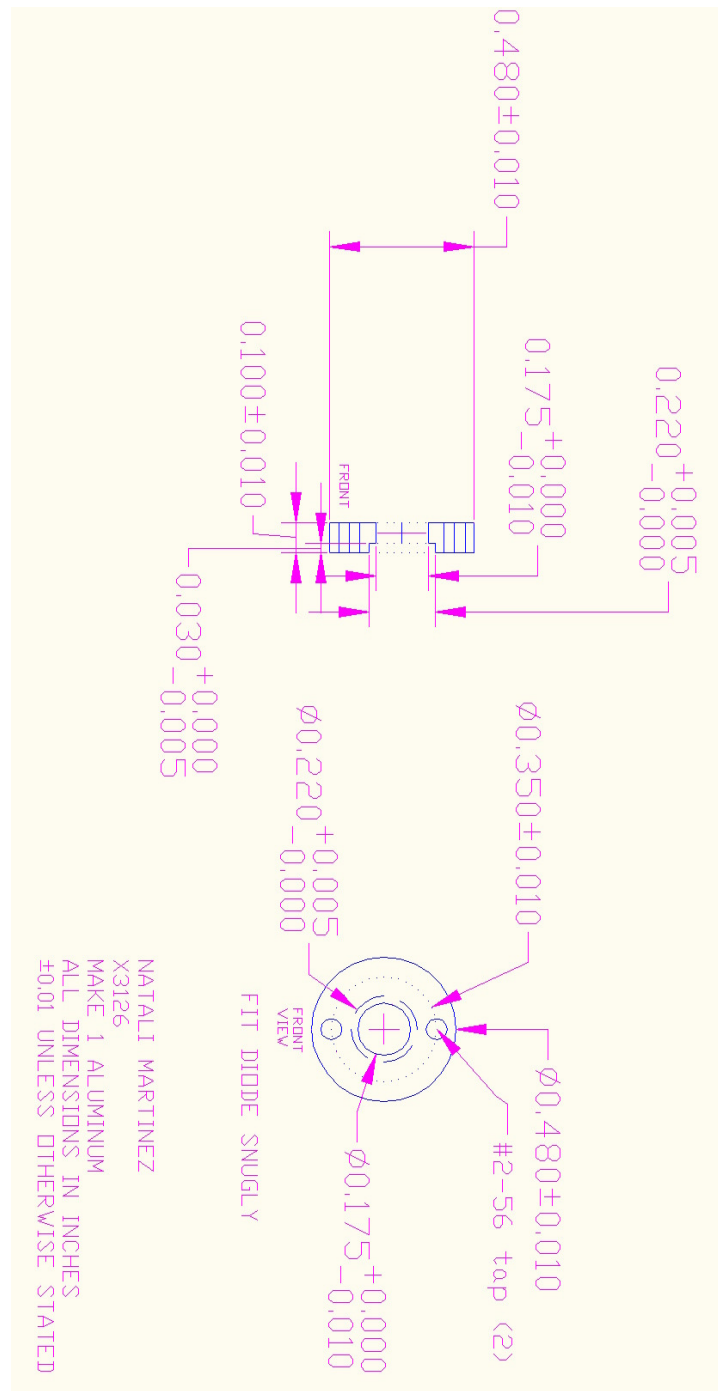


Figure A.55 : Miniature laser diode mount cap (made originally from Brass). This cap and its mount (Fig. A.56) hold 5.6 mm outer diameter laser diodes.

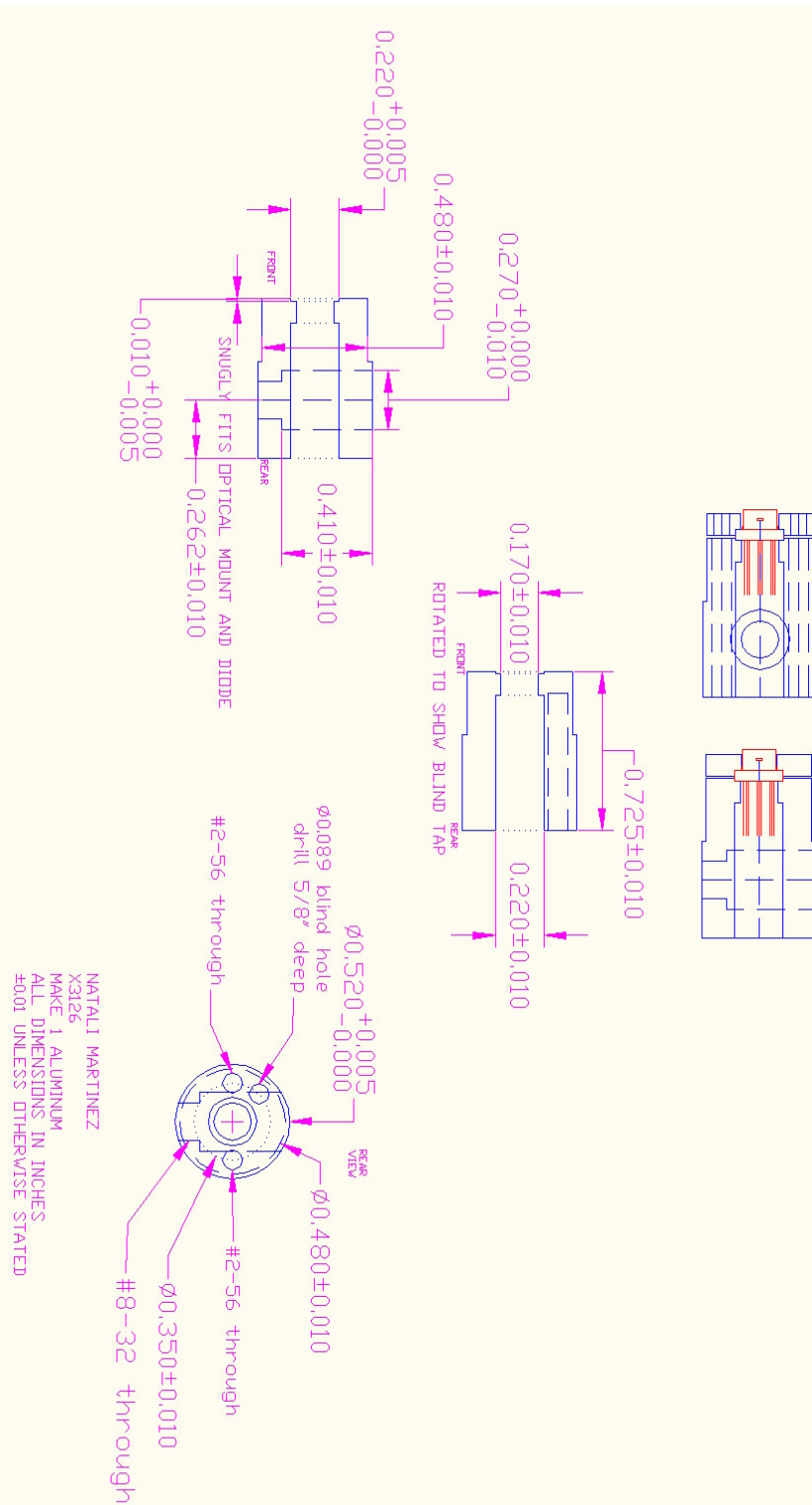


Figure A.56 : Miniature laser diode mount (made originally from Brass). This mount and its cap (Fig. A.55) holds 5.6 mm outer diameter laser diodes.

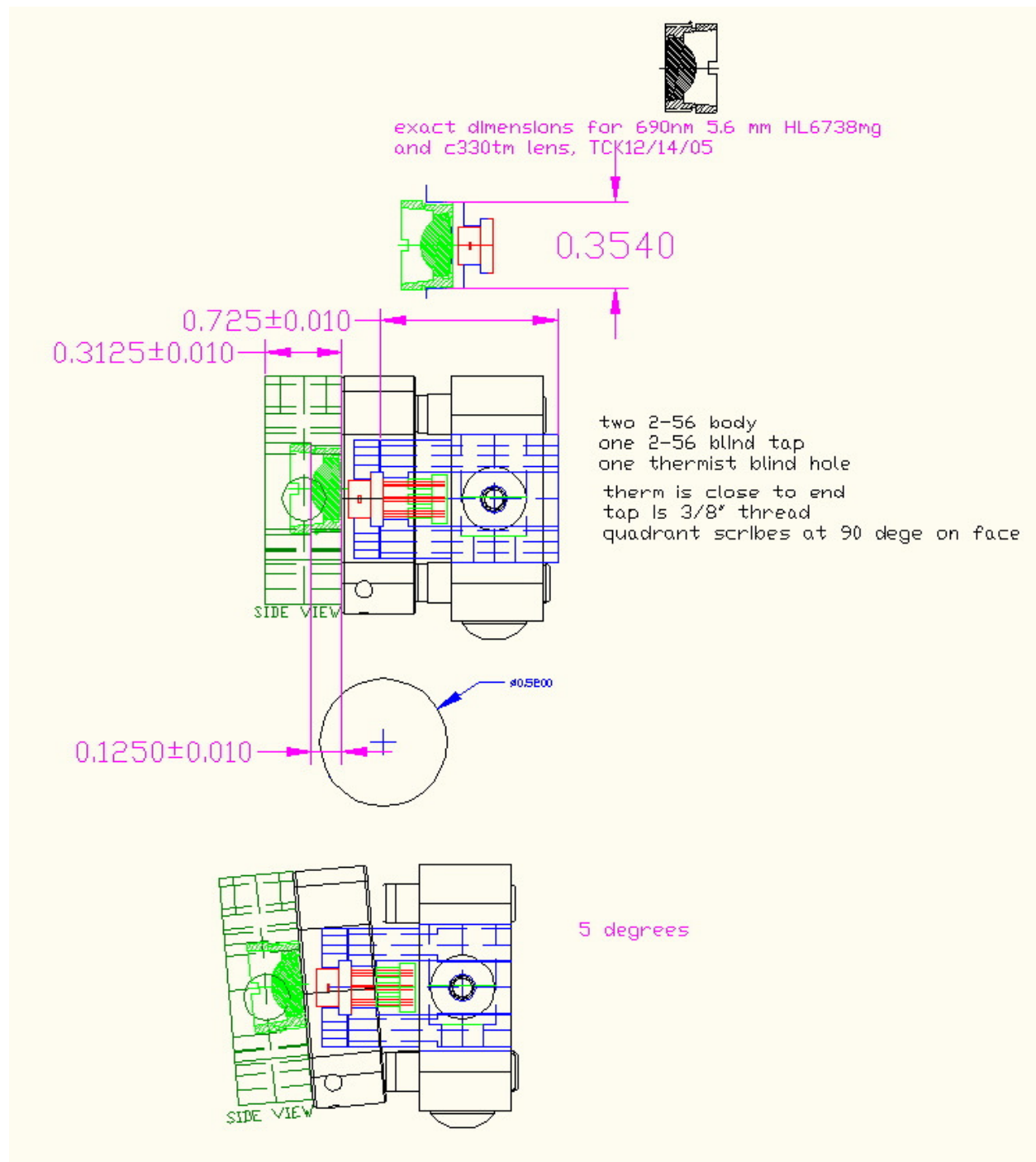


Figure A.57 : Assembled miniature laser diode collimating system.

Appendix B

Lynx 922 nm laser Status Report

The 922 nm laser diode that the Neutral Atom setup uses was manufactured by the German company Sacher Lasertechnik. This laser diode gave us quite a bit of problems for a couple of years. The last time (as of May 2010) the laser performance degraded was around September 2007 (when we noticed a problem because we turned the laser on). I then prepared a Status Report and sent it to Sacher in order to get the laser fixed. I include the entire Status Report (written on October 4, 2007) in this appendix for future reference. The laser head was subsequently sent back to Sacher with RMA# RWYK-788M2C and returned fixed.

Dear Dr. Markus Horstjann,

4th of October, 2007

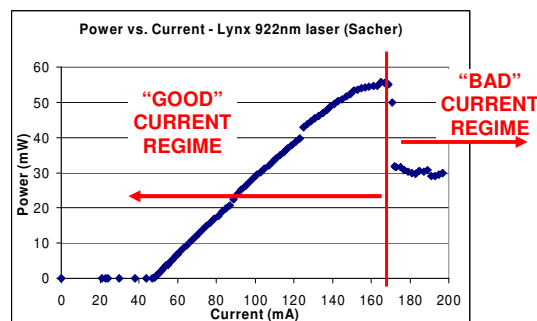
Thank you for emailing me information to help us diagnose and accelerate the process of improving our diode laser performance. I am sorry I have taken a long time in responding to your email since the last time I wrote to you, but we have been busy trying to work with the Lynx 922nm laser as it is with minimal success. This is why we decided that it is time to get it fixed and why I am finishing this report to send to you. I received the STATUS REPORT file that you sent me and even though I cannot supply you with all of the information you request, I believe that what I send you may be very helpful.

FORMAL INFORMATION:

Our laser head serial number is ST922-6395-04-028. It was repaired under RMA # JS07030701 in April 2007. Our laser controller serial number is 1444 (model number MLD1000).

PI CURVE:

Please see the following figure. Since my email on the 4th of September, the performance of the Lynx laser has degraded even more, and this behavior is visible in the PI curve below.

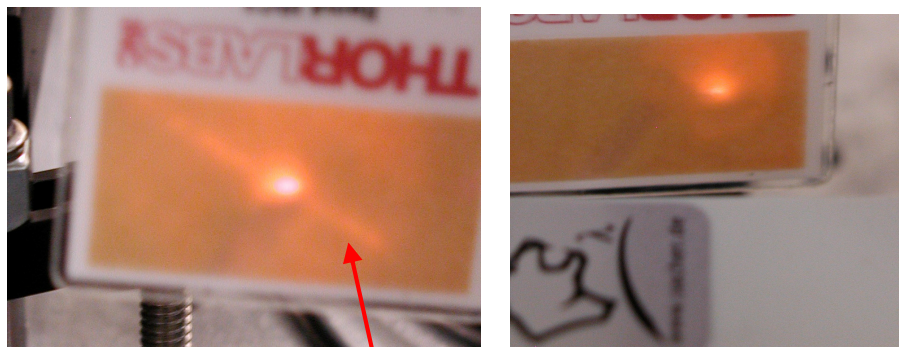


BEAM PROFILE:

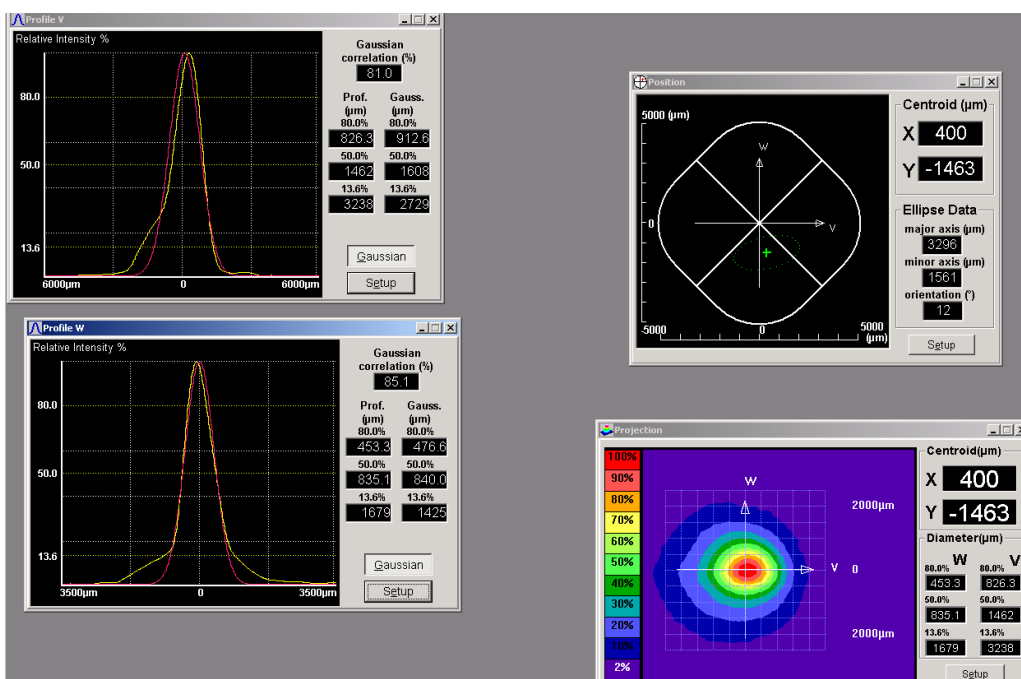
I have taken a couple of profiles of the beam with our Beam Profiler (not necessary a laser camera, even though it gives us an image of the beam profile). I have taken them at different laser currents to show how the beam shape changes in the "good" and "bad" lasing regimes (see PI Curve above for my labeling of the different regimes). I have also tried to take pictures of our IR card to show different details that concern us (lacking a laser camera).

This picture shows the "halo" I described in my first email – taken about 2-3 cm from Lynx laser head. There's not a lot of optical power in the halo, it seems. Taken at 170 mA, 18.7 °C.

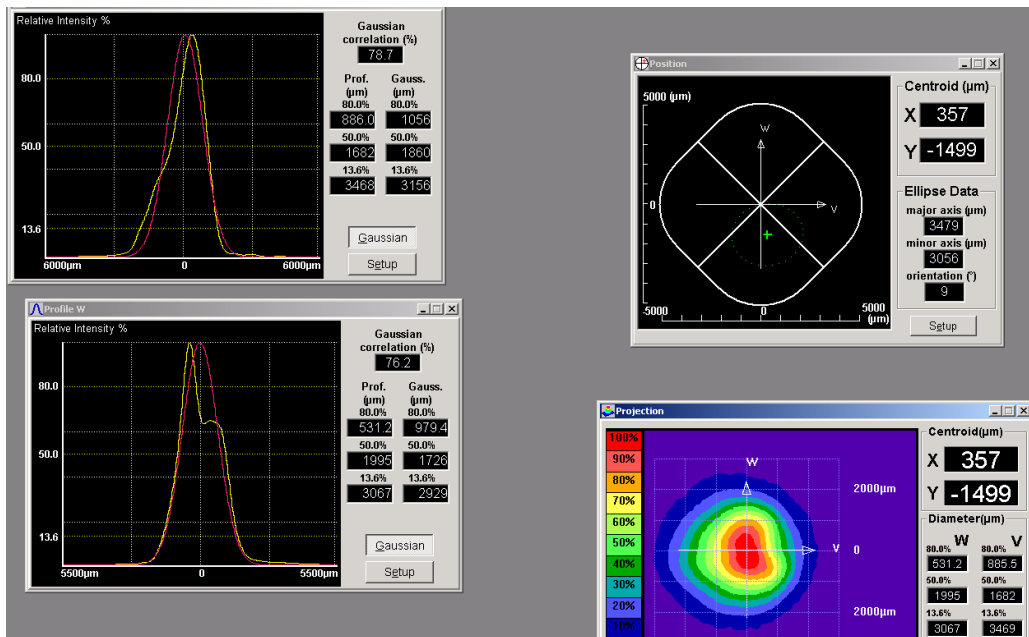




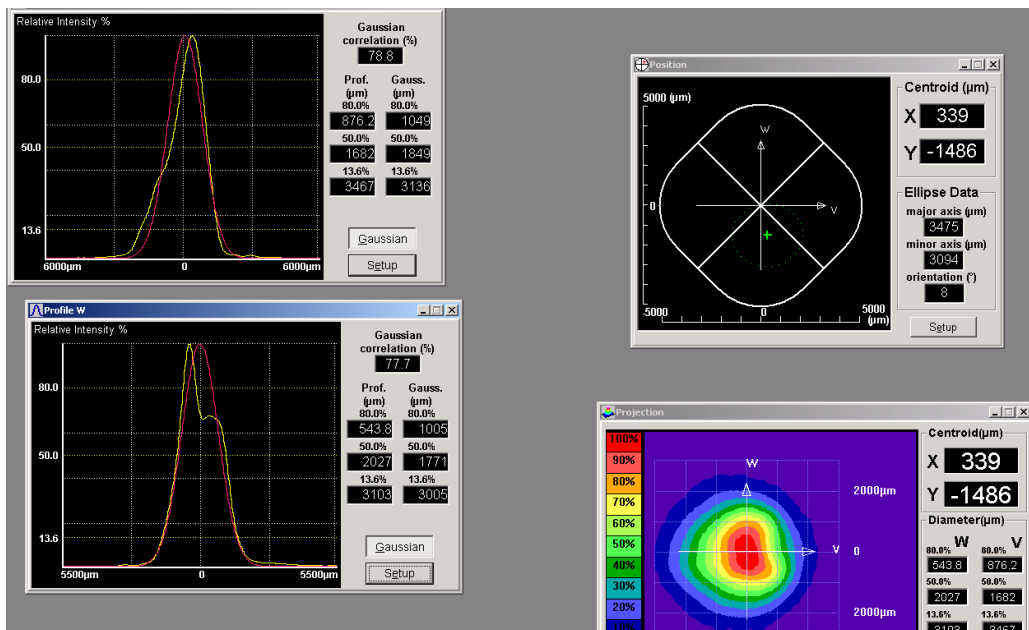
This "stripe" on the output beam is also a concern to me. Again, there doesn't seem to be a lot of optical power in the stripe. Picture taken ~ 10 cm away from Lynx laser head.



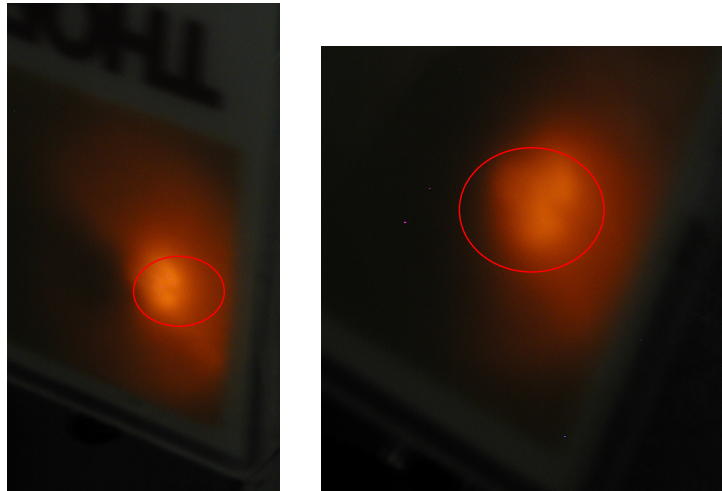
PROFILE OF BEAM AT 17°C, 160 mA, ~13 cm AWAY FROM LYNX 922nm LASER HEAD. The red trace is a Gaussian "best-fit" to the beam profile. This profile is taken in the "good" current regime, although the beam shape looks bad (see the shoulder present in the top profile). The "halo" is probably the shoulders visible on the bottom profile.



PROFILE OF BEAM AT 17°C, 175 mA, ~13 cm AWAY FROM LYNX 922nm LASER HEAD. The red trace is a Gaussian “best-fit” to the beam profile. You can see that the beam shape has worsened in the bad current regime.



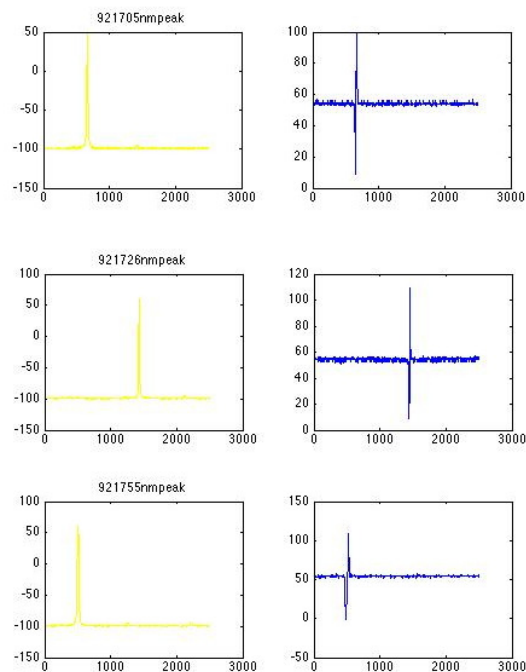
PROFILE OF BEAM AT 17°C, 185 mA, ~13 cm AWAY FROM LYNX 922nm LASER HEAD. I took this profile in the bad current regime to show that its shape stays very ugly as current is increased.



PICTURES TAKEN AT 185 mA, 17 °C, ~2-3 cm AWAY FROM LYNX LASER OUTPUT. The horrible shape of the beam is fairly visible.

OPTICAL SPECTRUM AND PIEZO TUNING BEHAVIOR:

We lack an optical spectrum analyzer to provide you with item #3 of the STATUS REPORT. However, we used a FP cavity to determine how far the laser can sweep and stay single mode. This sweep was done by manually turning the PZT to see how far the laser can stay single mode with the cavity acting as a frequency discriminator (these tests were done on the 13th of September). The laser remains single mode from about 921.705 nm to about 921.755 nm. I have inserted the scope traces of our cavity modes below to show this behavior (the blue traces are the error signals produced and are not important).



However, we have encountered a problem we cannot explain with a "frequency instability" that hampers our ability to utilize the Lynx laser for our experiments. I explained this problem in my email to you, but I will paste my comments here for completeness of the report:

We have been trying to work with the Lynx laser as it is since I last wrote to you but it has not been possible to lock our doubling cavities with this laser as a seed laser to our tapered amplifier (TA) system due to a "frequency instability" (for lack of a better term) that is on the laser, almost right on top of our error signal, which hampers the cavity lock. This disturbance seems to repeat itself every 200-300 MHz or so, and it seems to drift slowly within 50 MHz in an indefinite direction. To try to explain what I mean by the "frequency instability", I mean that as you tune the frequency of the laser with PZT voltage, for instance, the frequency of the laser is good for about 200-300 MHz, our cavity error signal is stable in frequency (not jittering around) and of a certain size. As we reach this frequency instability, our cavity error signal doubles (if not triples) in size and it fluctuates in frequency within about 10 MHz. This behavior occurs while we're at this specific frequency. Then when we continue the frequency tuning of the laser, the frequency becomes stable again for another 200-300 MHz, and the cycle repeats itself over again. We have been trying to determine the source of this instability but are at a loss as to why it is present. To try to get around it (and we hypothesized that probably it was being written onto the laser frequency because of our modulation on the laser frequency) and lock our cavity, we tried different setups for modulating the laser frequency and different frequency ranges, but we were not successful at overcoming this problem. When we seed our TA system with our Ti-Saph laser at 922 nm we do not have this problem with our doubling cavities, so the problem is not with our TA.

I hope this report helps both you and I to determine what has happened to the laser diode and to mobilize its repair.

Sincerely,

Mrs. Natali Martinez de Escobar

Appendix C

“Cross-over” transitions in the 689 nm sat. abs. error signal

To separate the magnetic sublevels m_J of the 3P_1 state (689 nm transition) for our saturated absorption setup we apply a static magnetic field produced by wire coils running parallel to the long cell. The 689 nm light polarization has to be aligned to the axis of this magnetic field (vertically polarized light coming out of the sat. abs. fiber) to avoid exciting “cross-over” transitions produced when the unaligned light polarization drives $\Delta m_J = \pm 1, 0$ transitions. Mi Yan demonstrated this effect by changing the sat. abs. beam polarization before being coupled into the sat. abs. optical fiber, as described in the annotations of his lab notebook presented in this Appendix.

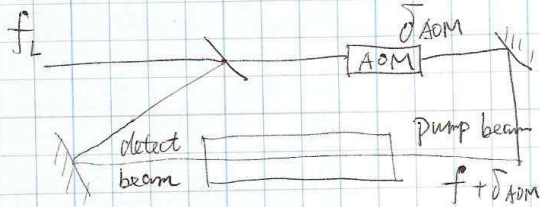
Name:

Date: 6/10/2009

26

Experiment: ⁸⁷Sr Red Trap Beam Check

The Red Saturation Absorption Chamber.



$$kv + f_L + \delta_{AOM} = f_0$$

$$-kv + f_L = f_0$$

$$2f_L + \delta_{AOM} = 2f_0$$

$$\Rightarrow f_L = f_0 - \frac{\delta_{AOM}}{2}$$

~~In this experiment, $f_0 = f_0^{87} = f_0^{88} - 1241 \text{ MHz}$~~

Now, Two Steps, (δ_{AOM} is always -160 MHz)

Step 1: $f_0 = f_0^{88}$, so that $f_L = f_L^{88} = f_0^{88} + 80 \text{ MHz}$

now $f_L^{87} = f_L^{88} - 1241 \text{ MHz}$

Step 2: $f_0 = f_0^{87} = f_0^{88} - 1241 \text{ MHz}$, $f_L = f_L^{87} = f_L^{88} - 1241 \text{ MHz} + 80 \text{ MHz}$

$$= f_0^{87} + 80 \text{ MHz}$$

So now in step 2 we can see the absorption from f_0^{87} ($1/2 \leftrightarrow 9/2$) w/o any changes.

Calculation:

Step 1. ⁸⁸Sr, $3P_1$, $S=1, L=1, J=1$,

$$g_J = 1 + \frac{J(J+1) + S(S+1) - L(L+1)}{2J(J+1)} = 1.5$$

$\therefore \Delta E_{88} = g_J M_J \mu_B B$ where $M_J = \pm 1, 0$, Bohr magneton is

The freq spacing between two sublevels

is $\Delta E'_{88} = g_J \mu_B B$

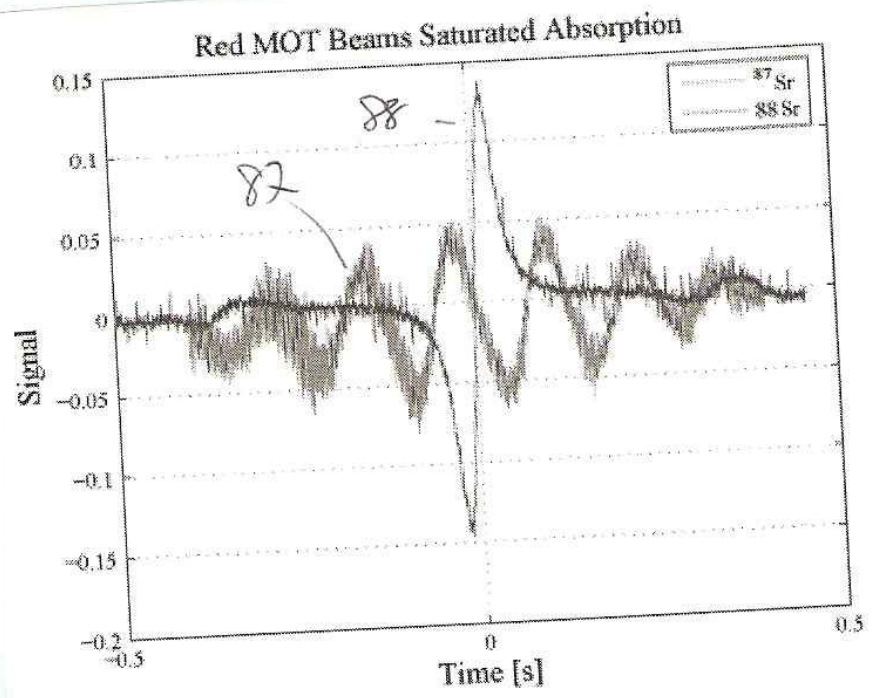
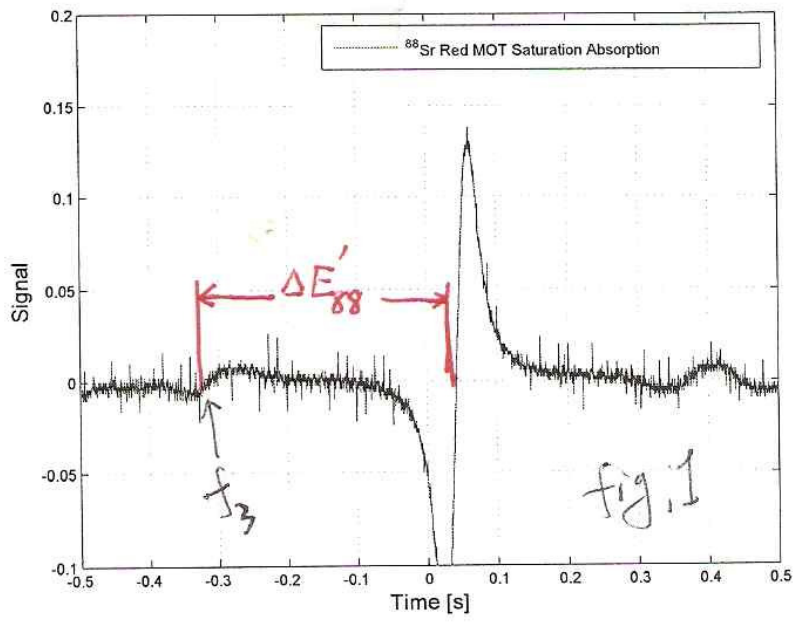
$$\mu_B = 9.274 \times 10^{-24} \text{ J/T}$$

$$= \frac{1.4 \times 10^6 \text{ Hz}}{10^4 \text{ G}}$$

$$= 1.4 \times 10^6 \text{ Hz/G}$$

Important: Place card under blue copy.

National Brand Laboratory



Name: _____

Date: _____

Experiment: _____

26

$^{87}\text{Sr}, ^3\text{P}_1, F=11/2, S=1, L=1, J=1, I=9/2$

From Boyd thesis. $A = -260.084 \text{ MHz}, Q = -35.658 \text{ MHz}$

$g_F = 3/11$

$\Delta E_{87} = g_F M_F \mu_B B$

② The freq spacing between two ^{nearest} sublevels is $\Delta E'_{87} = g_F \mu_B B$

Eq. ① & ② are in the same magnetic field B, so we have

$\frac{\Delta E'_{88}}{\Delta E'_{87}} = \frac{g_S}{g_F} = \frac{1.5}{3/11} = 5.5$ ③

Cal

★ Exp Data

scan 1.

$\Delta E'_{88} = 0.3146, 0.3184 \Rightarrow \Delta E'_{88} = 0.3165 \text{ S}$

$\Delta E'_{87} \approx 0.132 \text{ S} = 2.86 \text{ MHz}$

$\frac{\Delta E'_{88}}{\Delta E'_{87}} = 2.40$

Exp

④

$\frac{32}{3} \text{ V/S}, \times 2.034 \text{ MHz/V} = 21.696 \text{ MHz/S}$

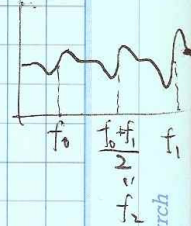
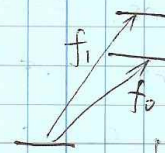
③ & ④ match not well.

However, as to a two-level system, there should be three Lamb dips.

The f_2 is because, that

$$\left. \begin{aligned} -kv + f_l &= f_0 \\ kv + f_l &= f_1 \end{aligned} \right\} \text{ or } \left. \begin{aligned} -kv + f_l &= f_1 \\ kv + f_l &= f_0 \end{aligned} \right\}$$

$\Rightarrow f_l = \frac{f_0 + f_1}{2}$



I have a hypothesis that the f_3 on the left fig. 1 is the $(f_0 + f_1)/2$ mentioned above so that the calculated

Important: Place card under blue copy.

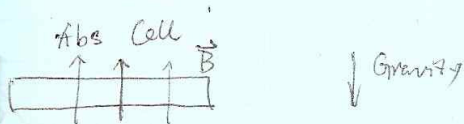
(see back)

$\frac{\Delta E_{32}}{\Delta E_{21}}$ should be half of the previous one, saying 2.75, which is in agreement with the measured value 2.40 very well.

To prove this hypothesis, I will do the following things.

1. Decrease the B field by lowering the coils voltage so that we ~~can~~^{may} see all ~~the~~ three expected clips in either side.
2. The wave plate will be used to increase the intensity contributed by

$$m = \pm 1$$



If the linear polarization of laser is vertical, $\Delta m = 0$ occurs. If the linear polarization is horizontal, $\Delta m = \pm 1$ occurs. Now the polarization is mixed, so we can see all the transitions.

Bibliography

- [1] M. H. Anderson, J. R. Ensher, M. R. Matthews, C. E. Wieman, and E. A. Cornell. Observation of Bose-Einstein Condensation in a Dilute Atomic Vapor. *Science*, 269:198, 1995.
- [2] K. B. Davis, M. O. Mewes, M. R. Andrews, N. J. van Druten, D. S. Durfee, D. M. Kurn, and W. Ketterle. Bose-Einstein Condensation in a Gas of Sodium Atoms. *Phys. Rev. Lett.*, 75:3969, 1995.
- [3] C. C. Bradley, C. A. Sackett, J. J. Tollett, and R. G. Hulet. Evidence of Bose-Einstein Condensation in an Atomic Gas with Attractive Interactions. *Phys. Rev. Lett.*, 75:1687, 1995.
- [4] C. C. Bradley, C. A. Sackett, and R. G. Hulet. Bose-Einstein Condensation of Lithium: Observation of Limited Condensate Number. *Phys. Rev. Lett.*, 78:985, 1997.
- [5] A. Einstein. Quantentheorie des einatomigen idealen Gases. *Sitzungsber. Kgl. Preuss. Akad. Wiss.*, 1924:261, 1924.
- [6] S. N. Bose. Planck's Law and the Light Quantum Hypothesis. *Zeits. f. Physik*, 26:178, 1924.

- [7] P. Kapitza. Viscosity of Liquid Helium below the λ -Point. *Nature*, 141:74, 1938.
- [8] J. F. Allen and A. D. Misener. Flow of Liquid Helium II. *Nature*, 141:75, 1938.
- [9] F. London. The I-Phenomenon of Liquid Helium and the Bose-Einstein Degeneracy. *Nature*, 141:643, 1938.
- [10] H. K. Onnes. On the sudden rate at which the resistance of mercury disappears. *Akad. von Wetenschappen*, 14:113, 1911.
- [11] J. Bardeen, L. N. Cooper, and J. R. Schrieffer. Microscopic Theory of Superconductivity. *Phys. Rev.*, 106:162, 1957.
- [12] J. Bardeen, L. N. Cooper, and J. R. Schrieffer. Theory of Superconductivity. *Phys. Rev.*, 108:1175, 1957.
- [13] D. D. Osheroff, R. C. Richardson, and D. M. Lee. Evidence for a New Phase of Solid ^3He . *Phys. Rev. Lett.*, 28:885, 1972.
- [14] A. J. Leggett. Interpretation of Recent Results on He^3 below 3 mK: A New Liquid Phase? *Phys. Rev. Lett.*, 29:1227, 1972.
- [15] P. Sokol. Bose-Einstein Condensation in Liquid Helium. In A. Griffin, D. W. Snoke, and S. Stringari, editors, *Bose Einstein Condensation*, Cambridge, 1995. Cambridge University Press.
- [16] C. E. Hecht. The possible superfluid behaviour of hydrogen atom gases and liquids. *Physica*, 25:1159, 1959.

- [17] W. C. Stwalley and L. H. Nosanow. Possible “New” Quantum Systems. *Phys. Rev. Lett.*, 36:910, 1976.
- [18] H. F. Hess, G. P. Kochanski, J. M. Doyle, N. Masuhara, D. Kleppner, and T. J. Greytak. Magnetic trapping of spin-polarized atomic hydrogen. *Phys. Rev. Lett.*, 59:672, 1987.
- [19] R. van Roijen, J. J. Berkhout, S. Jaakkola, and J. T. M. Walraven. Experiments with Atomic Hydrogen in a Magnetic Trapping Field. *Phys. Rev. Lett.*, 61:931, 1988.
- [20] J. M. Doyle, J. C. Sandberg, N. Masuhara, I. A. Yu, D. Kleppner, and T. J. Greytak. Energy distributions of trapped atomic hydrogen. *J. Opt. Soc. Am. B*, 6, 1989.
- [21] J. M. Doyle, J. C. Sandberg, I. A. Yu, C. L. Cesar, D. Kleppner, and T. J. Greytak. Hydrogen in the submillikelvin regime: Sticking probability on superfluid ^4He . *Phys. Rev. Lett.*, 67:603, 1991.
- [22] John Morrissey Doyle. *Energy distribution measurements of magnetically trapped spin polarized atomic hydrogen: evaporative cooling and surface sticking*. PhD thesis, Massachusetts Institute of Technology, 1991.
- [23] N. Masuhara, J. M. Doyle, J. C. Sandberg, D. Kleppner, T. J. Greytak, H. F. Hess, and G. P. Kochanski. Evaporative Cooling of Spin-Polarized Atomic Hydrogen. *Phys. Rev. Lett.*, 61:935, 1988.

- [24] T. Kurosu and F. Shimizu. Laser cooling and trapping of calcium and strontium. *Jpn. J. Appl. Phys.*, 29:2127, 1990.
- [25] Y. Takasu, K. Maki, K. Komori, T. Takano, K. Honda, M. Kumakura, T. Yabuzaki, and Y. Takahashi. Spin-Singlet Bose-Einstein Condensation of Two-Electron Atoms. *Phys. Rev. Lett.*, 91:040404, 2003.
- [26] T. Fukuhara, S. Sugawa, and Y. Takahashi. Bose-Einstein condensation of an ytterbium isotope. *Phys. Rev. A*, 76:051604, 2007.
- [27] T. Fukuhara, S. Sugawa, Y. Takasu, and Y. Takahashi. All-optical formation of quantum degenerate mixtures. *Phys. Rev. A*, 79:021601, 2009.
- [28] S. Kraft, F. Vogt, O. Appel, F. Riehle, and U. Sterr. Bose-Einstein Condensation of Alkaline Earth Atoms: Ca^{40} . *Phys. Rev. Lett.*, 103:130401, 2009.
- [29] S. Stellmer, M. K. Tey, B. Huang, R. Grimm, and F. Schreck. Bose-Einstein Condensation of Strontium. *Phys. Rev. Lett.*, 103:200401, 2009.
- [30] Y. N. Martinez de Escobar, P. G. Mickelson, M. Yan, B. J. DeSalvo, S. B. Nagel, and T. C. Killian. Bose-Einstein Condensation of ^{84}Sr . *Phys. Rev. Lett.*, 103:200402, 2009.
- [31] P. G. Mickelson, Y. N. Martinez de Escobar, M. Yan, B. J. DeSalvo, and T. C. Killian. Bose-Einstein Condensation of ^{88}Sr Through Sympathetic Cooling with ^{87}Sr . arXiv:1003.3867, submitted to *Phys. Rev. A* (R), 2010.

- [32] M. Hermele, V. Gurarie, and A. Maria Rey. Mott Insulators of Ultracold Fermionic Alkaline Earth Atoms: Underconstrained Magnetism and Chiral Spin Liquid. *Phys. Rev. Lett.*, 103:135301, 2009.
- [33] M. Foss-Feig, M. Hermele, and A. M. Rey. Probing the Kondo Lattice Model with Alkaline Earth Atoms. arxiv.org/pdf/0912.4762, (to be published), 2009.
- [34] A. V. Gorshkov, M. Hermele, V. Gurarie, C. Xu, P. S. Julienne, J. Ye, P. Zoller, E. Demler, M. D. Lukin, and A. M. Rey. Two-orbital SU(N) magnetism with ultracold alkaline-earth atoms. *Nat. Phys.*, <http://dx.doi.org/10.1038/nphys1535>, 2010.
- [35] M. Takamoto, F.-L. Hong, R. Higashi, and H. Katori. An optical lattice clock. *Nature*, 435:321, 2005.
- [36] D. Jaksch, C. Bruder, J. I. Cirac, C. W. Gardiner, and P. Zoller. Cold Bosonic Atoms in Optical Lattices. *Phys. Rev. Lett.*, 81:3108, 1998.
- [37] M. Greiner, O. Mandel, T. Esslinger, T. W. Hansch, and I. Bloch. Quantum phase transition from a superfluid to a Mott insulator in a gas of ultracold atoms. *Nature*, 415:39, 2002.
- [38] D. Hayes, P. S. Julienne, and I. H. Deutsch. Quantum Logic via the Exchange Blockade in Ultracold Collisions. *Phys. Rev. Lett.*, 98:070501, 2007.
- [39] I. Reichenbach and I. H. Deutsch. Sideband Cooling while Preserving Co-

- ferences in the Nuclear Spin State in Group-II-like Atoms. *Phys. Rev. Lett.*, 99:123001, 2007.
- [40] A. J. Daley, M. M. Boyd, J. Ye, and P. Zoller. Quantum Computing with Alkaline-Earth-Metal Atoms. *Phys. Rev. Lett.*, 101:170504, 2008.
- [41] A. V. Gorshkov, A. M. Rey, A. J. Daley, M. M. Boyd, J. Ye, P. Zoller, and M. D. Lukin. Alkaline-Earth-Metal Atoms as Few-Qubit Quantum Registers. *Phys. Rev. Lett.*, 102:110503, 2009.
- [42] K. M. Jones, E. Tiesinga, P. D. Lett, and P. S. Julienne. Ultracold photoassociation spectroscopy: Long-range molecules and atomic scattering. *Rev. of Mod. Phys.*, 78:483, 2006.
- [43] T. Zelevinsky, S. Kotochigova, and Jun Ye. Precision Test of Mass-Ratio Variations with Lattice-Confined Ultracold Molecules. *Phys. Rev. Lett.*, 100:043201, 2008.
- [44] R. Ciuryło, E. Tiesinga, and P. S. Julienne. Optical tuning of the scattering length of cold alkaline-earth-metal atoms. *Phys. Rev. A*, 71:030701, 2005.
- [45] K. Enomoto, K. Kasa, M. Kitagawa, and Y. Takahashi. Optical Feshbach Resonance Using the Intercombination Transition. *Phys. Rev. Lett.*, 101:203201, 2008.

- [46] H. Saito and M. Ueda. Dynamically Stabilized Bright Solitons in a Two-Dimensional Bose-Einstein Condensate. *Phys. Rev. Lett.*, 90:040403, 2003.
- [47] M. I. Rodas-Verde, H. Michinel, and V. M. Pérez-García. Controllable Soliton Emission from a Bose-Einstein Condensate. *Phys. Rev. Lett.*, 95:153903, 2005.
- [48] M. P. A. Fisher, P. B. Weichman, G. Grinstein, and D. S. Fisher. Boson localization and the superfluid-insulator transition. *Phys. Rev. B*, 40:546, 1989.
- [49] F. Dalfovo, S. Giorgini, L. P. Pitaevskii, and S. Stringari. Theory of Bose-Einstein condensation in trapped gases. *Rev. Mod. Phys.*, 71:463, 1999.
- [50] M. R. Andrews, M.-O. Mewes, N. J. van Druten, D. S. Durfee, D. M. Kurn, and W. Ketterle. Direct, Nondestructive Observation of a Bose Condensate. *Science*, 273:84, 1996.
- [51] J. Lawall, S. Kulin, B. Saubamea, N. Bigelow, M. Leduc, and C. Cohen-Tannoudji. Three-Dimensional Laser Cooling of Helium Beyond the Single-Photon Recoil Limit. *Phys. Rev. Lett.*, 75:4194, 1995.
- [52] W. Ketterle and N. J. van Druten. Evaporative cooling of trapped atoms. *Adv. Atom. Mol. Opt. Phys.*, 37:181, 1996.
- [53] J. T. M. Walraven. Atomic hydrogen in magnetostatic traps. In G. L. Oppo, S. M. Barnett, E. Riis, and M. Wilkinson, editors, *Quantum Dynamics of Simple Systems*, London, 1996. Institute of Physics.

- [54] C. J. Foot. *Atomic Physics*. Oxford University Press, Oxford, 2004.
- [55] C. J. Pethick and H. Smith. *Bose-Einstein Condensation in Dilute Gases*. Cambridge University Press, 2nd edition, 2008.
- [56] T. C. Killian, D. G. Fried, L. Willmann, D. Landhuis, S. C. Moss, D. Kleppner, and T. J. Greytak. Cold Collision Frequency Shift of the 1S-2S Transition in Hydrogen. *Phys. Rev. Lett.*, 81:3807, 1998.
- [57] W. Petrich, M. H. Anderson, J. R. Ensher, and E. A. Cornell. Stable, Tightly Confining Magnetic Trap for Evaporative Cooling of Neutral Atoms. *Phys. Rev. Lett.*, 74:3352, 1995.
- [58] K. B. Davis, M.-O. Mewes, M. A. Joffe, M. R. Andrews, and W. Ketterle. Evaporative Cooling of Sodium Atoms. *Phys. Rev. Lett.*, 74:5202, 1995.
- [59] R. Grimm, M. Weidemüller, and Y. B. Ovchinnikov. Optical dipole traps for neutral atoms. *Adv. Atom. Mol. Opt. Phys.*, 42:95, 2000.
- [60] M. D. Barrett, J. A. Sauer, and M. S. Chapman. All-optical formation of an atomic Bose-Einstein condensate. *Phys. Rev. Lett.*, 87:010404, 2001.
- [61] M. Machholm, P. S. Julienne, and K.-A. Suominen. Calculations of collisions between cold alkaline-earth-metal atoms in a weak laser field. *Phys. Rev. A*, 64, 2001.

- [62] P. G. Mickelson, Y. N. Martinez, A. D. Saenz, S. B. Nagel, Y. C. Chen, T. C. Killian, P. Pellegrini, and R. Cote. Spectroscopic determination of the s -wave scattering lengths of ^{86}Sr and ^{88}Sr . *Phys. Rev. Lett.*, 95:223002, 2005.
- [63] Y. N. Martinez de Escobar, P. G. Mickelson, P. Pellegrini, S. B. Nagel, A. Traverso, M. Yan, R. Côté, and T. C. Killian. Two-photon photoassociative spectroscopy of ultracold ^{88}Sr . *Phys. Rev. A*, 78:062708, 2008.
- [64] T. Ido, Y. Isoya, and H. Katori. Optical-dipole trapping of Sr atoms at a high phase-space density. *Phys. Rev. A*, 61, 2000.
- [65] G. Ferrari, R. E. Drullinger, N. Poli, F. Sorrentino, and G. M. Tino. Cooling of Sr to high phase-space density by laser and sympathetic cooling in isotopic mixtures. *Phys. Rev. A*, 73:023408, 2006.
- [66] T. W. Hänsch and A. L. Schawlow. Cooling of gases by laser radiation. *Optics Communications*, 13:68, 1975.
- [67] D. Wineland and H. Dehmelt. Proposed $10^{14} \delta\nu/\nu$ Laser Fluorescence Spectroscopy on Tl^+ Mono-Ion Oscillator. *Bull. Am. Phys. Soc.*, 20:637, 1975.
- [68] H. J. Metcalf and P. van der Straten. *Laser Cooling and Trapping*. Springer-Verlag, New York, 1999.
- [69] E. L. Raab, M. Prentiss, A. Cable, S. Chu, and D. E. Pritchard. Trapping of Neutral Sodium Atoms with Radiation Pressure. *Phys. Rev. Lett.*, 59:2631,

1987.

- [70] P. G. Mickelson, Y. N. Martinez de Escobar, P. Anzel, B. J. DeSalvo, S. B. Nagel, A. J. Traverso, M. Yan, and T. C. Killian. Repumping and spectroscopy of laser-cooled Sr atoms using the $(5s5p)^3P_2 - (5s4d)^3D_2$ transition. *J. Phys. B: At. Mol. Opt. Phys.*, 42:235001, 2009.
- [71] Y. Castin, H. Wallis, and J. Dalibard. Limit of Doppler cooling. *J. Opt. Soc. Am. B*, 6:2046, 1989.
- [72] T. Loftus, T. Ido, A. D. Ludlow, M. M. Boyd, and J. Ye. Narrow Line Cooling: Finite Photon Recoil Dynamics. *Phys. Rev. Lett.*, 93:073003, 2004.
- [73] H. Katori, T. Ido, Y. Isoya, and M. Kuwata-Gonokami. Magneto-Optical Trapping and Cooling of Strontium Atoms down to the Photon Recoil Temperature. *Phys. Rev. Lett.*, 82:1116, 1999.
- [74] Sarah B. Nagel. *Ultracold Collisions in Atomic Strontium*. PhD thesis, Rice University, February 2008.
- [75] Pascal G. Mickelson. *Trapping and Evaporation of ^{87}Sr and ^{88}Sr Mixtures*. PhD thesis, Rice University, April 2010.
- [76] T. C. Killian, Y. C. Chen, P. Gupta, S. Laha, Y. N. Martinez, P. G. Mickelson, S. B. Nagel, A. D. Saenz, and C. E. Simien. Absorption imaging and

- spectroscopy of ultracold neutral plasmas. *J. Phys. B: At. Mol. Opt. Phys.*, 38, 2005.
- [77] M. Yasuda and H. Katori. Lifetime Measurement of the 3P_2 Metastable State of Strontium Atoms. *Phys. Rev. Lett.*, 92:153004, 2006.
- [78] S. B. Nagel, C. E. Simien, S. Laha, P. Gupta, V. S. Ashoka, and T. C. Killian. Magnetic trapping of metastable 3P_2 atomic strontium. *Phys. Rev. A*, 67:011401, 2003.
- [79] X. Xu, T. H. Loftus, J. W. Dunn, C. H. Greene, J. L. Hall, A. Gallagher, and J. Ye. Single-Stage Sub-Doppler Cooling of Alkaline Earth Atoms. *Phys. Rev. Lett.*, 90:193002, 2003.
- [80] N. Poli, R. E. Drullinger, G. Ferrari, J. Léonard, F. Sorrentino, and G. M. Tino. Cooling and trapping of ultracold strontium isotopic mixtures. *Phys. Rev. A*, 71:061403, 2005.
- [81] M. Bode, I. Freitag, A. Tünnermann, and H. Welling. Frequency-tunable 500-mW continuous-wave all-solid-state single-frequency source in the blue spectral region. *Opt. Lett.*, 22:1220, 1997.
- [82] Aaron D. Saenz. 461nm laser for studies in ultracold neutral strontium. Master's thesis, Rice University, 2005.
- [83] C. Wieman and T. W. Hänsch. Doppler-Free Laser Polarization Spectroscopy.

- Phys. Rev. Lett.*, 36:1170, 1976.
- [84] W. Demtröder. *Laser Spectroscopy*. Springer-Verlag, Berlin, 3rd edition, 1981.
- [85] B. A. Bushaw and W. N. Resonance ionization spectroscopy of stable strontium isotopes and ^{90}Sr via $5s^2\ ^1S_0 \rightarrow 5s5p\ ^1P_1 \rightarrow 5s5d\ ^1D_2 \rightarrow 5s11f\ ^1F_3 \rightarrow \text{Sr}^+$. *Spectrochimica Acta Part B: Atomic Spectroscopy*, 55:1679, 2000.
- [86] M. G. Littman and H. J. Metcalf. Spectrally narrow pulsed dye laser without beam expander. *Appl. Opt.*, 17:2224, 1978.
- [87] R. W. P. Drever, J. L. Hall, F. V. Kowalski, J. Hough, G. M. Ford, A. J. Munley, and H. Ward. Laser Phase and Frequency Stabilization Using an Optical Resonator. *Appl. Phys. B*, 31:97, 1983.
- [88] T. Fukuhara, Y. Takasu, M. Kumakura, and Y. Takahashi. Degenerate Fermi Gases of Ytterbium. *Phys. Rev. Lett.*, 98:030401, 2007.
- [89] S. Friebel, C. D'Andrea, J. Walz, M. Weitz, and T. W. Hänsch. CO_2 -laser optical lattice with cold rubidium atoms. *Phys. Rev. A*, 57:R20, 1998.
- [90] J. Ye, H. J. Kimble, and H. Katori. Quantum State Engineering and Precision Metrology Using State-Insensitive Light Traps. *Science*, 320:1734, 2008.
- [91] J. J. Sakurai and S. F. Tuan. *Modern Quantum Mechanics*. Addison-Wesley Publishing, Reading, Massachusetts, Revised edition, 1994.

- [92] L. D. Landau and E. M. Lifshitz. *Quantum Mechanics: Non-relativistic Theory*. Pergamon Press, Oxford, 3rd. edition, 1977.
- [93] J. Dalibard. Collisional dynamics of ultra-cold atomic gases. In M. Inguscio, S. Stringari, and C. E. Wieman, editors, *Bose-Einstein Condensation in Atomic Gases, Proceedings of the International School of Physics “Enrico Fermi”, Course CXL*, Amsterdam, 1999. IOS Press.
- [94] G. F. Gribakin and V. V. Flambaum. Calculation of the scattering length in atomic collisions using the semiclassical approximation. *Phys. Rev. A*, 48:546, 1993.
- [95] J. Weiner, V. S. Bagnato, S. Zilio, and P. S. Julienne. Experiments and theory in cold and ultracold collisions. *Rev. Mod. Phys.*, 71:1, 1999.
- [96] F. Riehle. *Frequency Standards: Basics and Applications*. Wiley-VCH, Germany, 2004.
- [97] J. Tennyson. *Astronomical Spectroscopy*. Imperial College Press, London, 2005.
- [98] T. Zelevinsky, M. M. Boyd, A. D. Ludlow, T. Ido, J. Ye, R. Ciuryło, P. Naidon, and P. S. Julienne. Narrow Line Photoassociation in an Optical Lattice. *Phys. Rev. Lett.*, 96:203201, 2006.
- [99] R. Napolitano, J. Weiner, C. J. Williams, and P. S. Julienne. Line shapes of high resolution photoassociation spectra of optically cooled atoms. *Phys. Rev.*

- Lett*, 73:1352, 1994.
- [100] J. L. Bohn and P.S. Julienne. Semianalytic treatment of two-color photoassociation spectroscopy and control of cold atoms. *Phys. Rev. A*, 54:R4637, 1996.
- [101] R. Ciuryło, E. Tiesinga, S. Kotochigova, and P. S. Julienne. Photoassociation spectroscopy of cold alkaline earth atoms near the intercombination line. *Phys. Rev. A*, 70:062710, 2004.
- [102] K. M. Jones, P. D. Lett, E. Tiesinga, and P. S. Julienne. Fitting line shapes in photoassociation spectroscopy of ultracold atoms: A useful approximation. *Phys. Rev. A*, 61:012501, 1999.
- [103] Eugene P. Wigner. On the Behavior of Cross Sections Near Thresholds. *Phys. Rev.*, 73:1002, 1948.
- [104] S. B. Nagel, P. G. Mickelson, A. D. Saenz, Y. N. Martinez, Y. C. Chen, T. C. Killian, P. Pellegrini, and R. Côté. Photoassociative Spectroscopy at Long Range in Ultracold Strontium. *Phys. Rev. Lett.*, 94:083004, 2005.
- [105] M. Yasuda, T. Kishimoto, M. Takamoto, and H. Katori. Photoassociation spectroscopy of ^{88}Sr Reconstruction of the wave function near the last node. *Phys. Rev. A*, 73:011403, 2006.
- [106] H. R. Thorsheim, J. Weiner, and P. S. Julienne. Laser-induced photoassociation of ultracold sodium atoms. *Phys. Rev. Lett.*, 58:2420, 1987.

- [107] A. Fioretti, D. Comparat, A. Crubellier, O. Dulieu, F. Masnou-Seeuws, and P. Pillet. Formation of Cold Cs_2 Molecules through Photoassociation. *Phys. Rev. Lett.*, 80, 1998.
- [108] A. Stein, H. Knöckel, and E. Tiemann. Fourier-transform spectroscopy of Sr_2 and revised ground state potential. *Phys. Rev. A*, 78:042508, 2008.
- [109] E. G. M. van Kempen, S. J. J. M. F. Kokkelmans, D. J. Heinzen, and B. J. Verhaar. Interisotope Determination of Ultracold Rubidium Interactions from Three High-Precision Experiments. *Phys. Rev. Lett.*, 88:093201, 2002.
- [110] M. Yan, R. Chakraborty, P. G. Mickelson, Y. N. Martinez de Escobar, and T. C. Killian. Numerical modeling of collisional dynamics of Sr in an optical dipole trap. *arxiv:0905.2223*, 2009.
- [111] H. F. Hess. Evaporative cooling of magnetically trapped and compressed spin-polarized hydrogen. *Phys. Rev. B*, 34:3476, 1986.
- [112] C. R. Monroe, E. A. Cornell, C. A. Sackett, C. J. Myatt, and C. E. Wieman. Measurement of Cs-Cs elastic scattering at $T=30 \mu\text{K}$. *Phys. Rev. Lett.*, 70:414, 1993.
- [113] K. B. Davis, M.-O. Mewes, and W. Ketterle. An analytical model for evaporative cooling of atoms. *Appl. Phys. B*, 60:155, 1995.
- [114] O. J. Luiten, M. W. Reynolds, and J. T. M. Walraven. Kinetic theory of the

- evaporative cooling of a trapped gas. *Phys. Rev. A*, 53:381, 1996.
- [115] K. M. O'Hara, M. E. Gehm, S. R. Granade, and J. E. Thomas. Scaling laws for evaporative cooling in time-dependent optical traps. *Phys. Rev. A*, 64:051403, 2001.
- [116] Kenneth M. O'Hara. *Optical Trapping and Evaporative Cooling of Fermionic Atoms*. PhD thesis, Duke University, 2000.
- [117] K. Huang. *Statistical Mechanics*. John Wiley & Sons, New York, 2nd edition, 1987.
- [118] K. Berg-Sørensen. Kinetics for evaporative cooling of a trapped gas. *Phys. Rev. A*, 55:1281, 1997.
- [119] K. Berg-Sørensen. Erratum: Kinetics for evaporative cooling of a trapped gas. *Phys. Rev. A*, 56:3308, 1997.
- [120] Y. N. Martinez de Escobar, P. G. Mickelson, M. Yan, and T. C. Killian. Modification of atom scattering using an intercombination-line optical feshbach resonance at large detuning, 2009.
- [121] V. Bagnato, D. E. Pritchard, and D. Kleppner. Bose-Einstein condensation in an external potential. *Phys. Rev. A*, 35:4354, 1987.
- [122] V. V. Goldman, I. F. Silvera, and A. J. Leggett. Atomic hydrogen in an inhomogeneous magnetic field: Density profile and Bose-Einstein condensation.

- Phys. Rev. B*, 24:2870, 1981.
- [123] D. A. Huse and E. D. Siggia. The Density Distribution of a Weakly Interacting Bose Gas in an External Potential. *J. Low Temp. Phys.*, 46:137, 1982.
- [124] W. Ketterle, D. S. Durfee, and D. M. Stamper-Kurn. Making, probing and understanding Bose-Einstein condensates. In M. Inguscio, S. Stringari, and C. E. Wieman, editors, *Bose-Einstein condensation in atomic gases, Proceedings of the International School of Physics “Enrico Fermi”, Course CXL*, Amsterdam, 1999. IOS Press.
- [125] A. L. Fetter and J. D. Walecka. *Quantum Theory of Many-Particle Systems*. Dover Publications, New York, 2003.
- [126] L. Pitaevskii and S. Stringari. *Bose-Einstein Condensation*. Oxford University Press, Oxford, New edition, 2003.
- [127] N. N. Bogolubov. On the theory of superfluidity. *J. Phys. (USSR)*, 11:23, 1947.
- [128] E. P. Gross. Structure of a quantized vortex in boson systems. *Nuovo Cimento (Italy)*, 20:454, 1961.
- [129] E. P. Gross. Hydrodynamics of a Superfluid Condensate. *J. Math. Phys.*, 4:195, 1963.
- [130] L. P. Pitaevskii. Vortex lines in an imperfect Bose gas. *Sov. Phys. JETP (USA)*, 13:451, 1961. Originally published: *Zh. eksper. teor Fiz. (USSR)* 40, 646 (1961).

- [131] Y. Castin and R. Dum. Bose-Einstein Condensates in Time Dependent Traps. *Phys. Rev. Lett.*, 77:5315, 1996.
- [132] D. M. Stamper-Kurn, M. R. Andrews, A. P. Chikkatur, S. Inouye, H.-J. Miesner, J. Stenger, and W. Ketterle. Optical Confinement of a Bose-Einstein Condensate. *Phys. Rev. Lett.*, 80:2027, 1998.
- [133] M.-O. Mewes, M. R. Andrews, N. J. van Druten, D. M. Kurn, D. S. Durfee, and W. Ketterle. Bose-Einstein Condensation in a Tightly Confining dc Magnetic Trap. *Phys. Rev. Lett.*, 77:416, 1996.
- [134] J. Söding, D. Guéry-Odelin, P. Desbiolles, F. Chevy, H. Inamori, and J. Dalibard. Three-body decay of a rubidium Bose-Einstein condensate. *Appl. Phys. B*, 69:257, 1999.
- [135] E. A. Burt, R. W. Ghrist, C. J. Myatt, M. J. Holland, E. A. Cornell, and C. E. Wieman. Coherence, Correlations, and Collisions: What One Learns about Bose-Einstein Condensates from Their Decay. *Phys. Rev. Lett.*, 79:337, 1997.
- [136] P. O. Fedichev, M. W. Reynolds, and G. V. Shlyapnikov. Three-Body Recombination of Ultracold Atoms to a Weakly Bound s Level. *Phys. Rev. Lett.*, 77:2921, 1996.
- [137] B. D. Esry, C. H. Greene, and J. P. Burke. Recombination of Three Atoms in the Ultracold Limit. *Phys. Rev. Lett.*, 83:1751, 1999.

- [138] Yu. Kagan, B. V. Svistunov, and G. V. Shlyapnikov. Effect of bose condensation on inelastic processes in gases. *JETP Lett.*, 42:209, 1985. Originally published: *Pis'ma Zh. Eksp. Teor. Fiz.* 42, 169 (1985).
- [139] H. Kogelnik and T. Li. Laser beams and resonators. *Appl. Opt.*, 5:1550, 1966.
- [140] Clayton Simien. 422 nm laser. Master's thesis, Rice University, 2003.
- [141] Sarah B. Nagel. A narrow linewidth diode laser system for strontium laser cooling applications. Master's thesis, Rice University, 2004.